Modélisation, estimation et contrôle de Microscope á Force Atomique

Michal Hrouzek

To cite this version:

Michal Hrouzek. Modélisation, estimation et contrôle de Microscope á Force Atomique. Automatique / Robotique. Université Joseph-Fourier - Grenoble I, 2007. Français. NNT : . tel-00267958

HAL Id: tel-00267958
https://theses.hal.science/tel-00267958

Submitted on 29 Mar 2008

UNIVERSITÉ JOSEPH FOURIER-GRENOBLE
and
BRNO UNIVERSITY OF TECHNOLOGY

THESIS

for obtaining the degree of

DOCTEUR DE L'UNIVERSITÉ JOSEPH FOURIER (Ph.D.)

IN AUTOMATIQUE - PRODUCTIQUE

prepared at *Laboratoire d'Automatique de Grenoble,*
Department of Control and Instrumentation, FEEC BUT
and The European Synchrotron Radiation Facility

presented and sat by

Michal Hrouzek

30 May 2007

Atomic Force Microscopy, modeling, estimation and control

Didier Georges	Professor at INPG Grenoble, FR	President
Antoine Ferreira	Assoc.Professor at ENSI/LVR Bourges, FR	Reviewer
Pavel Tománek	Professor at FEEC BUT, CZ	Reviewer
Alina Voda	Assoc.Professor at UJF, FR	Thesis director
Joël Chevrier	Professor at UJF, FR	Thesis director
Pavel Jura	Professor at FEEC BUT, CZ	Thesis director
Frantisek Zezulka	Professor at FEEC BUT, CZ	Examinator

To Camille.

Acknowledgement

There are so many people, whom I should thank to.

First of all, I would like to express my sincere gratitude to my supervisors, Prof. Joël Chevrier, Assoc. Prof. Alina Voda and Prof. Pavel Jura, who helped me to find the topic of my thesis and advised me during my thesis to successfully contribute to this challenging subject.

This thesis has took me to field of surface physics. I would like to thank to Mario Rodrigues, Joël Chevrier and Martin Stark to help me to enter this completely new subject. Furthermore, I have to say “obrigado" to Mario Rodrigues for taking the time to explain me the physics and discussing with me many important parts of my thesis.

I would like to express my recognition to all the people that I have been working with at the Surface Science Laboratory: Guillaume Jourdan, Simon Ledenmat, Olivier Dhez, Wilfrid Schwartz, Justine Etienne, Alessandro Siria, Florence Marchi, Frederico Martins, Raphaelle Dianoux, Yannick Sonnefraud, Emilie Dubard.

I also would like to thank to Fabio Comin for all the scientific, organization and technical support. As well, for the opportunity to stay at the European Synchrotron Radiation Facility during my thesis and profit from this great scientific environment.

Finally, I cannot miss the occasion to thank to my family for their support.

Michal Hrouzek
Grenoble, May 2007

This thesis has been partially supported by the European Commision (Marie Curie Fellowship) and the European Synchrotron Radiation Facility, Grenoble, France.

Contents

List of Figures

List of Tables

Résumé

Introduction:

Ces dernières années la nanoscience est l'un des champs d'etude les plus développés de la science. L'application et la recherche fondamentale sont concentrées sur différents domains qui ont en commun l'interprétation à l'echelle du nano.
Pour être capable d'accomplir la recherche à l'echelle du nano, les scientifiques ont utilisé une large variété de techniques caractérisants le sujet d'étude. Ainsi, à ce niveau la microscopie à sonde locale (SPM - Scanning Probe Microscopy) représente l'un des plus importants outils de mesure d'objet et de surface. Cette technique existe depuis plus de 20 ans et a surmonté plusieurs développements techniques et scientifiques. Les domaines d'application du SPM sont très larges, ils vont de la physique de surface à la science des matières, à la micro-électronique, à la biologie et à la chimie. L'utilisation du balayage à sonde microscopique se combine à d'autres techniques lui imposant de nouvelles éxigences quant à l'outil et stimule le développement de cette technologie. La microscopie à force atomique (AFM - Atomic Force Microscopy) est un type particulier du SPM, elle utilise des forces inter-atomique entre la pointe et la surface dans le but d'obtenir la topographie de surface.
Ma thèse essaye de contribuer à ce développement, et par ce biais, d'améliorer les techniques existantes de l'AFM par l'utilisation de stratégies de contrôle avancé. Je traite en particulier d'une nouvelle méthode pour les opérations de l'AFM en milieu liquide. Ce travail n'est pas exhaustif et il faut étendre les références pour approfondir le sujet.
Cette thèse a été effectuée grâce à la supervision entre l'Université de Technologie de Brno (B.U.T) en République Tchèque, département de contrôle et intrumentalisation, et l'Université Joseph Fourrier de Grenoble (U.J.F) en France, laboratoire d'Automatique de Grenoble (L.A.G). Ces deux institutions ont fourni le support scientifique nécessaire. Les activités de recherches ont été réalisées à l'European Synchrotron Radiation Facility de Grenoble (E.S.R.F). L'institut européen de recherche a concentré ses activités sur la recherche utilisant la radiation par rayons X. À l'intérieur de l'E.S.R.F, le laboratoire de Science de Surface a approfondi ses recherches au domaine du balayage à sonde microscopique. Le laboratoire est constitué de chercheurs professionnels et d'étudiants, dirigé par Monsieur Fabio Comin, E.S.R.F divison expérimentale, et Monsieur Joel Chevrier, professeur de physique à l'U.J.F.

Centres dintérêts de la thèse :

Le travail présenté se concentre sur une complète compréhension de l'AFM du point de vue du contrôle. Cette analyse nous permet de proposer des améliorations au fonctionnement standard de l'AFM. En outre, avec cette connaissance nous pourrons concevoir une nouvelle technique pour faire fonctionner l'AFM. L'approche du contrôle joue un rôle important dans tout ce développement mais une profonde compréhension des instruments de physique a été requise.

Le second chapitre , plus court mais complet, a une vue d'ensemble des techniques les plus importantes pour faire fonctionner la microscopie à sonde locale (SPM) et plus précisement la microscopie à force atomique (AFM). Ce chapitre dévoile les avantages et inconvénients des techniques existantes. Les fonctions les plus basiques de l'AFM sont représentées : les sondes, les leviers de détection de position, le scanner d'échantillons et enfin le levier d'exitation et son utilisation comme un oscilateur harmonique. S'en suit un résumé des modes d'opération de contacte (statique) et modes d'opération de non-contacte (dynamique). Pour finir, un résumé des publications concernants l'application de la technique de contrôle avancé pour l'AFM.

Le troisième chapitre se concentre sur les interactions du modèle de surface et la dynamique du levier avec la pointe. Une simplifiacation des interactions du modèle de surface est présentée et utilisée comme base pour accomplir des simulations. S'en suit un modèle de levier simplifié et un modèle multimode plus complexe, basé sur la théorie du faisceau avec l'implantation d'un modèle pour une excitation thermique. Les deux modèles présentés sont basés sur des leviers mécaniques dont les propriétés sont fournies par un constructeur et ne requièrent aucune information complémentaire. Les simulations du modèle de levier thermique excité sont comparées aux mesures obtenues par le microscope à force atomique de Nanotec. Une méthode de minimisation est introduite pour ajuster les propriétés mécaniques obtenues afin d'améliorer le modèle avec précision. La fin de ce chapitre est consacrée à la simulation de modulation d'amplitude et le Tapping Mode avec pour objectif d'explorer l'importance des modes de levier à haute harmonie pour les méthodes de mesure.

Le quatrième chapitre présente une application des techniques de l'observateur pour l'AFM. Un courte introduction présente les perturbations de mesures et les perturbations données par la détection au début. Suit ensuite l'introduction théorique de l'observateur et ses applications pour le contrôle. Puis sont présentés deux observateurs d'application pour l'AFM dans une technique de modulation d'amplitude et une nouvelle mesure de force statique. Le premier observateur est capable de détecter une interaction de force qui utilise un mode standard de modulation d'amplitude. La deuxième méthode utilise un levier non excité pour mesurer l'interaction de force « pointe-surface » dans un mode statique et détermine directement l'intensité de la force.

Le cinquième chapitre présente un nouveau mode d'opération de l'AFM basé sur la mesure statique de la force d'interaction. Une technique « cold damping » est utilisée dans le but de faire fonctionner le levier dans un régime complètement statique, la description est faite en début de chapitre. Suivent une définition et une description théorique d'un nouveau mode dopération nommé « Cooling Mode ». Les principaux avantages et inconvénients qui sont comparés aux modes d'utilisation standard de l'AFM sont listés pour constater les améliorations des performances et d'en apprécier les limites. Le concept proposé requière une capacité pour actionner la fin libre du levier et un nouveau dessin actuateur électro-statique est présente. L'expérimentation menée prouve que ce concept est concu et identifié dans le texte suivant. Cette information nous permet de concevoir un contrôleur stable dans la technique de placement du pôle et qui obtient un système de contrôle robuste dont la compétence peut atténuer la distortion thermique du levier. Un modèle de tout le système expérimental a été construit et un système complet de simulation a été réalisé pour montrer des résultats similaires aux données expérimentales déjà éxistantes. Les résultats de mesures en temps réel sont présentés à la fin du chapitre. Le dernier chapitre conclue l'élaboration de ce travail et anticipe sur un éventuel développement du système proposé.

Conclusions et perspectives :

Le travail présenté dans cette thèse a demandé un nouveau point de vue ; Comment faire fonctionner la microscopie à force atomique et comment la stratégie de contrôle peut l'améliorer avec précision? Cette thèse est une interface entre la physique de surface avec son instrumentation et les techniques de contrôle avancé. Les résultats obtenus sont relayés par les échanges entre ces deux champs de la science qui permettent de proposer une nouvelle approche de l'AFM. L'introduction du contrôle dans les expériences de physique avec l'AFM permet d'aborder les problèmes qui ne sont pas nécessairement résolus par les améliorations des expériences. Le problème le plus important est la perturbation spontanée du système micromécanique utilisé comme capteur de force grâce à l'agitation thermique. Ce phénomène est connu sous le nom de mouvement de Brownian. Si il n'y a pas de raison pour limiter l'utilisation de l'AFM à très basse température, la mesure fondamentale de perturbation ne peut être éliminée. Cette thèse essaye de montrer les perturbations thermiques et propose de nouvelles méthodes pour améliorer avec justesse l'AFM en utilisant une température ambiante.
Les résultats peuvent être résumés en trois parties distinctes :

1. modelage du levier
2. application de l'observateur utilisant l'AFM
3. nouveau mode d'opération de l'AFM

Une attention particulière est donnée au modelage du levier comme un système dynamique multimode. L'approche de cette modélisation permet de bien comprendre le comportement dynamique du levier thermique excité qui est complexe. En outre, il permet de comprendre en profondeur la réponse du levier lorsqu'il attire ou repousse les forces d'interaction.

Le chapitre trois présente la possibilité de construire précisement un modèle de levier multimode basé sur les informations obtenues par le mouvement du levier libre thermiquement excité. L'identification du levier basée sur l'excitation thermique a été présentée et le modèle obtenu a été comparé avec les résultats de mesure. Deuxièmement, il a été montré un modèle de levier basé sur ses propres capacités mécaniques sans aucune autre identification. Avec ce modèle il est obtenu une divergence sur les données de mesures mais il permet d'obtenir une approximation très simple du comportement du système. Pour réduire cette erreur il est utilise une méthode de minimisation numérique permettant d'obtenir de nouveaux paramètres mécaniques du levier pour le modèle et de mieux correspondre au spectre mesuré du système agité thermiquement.
Les modèles dévelopés ont été utilisés dans l'étude de comportement du levier dans le mode dynamique « non-contacte » et l'opération dans le mode « Tapping mode ». Quand le levier oscillant approche la surface de mesure les forces jouent sur la pointe du levier modulant son mouvement. La force d'interaction est fortement non linéaire ce qui cause l'agitation simultanée de multiples modes harmoniques du levier, ce qui est démontré par simulation. Ceci contribue à baisser l'amplitude du premier mode de vibration en mode harmonique même si l'interaction de force ne se dissipe pas. L'énergie du levier oscillant librement est stockée à la première fréquence de résonnance. Quand le système est perturbé par une force non linéaire, une partie de l'énergie est transformée vers des harmoniques plus hautes et l'amplitude de vibration d'origine baisse.

Les résultats de cette modélisation ont été une étape nécessaire pour proposer de nouvelles techniques de détection de force basées sur un observateur d'état d'espace. Les modèles proposés ont été utilisés comme des modèles internes des observateurs. L'observateur d'état

d'espace est capable de refléter le système de mesure et d'estimer ses états internes bien qu'ils ne soient pas directement mesurables.
Ce fonctionnement a été utilisé pour une technique standard de modulation d'amplitude. L'observateur construit à sa propre saisie de la mesure de position du levier et estime la position actuelle de tous les modes harmoniques du levier. Ceci permet d'améliorer avec précision la détection de l'amplitude de vibration.
Il a été proposé de modifier le système de détection pour mieux explorer les possibilités de capacités de l'observateur afin d'estimer les forces d'interaction de surface. L'observateur d'état d'espace standard a été étendu avec un nouvel état représentant une force d'interaction inconnue. Ainsi l'observateur peut estimer la position du levier comme avant mais il a un nouvel état qui représente la force d'interaction. Il est important de réaliser que la véritable force d'interaction est fortement non linéaire mais que l'observateur utilisé est, lui, linéaire. C'est la raison pour laquelle la force d'interaction estimée ne correspond pas précisément à la forme de la vraie force, mais elle estime une énergie nécessaire pour obtenir une déviation semblable de la fréquence de résonnance originale du système. Si les valeurs de la force d'interaction réelle et estimée sont comparées, il est demontré que la technique d'estimation de force proposée a une précision supérieure à 0,5 pN.
Il est proposé un autre observateur basé sur la technique de l'AFM qui est la mesure de la force d'interaction avec un levier non excité en interaction attractive avec une surface étudiée. Cette technique de mesure non-contacte détecte l'interaction de force statique sans excitation du levier à sa fréquence de résonnance. Il a été démontré qu'une résolution meilleure à 1pN peut être obtenue.

Le principal résultat de cette thèse est une définition du nouveau mode d'opération de l'AFM qui a été nommé le « Cooling Mode ». Ce mode développe largement l'idée de la mesure de la force d'interaction de surface en régime de non-contacte avec un levier non exciteé. Cette approche de la mesure révèle plusieurs possibilités pour créer une image rapide en milieu liquide. L'AFM a été modifié pour opérer dans ce mode et un actionneur électrostatique a été ajouté au système déjà éxistant pour actionner le levier en fin libre. Les vibrations du levier provoquées par l'excitation thermique sont atténuées au travers d'une boucle active à l'aide d'un actionneur. Le circuit de contrôle stabilisant la position du levier contrebalance à la fois le mouvement de Brownian et les forces d'interaction de surface pour maintenir le levier en position (zero) non évitée. La force d'interaction est détectée directement par l'effort néccessaire pour stabiliser le levier en position non évitée. La mesure de force interprète de bons résultats déterminants une distance constante entre la surface et le comportement non linéaire de la force d'interaction non appliquée. La force est mesurée dans la bande passante d'origine de l'interaction. Il n'y a pas nécessairement de modulation de fréquence ou de modulation d'amplitude. Les propriétés dynamiques du levier sont supprimées et la mesure peut être accomplie à de très grandes vitesses. Ce mode convient pour les expériences en milieu liquide grâce à l'opération statique. Le Cooling Mode a été testé en simulation et des mesures préliminaires de vérification ont été faites. Par conséquent, une validation expérimentale approfondie n'était pas réalisable à cause de problèmes techniques. Cependant, une vérification de l'opération en Cooling Mode à grande vitesse en milieu liquide devra être effectuée.

Le Cooling Mode a un grand potentiel industriel et a été protégé par le brevet numéro FR06/04674. Le Cooling Mode sera développé dans le cadre de travail d'un nouveau projet nommé « Small Infinity ». Ce projet va transférer la technologie développée dans un produit commercial qui peut être utilisé par les chercheurs dans différents domaines.
Cette thèse démontre l'opportunité à appliquer des systèmes de contrôle avancé pour les expériences de physique, ainsi elle contribue à leur large développement. Les techniques de

contrôle montrent un fort potentiel en technologie où ils permettent d'éliminer certaines difficultés qui ne peuvent être surmontées par les expériences conçues. Le mouvement de Brownian traité dans cette thèse est l'un des exemples d'une longue liste de défis auquels la nanoscience fait face. On peut dire que le nano positionnement et la manipulation sont une aire de la nanoscience qui ne peut être réalisée sans les systèmes de contrôle actif.

Chapter 1

Introduction

In recent years nanoscience has become one of the most fast developing fields of science. The applied and fundamental research is concentrating on many different domains that have in common the fact that research is performed at the nano scale.

To be able to perform research at the nano scale, scientists use a wide variety of a techniques for the characterization of a studied object. The Scanning Probe Microscopy (SPM) represent one of the most important tools used to characterize/measure objects and surfaces at such a scale. This technique has existed for more than twenty years and has gone through many technical and scientific developments. The applications of Scanning Probe Microscopy is quite large: from physics of surface to material science, microelectronics, biology and chemistry. Many new applications combine the SPM with other techniques. All these applications put new requirements on the tool and stimulate continuous development of this technology. The Atomic force Microscopy (AFM) is a particular type of SPM and uses inter-atomic forces between a tip and a surface for the surface measurements.

My thesis is trying to contribute to this development and further improve existing techniques for Atomic Force Microscopy by application of advanced control strategies. In particular I dealt with a new strategy for the operation of AFM in liquids. The work is not exhaustive and extensive references are given for deepening the subject.

The thesis has been carried out under joint supervision between Brno University of Technology (BUT), Czech republic, department of control and instrumentation and Université Joseph Fourier (UJF), France, Laboratoire d'Automatique de Grenoble (LAG). These two institutions have provided the necessary scientific support. The research activities have been performed at the European Synchrotron Radiation Facility (ESRF). This European research institute focuses its scientific activities on research related to the synchrotron X-ray radiation. Within the ESRF, the Surface Science Laboratory extensively explores the Scanning Probe Microscopy domain. This laboratory consists of students and researchers led by Mr. Fabio Comin - ESRF Experimental division and Mr. Joel Chevrier - professor of physics at UJF.

Focus of the thesis

The presented work concentrates on a complete and deep understanding of the Atomic Force Microscopy from the control point of view. This analysis allows us to propose improvements for the AFMs standard functions. Furthermore, with this knowledge we can design a new technique to operate the Atomic Force Microscope. Control approach plays an important role in all this development but profound understanding of the instruments physics has to be reached as well.

The second chapter briefly but completely overviews the most important techniques to operate the Scanning Probe Microscope and more precisely the Atomic Force Microscope. This chapter should unveil advantages and difficulties of the existing techniques. The most basic function parts of AFM are presented: probes, cantilever position detection, sample scanner and finally, cantilever excitation and its use as a harmonic oscillator. Followed by a summary of Contact (static) operation mode and Non-contact (dynamic) operation mode. An overview of publication concerning the application of advanced control techniques to Atomic Force Microscopy is given at the end.

The third chapter concentrates on the modeling of surface interactions and the dynamic of the cantilever with the tip. A simplified model of the surface interaction forces is presented and used as a base to performe simulations later on. Followed by a simplified cantilever model and a more complex multi-mode model based on the beam theory with implemented model for the thermal excitation. Both models presented are based on cantilevers mechanical properties provided by the manufacturer and do not require any additional information. The simulation of a thermally excited cantilever model are compared with the measurements obtained with Nanotec atomic force microscope. A minimization method is introduced to adjust given mechanical properties to improve model accuracy. The end of this chapter is dedicated to simulation of Amplitude Modulation and Tapping mode with the goal to explore the importance of the cantilever higher harmonic modes for these measurement methods.

The fourth chapter presents an application of observer techniques to Atomic Force Microscopy. A short introduction to all present measurements and detection disturbances is given at the beginning. Theoretical introduction of the observer and its application in control follows. Then two observer applications to Atomic Force Microscope in Amplitude Modulation technique and a new static force measurement are presented. The first one is able to directly detect interaction force while using standard Amplitude Modulation mode. The second method is using non-excited cantilever to measure tip-surface interaction force in a static mode and directly determine the force intensity.

The fifth chapter presents a new operation mode of Atomic Force Microscope based on static measurement of the interaction force. A cold damping technique is used to be able to operate the cantilever in completely static regime and its description is given at the beginning of the chapter. Followed, by theoretical definition and description of a new operation mode called “Cooling mode". The main advantages and disadvantages compared to the standard AFM operation modes are listed to see the functionality improvements and limitations. The proposed concept requires the ability to actuate at the cantilever free end and newly designed capacitive actuators are presented. Experimental setup used to prove this concept is designed and identified in the following text. This information allows us to design a stabilizing controller using pole placement techniques and obtain a robust control system that can efficiently attenuate the thermal distortion of the cantilever. A model of the entire experimental system has been constructed and simulation of the complete system has been performed to show results similar to the experimental data. The real-time measurement results are presented at the end of this chapter.

The last chapter gives conclusions on the performed work and a vision of a possible future development of the proposed system.

Chapter 2

Scanning Probe Microscopy

First example of the Scanning Tunneling Microscopy (STM) has been introduced by *Gerd Binnig* and his colleagues in 1981 at the IBM Zurich Research Laboratory [1]. The STM is capable of obtaining three-dimensional images of solid surfaces with atomic resolution. Four years later, in 1985, the same group introduced another technique called Atomic Force Microscopy (AFM) [2]. *Binnig* and *Rohrer* received a Nobel Prize in Physics in 1986 for their discovery. These two tremendous inventions have been the basis for the development of an absolutely new category of instruments called Scanning Probe Microscopy (SPM). Since then many other instrument variations have been developed and used in a wide range of applications covering fields such as material science, electro-magnetism, chemistry, biology, medicine as well as industrial applications and electronic device development, Micro-Electro-Mechanical Systems (MEMS) and memory devices. Many other applications exist already and many other will emerge in the future.

The family of Scanning Probe Microscopy can be divided into these classes:

- Scanning Tunneling Microscopy (STM) [1, 3, 4],
- Atomic Force Microscopy (AFM) [2, 5],
- Friction Force Microscopy (FFM) [6, 7, 8, 9],
- Scanning Electrostatic Force Microscopy (SEFM) [10, 11],
- Magnetic Force Microscopy (MFM) [12],
- Scanning Near Field Optical Microscopy (SNOM) [13, 14, 15],
- Scanning Kelvin Probe Microscopy (SKPM) [16, 17, 18, 19],
- and many others [20, 21, 22].

All techniques listed above are just certain variations of a common principle which is based on using a very sharp probe (tip) to investigate properties of given sample. To be capable of obtaining complete “map” of measured sample property like topography, friction, stiffness, adhesion, module of elasticity, charge, luminescence or others, scanning has to be done in a controlled way, so that the information of lateral position (x and y axis) is clearly related to the measured values, see figure 2.1. In section 2.1.4 the problematic of the lateral scanners will be explained in more details.

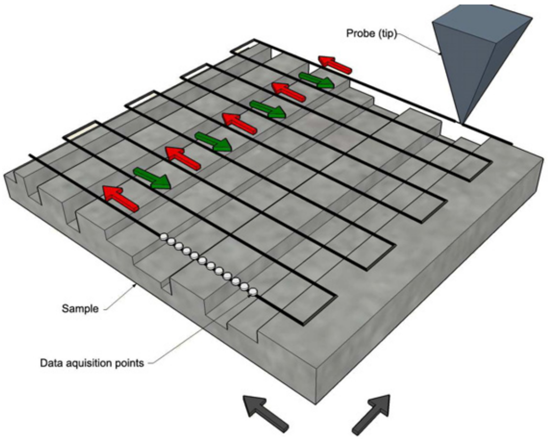

Figure 2.1: Lateral sample scanning (x and y axis) with the probe. The final topography image is later reconstructed from the line by line scanning information. Each measured current has a well defined x and y position.

Scanning Tunneling Microscopy (STM)
The principle of electron tunneling has been published by *Giaever* in 1960 [23]. The tunneling effect can occurs between two metallic surfaces having an electric potential between them. If the surfaces are brought into close proximity (less than 5nm), the electrons are able to penetrate (tunnel) the thin isolating film in between the electrodes. Then tunneling current occurs and is exponentially dependent on the surface separation distance. This leads to very high vertical resolution.
Binnig and his colleagues combined this idea, modified for a sharp tip, with lateral scanning and have been able to reach a vertical resolution of 0.1nm which allows to observe the surface topography with atomic resolution. The limitation of the measurement accuracy is given by sharpness of a tip and external distortion.
The functionality of the STM is straightforward. A sharp tip is brought in close proximity to the investigated surface (0.3-1nm) and a constant voltage is applied between them (10mV-1V). Then the tunneling current is an exponential function of the separation distance, usually in a range of 10pA to 10nA. Two standard STM operation modes exist: In the **constant current mode**, the distance between tip and surface is maintained constant using a feedback loop which is displacing the sample in z (vertical) direction. This results in a constant tunneling current and the topography of the surface is directly determined from the position of the sample under the probe. In the second technique called **constant height mode**, the position of the sample as well as the probe are kept constant during the measurement. Then the topography is directly obtained from the tunneling current. For more details about STM see [3, 4, 1, 24].
The main limitation of Scanning Tunneling Microscopy is the necessity of working with conductive materials, which puts strong constrains on possible applications. Further on will be described and deeply treated the Atomic Force Microscopy, which has overcome this limitation and operates with any material. The Atomic Force Microscopy is the main interest of this dissertation thesis.

2.1 Atomic Force Microscopy

Atomic Force Microscopy has similar capabilities as STM with one big advantage: an AFM is able to measure any solid material without the condition of surface conductivity. Here, the topography is determined from the deflection of the soft cantilever with a sharp tip mounted at its free end. The AFM techniques have been developed for twenty years during which three main operation modes have been established:

Contact (Static) mode (sometimes called DC-mode): the cantilever is in full contact with the surface. The repulsive interaction forces (topography) is determined by measuring the static deflection of the cantilever. This technique is capable of detecting the topography of atomic scale resolution. Strong repulsive interaction force and friction are present between tip and surface and this technique is harsh to the sample.

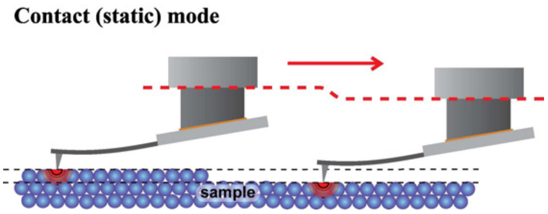

Figure 2.2: Contact (static) operation mode.

Non-contact (Dynamic) mode (sometimes called NC-mode): In this measurement mode, the cantilever is usually driven close to its resonant frequency, with vibration amplitudes less than 100 nm. The cantilever driver usually is a piezo-electric element, but many experiments have been performed with electrostatic, magnetic, thermo-optic or acoustical coupling drivers. The driver is mounted to the head of the microscope and the chip with the cantilever is mounted on top of the driver. The interaction force is modulating the vibration frequency, amplitude and phase. From the oscillator modulation can be distinguished surface topography.

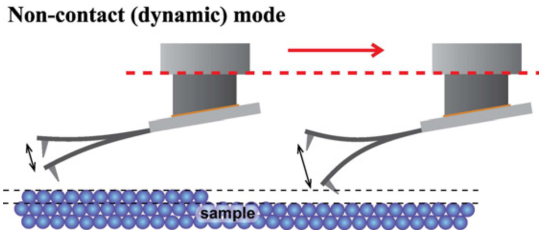

Figure 2.3: Non-contact (dynamic) operation mode.

Tapping mode^{TM} (patented by Veeco): This mode is a combination of the static and dynamic modes. It allow to minimize friction between tip and measured surface which is strongly present in the contact mode. The oscillating tip only touches the measured surface at maximum deflection of the cantilever towards measured surface. In this moment, there is direct mechanical contact with strong repulsive interaction forces between tip and surface. Due to the dynamic operation of the cantilever and very short contact time this technique can be considered as non-contact.

Before explaining the existing operation modes in detail, following section provide some basic information about the cantilevers, cantilever detection and scanner.

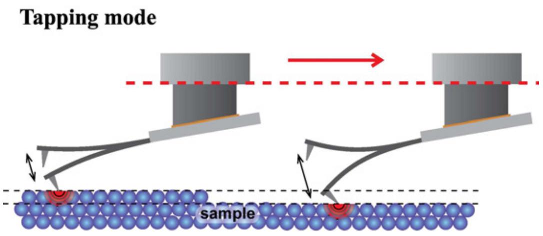

Figure 2.4: Tapping operation mode.

2.1.1 AFM probe properties and construction

The cantilever with its sharp tip is the sensor determining the AFM resolution for specific applications. As shown in the introduction, there exists a wide variety of measurements that can be done with an AFM. The probes have different properties tuned to achieve maximal accuracy, according to the specific application. The micro-fabricated cantilevers used nowadays were invented by *C. F. Quate* [25, 26] and *Wolter* [27]. Rectangular and triangular cantilevers are easily accessible and mainly used. In the early years of the AFM, the cantilevers were made from wires and had different shapes, but with the development of micro-fabrication techniques this become completely obsolete. The main advantage of triangular cantilevers is their much higher lateral stiffness (100-1000 times) compared to rectangular beams with similar stiffness in horizontal direction (vertical deflection of triangular cantilever can be approximated as a two parallel rectangular beams). This can become an advantage in contact measurements with strong interaction, where the lateral deflection of the cantilever is compromising the measurement accuracy. Still, in most cases rectangular beams are used because they are simple to manufacture and working with them is easier compared to triangular ones.

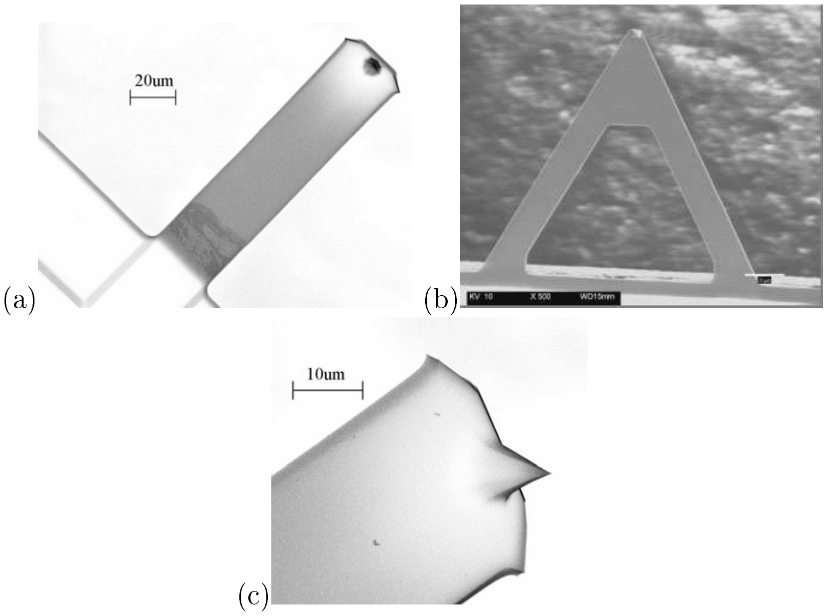

(a) (b) (c)

Figure 2.5: Scanning Electron Microscope (SEM) images of a rectangular cantilever (a), triangular AFM probe (b) and detail of a tip (c).

The characteristic properties of the probes are:

- Horizontal spring constant (stiffness) - In order to measure deflection caused by small forces (from tenths of pN in non contact mode to nN in contact mode), the cantilever spring constant requires to be in a range of $10^{-2}$to 10^{2} N/m.

- Resonant frequency - To achieve a large imaging bandwidth, the AFM cantilever should have a resonance frequency higher than 10 kHz. This requirement is important to eliminate the influence of thermal drifts, which have low frequency bandwidth and significantly disturb the measurement performed at slow-scanning speeds.
- Quality factor - The frequency modulation technique (see section 2.2.2) uses a resonance slope detection method where a high quality factor increases the detection sensitivity. For measurement in the air, the quality factor is typically in the range of 10 to 1000. In contact mode, the quality factor does not make significant difference in functionality.
- Lateral spring constant (stiffness) - As lateral bending results in topography measurement error, high lateral spring constant minimizes this error.
- Torsional spring constant - Accuracy of friction measurement in lateral direction highly depends on the length of the tip and torsional spring constant. For this very specific measurement is necessary to use cantilever with low torsional spring constant.
- Good optical reflectivity for detection - This requirement only needed for optical detection techniques.
- Sharp tip - The tip radius determines the lateral resolution of the AFM. Preferably, the tip should be as small as possible. For example in friction measurements, this minimizes the resulting force applied on the cantilever. Moreover, in topographical measurements, the tip radius should be smaller than the radii of corrugations in the sample to able to reach the real topographical resolution of the sample.

As can be seen from the given overview, the choice of proper cantilever and tip for a certain application is a difficult and complex decision. Some compromises have to be done to achieve desired functionality. Most of the listed properties, i.e. resonance frequency and vertical stiffness, can be directly calculated from the mechanical dimensions of the cantilever and known material properties, see figure 2.6. Here, only the properties of a rectangular cantilever are shown as it is the mostly used probe and is the main interest of the following chapters of identification and modeling.

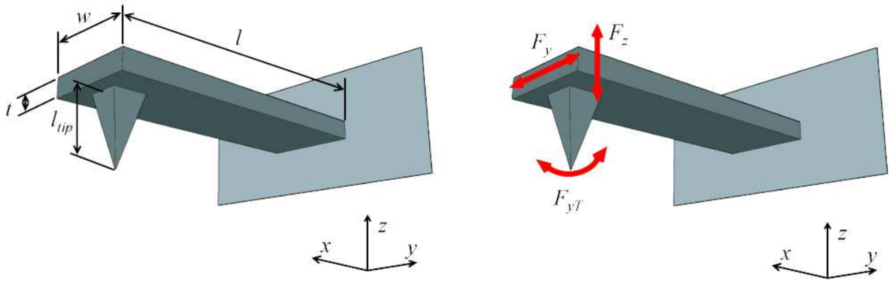

Figure 2.6: An AFM probe's mechanical dimensions and applied interaction forces.

The typical ranges of cantilever dimensions are shown in table 2.1. The majority of cantilevers used in standard AFM is made out of silicon, but materials as diamond, tungsten and iridium can be used to reach specific requirements (see table 2.2 for details about material properties).

mechanical property	minimal	maximal
length (l) [μm]	50	600
width (w) [μm]	20	50
thickness (t) [μm]	0.5	5
tip length (l_{tip}) [μm]	3	30

Table 2.1: Usual cantilever dimensions.

Material property	Young's Modulus (E) [GPa]	Density (ρ) [kg/m^3]
Si_3N_4	310	3180
Si	130-188	2330
W	350	19310
Ir	530	22650
diamond	900-1050	3515

Table 2.2: Material properties.

With knowledge of these values, we can calculate the following cantilever properties:

Total mass

$$m = l \cdot w \cdot t \cdot \rho \tag{2.1}$$

Basic information about the cantilever dynamics, which can be directly determined from mechanical dimensions and used material.

Effective mass

$$m_{eff} = 0.24 \cdot m = 0.24 \cdot l \cdot w \cdot t \cdot \rho \tag{2.2}$$

Very often, the dynamic behavior of the system is approximated (modeled) with a simple harmonic oscillator containing mass, spring and damper, see section 2.1.2. It can be shown, that in this case only part (one quarter) of the total cantilever mass is contributing to the harmonic movement of the free end of the lever.

Vertical spring constant

$$k_z = \frac{Ewt^3}{4l^3} \tag{2.3}$$

This is the most important parameter of the cantilever which directly determines the sensitivity and the application. Very soft levers are used for contact (static) measurements to minimize the damage done to the sample by scanning. Stiffer levers are required for non-contact (dynamic) mode and Tapping mode. In contact operation mode, the force deflecting the cantilever in vertical direction F_z (often called **Normal force** F_N) can be written as $F_z = F_N = z \cdot k_z$, where z is the vertical displacement of the cantilever. The usual range of normal force in topography mapping is 10^{-2} to $10^2 Nm^{-1}$. In the following text the vertical spring constant will be used without the index "z" though as a simple k to be consistent with standard mark for this variable in most of the publications.

Resonant frequency

$$\omega_0 = \sqrt{\frac{k}{m_{eff}}} \simeq \sqrt{\frac{Et^2}{l^4 \rho}} \tag{2.4}$$

This parameter is significant mainly for the dynamic mode providing information about the bandwidth of the measurement. Typical resonance values of resonance are 10kHz to 100kHz. To increase the measurement bandwidth, it is necessary to increase the resonance frequency. Fast imaging has a great importance, because low frequency thermal drifts disturb the measurement and are limiting the scanning time.

Quality factor

$$Q = \frac{\omega_0}{\gamma} \tag{2.5}$$

where ω_0 is the resonant angular frequency of a damped oscillator and γ is the damping coefficient. This approximation is only valid if the damping coefficient is much smaller than the resonant frequency: $\omega_0 \gg \gamma$. The damping coefficient γ is determined by the full width, at mid height, of the squared Lorentzian fit of the resonance peak in frequency domain, see section 2.1.2, figure 2.7. A more general definition of the quality factor being also valid for lower quality factors can be based on the comparison of the lever's internal energy with the imposed work on the cantilever. Then, the quality factor can be written as

$$Q = \frac{\omega^2 + \omega_0^2}{2\gamma\omega} \tag{2.6}$$

Typical value in the air is 100-1000. Quality factor has small importance in case of contact measurement. In the dynamic mode the quality factor determines the settling time of the cantilever, which can be considered as a limiting parameter to the measurement bandwidth. On the other hand, high quality factors are very important to reach good accuracy in the slope detection technique, see chapter 2.2.2. Hence, a good compromise has to be found between these needs.

Lateral spring constant

$$k_y = \frac{Ew^3t}{4l^3} \quad [\mathrm{N/m}]$$

This parameter limits the resolution in friction measurements, thus it should be as high as possible. The force deflecting the cantilever in lateral direction can be written as $F_y = y \cdot k_y$.

Torsional spring constant

$$k_{yT} = \frac{Gwt^3}{3l^3 l_{tip}} \quad [\mathrm{N/m}]$$

where G is the modulus of rigidity $G = E/2(1+\nu)$ with the Poisson ratio ν. The force twisting the cantilever is often called **lateral force** F_L: $F_{yT} = F_L = y_{tip} \cdot k_{yT}$. The lateral force is often used in friction measurements and if the scanning is done in y direction, then the lateral force is equal to friction force. The friction measurement can be done in x direction as well. Then, the friction force can be determined from the normal force, see [9].

Tip

The shape of the tip is directly determined by the application and the specific needs of the experiment. Most of the cantilever tips have a pyramidal shape with three or four side walls under angle (usually) 35 deg and the length about $4\mu m$ between the tip end and the cantilever. The tip is made out of the same material as the cantilever with a radius about $20 - 50nm$. These tips are used for the majority of the measurements and are easily accessible. In case of imaging, a topography in thin and deep trenches these tips are useless because they do not reach the bottom of the trenches. For this application, high aspect ratio tips are used. One technique to obtain such a tips is based on a standard pyramid tips. By using a focused ion beam, a thin filament can be grown at the apex of the tip. A second possibility is to attach a Single Wall Nano-Tube (SWNT) or a Multi Wall Nano-Tube (MWNT) at the apex of a standard tip. The single wall nano-tubes are suitable for high resolution imaging in non-contact or tapping mode. In contact mode, it is better to use a multi wall nano-tube because of its higher stiffness. For quantitative measurements of interaction forces, cantilevers with a sphere at their free end are used. These spheres usually have a radius of about $10\mu m$ to $100\mu m$. The information obtained with these "tips" have low lateral resolution. Still, they are very useful for detecting and characterizing of weak interaction forces.

2.1.2 Harmonic oscillator

The dynamic behavior of a cantilever can be described as a mechanically driven damped oscillator with three motion parameters: amplitude, frequency and phase, see figure 2.7 a). In chapter 3.3, this simplified description will be developed into a multi-mode model of the lever taking into account higher harmonic modes. Here, just the simple oscillator model is discussed. By many authors, it is considered as a sufficient model to easily explain the dynamic operation mode. The cantilever is driven by a periodic external force $F_{drive} = A_{drive}cos(\omega_{drive}t) = k \cdot z_{drive}cos(\omega_{drive}t)$, where ω_{drive} is the driving frequency which is chosen close to the first resonant frequency of the cantilever, A_{drive} is the driving amplitude and z_{drive} is the driver's mechanical displacement. The oscillator can be described as a differential equation of the second order:

$$m_{eff}\frac{d^2z}{dt^2} + m_{eff}\gamma\frac{dz}{dt} + m_{eff}\omega_0^2 z = F_{drive} \tag{2.7}$$

where m is the cantilever's mass, γ is the damping coefficient and z is the cantilever's vertical displacement.

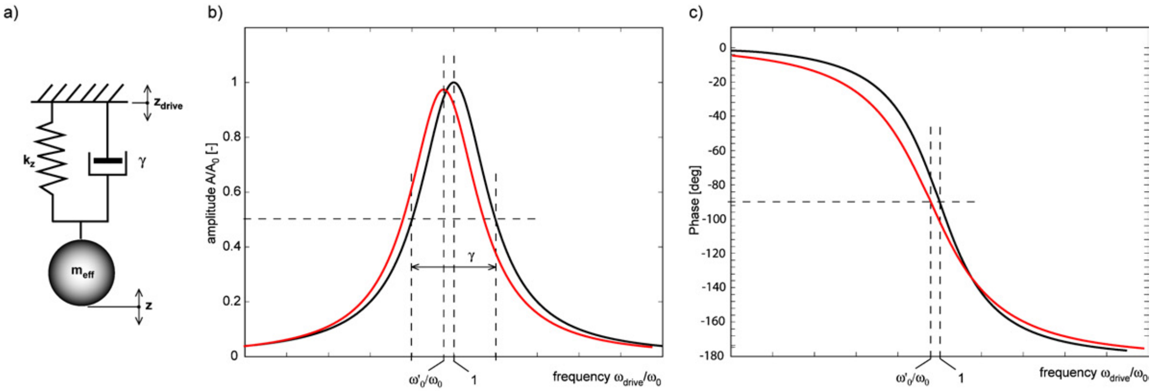

Figure 2.7: a) The driven damped harmonic oscillator represented as a mechanical system with spring (k), damper (γ), and mass (m_{eff}); b) and c) Amplitude and phase shift as functions of the driving frequency ω_{drive} (black: resonance with arbitrary friction; red: resonance with increased friction in comparison with black)

By applying two complex substitutions: $F_{drive} = \hat{F}e^{i\omega_{drive}t}$, where $\hat{F}$ is the real part of the driving force and $z = \hat{z}e^{i\omega_{drive}t}$, where $\hat{z}$ is the real part of the cantilever position, the equation 2.7 can be written as:

$$\left[(i\omega_{drive})^2\hat{z} + \gamma(i\omega_{drive})\hat{z} + \omega_0^2\hat{z}\right]e^{i\omega_{drive}t} = \frac{\hat{F}_{drive}}{m_{eff}}e^{i\omega_{drive}t} \tag{2.8}$$

where

$$\hat{z} = \frac{\hat{F}_{drive}}{m_{eff}(\omega_0^2 - \omega_{drive}^2 + i\gamma\omega_{drive})} = \widehat{Z} \cdot \hat{F}_{drive} \tag{2.9}$$

This shows that the movement of the cantilever is a direct function of the driving force:

$$z(t) = A_0 cos(\omega_{drive} t + \varphi) \tag{2.10}$$

where A_0 is the vibration amplitude and φ is the phase shift to the driving signal in the settle state of the oscillator. The vibration amplitude A_0 can be written as:

$$A_0 = \frac{A_{drive}}{m_{eff}\sqrt{(\omega_{drive}^2 - \omega_0^2)^2 + \gamma^2\omega_{drive}^2}} \tag{2.11}$$

and the phase shift

$$\varphi = arctan\left(\frac{Im(\hat{z})}{Re(\hat{z})}\right) = arctan\left(\frac{\gamma\omega_{drive}}{\omega_0^2 - \omega_{drive}^2}\right) \tag{2.12}$$

The amplitude and frequency diagrams for this driven damped oscillator are shown in black in figure 2.7 b) and c). In the case where the quality factor Q is very low (approximately below 100), we have to take into account the frequency shift caused by the damping. The new resonance frequency for this more strongly damped oscillator is

$$\omega_0' = \omega_0\sqrt{1 - \frac{1}{2Q^2}} \tag{2.13}$$

The resulting amplitude and frequency diagrams are shown in red color in figure 2.7 b) and c).

2.1.3 The cantilever position detection

The accuracy in measuring the cantilever displacement is very important for reaching a good resolution of AFM images. Many techniques have been developed for this measurement based on different physical principles:

- Tunneling Current Detection [2]
- Optical Interferometer detection systems [28, 29, 30]
- Fiber-optical Interferometer [31, 32, 33]
- Optical Beam/Lever [34, 35]
- Piezo-resistive Detection [36, 37]
- Capacitive Detection [38]

Each technique has specific advantages, for further details see listed references. Here, we will concentrate on the optical techniques: the Optical Lever and the Fiber-optical Interferometer, which are dominating in AFM. They have been used in many different setups and measurements.

Optical beam detection
A method used by many manufacturers of AFM is the Optical Lever deflection technique shown in figure 2.8. A collimated light beam is reflected on the back side of the cantilever and projected on the photo detector. Any change in the angle of the reflecting surface (the

lever's back side) changes the beam's position on the photo-detector. The photo-detector is usually divided into four quadrants to be able to detect the incident light ray displacement in two directions. These directions represent deflections caused by either normal or lateral forces acting onto the cantilever. Thus, optical lever detection is a very elegant and simple way to detect cantilever vertical and torsional deflection simultaneously. Furthermore, the demand for the cantilever back side high reflectivity is very easy to reach, for example by coating.

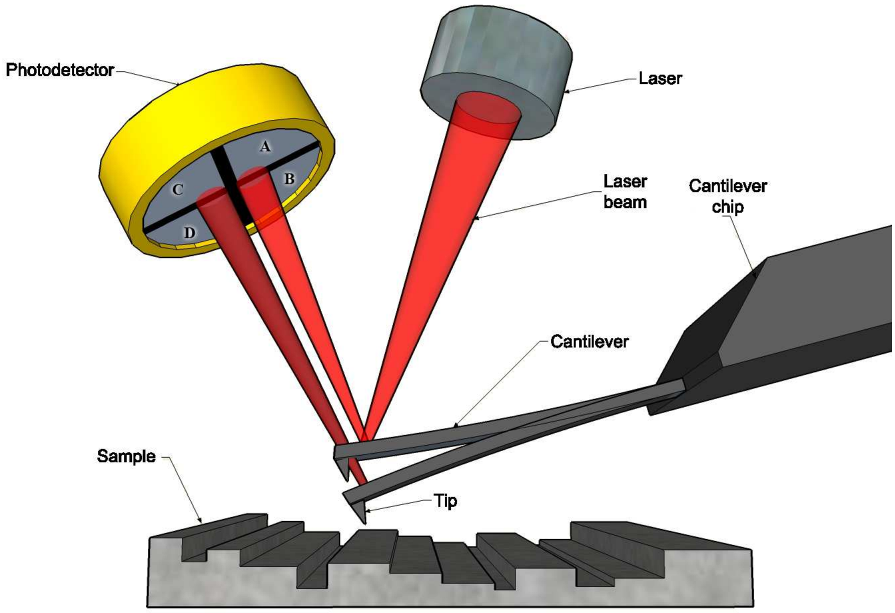

Figure 2.8: The detection principle of the cantilever vertical displacement. The laser beam is reflected from the cantilever under different angels according to the actual deflection (position) of the beam.

The photo-detector receiving the reflected laser beam from the cantilever is divided into four quadrants A, B, C and D having the output currents I_A, I_B, $I_C\ and\ I_D$. Due to the macroscopic length of the reflected light path, any deflection cause a magnified displacement of the reflected laser spot on the photo-diode. The relative amplitudes of the signals from the segments of the photo-diode change in response to the motion of the laser spot. In total, three signals can be obtained from the photo-detector outputs with additional electronic.

The *Sum* signal is used as a normalization signal for F_N and F_L to eliminate the dependency on the laser source intensity: $Sum = I_A + I_B + I_C + I_D$

The vertical deflection z corresponds to a normal force F_N deflecting the cantilever (see figure 2.8): $F_N = z \cdot k = \frac{(I_A+I_B)-(I_C+I_D)}{I_A+I_B+I_C+I_D}$. The vertical deflection of the cantilever is usually the value observed in most of the measurements and k is the spring constant provided by cantilever manufacturer.

The twisting of the cantilever, also named torsional deflection z_{yT}, corresponds to a lateral force F_L that is deflecting (twisting) the cantilever (see figure 2.9). Here, $F_L = z_{yT} \cdot k_{yT} = \frac{(I_A+I_C)-(I_B+I_D)}{I_A+I_B+I_C+I_D}$, where k_{yT} is cantilever torsional spring constant. This deflection is very small and it has relevant amplitudes only in contact mode (see below). The spring constant k_{yT} is significantly higher than the one for vertical deflection k, and is not provided by manufacturers.

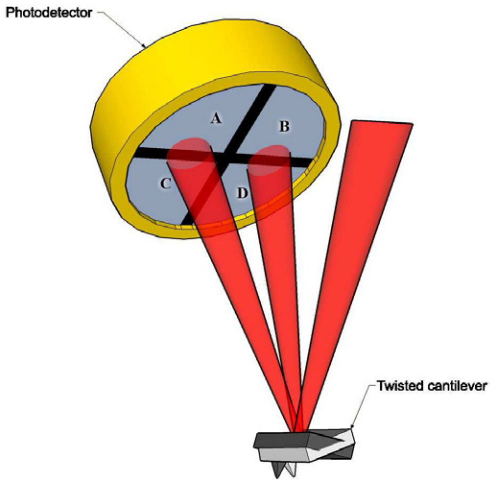

Figure 2.9: The cantilever's torsional deflection.

A laser beam has a Gaussian distribution and an opening angle β at the point far from the light source. If the mirror changes its angle by α, the reflected beam change its angle to 2α and the light beam displacement at the photo-detector is directly related to this angle. For our cantilever, α is proportional to the lever position: $\alpha{=}\frac{3z}{2l}$, where z is the cantilever displacement in vertical direction and l is the lever length. The movement of the light beam center on the photo-detector is given by

$$\Delta_{normal} = 3z\frac{Ds}{l}$$

where Δ_{normal} is the beam displacement on the photo-detector in normal direction and Ds is the separation distance between the lever and the detector. The photo-current at the detector output I_{out} is calculated as a differential value from the four quadrants $((I_A + I_B) - (I_C + I_D)$ for vertical or $(I_A + I_C) - (I_B + I_D)$ for horizontal displacement). For small deflection angles this current can be directly approximated from the angles β and α

$$I_{out} = 4\frac{\alpha}{\beta}I_{total}$$

where I_{total} stands for the sum of the currents produced by the four quadrants of the photo-detector. The photo-current I_{total} is proportional to the total number of photons N_D hitting the photo-detector. The number of photons decrease with increasing separation distance.

$$N_D \approx \theta N_0 \Rightarrow I_{total} \approx \eta\theta N_0$$

where N_0 is the total number of photons emitted from the light source, θ is the laser power attenuation coefficient and η is the efficiency of the light-to-current conversion at the photo-detector.
Hence, the differential photo-current at the photo-detector output can be written as:

$$I_{out} = 6z\frac{\eta\theta N_0}{l\beta}$$

As can be seen, the photo-current output is independent of the separation distance between the photo-detector and the cantilever.

The optical beam detection has good linearity up to large deflections, compared to other measurement methods. The maximum reachable deflection in linear regime depends on the cantilever's length. The measured value is angle and, for lever of lenght about $400\mu m$ it has been measured deflection around $250nm$. Above this amplitude non-linearity become significant, mainly due to the limited size of the photo-detector. In reality the non-linear behavior is caused by effects of the laser spot motion on the cantilever, the reflected light is not perpendicular to the receiving photo-diode surface any more, and the displacement of the laser beam caused by a highly deflected lever. For certain techniques, an array of photo diodes has been developed to measure deflection up to $600nm$, see [39].

The sensitivity limitation of the optical beam detection. The accuracy of the measurement depends on the intensity of the laser beam. The upper limit of the laser power is given by saturation of the photo-detector diodes. This can be adjusted in certain limits. The second parameter improving accuracy is the divergence of the laser beam. This is a much stronger constrain for the design and the construction of the detection system. By increasing the beam divergence, accuracy improvement can be achieved, but the size of the laser spot on the back side of the lever increases as well. If the laser spot has the same or a greater size then the cantilever width w, there occur interferences at the edge of the lever. Then, a part of the laser beam is not reflected onto the photo-detector. Thus, according to these limitations the optimal diameter of the laser spot is found to be a function of the cantilever width: $d_{opt} \simeq w/\sqrt{2}$.
The theoretical sensitivity is limited by the shot noise of the light hitting the photo-detector. The spectral density of the shot noise for a light beam of intensity P is $i_n = \sqrt{hcB/\lambda P}$ $[W/\sqrt{Hz}]$, where h is the Planck constant, c is the speed of light, λ is the light wavelength and B is the measurement bandwidth. This noise induces a laser intensity fluctuation, which then induces the fluctuation of the measured angle $\delta\alpha$ or the position δz.

$$\delta\alpha = \frac{1}{\sqrt{2\pi}}\frac{\lambda}{w}\sqrt{\frac{hcB}{\lambda P}} \text{ and } \delta z = \frac{\delta\alpha \cdot l}{3}$$

In the experiments other noises are also present, but their contribution to the measurement is negligible in air at room temperature. The sole noise being extremely important in standard laboratory conditions, is the thermal fluctuation which will be treated in chapter 3.2.

Interferometric measurement
The interferometry has been introduced to Atomic Force Microscopy by *D. Rugar* in 1988, see [31, 32, 33]. The basic principle of the unsymmetrical measurement with an optical fiber is shown in figure 2.10. The light from a laser diode is fed into an optical fiber. This fiber is connected to a coupler which splits the incoming light into two optical fibers. One end is left as an open end, that can be later used for eliminating the noise coming from the laser diode intensity fluctuation. The second end is used to create a Fabry-Perot cavity between the polished end of the fiber and the back side of the cantilever. The polished end of the cantilever can be metalized to achieve higher reflectivity and increase the finesse of the optical cavity. The light is emerging from the fiber and affter passing the cavity is reflected on the cantilever back to the fiber. The wave reflected from the lever and the wave reflected from the fiber ending interfere" and the product is guided back to the coupler. There, half of the light is sent to the detector and half to the laser diode. The distance between the cantilever and the fiber end has to be set to $\lambda(n + 1/4)$, where λ is the laser wave length and n can be any positive rationale number. The distance should be set as short as possible to collect maximum of the reflected light. Usually, only 4% of the reflected light reaches the detector and is used for the measurement.

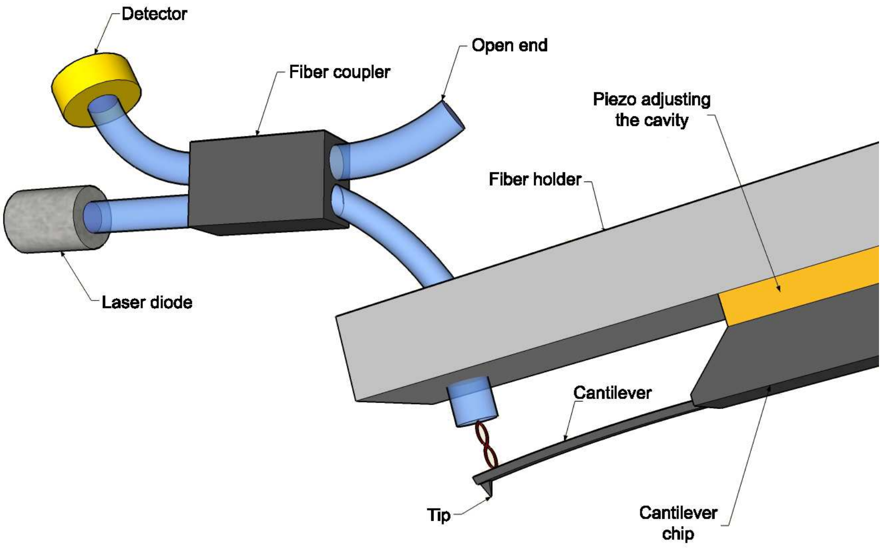

Figure 2.10: The interferometric measurement of the cantilever position.

The sensitivity limitation: The maximum sensitivity of the interferometer is reached when the relative phase shift between the two reflected laser beams is equal to $\pi/2$. To simplify the definition of the maximal sensitivity, we will take into account the influence of the multiple reflections of the laser in the interferometric cavity. Then the laser power at the photo-detector is $P_{det} = P_{avr} + P_{lev} sin(\omega t)$, where P_{avr} is the average signal at the detector and P_{lev} is the signal coming from the lever deflection as a function of $sin(\omega t)$. The P_{lev} is determined by the optical cavity finesse. The average photo-detector signal is $P_{avr} = P_{inc}(R_f + R_c)$ where P_{inc} is the incident optical power at the end of the fiber, R_f is the fiber end reflectivity and R_c is the cantilever reflectivity. The photo-detector signal from the vibrating cantilever is $P_{lev} = P_{inc}(8\pi/\lambda)\sqrt{R_f R_c}\sqrt{2}A_0$ where A_0 is the root mean square vibration amplitude of the cantilever. The photo-detectors current is

$$I_{det} = P_{det}\eta$$

where η is the efficiency of the light-to-current conversion at the photo-detector. The root mean square of the photo-current shot noise can be written as

$$I_{shot} = \sqrt{2eP_{det}\eta B}$$

where e is electronic charge and B is the measurement bandwidth. The minimum detectable root mean square cantilever displacement is equal to the virtual displacement induced at the photo-detector by the shot noise:

$$I_{shot} = \frac{P_{lev}\eta}{\sqrt{2}}$$

then for the rms equivalent of the noise vibration amplitude can be written as:

$$A_{noise} = \sqrt{\frac{eB}{2P_{avr}\eta}\frac{\lambda}{2\pi}}$$

Comparison of the Optical Beam and Interferometric detection

The main difference between two previously mentioned techniques is the quality they detect. The optical beam detection technique senses the angle changes of the lever back

side. The interferometric measurement detects the real position of the cantilever, see [40]. If we take into account the multimode behavior of the cantilever beam (see chapter 3.3) and as well, that the position of the laser spot can be placed to different positions on the lever, then the detected position has more complex behavior than it seems. In figure 2.11 the detector outputs for both methods are shown: on the left you find the optical beam detection, on the right, there is the interferometric detection and both compared to the real lever position below. The values of each harmonic mode are normalized. The optical beam detection is not capable to detect the levers position at any maximum of the beam wave function because the angle equals to zero at these points. On the other hand, the interferometric measurement is not capable detecting the real lever position in the knobs of the beam wave function. These detection properties are resulting in apparent hardening of the cantilever due to repositioning of the laser spot close to a wave maximum or to a knot. This needs to be taken into consideration when the laser position on the cantilever is set at the beginning of the experiment. The optimal setup for both methods is to focus the laser spot at the very end of the cantilever, the green zone in figure 2.11. In this zone both methods have the best resolution for all harmonic modes.
A second important difference is that the interferometric measurement is not capable of detecting friction forces resulting in torsional twisting of the cantilever. In this case the cantilever position stays the same and the angle change is not detected.

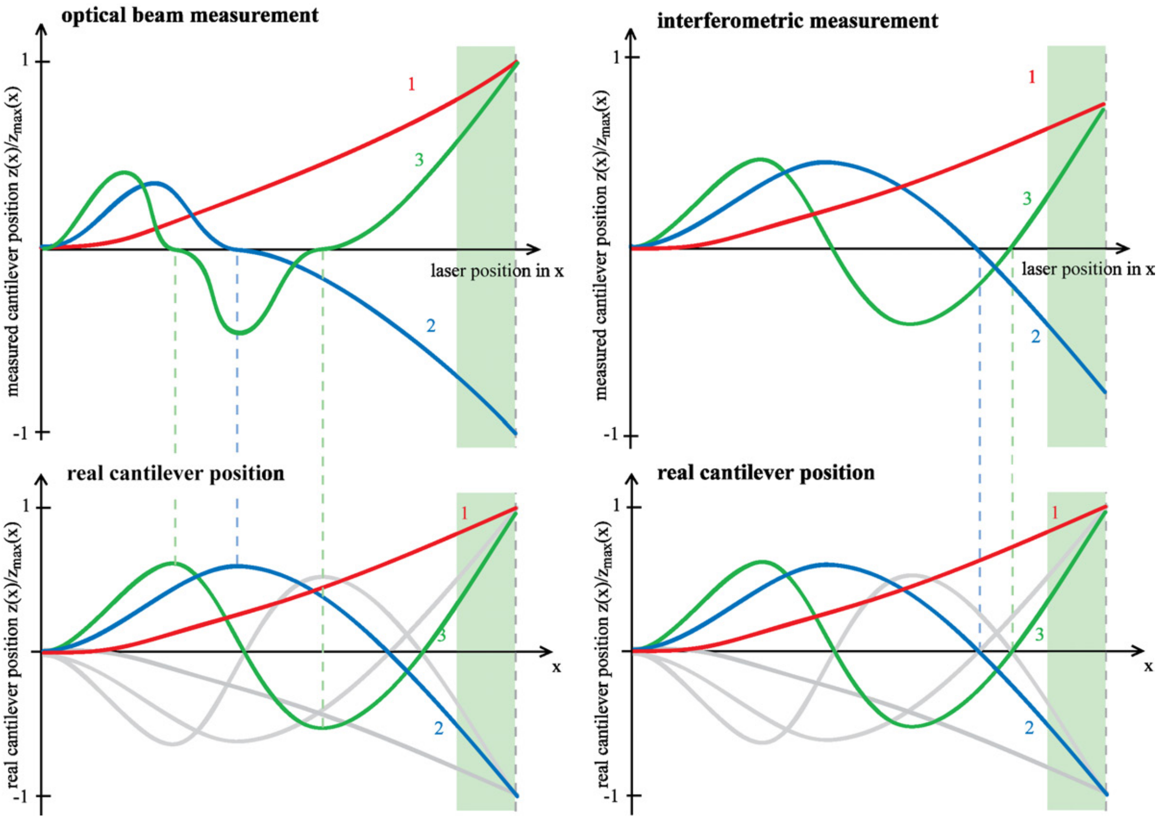

Figure 2.11: The differences between interferometric and optical beam measurements of the cantilever position. In all figures the first three harmonic modes of cantilever vibration are displayed in normalized scale. For further explanation of multimode beam vibrations see chapter 3.3.

2.1.4 x-y-z axis scanner

To reconstruct the topographical map (friction, charge, conductivity, ...) of a given sample, it is necessary to measure the height in well defined points of lateral scan (axis x, y), see figure 2.1. The tip is moving across the sample (or the sample is moving underneath the fixed cantilever holder) in straight lines that are evenly distributed over the sample with known gaps between them. The topography signal is measured simultaneously and the data are saved only for these defined points of lateral scan (white dots in figure 2.1). Usually the number of points and lines is given as a symmetric matrix of 100 to 1000 points in x and y direction. The number of acquired points is determined by the scan size and the desired lateral resolution. For example, if the scan size is $1\mu m \times 1\mu m$ to reach lateral resolution of *10nm*, the scan has to have at least 100×100 points. Another important constrain is the scanning speed. Reasonably fast scanning speed can significantly improve the accuracy thanks to eliminating thermal drifts, that occur during very long measurements. These drifts cannot be anyhow eliminated from the measurement. The scanning speed also has a higher limitation coming from the data acquisition speed and especially from the cantilevers settle time, which is defined by the quality factor (or damping coefficient) of the cantilever. Usually the scanning frequency per line is set between 0.1Hz and 10Hz, though for very big scans sizes, this frequency can be even lower to reach high lateral accuracy.

The first scanners used in AFM have been based on piezoelectric tubes [41, 42, 43], see figure 2.12. The top part of the tube is fixed directly to the head of the microscope and, on its free end, the cantilever holder is mounted, together with piezoelectric driver to excite the lever in dynamic mode. The same functionality can be achieved by mounting studied sample at the free end of the scanner while fixing the cantilever above. The cantilever holder is tilted, usually 15 to 20 degrees, to avoid the cantilever holder touching the studied surface. The scanner has four even 90 degree segment electrodes mounted on outside of the piezoelectric tube. At the two opposite quadrants of the tube ($+x$ and $-x$ or $+y$ and $-y$), a voltage is applied with the same amplitude but opposite sign. If an electric field is applied across the piezoelectric material, the crystal structure changes and expands in one direction and contracts in other. This effect bends the tube according to the field's amplitude in x or y direction. The inside electrode can be grounded if the tube is only used as a x-y scanner, othewise it can be used to control the z position of the x-y-z scanner. The scanner's displacement is considered as linear function of the applied voltage and there is

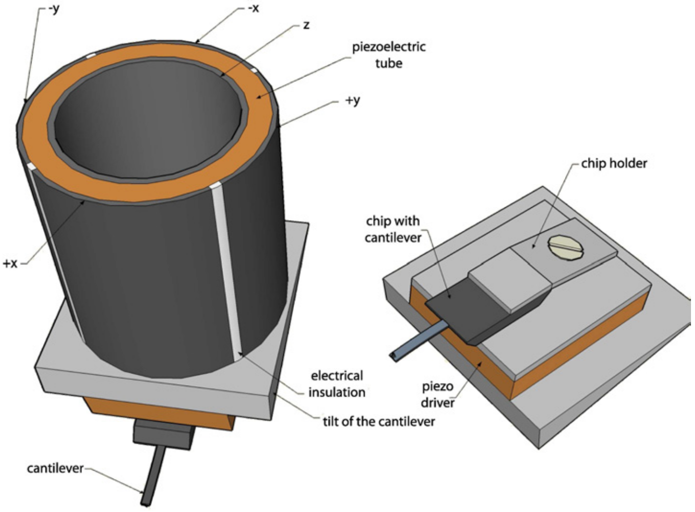

Figure 2.12: x-y-z axis scanner based on piezoelectric tube.

no information about the real position. Still, the piezoelectric tube is experiencing non-linearity and hysteresis effects that gain more significance with increasing scan size. The sensitivity of a piezoelectric material to an applied electrical field (displacement to volts ratio) is smaller for small electric field magnitudes. The hysteresis can cause a deviation up to 10% of the desired travel distance. To overcome these inaccuracies, closed loop scanners with position measurement and feedback control has been developed, for more details see chapter 2.3.

2.1.5 Cantilever excitation

The dynamic mode requires the cantilever to be driven at close proximity to the resonant frequency. The majority of the drivers is using a piezoelectric element that is mounted directly onto the cantilever holder. The driver is "shaking" the entire holder to maintain the lever vibration amplitude. This solution is simple, mechanically robust, and sufficient for standard operation in air or vacuum. Nevertheless, in some cases, this method is not sufficient and an other way has to be found. An electrostatic driver can be created by mounting an isolated electrode above the cantilever. Then, by applying a periodic voltage between the two plates, the electrostatic force excites the cantilever. At the same time this setup can be successfully used, as a position detector, see [44, 45, 38].

The dynamic operation mode in liquids is more difficult due to high viscosity of the liquid medium. If the driver moves in liquid, it induces many waves that are reflected by the sample and the surroundings and significantly disturb the measurement. A piezoelectric bi-morph cantilever [46, 36, 37, 47, 48] offers very elegant solution to overcome these difficulties. Such a cantilever is coated with two layers of piezoelectric material. They function as a bi-morph capable of exciting the cantilever even in an environment with very high viscosity. Tests have also been done with acoustic drivers which are not directly shaking the lever holder but, instead they induce small mechanical waves in the liquid cell above the lever. The moving wave is directly pushing the free end of the cantilever leading to better efficiency of excitation than the standard method while creating less distortion. Another technique is the electromagnetic driver that excites directly magnetically polarized cantilever using a solenoid, see [49]. A more advanced version of electromagnetic excitation uses a triangular cantilever as a one loop of a coil in a static magnetic field, see [50]. Here, the two "arms" of the cantilever are electrically isolated on the side of the chip and a harmonic current is flowing through the triangular cantilever. This creates an alternating magnetic field that is interacting with the static magnetic field created by a permanent magnet. The resulting force excites the cantilever at the required frequency and it only induces the vibration in the liquid in close proximity of the moving lever.

2.2 Standard AFM operation modes

An overview of standard Atomic Force Microscope's operation modes has been given in the beginning of chapter 2.1. In the folowing text deeper analysis of existing modes with mathematical description of their behavior will be developed. The Scanning Probe Microscopy has been developed for last twenty years. There is a large variety of techniques based on modifications of the standard operation modes. Here, only description of the most important ones will be given. To understand the differences of these operation modes, an introduction to surface interaction forces and to the regulation in AFM is given at first.

The interaction forces
Figure 2.13 shows a simple sketch of the interaction force F_{int} as a function of the separation

distance z_t between the tip end and the specimen is shown. A positive interaction force stands for a repulsive force pushing the tip away from the sample. This impose a positive deflection of the cantilever in a vertical direction. A negative interaction force stands for an attractive force pulling the tip towards the sample, which leads to a negative deflection of the cantilever. The sketch can be divided into three zones according to the presence of attractive and repulsive forces:

- only the **attractive forces** are present - these forces are used in non-contact (dynamic) operation mode. The attractive force zone starts at infinite distance z_t from the sample where the interaction force approaches zero and is undetectable. The zone ends when the repulsive interaction starts to contribute. At that moment, the highest force gradient is reached. If we continue approaching the sample with the tip, the force gradient starts to decrease again.
- **both kinds of forces** are present - in this zone, both kinds of forces contribute to the interaction. The most significant distance is reached when the gradients of attractive and repulsive forces are equals. Here, the attractive interaction force reaches its maximum. The distance that tip has to travel from this point to reach the full contact is equal to the intermolecular distance a_0. It depends on material properties of the tip and the sample, usually is in order of few Angstroms.
- only the **repulsive force** is present - this force is used in contact (static) operation mode. The “zero" point can be considered as beginning of full contact between tip and sample. The interaction force in this position is equal to zero and the cantilever is not deflected. If the tip continues to approach the sample, the interaction force increases very fast and the tip starts to deform the measured specimen.

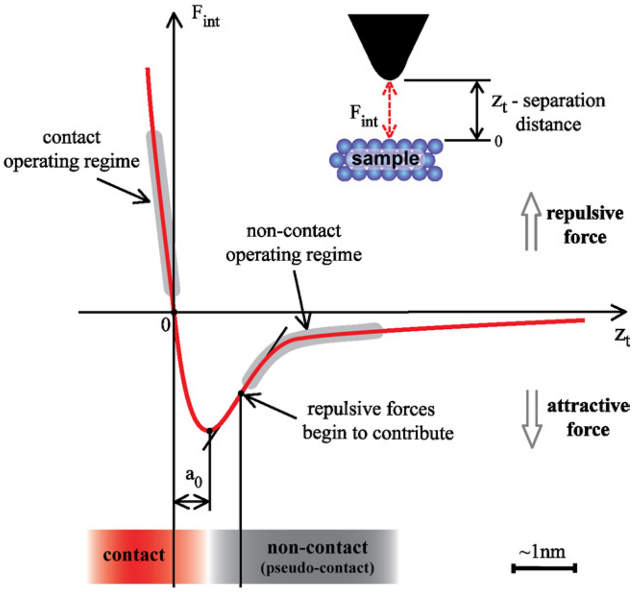

Figure 2.13: The interaction force sketch.

Cantilever interaction with the surface

The interaction forces shown in figure 2.13 are always present between the tip and surface. If the cantilever is used to measure this interaction force, the observed lever deflection has a very different behavior, including instability and hysteresis coming from adhesive forces, see figure 2.14. This measurement is called “Approach-Retract curve".

During the approach phase of the tip to the studied surface in the static (not excited) mode,

there is no tip-sample contact (point 1). Only “pseudo" interaction due to the wide variety of long distance attractive forces (Van der Walls, Casimir, electrostatic, electromagnetic, ...) is present. While approaching, the cantilever become deflected towards the sample but its stiffness keeps the tip away from the surface. The full tip-sample contact occurs at point 2 where the tip jumps into contact with the sample due to Van der Waals, Casimir, electrostatic and electromagnetic attractive forces. At this point the attractive forces have a bigger gradient than a restoring force from the cantilever spring. By continuing to decrease the distance z_c between the cantilever chip and the surface, the lever negative deflection (direction towards the surface) is decreasing. At point "zero" the cantilever has no remaining deflection and the attractive and repulsive interaction forces are equal. If the cantilever chip further approaches the surface, the cantilever starts to be positively deflected (direction away from the surface). Its deflection continues to increase until the maximum, point 4. Around point 3, the usual operation of the AFM in contact mode occurs. While retracting from the surface, the increasing displacement of the cantilever chip releases the deflection force from the cantilever until point 5. There, the cantilever is becoming negatively deflected keeping the tip in contact with the surface due to adhesive forces. Point 6 is the distance where the cantilever's negative deflection is large enough to break free from the adhesive attractive forces and return to non deflected zero position.
The force needed to "snap off” the sample is used as measurement of adhesion properties of the studied materials. The “Approach-Retract curve" is measured in static mode and it is very time consuming to do this measurement for the entire surface point by point. However, the Tapping mode technique is capable of obtaining a comparable information, but in dynamic operation mode measurement, see chapter 2.2.2.

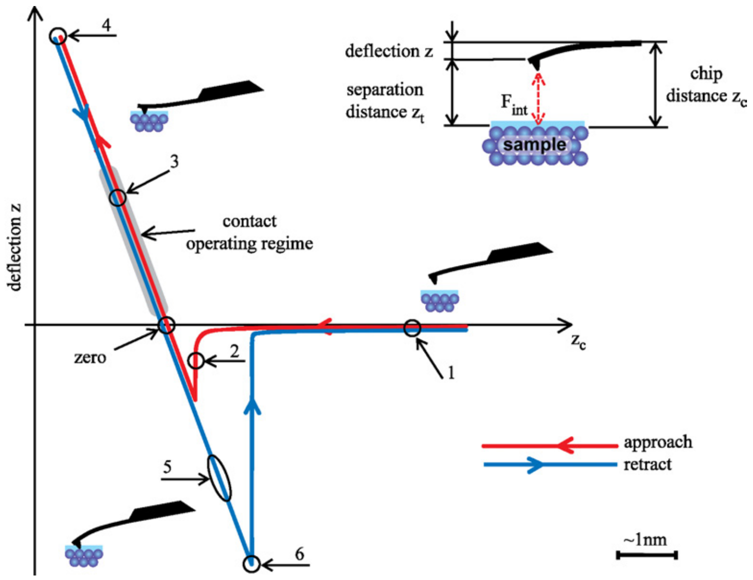

Figure 2.14: The approach-retract curve; the cantilever deflection as function of chip-sample separation distance.

As can be seen from the figure 2.14, there is instability of the cantilever position around point 2. This is the reason why it is impossible to operate the AFM in static non-contact mode. Commercial AFMs use dynamic non-contact operation mode to eliminate the instability, see chapter 2.2.2. The cantilever is excited at its resonant frequency and vibrates with an amplitudes 1 to 100 nm. When the tip approaches the studied sample, the vibrating cantilever is pre-deflected towards the surface. In this case, the restoring force is much higher than the attractive force. The stability of the system can be improved by increasing

the vibration amplitude. Therefore, this technique has a limitation and an agreement has to be found between the vibration amplitude and the interaction intensity.
A novel approach to operate the AFM in static non-contact mode has been developed by *A. Gannepalli*, see [51, 52, 53]. This technique is observing the changes in the resonant frequency of thermally excited cantilever. According to this frequency shift a feedback control is applied to maintain the tip-sample separation distance constant. This new technique only guaranties the stability for very small attractive forces and is not yet used as standard measuring method in any commercial AFM .

Regulation loops present in the AFM
The regulation in the AFM is a very important issue and it is absolutely necessary for the operation of the microscope. Figure 2.15 shows a basic schema of AFM control. There are two main loops: one is responsible for maintaining the cantilever in the interaction with the surface (z-scanner controller) and, in dynamic operation mode, the second loop excites the cantilever (driving controller). The feedback loops are functionally connected and in certain measurements, they can be reduced to just one. In certain cases, the output of the two loops can be set to a constant value, independent on the measured signal. Each standard operation techniques has a proper regulation scheme. For many years only function generators has been used to operate the x-y scanner. In recent years has been shown the advantages of using feedback control to eliminate the hysteresis and the creep of the scanner. The two control loops shown in figure 2.15 will be treated in section 2.3.1.

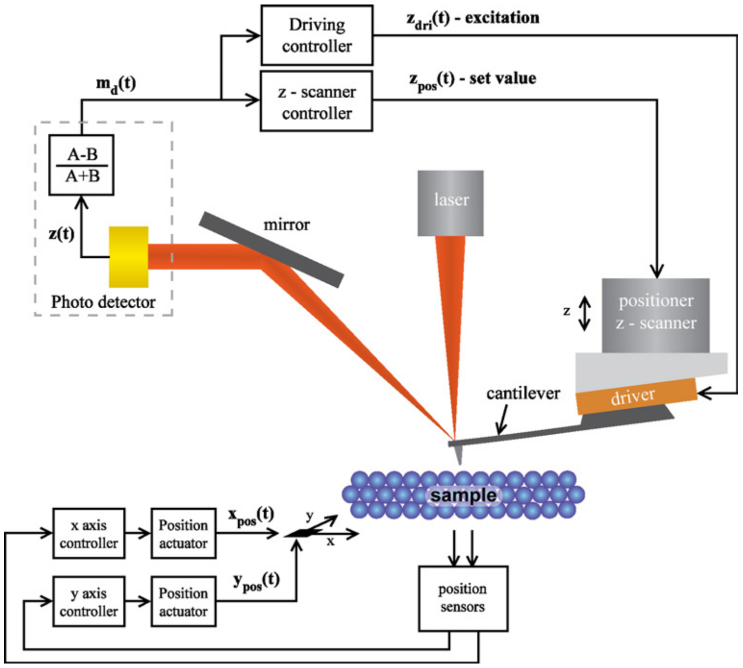

Figure 2.15: The AFM basic control loops.

2.2.1 Contact (static) operation mode

The contact (static) operation mode is the simplest way how to operate the atomic force microscope, see figure 2.2. This mode does not require any driver nor any demodulation electronics. The cantilever is held in permanent contact with the studied sample. This mode has very good capabilities to operate with high accuracy in liquid environment, see [54, 55], in comparison with difficult application of the dynamic operation mode. Another

advantage is the simplicity of the relation between the measured signal and the topography or any other information of our interest. The contact mode is as well one of the methods how to investigate the friction [9], elasticity, deformation and many other mechanical properties of studied surface at nanometric scale [56, 57].
In contact mode, the cantilever is positively deflected and the present forces are purely repulsive, see figure 2.14. Two basic operation modes exist:

Constant high mode

This operation mode is the simplest operation mode. It is used quiet rarely due to its incapability to measure large topographical differences. The cantilever approaches the sample and desired interaction intensity is found with knowledge $F_{int} = k \cdot z$, where k is the cantilever's spring constant and z is the deflection in vertical direction. Then the position of the head is fixed for the entire measurement. The scanner scans across the sample surface and the measured value is directly the cantilever deflection red out from the photo-detector. The drawback of this method is that the interaction force changes during the measurement. If the studied specimen is soft, deformations or permanent damage can occur.

Constant intensity mode

In this mode, the feedback control of the head position is required to operate the AFM. The cantilever approaches the surface and reaches the desired surface interaction intensity. This value is used as a “set point" for the head position controller. During the scanning, the controller regulates the head position to maintain the interaction force constant (the lever deflection constant) despite the changes in the topography. The measured signal is then directly determined from the “z" position of the head. Any changes in the cantilever deflection during the measurement are considered as a measurement error. This mode has no limitation in the topography height and always applies the same stress at the sample. However, the scan size and scan speed have to be chosen carefully, so the controller is capable of maintaining the desired interaction intensity without large errors. Too fast scanning of a very narrow sample can cause even damage to the sample. Nowadays, this method is considered as “standard" contact operation mode and in all publications it is simply called “contact mode", see figure 2.2.

2.2.2 Non-contact (dynamic) operation mode

A simplified analysis of the cantilever dynamics has already been given in chapter 2.1.2. The cantilever can be described as a harmonic oscillator. Motion of the cantilever is described with three values: the amplitude, the frequency and the phase. Each of these properties can be used as information channel of the interaction force. In other words, the surface interaction changes the oscillator properties which result in changes of amplitude, frequency or phase. The existing dynamic operation techniques can be divided according to the observed quality.
In this operation mode the cantilever is driven by the driver close to its resonant frequency with a certain amplitude and phase shift. The vibrating lever is brought in proximity to the measured surface (0.5-10nm). The attractive long distance interaction forces and the repulsive short distance interaction forces affect the cantilevers effective spring constant (conservative interaction) and the damping coefficient (dissipative interaction).

Amplitude modulation technique AM-AFM, Tapping mode

The Amplitude Modulation (AM) technique is an original non-contact dynamic operation mode for AFM. It has been developed by *Y. Martin* in 1986, see [10]. The cantilever is driven at frequency ω_{drive}, which is closely bellow the first resonant frequency ω_0, with constant driving force (amplitude). The amplitude of the vibration decreases and the phase shifts as function of the interaction force (cantilever-sample separation distance). The setup of the amplitude modulation technique AFM is shown in figure 2.16. The cantilever is excited by a piezoelectric actuator driven by a function generator with constant driving amplitude and frequency: $z_{drive} = A_{drive}cos(\omega_{drive}t)$. The position of the lever is detected by the photo-detector and fed into the Lock-in amplifier. It detects the vibration amplitude $A(\omega)$ and the phase shift $\phi(\omega)$ between the cantilever position *z(t)* and reference signal from the function generator. In this operation mode, the detected amplitude is used to measure the studied sample. It is as well fed into the controller of the vertical scanner (positioner). This controller generates a positioning signal $z_{pos}(t)$ from the regulation error towards the “set-point" (desired amplitude). The “Set-point" value of the amplitude is chosen by the user according to the desired intensity of the interaction and the free vibration amplitude, see figure 2.17. Usually, the set point is between 80-90% of the free vibration amplitude. If the set-point is too close to the free oscillation amplitude, the loss of contact with the sample can easily occur. On the other hand, if the interaction is very intense (the set-point is very low), the driver can experience difficulties to keep the lever vibrating and the cantilever can "snap in” into the static contact regime.

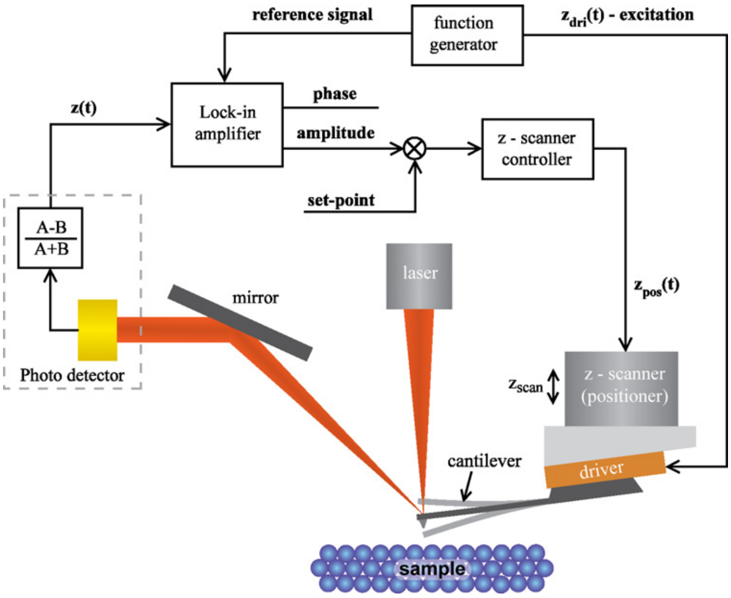

Figure 2.16: The AFM amplitude modulation mode - operation scheme.

The main difficulty of the amplitude modulation mode is the problematic explanation of relation between the measured amplitude change and the measured interaction force. For example, if the cantilever is excited directly at its free resonance frequency and dissipative surface interaction is introduced. Then, the oscillator changes its resonant frequency and the measured change in amplitude is caused by the interaction and as well by the changed resonant frequency. This coupled behavior is impossible to eliminate and there isn’t any quantitative theory for the amplitude modulation technique. Furthermore, instabilities and hysteresis are present in this operation mode. These effects compromise the measured results and the user has to be aware of these problems. This field has been deeply studied by *Anczykowski*, see [58, 59][60], and it has been shown that the non-linearity is very dependent on the choice of driving frequency. The best results are achieved with an excitation frequency equal or above the free resonant frequency [61, 62, 63].

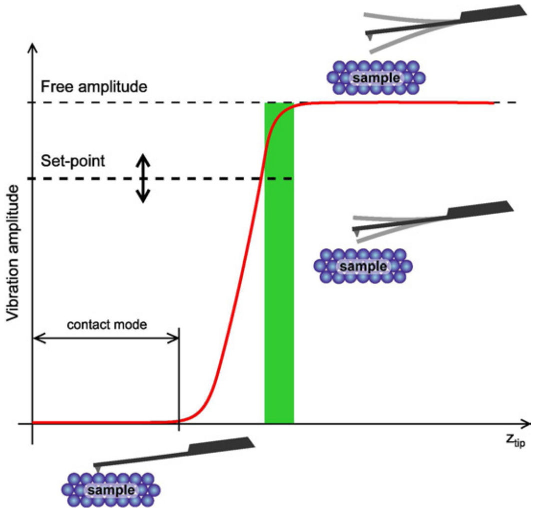

Figure 2.17: Selection of the Amplitude modulation “Set-point". The maximum amplitude stands for a free cantilever without interaction. If the tip-sample separation distance decreases, the resonant frequency changes and the vibration amplitude decreases. The green zone is the area where the interaction is only attractive and there is no energy dissipation. Below this zone the dissipative forces start to attenuate the lever motion. If the separation distance is smaller than a certain limit the cantilever enters the full contact mode.

Although the amplitude modulation technique is considered as non-contact technique, the mechanical contact with the studied surface can occur. If the set-point is close to the free amplitude only the attractive interaction forces are present. But, by choosing the set-point low, more repulsive forces are present in the interaction. For very low set-point, the repulsive forces are dominating. The contact with the surface occurs at the maximum deflection of the cantilever towards the surface and it only last a very small fragment of the oscillation period. In this case, the AFM is operating in the **Intermittent contact regime** [64].

To achieve maximal measurement sensitivity, a slope detection technique is used in dynamic operation mode of AFM. The measurement is based on detecting the change in amplitude or phase of the measured signal. To achieve highest sensitivity, the changes of vibration amplitude $A(\omega)$ or phase $\phi(\omega)$ are measured in the steepest slope on the side of the Lorentzian describing the resonance peak, see figure 2.18. Here, the smallest change in frequency or phase induces easily detectable changes. In the case of a high quality factor, the steepest slope of the resonance peek is at $\omega_m \simeq \omega_0(1 \pm 1/\sqrt{8}Q)$ and the gradient of amplitude is equal to

$$\frac{\partial A}{\partial \omega} = \frac{4A_0Q}{3\sqrt{3}\omega_0} \tag{2.14}$$

Dynamic properties of amplitude modulation technique has been studied by many authors [65, 66, 67, 68, 10], Here, only the results concerning the vibration amplitude in the weak attractive interaction with the surface will be given, see the green zone in figure 2.17. For large tip-sample separation distance, the influence of the interaction forces can be neglected and the vibration amplitude $A(\omega)$ is only function of frequency, with Lorentzian form

$$A(\omega) = \frac{A_0(\omega_0/\omega)}{\sqrt{1 + Q^2(\omega/\omega_0 - \omega_0/\omega)^2}} \tag{2.15}$$

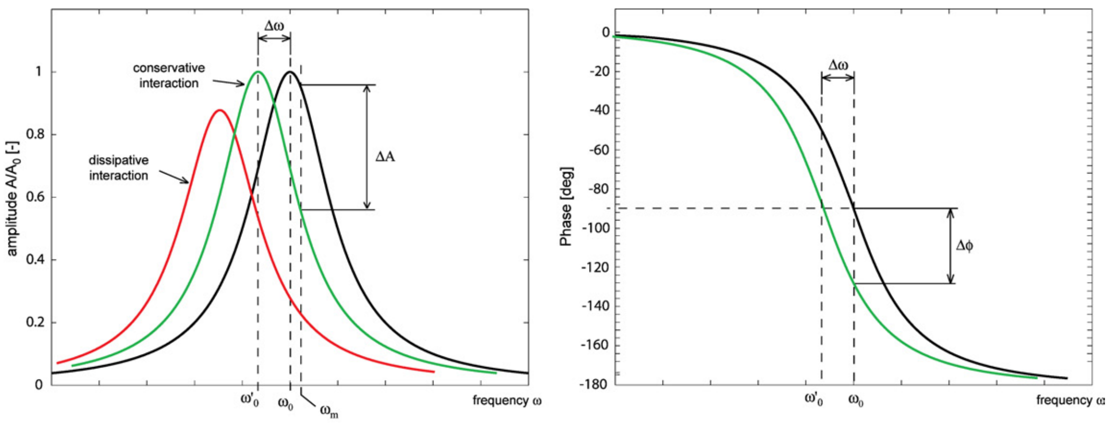

Figure 2.18: The slope detection of an amplitude and a phase as function of the frequency. The attractive interaction force decreases the oscillation frequency. The green curve displays the weak and not dissipative interaction related to the green zone in figure 2.17. The red curve is resonance peak with strong dissipative interaction. In this case the damping coefficient γ of the oscillator is changed.

where A_0 is the amplitude at the resonance frequency ω_0 and Q is the quality factor of the cantilever. As the separation distance between tip and surface is decreasing, Van der Waals force starts to affect the lever movement and needs to be taken into account. The interaction force acts as an additional spring between tip and surface. The resulting resonant frequency of the new system is:

$$\omega_0' = \sqrt{\frac{k - \frac{\partial F_{\text{int}}}{\partial z}}{m}} \tag{2.16}$$

where $\partial F_{\text{int}}/\partial z$ is the interaction force gradient. This is only valid for reasonably small gradient, which doesn't significantly affect the movement of the lever. If we insert this expression into equation 2.15, we can derive expression for the interaction force gradient as function of free amplitude $A_0(\omega)$ and amplitude with interaction $A(\omega)'$.

$$\frac{\partial F_{\text{int}}}{\partial z} = k\left(\frac{1 - 2a^2 + \sqrt{4Q^2(a^2-1)+1}}{2(Q^2 - a^2)}\right) \tag{2.17}$$

where $a = A_0/A(\omega)'$. By integrating $\partial F_{\text{int}}/\partial z$, we can obtain the interaction force. This equation assumes that the interaction is not dissipative. In other words, there is no energy loss and the interaction is weak and attractive (set-point is close to the free oscillation amplitude). Then, the interaction changes the resonant frequency of the oscillator according to equation 2.16 which results in a decrease of the vibration amplitude due to excitation off the resonance. If we further assume that the interaction force gradient is much smaller than the spring constant of the lever $\frac{\partial F_{\text{int}}}{\partial z} \ll k$, so that the vibration mode is not significantly modified (green zone in figure 2.17). Then, the detected change in the amplitude caused by the frequency shift 2.16 is equal to

$$\Delta A = \frac{2A_0Q}{3\sqrt{3}k} \cdot \frac{\partial F_{\text{int}}}{\partial z} \tag{2.18}$$

The thermal energy is the dominating disturbance in the AFMs and induces an amplitude fluctuation $A_{Ther} = \sqrt{2k_BT/k}$, where k_B is the Boltzmann constant and T stands for temperature. The vibration noise at frequency ω_m is $N = \sqrt{4k_BTQ\beta/k\omega_m}$, where β is the measurement bandwidth. The minimum detectable force, due to thermal noise disturbance, is then given by:

$$\left(\frac{\partial F_{\mathrm{int}}}{\partial z}\right)_{min} = \frac{1}{A_0}\sqrt{\frac{27kTk_{\mathrm{B}}\beta}{\omega_0 Q}} \tag{2.19}$$

The measurement bandwidth - the vibration amplitude does not change instantaneously according to the change of the tip-surface interaction. The new settled vibration amplitude is reached after a time delay of

$$\tau_{AM} = \frac{2Q}{\omega_0} \tag{2.20}$$

Hence, the amplitude modulation technique is slow for a cantilever with a high quality factor. Still, a good quality factor increases the measurement sensitivity (signal - thermal noise ration). This advantage has been combined with fast imaging in the frequency modulation technique.

Frequency modulation technique FM-AFM

One of the standard technique to operate the AFM in non-contact dynamic mode is the frequency modulation (FM) technique, which has been developed by *T.R. Albrecht* and *P. Grütter* in 1990, [69]. The first true atomic resolution using the frequency modulation has been achieved by *F. J. Giessibl* in 1995 on the pure silicon surface (111), [70]. The complete operation setup is shown in figure 2.20. As can easily be seen, this operation mode requires two regulation loops: one to keep the oscillation amplitude constant and the second to maintain the interaction set-point. The cantilever is driven at frequency ω_{drive}, with constant vibration amplitude A_0. The driven frequency is slightly off the free cantilever resonant frequency ω_0. The interaction with the surface is shifting the resonance frequency to ω_0', which is the observed quantity used in frequency modulation as set-point. We suppose that the actively controlled vibration amplitude A_0 remains constant during the measurement. Then, the information about the tip-surface interaction is directly related to the change in oscillation frequency ω_0' and is a function of the separation distance. The frequency modulation technique can operate with very high quality factors of the cantilever and at the same time can benefits from a smaller thermal noise disturbance.

To understand all the advantages of the shown set-up, a more profound description is necessary. The cantilever position is continuously red by the photo-detector and from its output, a signal amplitude and frequency are deduced. The Lock-in amplifier is used to

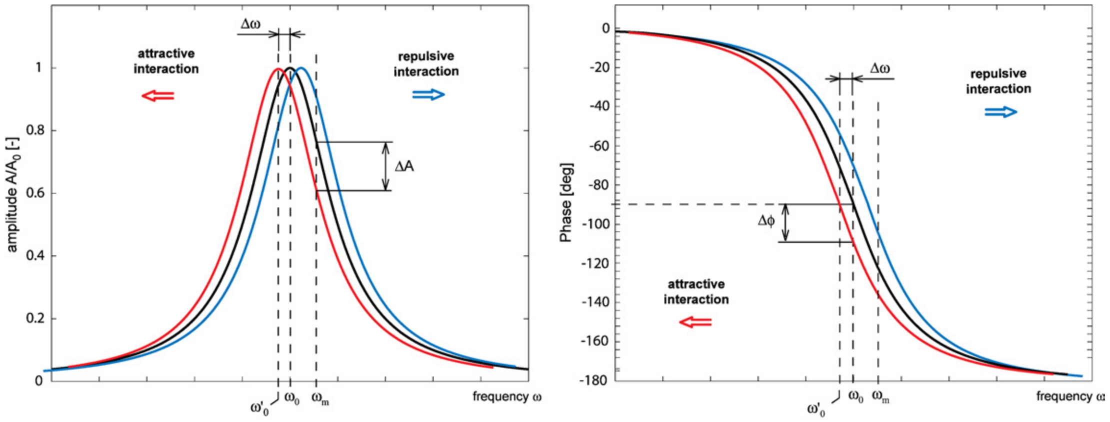

Figure 2.19: The amplitude and the phase as function of frequency. An attractive interaction force decreases the oscillation frequency whereas a repulsive interaction force increases it.

detect the vibration amplitude from the noisy signal and compare it with the desired amplitude. The error in the amplitude is fed into the excitation controller (usually PI) that selects the gain of the amplifier. The input of the amplifier is directly the photo-detector output, in some cases it is filtered. Afterwords, the amplifier output is phase shifted according to the user choice and resulting signal is directly exciting the piezoelectric driver. Hence, the lever is driven with a phase shifted and amplified read out of the photo-detector. For this reason, this mode is sometimes called **Self-Excitation mode** [71]. The second control loop is responsible for positioning the head together with the cantilever above the sample. The frequency demodulator converts the actual frequency into voltage that is then compared with the desired oscillation frequency, as well converted to volts. The frequency error is given to the head position controller (z-scanner controller) which displaces the head the way that the desired frequency is reached. Now, the topography is directly the saved vertical scanner position.

The output of the controller selecting the amplifier gain gives us information about the dissipative processes during the measurement, for example measure of the surface elasticity, see [72]. Without any surface interaction, a minimal gain value is necessary to keep the cantilever excited at the desired amplitude. If the cantilever is brought into non-dissipative interaction with the surface, this gain remains the same. But, in case that there is any interaction with loss of energy, the gain will have to change to maintain the same vibration amplitude. Which means, the gain is related to the dissipation in the system. In some specific operation modes, a dissipation can be used as desired set-point instead of the frequency shift. Another alternative is to use the phase shift of the excitation loop as set-point. Then instead of detecting frequency shift, a phase shift is detected. However, this is not a standard operation and requires an experienced user.

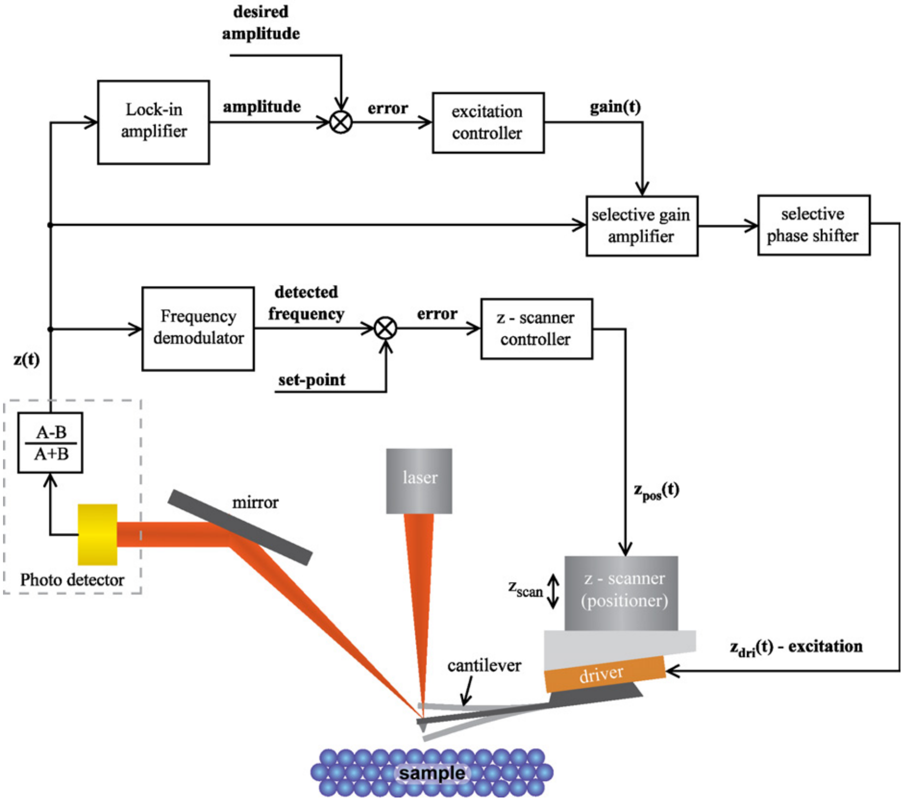

Figure 2.20: The AFM frequency modulation mode - operation schema.

Even in the standard frequency modulation, many information about the sample can be derived from the transient changes of the phase. The phase is very sensitive to high frequency

properties of the studied specimen, for example sharp edges. The vibrating cantilever has a certain settle time masking sudden changes in topography, but the phase is extremely sensitive to them. In certain experiments, this is another reason for using the phase shift as a set-point. For deeper understanding and an exploration of all operation possibilities see [68, 69].
This functionality description of the frequency modulation technique, is only a short overview and not all the possibilities how the AFM can be operated have been given. Many additional information about the sample can be extracted from the acquared signals.

The mathematical description of the frequency modulation mode is similar to that of the amplitude modulation mode. The surface interaction is affecting the effective spring constant of the cantilever

$$k_{eff} = k - \frac{\partial F_{\mathrm{int}}}{\partial z} \tag{2.21}$$

which results in the frequency change

$$\Delta\omega = \omega_0 - \omega_0' = \frac{k}{m_{eff}} - \frac{k_{eff}}{m_{eff}} = \frac{\frac{\partial F_{\mathrm{int}}}{\partial z}}{m_{eff}} \tag{2.22}$$

By decreasing the separation distance, the resonance frequency shifts to the new value ω_0'. The harmonic oscillator in amplitude modulation mode has a new solution of steady state vibrations, which now contains a transient term

$$z(t) = A_0' \cos(\omega_{\mathrm{d}} t + \vartheta_0') + A_t' e^{-\omega_0' t/2Q} \cos(\omega_{\mathrm{t}} t + \vartheta_{\mathrm{t}}') \tag{2.23}$$

where, A_0' and ϑ_0' are the new steady-state amplitude and phase, A_t' and ϑ_{t}' are adjusted to fit boundary conditions and ω_{t} is the resonant frequency for free oscillations given by

$$\omega_{\mathrm{t}} = \omega_0' \sqrt{1 - (1/4Q^2)} \tag{2.24}$$

As can be seen, the second part in equation 2.23 gives the transient behavior of the oscillator. The exponential part defines the transient decay, leading to the settling time of the system. The periodic term is the transient beat of the system. In the frequency modulation technique, the transient behavior is suppressed by the amplitude control loop. Thus, the settling time does not depend on the quality factor any more

$$\tau_{FM} = \frac{1}{\omega_0} \tag{2.25}$$

Many careful analysis have been done in the past. They proofed that the minimum detectable force, due to thermal noise disturbance, is given by:

$$\left(\frac{\partial F_{\mathrm{int}}}{\partial z}\right)_{min} = \frac{1}{A_0}\sqrt{\frac{4kTk_{\mathrm{B}}\beta}{\omega_0 Q}} \tag{2.26}$$

where A_0 is the vibration amplitude of the cantilever, β is the measurement bandwidth, k_{B} is the Boltzmann constant and T is the temperature. As we have seen, this equation is valid in close proximity of free resonance frequency ω_0. This equation is almost identical to the amplitude modulation mode's minimal sensitivity. The main difference is that the frequency modulation is capable to operate with very high quality factors, significantly improving the operation mode sensitivity.

The exact formulation of the relation between interaction force and frequency shift has been developed in many publications with different approaches, see [68, 73, 74, 75, 76]. Here, only the latest result published by *E. Sader* [76] is given. This is a simple analytical relation between frequency shift and interaction force (energy). The solution is valid for any amplitude of the cantilever vibration and any interaction force. The main advantage of this solution is its simplicity, so that does not require enormous computing power and provides freedom in the vibration amplitude.

$$F_{\text{int}} = 2k \int_{z}^{\infty} \left(1 + \frac{\sqrt{A_0}}{8\sqrt{\pi\left(t-z\right)}}\right) \frac{\Delta\omega(t)}{\omega_0} - \frac{\sqrt{A_0^3}}{\sqrt{2\left(t-z\right)}} \frac{d\left(\frac{\Delta\omega(t)}{\omega_0}\right)}{dt} dt \tag{2.27}$$

2.3 Control approach for SPM

In recent years, the scanning probe microscopy community has shown increasing interest in control. The potential of applying advanced control strategies has been demonstrated in many publications and, recently, the newest versions of commercial scanning probe microscopes successfully adopt these results. This sudden development of control systems in SPM is strongly influenced by new technologies allowing the application of more complex operation controllers and data treatment. Digital Signal Processors (DSP) and Fully Programmable Gate Arrays (FPGA) are the leading technologies used to implement complex operation controllers, capable of operating at high speed. The older SPMs mainly used proportional-integral (PI) regulators to operate the basic functionality of the microscope and most of the modulation and data treatment has been done analogically.
In the following section, the most important results in the application of advance control approaches in Scanning Probe Microscopy are presented.

2.3.1 Lateral scanners and z - axis positioning

In the section 2.1.4, basic scanner based on a piezo-electric tube acting as x,y scanner (lateral scanner) and z positioner has been presented. The principal difficulty of using the precalibrated open loop scanners is the non-linearity and the hysteresis of the piezoelectric actuator. Certain techniques have been developed to eliminate these effects by data treatment with inverse filters, see [77, 78] and feedforward techniques for vertical positioning enhancement, see [79, 80]. To improve the capabilities of the instrument, some attention has been given to the optimalization of the scanner movement in time domain [81] and also to the decoupling of the lateral scanner movement from the head's z position of the microscope [82]. The resolution has been improved, but these techniques cannot be recognized as ultimate solution to the given problem.

The scanners have rapidly evolved from the original open loop operation to closed loop schemes with position sensors capable to detect displacements in the order of the Angstrom. This technique is capable to eliminate the non-linearity of the actuator relatively independently on the scanner motion speed. It also allows to easily operate the scanner as a manipulator capable of complex movements with guaranteed repeatability and accuracy. First steps in adopting advanced control techniques instead of classical PI and PID controllers have been published in [83, 84, 85]. They clearly demonstrate that the accurate positioning of the sample is possible even at high operation velocities. To achieve a good noise rejection, a higher bandwidth and stability of the lateral scanner, many author recently concentrate on the application of robust control strategies, see [86, 87, 88, 89].

Robust control techniques have been used as well in standard tapping mode to improve the properties of the z positioning loop and to increase the scanning speed. The improved ability to follow studied topography with smaller error in comparison to standard PI-controllers, has been shown in [90].

A lot of development has been done not only on the control side, but as well in the mechanical design. New stages are capable of moving trough larger ranges with high speeds. Very important for the wide range movement is the “stick-slip" technique, which has been adopted for an application in SPM by different authors, see [91, 92, 93]. The stick-slip stages are capable of travel distances in the order of millimeters in a small steps (few micrometers). Once the desired position is reached, it can be used as open loop scanner. New lateral scanners for extreme high speed operation have been developed as well. These stages have to be carefully identified and usually robust controllers are used to operate them, see [78, 94].

2.3.2 Measurement improvement

Another wide field of implementation of new control strategies in AFM is focused on the measuring methods and the detection of surface interaction. In the following, few paragraphs mention only a selection of the most important techniques which have been proposed. Some of the techniques are very specific and have very limited application in general scanning probe microscopy.

Q-control technique
The amplitude modulation (AM) technique developed by *Y. Martin* in 1986, see [10], opened new possibilities to profit from the dynamic properties of cantilever being mechanically excited at its resonant frequency, to operate the AFM in non-contact mode. The cantilever stays in non-contact mode only if the vibration amplitude is large enough, so that the restoring force overcomes the attractive interaction force.
The minimal detectable interaction force gradient in amplitude and frequency modulation technique depends on the cantilever quality factor, see equations 2.19 and 2.26. In high viscosity media the quality factor is lowered by the environment and in some cases can become difficult to drive the oscilator. These were the main motivations to develop a new methods to activelly adjust the oscillator's quality factor and in order to reach better sensitivity. With increased quality factor, a vibration amplitude and frequency with the slope detection technique can be as well more precisely detected.

To meet these requirements Q-control technique [95] has been introduced, that is enhancing the effective quality factor of the cantilever by applying feedback control. This technique has been further developed [96] and successfully applied to liquid environments [97, 98]. A theoretical analysis of the Q-control technique can be found in [99].

Though a high quality factor results in better imaging resolution, at the same time it extends the cantilever settling time and imposes constrain on the scanning speed. As response to demand for high scanning speed in environments with low viscosity has been developed, Q-control technique allowing via feedback loop artificially decrease the cantilever's quality factor. Like this a higher scanning speeds can be reached with in drawback in lower detection sensitivity, see [100, 101].

New measurement strategies
Recent years have shown the potential in applying observer based detection techniques in SPM. The first publication about observer enhanced sample detection used the observer innovation signal as measurement of the topography [102]. This technique is capable of detecting sudden changes in the surface topography by detecting the transient signal in the phase and amplitude of the cantilever position. Main drawback is that the technique is not able to detect smooth (or sufficiently slow) topographical changes or to measure flat

parts of the topography.

A combination of Q enhancement based on an observer has been presented in [103]. The observer allows the user to change the effective quality factor of the cantilever to achieve maximum sensitivity for a given scanning speed. The system allows to choose the compromise between measurement speed and sensitivity while, at the same time, it profits from the detection of transient changes in the phase and the amplitude.
Some authors are focusing on developing a force detection system similar to the frequency modulation technique but the sole source of cantilever excitation is the thermal noise, which is always present in the system, see [53, 52, 51]. To be able to guaranty the stability of a non-contact measurement and to avoid the snapping effect in certain distance range, the authors have used relatively stiff cantilever. While the tip was approaching to the measured surface, the frequency shift thermally induced vibrations of a cantilever have been measured. From this frequency shift the interaction force has been calculated. The difficulty of this technique is the long period of time needed to obtain the frequency spectra from the measured pseudo-random cantilever deflection.

New sensors
A quartz tuning fork has been introduced as a new sensors for scanning probe microscopy [104, 105]. Their main advantages are a very high quality factor of the oscillator which has order up to tens of thousands and capability of self sensing. The extremely high quality factor of this new type of sensor allows to detect an interaction force with high accuracy. The tuning fork does not need any external detection of its position due to its capability of self sensing based on the piezoelectric effect converting the mechanical stress into electrical charge. Its additional quality is the higher stiffness allowing operate with small vibration amplitude in close proximity to the sample without instability problems like the snap-on effect, see [106]. The negative consequence of the high stiffness is the very strong impact, which usually damages the measured surface and the tip if it gets into the contact regime.

A new sensor for SPM based on a thin flexible membrane driven by electrostatic actuator was presented in [107]. Sensor has a round shape with a sharp tip mounted in the middle and its function is very similar to microphone sensor. The difference is that the imposed force is not induced by incoming acoustic waves but by sharp tip interaction with the studied surface. This sensor can be used for contact and non-contact operation. The excitation in the dynamic operation mode is done by applied electrostatic force between the flexible membrane and the fixed electrode mounted above it. The position is detected optically from the diffraction pattern created by the reflected light form the back of the membrane and from the fixed electrode which has a diffraction gratings.

The difficulties of the dynamic excitation of a cantilever emerged in liquids have been addressed in [50]. The direct mechanical excitation of the cantilever in liquid is very difficult due to the high viscosity of the liquid. It intensively lowers the cantilever quality factor and the acoustic reflection from the surrounding objects that disturb its motion. A proposed sensor uses a triangular cantilever as single loop of an electromagnetic coil which is put into a static magnetic field. If an electric current starts to flow trough this simple loop with a frequency close to resonance frequency of the cantilever, the induced electromagnetic force starts to excite the cantilever.

Chapter 3

Dynamic modeling

This chapter introduces dynamic model of the cantilever and simplified model of surface interaction forces. Presented model is one of many existing possibilities, how to represent given system. The model developed in this chapter allows to perform the analysis of higher harmonic modes influence in Amplitude modulation technique. It will be as well used in folowing chapter to construct a state space observer and explore its aplication to Atomic Force Microscopy.

3.1 Interaction forces

In close proximity to a studied sample, a cantilever tip interacts with a great variety of forces. The appearance of certain forces and their intensity depends on many different properties. Many of them can be eliminated, if needed, by appropriate experiment design and construction. A detailed description of all of them is behind the scope of this thesis and only a short overview will be given in the following sections. Only those forces which have a considerable importance for our experiment, will be analyzed in greater details.

Electrostatic force, also known as Coulomb's law, appears between two charged objects. It is proportional to their charges and inversely proportional to a square distance between them. The force is either attractive or repulsive, depending on the polarity of the charges. Usually in Scanning Probe Microscopy this force is present because of residual charges on the surface imposing distortion to the measurement. In standard topographical measurement this charge then appears as a non-existing topography. This residual or intended local charge of a sample and its time propagation is not always undesirable, and in certain cases, it is even a property of interest, see [108].

Magnetic force can be generated by a permanent magnet or by a changing electric field in proximity of the experiment. In topographical measurements, most of these forces are considered as parasite and can be eliminated or at least minimized by shielding. In case, the surface has a magnetic properties, Magnetic Force Microscopy (MFM) offers possibility to locally study the magnetic properties of the specimen via force field induced by studied material, see [12].

Friction force, occur between moving tip and studied specimen in contact mode measurements and depends on material properties, the surrounding media and imposed force. In case of topographical measurements of soft samples, this force is not desirable and decreases the measurement accuracy. To eliminate this problem, Tapping mode technique has been developed. This technique minimizes the friction force effects during the measurement and the tip stays in direct contact with the sample only for fragment of the cantilever's vibration period. In certain cases, the friction force is the studied property of the sample, see [6, 7, 8, 9].

Viscous force are caused by the media between tip and surface when the media is experiencing share stress induced by the moving tip. In non-contact (dynamic) measurements, this force can be neglected due to large tip-surface distance for most of vibration period. However, in contact mode it can play a significant role. The viscosity of the surrounding environment contributes to the effective damping factor of the cantilever in the dynamic operation mode and it significantly affects the position of the resonance frequency.
In contact measurements, a very important effect related to surrounding media is the capillarity force is present which keeps the tip in the contact and causes the hysteresis of approach-retract curve, see section 2.2, figure 2.14. The capillarity is usually caused by water being always present in the air and on the measured surface. This effect can be minimized either by replacing the air with controlled atmosphere or by working in vacuum.

Elastic restoring forces occur in the sample when it is elastically deformed by the cantilever's tip. The restoring force is mainly measurable on soft sample surfaces during full contact or Tapping mode measurements. The Tapping mode is usually used to measure the elasticity map of a soft sample because it can effectively eliminate the difficulties of friction tip-sample interaction that appears like a distortion in this measurement.

Chemical forces are the physical description of chemical bonds. The atomic bonds hold together by sharing or exchanging electrons. Strong chemical bonds are found in molecules, crystals or in solid metal and they organize the atoms in ordered structures. Weak chemical bonds are classically explained to be a consequence of polarity between molecules which contain strong polar bonds. Chemical bonding in Probe Microscopy is a result of chemical reactions between the cantilever tip, surface and surrounding substance. Chemical bonding can be minimized by working in vacuum or inert gas. In the laboratory, the air can be assumed as relatively neutral, and the influence of chemical forces can be neglected in comparison with other stronger interactions.

The main interest in Atomic Force Microscopy is the measurement of the weak tip-surface interaction force called: Van der Waals force. Through measurement of this force, the topography of the studied surface can be found. Due to an appropriate experiment design, we assume that all other forces listed above are equal zero or in its close proximity, so that they can be neglected.

Van der Waals force belongs to the group of chemical forces but it has outstanding properties that give great importance to this force. Sometimes, it is also called London force or London dispersion force. Unlike most of the chemical bond forces, the Van der Waals has a long distance range and it is much weaker. This force originates from transient dipoles created between molecules without any permanent bi-pole moment. Transient bipoles result in uneven distribution of electrons (electron cloud) around a nucleus, which results in weak positive charge on one side of the molecule and a negative one on the other side. This transient behavior occurs in all molecules of given object. If two materials are brought in close proximity, it results as an attractive force between these two objects. The Van der Waals force appears between all neutral atoms and molecules independent on their kind. Sometimes Van der Waals force is referred as "nanoscale gravitation". The description of the interaction forces given below is very simplified, but further text will show how this minimized family of forces is a very complex problem leading to many different behaviors of the cantilever.

Repulsive force, The last interaction force to be mentioned, with great importance for our experiments and simulations, is the **repulsive force**. It appears at very short distances between two atoms, and it is a direct consequence of Pauli's exclusion principle. When the two closest atoms of the tip and the sample are in the close vicinity, their electron clouds start to penetrate each other. But as each electron state must be occupied by a single electron, it results in a very strong repulsive force pushing the atoms apart.

3.1.1 Interaction force model

It exists a wide variety of interaction force models. One of the mostly used ways for modeling the interaction of a pair of atoms is the Lennard-Jones potential [109], also called 6-12 potential. This model is accurate mathematical representation of the empirical data. The L-J potential has the form:

$$V(z_t) = 4\varepsilon \left[\left(\frac{C_{12}}{z_t} \right)^{12} - \left(\frac{C_6}{z_t} \right)^{6} \right] \tag{3.1}$$

where C_{12} and C_6 correspond to the nearest neighbour distance between two atoms and 4ε corresponds to the energy of one atomic bond. These values depend on the used materials, [110, 75]. The term $(1/z_t)^6$ is the attractive part of the interaction dominating at long distances (Van der Waals force), the term $(1/z_t)^{12}$ is responsible for the repulsive part of the interaction dominating at short distances (repulsive force). The interaction force can be found by deriving the L-J potential with respect to z_t:

$$F(z_t) = - \bigtriangledown V(z_t) = 4\varepsilon \left[12{\frac{C_{12}}{z_t^{13}}}^{12} - 6{\frac{C_6}{z_t^{7}}}^{6} \right] \tag{3.2}$$

This equation describes the relation between one pair of atoms. If we consider that the two interacting objects (tip and sample) contain a large number of atoms, the sum over all possible atomic pair has to be done to quantitatively describe the interaction. Due to the enormous number of atoms, this sum/integral over the entire body of the interacting objects is technically impossible to do. An approximation overcoming this difficulty has been introduced by Hamaker, see [110]. This approximation is assuming three basic things which has to stay valid: first the interaction between the objects can be found by summing over all atomic pairs; second, the objects are from continues medium where the number of atoms is given directly by the density ρ; and the third, the material of the objects is homogeneous having constant density ρ and interaction constants C_{12} and C_6. In these conditions, the force between two arbitrarily shaped objects (numbered 1 and 2) can be formulated as:

$$F_{vdw} = \rho_1 \rho_2 \int_{v2} \int_{v1} F(z_t) dV_1 dV_2 \tag{3.3}$$

The following model development is based on this approximation. For further details see [111, 112].

3.1.2 Distances superior to a_0 (intermolecular distance)

The tip-surface separation distance has to fulfill the condition $z_t > a_0$, where a_0 is intermolecular distance depending on the material properties of tip and surface and for most of the materials is $a_0 \simeq 5$. Under this condition, only the attractive Van der Waals force is present and there is no repulsive or other force taking part in the interaction. Then, by using the Hamaker approximation [110], the interaction force can be found:

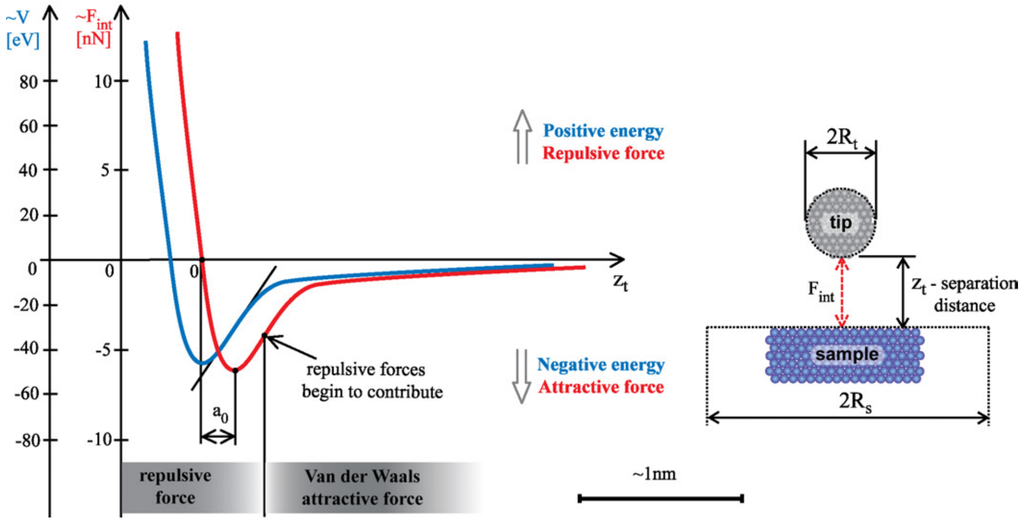

Figure 3.1: The Lennard-Jones potential (blue) and the interaction force (red) are shown as function of the separation distance z_t, on left. The tip can be approximated as sphere with radius R_t and the sample can be modeled as cylinder with radius R_c. In standard condition the relation between their radiuses $R_c \gg R_t$ stays always valid.

$$F_{vdW}(z_t) = 2\pi R_{eff} \frac{C_6}{z_t^2} \tag{3.4}$$

where C_6 is the Hamaker coefficient for Van der Waals interaction between two surfaces which is dependent on their shape. The combined effective radius R_{eff} of tip and sample is defined:

$$\frac{1}{R_{eff}^2} = \left(\frac{1}{R_{a1}} + \frac{1}{R_{b1}}\right)\left(\frac{1}{R_{a2}} + \frac{1}{R_{b2}}\right) + \sin^2\theta \left(\frac{1}{R_{a1}} - \frac{1}{R_{a2}}\right)\left(\frac{1}{R_{b1}} - \frac{1}{R_{b2}}\right) \tag{3.5}$$

where θ is the angle between the surface plane coordinates of the tip and sample (a and b). The variables R are the principal radii of curvature of both surfaces. Typically, the tip shape can be assumed as sphere of radius R_t interacting with a sample of cylindrical shape of radius R_s. For this simplification, these conditions are valid:

$$R_{a1} = R_{a2} = R_t \qquad\qquad R_{b1} = R_s,\ R_{b2} = \infty \tag{3.6}$$

Hence, the combined effective radius become:

$$R_{eff} = R_t \sqrt{\frac{R_s}{R_t + R_s}} \tag{3.7}$$

and the force gradient results in:

$$F_{vdW}(z_t) = 2\pi R_t \sqrt{\frac{R_s}{R_t + R_s}} \left(\frac{C_6}{z_t^2}\right) \tag{3.8}$$

In most applications, other further assumptions can be used. First, the radius of the sample cylinder is significantly larger than the radius of the tip $R_s \gg R_t$. Second, the regular Van der Waals interaction coefficient C_6 can be simplified by Hamaker theory to be replaced by $A_H/12\pi$, where A_H is the so-called Hamaker coefficient. Finally the equation for attractive Van der Waals force between spherical tip and planar surface is:

$$F_{vdW}(z_t) = -\frac{A_H R_t}{6z_t^2} \tag{3.9}$$

In non-contact Atomic Force Microscopy (dynamic operation), the main quantity of our interest is the gradient of attractive forces, applying between tip and surface. The gradient of attractive Van der Waals force ∇F_{vdW} can be written as

$$\nabla F_{vdW}(z_t) = -\frac{A_H R_t}{3z_t^3} \tag{3.10}$$

For a deeper theoretical explanation and further information see [110, 112, 113, 114, 115, 116, 117, 118].

3.1.3 Distances in the order of a_0 (intermolecular distance)

The tip-surface separation distance has to fulfill the condition $z_t \leq a_0$. The direct overlap between the electron wave functions (electron clouds) of tip and sample gives an important contribution to interaction as repulsive force. In other words, at very short distances, the strong repulsive forces are the consequence of Pauli's exclusion principle. Here, the presented model of the contact repulsive force is just one of any existing possibilities. For more details about other models see [111, 112, 119, 113, 120]

In the case of negligible energy dissipation in the tip-sample contact, a Derjaguin-Müller-Toporov (DMT) model [121] can be used to approximate the repulsive regime:

$$F_{DMT}(z_t) = -\frac{A_H R_t}{6a_0^2} + \frac{4}{3}E_{eff}\sqrt{R_t(a_0 - z_t)^3} \tag{3.11}$$

where A_H is the Hamaker constant, R_t is the tip radius, a_0 intermolecular spacing and E_{eff} is the effective modulus of elasticity:

$$\frac{1}{E_{eff}} = \frac{(1-\nu_t^2)}{E_t} + \frac{(1-\nu_s^2)}{E_s} \tag{3.12}$$

E_t and E_s are respectively the modulus of elasticity of tip and sample, while ν_t and ν_s stands for the Poisson ratios of tip and sample.

3.2 Thermal noise

In Atomic Force Microscopy a wide family of noise sources is present. However, in air at room themperature, the thermal noise of the cantilever is the main source of measurement distortion. This thermal distortion causes a random displacement of the end of the cantilever in all three dimensions, thus including the sharp tip. Due to a very high lateral stiffness of the cantilever (x and y axes in figure 2.6) the lateral Brownian motion magnitude is neglectable and we will only consider the vertical (z axis) deflection of the cantilever caused by the thermal distortion. As we have seen it in figure 2.7, the system can be represented by a spring, a damper and a mass, which is, in this case, excited by a force with random magnitude and orientation.

A random movement of a small particles in water has been for the first time observed by R. Brown in 1801. Since, the random movement is very often called Brownian motion after its founder. A small particles are experiencing a process called random walk over longer time periods. This randomly induced motion is caused by random interaction between the surface of the observed object and the surrounding medium. Due to the random direction and magnitude of the thermal force pushing onto the particle, the final trajectory is greater than zero with arbitrary direction and speed. This random motion has been given

a mathematical framework and it was generalized for any particle (atoms and molecules) by A. Einstein in 1905. He established a direct connection between the temperature of the system, the viscosity of medium and the speed of motion. Because of energetic or thermal origin of this fluctuation of atoms and molecules, this motion is often referred as a thermal noise. Other information can be found in [122, 123, 124, 125, 126].
Before approaching to Nyquist Theorem and its application in a micro-mechanical system, some mathematical tools necessary for operations with power spectral densities, have to be introduced. The Wiener-Khinchin theorem states that the power spectral density of stationary random process equals the Fourier transformation of its autocorrelation function.

$$S_{xx}(f) = \int_{-\infty}^{+\infty} C_{xx}(\tau) e^{-j2\pi f \tau} d\tau \tag{3.13}$$

where the autocorrelation function is defined as:

$$C_{xx}(\tau) = \langle x(t) \cdot x(t-\tau) \rangle \tag{3.14}$$

The power spectral density can be calculated from measured signals by:

$$S_{xx}(f) = lim_{Ti \to \infty} \left\langle \frac{2}{Ti} \left| \int_0^{Ti} x(\tau) \cdot e^{-j2\pi f \tau} d\tau \right|^2 \right\rangle = \left\langle x^2(t) \right\rangle \tag{3.15}$$

where Ti is the measurement period.
In case of a Linear Time Invariant (LTI) dynamic system with a complex response function *Z(f)* and a random input signal of power spectral density $S_{ii}(f)$, the output power spectral density can be written as:

$$S_{oo}(f) = |Z(f)|^2 \cdot S_{ii}(f) \tag{3.16}$$

The mean square value of the output fluctuation *x(t)* can be written as:

$$\left\langle x^2(t) \right\rangle = \int_0^{+\infty} S_{oo}(f) df = \int_0^{+\infty} |Z(f)|^2 \cdot S_{ii}(f) df \tag{3.17}$$

For a microscopic system of weight m_s (cantilever), placed in thermal bath of molecules (particles) with a mean mass m_m, it stays always valid that the system mass is significantly greater than the mass of the surrounding particles ($m_m \ll m_s$). The influence of collisions between the particles and the cantilever is weak and fluctuation response time t_f is significantly shorter in comparison with dissipation time response t_d ($t_f \ll t_d$). In this case the system reaches thermal equilibrium with surrounding medium which results in random motion of the microsystem. The thermal bath of temperature T taken as the input of the system, then the power spectral density of this input is described by the Nyquist theorem:

$$S_{ii} = 2k_B T \gamma m \tag{3.18}$$

where k_B is the Boltzmann constant and γ is the damping coefficient.
Coupling of a system to the thermal bath is often described with help of Langevin force F_T which is acting on the system. A harmonic oscillator excited by the Langevin force F_T (thermal excitation) is described by:

$$m\ddot{z} + \gamma \dot{z} + kz = F_T \tag{3.19}$$

With the solution of this differential equation and the help of equation 3.17, the power spectral density of the cantilever position can be found to be:

$$\left\langle z^2(t) \right\rangle = \frac{1}{2\gamma m k} S_{ii} = \frac{k_B T}{k} \tag{3.20}$$

where $\langle z^2 \rangle$ represents the deflection variance of the cantilever caused by thermal excitations. The same result can be easily obtained directly from the equipartition theorem. It states that, in thermal equilibrium, the thermal energy is evenly distributed over all degrees of freedom of given system with a mean value equal to

$$\frac{1}{2} k_B T \tag{3.21}$$

When the cantilever is statically bent in the vertical direction (by a small amount) its potential energy is

$$\frac{1}{2} k \langle z^2 \rangle \tag{3.22}$$

The equipartition theorem demands both energies to be equal:

$$\frac{1}{2} k_B T = \frac{1}{2} k \langle z^2 \rangle \tag{3.23}$$

This equation can be rearranged to directly calculate mean square displacement of the lever as function of temperature and spring constant.

$$\langle z^2 \rangle = \frac{k_B T}{k} \tag{3.24}$$

3.3 Multi mode cantilever model

Since the beginning of Scanning Probe Microscopy, a wide variety of cantilever models have been developed. Usually, these models are used for simulation of specific properties of the cantilevers, which results in different approaches taken by authors. There exist mechanical, electromechanical [38] physical models and finite element [127] numerical models. For many years, the cantilever was described as a single mode harmonic oscillator where only the first and most significant harmonic mode was taken into account.

3.3.1 Basic model

A simple harmonic oscillator has been introduced in chapter 2.1.2. Lets shortly summarized the basic oscillator parameters shown in figure 2.7. The effective mass m_{eff} (see equation 2.2) is attached to a spring with stiffness k (see equation 2.3) and to a dash-pot with damping coefficient γ (see equation 2.5). The mathematical description of the cantilever's dynamic behavior can be described by:

$$m_{eff} \frac{d^2 z}{dt^2} + m_{eff} \gamma \frac{dz}{dt} + kz = F_{\text{ext}} = F_{\text{dri}} + F_{\text{per}} + F_{\text{int}} \tag{3.25}$$

where F_{ext} is the sum of all external forces applied to the cantilever: the driving force from the piezoelectric element F_{dri}, the interaction force F_{int} and all perturbation forces F_{per}. This model is used in many published works and it is very useful in describing the behavior of the cantilever working around its first resonance frequency. For example, the description of the dynamic operation mode can be very elegantly simplified by using this basic model without a significant lost of accuracy as long as the surface interaction forces stays very weak. In the case of strong interaction, for example hard tapping, the higher harmonic modes start to contribute to the cantilever position and certain properties of the interaction cannot be accurately modeled.

3.3.2 More complex models of the cantilever

To describe the cantilever behavior as accurately as possible and to take into account its higher harmonic modes, more complex models have been introduced, describing the cantilever as a flexible beam [128]. In this model, the cantilever is described as a beam clamped at one end and freely vibrating at the other end. This description includes different modes of vibration at their specific resonance frequencies. The first ten vibration modes of the beam cover up to 96% of the root-mean-square (RMS) deflection amplitude in free vibrations. The shape of the first five harmonic modes is shown in 3.2. This model has been used in many publications, see [67, 129, 130, 131, 132, 133, 126, 123, 134].
The mathematical description [135] of the cantilever movement is based on the one-dimension Euler-Bernoulli equation which fully describes the dynamics of a rectangular cantilever. The mathematical description can be simplified by assuming, that all significant physical properties are constant along the beam span. Implies, that the moment of inertia $I(x)$, the Young's modulus $E(x)$, the mass per unit length $\bar{m}(x)$ (see equation 3.27), and the cross section are constant everywhere on the cantilever. Most cantilevers used in AFM are square or rectangular at their cross-sections and are sufficiently homogeneous to fulfill the requirements. The mathematical description of the free vibration is given by the differential equation of fourth order:

$$EI\frac{\partial^4 v(x,t)}{\partial x^4} + \bar{m}\frac{\partial^2 v(x,t)}{\partial t^2} = 0 \tag{3.26}$$

where $v(x,t)$ is the time dependent transverse displacement from the neutral position at the lateral position x along the cantilever span, $\bar{m}$ is the mass per unit length, and I is the area moment of inertia:

$$\bar{m} = wt\rho \tag{3.27}$$

$$I = \frac{wt^3}{12} \tag{3.28}$$

where ρ is the mass density ($\approx 2300 kg/m^3$ for silicon). One solution for equation 3.26 can easily be obtained by variables separation using substitution:

$$v(x,t) = \phi(x)Y(t) \tag{3.29}$$

where $\phi(x)$ stands for the motion shape and $Y(t)$ is the time dependant amplitude of the motion. After applying equation 3.29 to equation 3.26, the newly obtained motion equation is

$$\frac{\phi^{iv}(x)}{\phi(x)} = -\frac{\bar{m}}{EI}\frac{\ddot{Y}(t)}{Y(t)} = a^4 \tag{3.30}$$

the constant solution is chosen in a form a^4 for later mathematical convenience. The equation yields two ordinary differential equations

$$\begin{aligned} \ddot{Y} + \omega^2 Y(t) &= 0 \\ \phi^{iv}(x) - a^4\phi(x) &= 0 \end{aligned} \tag{3.31}$$

where

$$\omega^2 = \frac{a^4 EI}{\bar{m}} \qquad a^4 = \frac{\omega^2 \bar{m}}{EI} \tag{3.32}$$

the first line of equation 3.31 is the equation of an un-damped harmonic oscillator and the solution is

$$Y(t) = Y(0)\cos\omega t + \frac{\dot{Y}(0)}{\omega}\sin\omega t \tag{3.33}$$

where $Y(0)$ and $\frac{\dot{Y}(0)}{\omega}$ are the initial conditions: position and speed respectively. The second line of equation 3.31 can be solved by introducing a solution of the form

$$\phi(x) = D\,exp(pt) \tag{3.34}$$

This leads to $(p^4 - a^4)D\,exp(pt) = 0$ and the equation has a two imaginary $p_{1,2} = \pm ia$ and two real $p_{3,4} = \pm a$ solutions. Incorporating these solutions into the equation 3.34 and adding all four terms, we obtain a complex solution with four constants D_1, D_2, D_3, D_4

$$\phi(x) \quad = \quad D_1\exp(iax) + D_2\exp(-iax) + D_3\exp(ax) + D_4\exp(-ax)$$

Expressing the exponential functions in terms of their trigonometric equivalents and setting the entire imaginary part to zero leads to

$$\phi(x) \quad = \quad A_1\cos(ax) + A_2\sin(ax) + A_3\cosh(ax) + A_4\sinh(ax) \tag{3.35}$$

where A_1, A_2, A_3, and A_4 are real constants. The parameters can be found with the help of boundary and linking conditions.

A freely vibrating beam, fixed on one side fulfills four boundary conditions

$$\phi(0) = 0 \qquad \phi'(0) = 0 \qquad EI\phi''(L) = 0 \quad EI\phi'''(L) = 0 \tag{3.36}$$

The first two conditions are a consequence of fixing the cantilever to the support which results in zero amplitude and zero inclination at *x=0*. In other words, at the fixed end, the deflection and speed are equal to zero. The third boundary condition claims that at x=L the torque force vanishes (zero bending). The fourth conditions implies that the external force is zero at the end of the cantilever (zero shear). Introducing these conditions into equation 3.35 and it derivatives results in:

$$\begin{aligned}
\phi(0) &= (A_1\cos(0) + A_2\sin(0) + A_3\cosh(0) + A_4\sinh(0)) = 0\\
\phi'(0) &= a(-A_1\sin(0) + A_2\cos(0) + A_3\sinh(0) + A_4\cosh(0)) = 0\\
\phi''(L) &= a^2(-A_1\cos(aL) - A_2\sin(aL) + A_3\cosh(aL) + A_4\sinh(aL)) = 0\\
\phi'''(L) &= a^3(A_1\sin(aL) - A_2\cos(aL) + A_3\sinh(aL) + A_4\cosh(aL)) = 0
\end{aligned}$$

By using the trigonometrical rules $\cos 0 = \cosh 0 = 1$ and $\sin 0 = \sinh 0 = 0$, the first two equations simplify to $A_3 = -A_1$ and $A_4 = -A_2$. The last two equations can be rewritten as functions of the parameters A_1 and A_2

$$\begin{aligned}
A_1(\cos(aL) + \cosh(aL)) + A_2(\sin(aL) + \sinh(aL)) = 0\\
A_1(\sinh(aL) - \sin(aL)) + A_2(\cos(aL) + \cosh(aL)) = 0
\end{aligned} \tag{3.37}$$

These equations have non zero solutions if

$$\cos a_i L = -(1/\cosh a_i L) \tag{3.38}$$

The first four accurate numerical solutions and fifth and higher approximate solutions for a_i are given below

$$
\begin{aligned}
a_1L = &\quad 1.875 \quad & a_2L = 4.694 \\
a_3L = &\quad 7.855 \quad & a_4L = 10.996 \\
a_iL \doteq &\quad (i - \tfrac{1}{2})\pi \quad & for\ i \geq 5
\end{aligned}
\tag{3.39}
$$

The corresponding angular frequency for a given solution of a_i is

$$
\omega_i = (a_iL)^2 \sqrt{\frac{EI}{\bar{m}L^4}} \tag{3.40}
$$

where $i = \mathbb{N}$ is the index for the harmonic vibration mode and their resonant frequencies, see figure (3.2). Now, with equation 3.37, A_2 can be expressed as function of A_1. By substitution of A_2 in equation 3.35 we obtain the general solution of the beam shape, see figure 3.2

$$
\phi_i(x) \quad = \quad A_1 \left[(\cos a_ix - \cosh a_ix) - \frac{(\cos a_iL + \cosh a_iL)}{(\sin a_iL + \sinh a_iL)} (\sin a_ix - \sinh a_ix) \right] \tag{3.41}
$$

where A_1 is the vibration amplitude which has to satisfied the initial conditions. The easiest is to normalize this constant and to just use a function 3.41 to determine the beam shape. Then, the complete harmonic equation for all harmonic modes with frequencies ω_i can be written as a sum:

$$
z(t) \quad = \quad \sum_{i=1}^{\infty} C_i sin(\omega_i t + \delta_i)\phi_i(x) \tag{3.42}
$$

Each term in the sum represents one harmonic mode. This is a product of a time dependent function and a function only depending on the position x along the cantilever span (shape function). The C_i is the amplitude of a certain vibration mode and the phase shift δ_i only depends on the initial conditions.

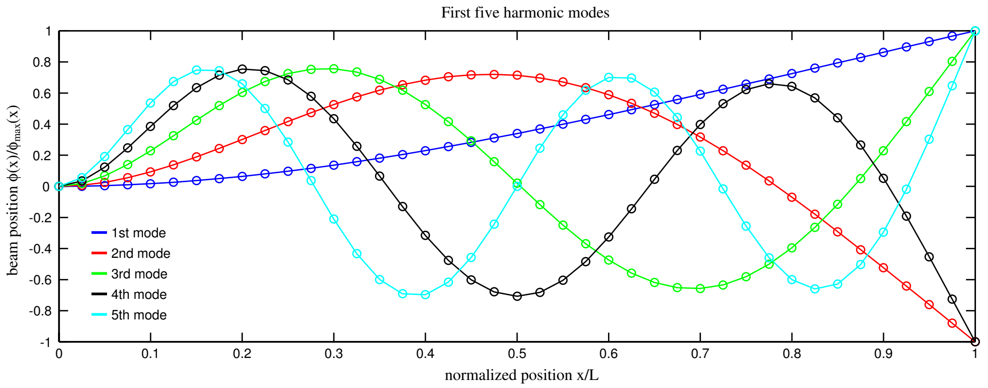

Figure 3.2: First five harmonic modes of a cantilever modeled by equation 3.41, in normalized scale.

The given solution can be further simplified by assuming that our interest is to observe the very end of the cantilever $x = L$. Then, the function 3.41 appears as constant with alternating sign ($\phi_1 = -1, \phi_2 = 1, \phi_3 = -1, ...$). This represents, in dynamic systems point of view, an alternating phase. Each harmonic mode can be described as an oscillator with an effective spring constant:

$$k_i \quad = \frac{EI}{\phi_i^2(L)} \int_0^L (\phi_i''(x))^2 dx \tag{3.43}$$

an effective mass:

$$m_{eff} \quad = \frac{\rho w t}{\phi_i^2(L)} \int_0^L \phi_i^2(x) dx \quad \simeq 0.24 \rho w t L \tag{3.44}$$

and an effective damping coefficient:

$$\gamma_{eff} \quad = \frac{\gamma}{\phi_i^2(L)} \int_0^L \phi_i^2(x) dx \tag{3.45}$$

For most experiments, this concept of a free rectangular cantilever with a small light tip is a sufficiently accurate and useful model. In experiments related to cold damping technique, which will be presented later, there may be a small modification of the cantilever, for example a small sphere with not neglectable mass can be mounted at the free end instead of a tip. For this particular case, this model needs to be further modified to correctly describe dynamic behavior of the system. Due to the non zero mass m_{sphere} and the moment of inertia j_{sphere} of the mounted sphere, the boundary condition 3.36 have to be reformulated to take into account these parameters. The new boundary conditions are:

$$\begin{array}{ll} \phi(0) = 0 & \phi'(0) = 0 \\ EI\phi''(L) = \omega^2 \phi'(L) j_{sphere} & EI\phi'''(L) = -\omega^2 \phi(L) m_{sphere} \end{array} \tag{3.46}$$

The first two conditions stay the same, like in the free case. The third boundary condition claims that, at x=L, the torque force is proportional to the sphere's moment of inertia j_{sphere}. The fourth conditions implies that the external force is proportional to sphere's mass m_{sphere}. The solution of the motion equation can be derived in analogue manner as for the free lever, leading to a new parameter a_i which determines the resonance frequency and the shape of the lever deflection. The solution becomes very complex and has two open parameters j_{sphere} and m_{sphere}. The moment of inertia of the sphere will be neglected due to very small value ($j_{sphere} \approx 10^{-21} kg\, m^2$). This assumption simplifies the solution and parameter a_i can be found as function of the rate of the sphere mass and the cantilever mass: $R_{mass} = m_{sphere}/m_{lever}$. To generalize this solution, parameter a_i has been numerically calculated for different rates of masses. An approximation has been found which allows to easily and directly calculate the a_i. Here, only the results for the approximation of first four harmonic modes are given

$$a_i = G1 \cdot exp(G2 \cdot R_{mass}) + G3 \cdot exp(G4 \cdot R_{mass}) \tag{3.47}$$

where the parameters G1, G2, G3, G4 are listed in table 3.1 and the numerically calculated points and their fits are shown in figure 3.3.

A numerical calculation of the beam's deflection shape for different sphere masses and different modes is shown in figures 3.4 and 3.5. As it can be seen, the originaly free end is becoming to act as flexibly fixed end and the vibration amplitude decreases with increasing sphere mass. The vibration amplitude of higher modes is decreased faster in comparison with lower modes, see figure 3.5. This behavior can be explained by considering the energy distribution along the beam span. For higher harmonic modes, the beam's vibration energy is distributed between the beam's knobs. The sphere is only displaced by the energy stored between the last knob and the end of the beam. Consequently, more knobs beam has less energy is stored in between the knobs and less energy is displacing the sphere.

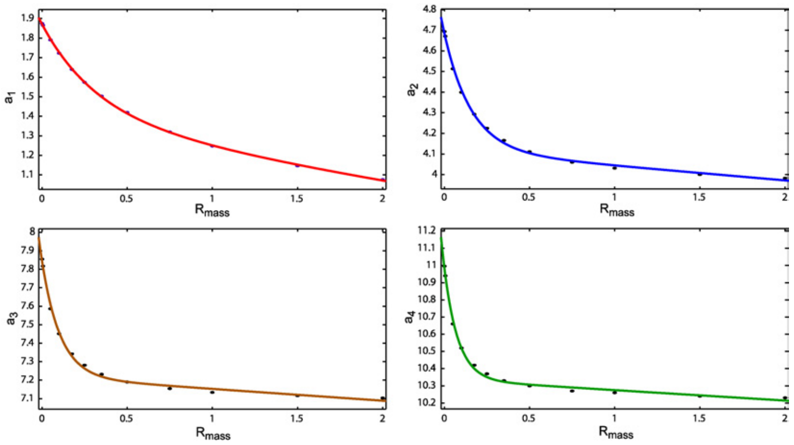

Figure 3.3: a_i approximation for the first four harmonic modes of the cantilever.

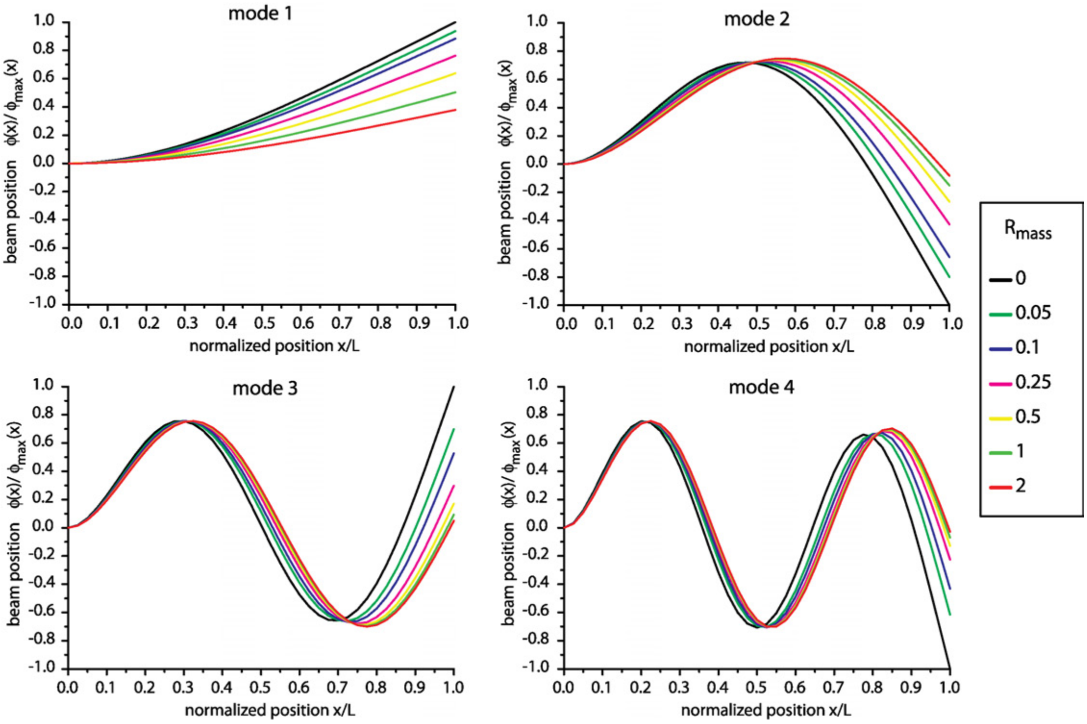

Figure 3.4: The first four harmonic modes as functions of changing sphere mass.

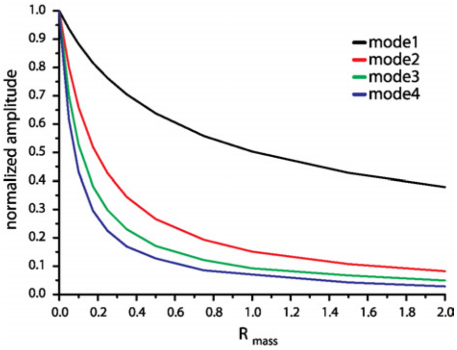

Figure 3.5: The vibration amplitude of the levers free end for the first four harmonic modes as functions of changing sphere mass.

Mode	G1	G2	G3	G4
1 (a_1)	0.4527	-3.176	1.418	-0.1407
2 (a_2)	0.5683	-6.329	4.117	-0.0179
3 (a_3)	0.6268	-9.243	7.217	-0.00896
4 (a_4)	0.6469	-12.26	10.34	-0.00592

Table 3.1: a_i approximation parameters

3.4 Energy of vibrating cantilever

In the previous two chapters a basic theory for describing the thermal noise and the cantilever's multi-mode model have been developed. To describe the cantilever motion, especially with respect to the thermal noise and interaction forces, a precise description of the system energy has to be done. The vertical vibrations of the cantilever have much larger amplitude than any other vibrations (lateral or torsional). For our description, only vertical vibrations will be taken into account. We assume that other vibrations are not energetically large enough to represent an important part of the total energy of the system. The energy for a vertically vibrating cantilever is

$$W = \frac{1}{2}kz^2 + \frac{1}{2}m\left(\frac{dz}{dt}\right)^2 \tag{3.48}$$

where k is the spring constant, m is the mass and z is the vertical displacement of the harmonic oscillator. In the frame of beam theory, the equation can be reformulated into:

$$W = \frac{Ewt^3}{24}\int_0^L \left(\frac{d^2z}{dx^2}\right)^2 dx + \frac{\rho wt}{2}\int_0^L \left(\frac{dz}{dt}\right)^2 dx \tag{3.49}$$

The first term represents potential and the second kinetic energy of the oscillator. The integration along the cantilever in x direction needs to be done over the entire length of the cantilever. By substituting the derivatives of deflection in z direction from equation 3.42 into equation 3.49, we obtain the total energy composed of all independent harmonic modes:

$$\begin{aligned} W &= \frac{Ewt^3}{24}\int_0^L \left(\sum_{i=1}^{\infty} C_i sin(\omega_i t + \delta_i)\frac{d^2\phi_i(x)}{dx^2}\right)^2 dx \\ &+\frac{\rho wt}{2}\int_0^L \left(\sum_{i=1}^{\infty} C_i cos(\omega_i t + \delta_i)\phi_i(x)\right)^2 dx \end{aligned} \tag{3.50}$$

The solution of this equation can also be found in [129], here, only the results will be deduced as follow.

$$\begin{aligned} W &= \frac{Ewt^3}{24L^3}\sum_{i=1}^{\infty} C_i^2 a_i^4 \left(sin(\omega_i t + \delta_i)\right)^2 N_i \\ &+\frac{\rho wtL}{2}\sum_{i=1}^{\infty} C_i^2 \omega_i^2 \left(cos(\omega_i t + \delta_i)\right)^2 N_i \end{aligned} \tag{3.51}$$

where N_i is a constant for each harmonic mode

$$N_i = \frac{1}{L}\int_0^L \phi_i^2(x)dx = (sin\, a_i + sinh\, a_i)^2 \tag{3.52}$$

Equation 3.51 contains the total energy of all harmonic modes. It can be further simplified in analogy to equation 3.48. The energy for only one harmonic mode can be written as

$$\begin{aligned} W_i &= \frac{k}{2} C_i^2 a_i^4 \left(sin(\omega_i t + \delta_i)\right)^2 \frac{N_i}{3} \\ &\quad + \frac{m}{2} C_i^2 \omega_i^2 \left(cos(\omega_i t + \delta_i)\right)^2 N_i \end{aligned} \tag{3.53}$$

where k is the oscillator spring constant

$$k = \tfrac{Ewt^3}{4L^3} \tag{3.54}$$

and $m = \rho wtL$ is the oscillator mass.
The equipartition theorem demands that the mean energy of each harmonic mode is equal to the $k_BT/2$. Thus, a new energy equation can be formulated for each harmonic mode

$$\frac{k_BT}{2} = \frac{k}{2} C_i^2 \, (\widehat{sin(\omega_i t} + \delta_i))^2 a_i^4 \frac{N_i}{3} \tag{3.55}$$

Equation 3.42 can be squared and rewritten for one harmonic mode. Then, the mean displacement of the cantilever free end becomes:

$$C_i^2 \widehat{sin(\omega_i t} + \delta_i)^2 = \frac{\widehat{z_i^2}}{\phi_i^2(L)} \tag{3.56}$$

By introducing this substitution, the mean deflection for this harmonic mode can be obtained as function of thermal energy:

$$\widehat{z_i^2} = \tfrac{k_BT}{k} \, \frac{3\phi_i^2(L)}{a_i^4 N_i} \tag{3.57}$$

Furthermore, $\phi_i^2(L)/N_i = 4$, see [129] for solution. Hence the mean harmonic deflection at the free end of the lever of the observed harmonic mode i becomes:

$$\widehat{z_i^2} = \tfrac{12k_BT}{ka_i^4} \tag{3.58}$$

3.5 Multi-mode model state-space representation

For the successful and easy implementation of a Linear Time Invariant (LTI) system into a Matlab/Simulink environment, the presented multi-mode model has to be reformulated into the state space representation. This representation of the studied system is convenient in a control point of view and also allows easy manipulation and simulation.

Each harmonic mode of the dynamic model can be written as a second order differential equation. We can use the equation 2.7 for harmonic oscillator with specific spring constant k_i and angular frequency ω_i for each harmonic mode i, then the equation becomes:

$$m_{eff}\ddot{z}_i(t) + m_{eff}\gamma\dot{z}_i(t) + k_i z_i(t) = F_{\mathrm{dri}}(t) + F_{\mathrm{int}}(t) + F_{\mathrm{per}}(t) \tag{3.59}$$

where $F_{\mathrm{dri}}(t)$ is the driving force, $F_{\mathrm{int}}(t)$ is the tip-surface interaction and $F_{\mathrm{per}}(t)$ is the systems perturbation, including thermal noise and other external perturbations like mechanical vibration, acoustic waves, etc.. The driving force depends on the users choice and it can be sinusoidal with constant amplitude and frequency (amplitude modulation) or with varying amplitude and frequency (frequency modulation). The interaction force simply follows equation 3.9 and 3.11. The stiffness of the specific harmonic mode k_i is determined from the angular frequency ω_i (equation 3.40):

$$\frac{k_i}{m_{eff}} = \omega_i^2 \tag{3.60}$$

and then:

$$k_i = \omega_i^2 m_{eff} = \frac{a_i^4 E w t^3}{48L^3} \tag{3.61}$$

Equation 4.19 can be reformulated into:

$$\ddot{z}_i(t) = -\frac{\omega_i}{Q_i}\dot{z}_i(t) - \frac{k_i}{m_{eff}} z_i(t) + \frac{F_{dri}(t)}{m_{eff}} + \frac{F_{\text{per}}(t)}{m_{eff}} + \frac{F_{\text{int}}(t)}{m_{eff}} \tag{3.62}$$

Now, we can directly formulate the state space representation in the form:

$$\dot{\mathbf{x}}(t) \quad = \quad \mathbf{A}\mathbf{x}(t) + \mathbf{B}\mathbf{u}(t) \tag{3.63}$$

$$\mathbf{y}(t) = \mathbf{C}\mathbf{x}(t) + \mathbf{D}\mathbf{u}(t) \tag{3.64}$$

where $\mathbf{x}(t)$ is the system state vector, $\dot{\mathbf{x}}(t)$ is derivation of the state vector, $u(t)$ is the input scalar (force) and $\mathbf{y}(t)$ is the output vector of the cantilever model. The multi mode cantilever model state space representation has a form:

$$\begin{bmatrix} \dot{x}_{11}(t) \\ \dot{x}_{12}(t) \\ \vdots \\ \dot{x}_{n1}(t) \\ \dot{x}_{n2}(t) \end{bmatrix} = \begin{bmatrix} 0 & 1 & \dots & 0 & 0 \\ -\frac{k_1}{m_{eff}} & -\frac{\sqrt{k_1 m_{eff}}}{m_{eff} Q_1} & \dots & 0 & 0 \\ \vdots & \vdots & \ddots & \vdots & \vdots \\ 0 & 0 & \dots & 0 & 1 \\ 0 & 0 & \dots & -\frac{k_n}{m_{eff}} & -\frac{\sqrt{k_n m_{eff}}}{m_{eff} Q_n} \end{bmatrix} \times \begin{bmatrix} x_{11}(t) \\ x_{12}(t) \\ \vdots \\ x_{n1}(t) \\ x_{n2}(t) \end{bmatrix}$$
$$+ \begin{bmatrix} 0 \\ \frac{1}{m_{eff}} \\ \vdots \\ 0 \\ \frac{1}{m_{eff}} \end{bmatrix} \cdot u(t) \tag{3.65}$$

$$\left[\; y(t) \;\right] = \left[\; 1 \quad 0 \quad \dots \quad 1 \quad 0 \;\right] \times \begin{bmatrix} x_{11}(t) \\ x_{12}(t) \\ \vdots \\ x_{n1}(t) \\ x_{n2}(t) \end{bmatrix} \tag{3.66}$$

and

$$u(t) = F_{dri}(t) + F_{\text{per}}(t) + F_{\text{int}}(t) \tag{3.67}$$

Each harmonic mode has two states representing speed $\dot{x}_{n2}(t)$ and position $\dot{x}_{n1}(t)$ of the cantilever. The order of the system, or dimension of matrix $\mathbf{A}$, is twice the number of harmonic modes multiplied by two.

3.6 Identification

To evaluate the presented models, a comparison with measurements is necessary. Most of the measurements will be performed on the Nanotec AFM (www.nanotec.es) shown in figure 3.6. This instrument is a standard AFM with complete electronics to operate in different modes. For the X-Y-Z scanner, a calibrated piezo-electric tube in open loop is used, which can cause certain inaccuracy. The scanner is placed in the base of the microscope and a sample is mounted on top of it. A head of the microscope with cantilever and photo-detection system is placed on top of the base. The head is standing on tripod equipped with threads that allow the user to manually set the distance between the sample and the tip in the range of the approach motor. Rough approach of the tip to the sample is done by the electric-motor, displacing the entire head above the base. Fine approach is then achieved by the piezoelectric scanner. The detection of the cantilever is based on an optical beam technique with a four quadrant photo-detector. The laser beam is focused on the cantilever's end by two manually adjustable polarizing cubes. The chip with the cantilever is glued with a silver paint on the removable holder for easy manipulation. The main advantage of this microscope is the ease of use and great accessibility of all signals. The microscope is constructed so that all parts are easily detachable and certain modifications can be done. Further information concerning technical details of the microscope are behind the scope of this thesis, please refer to the manufacturer.

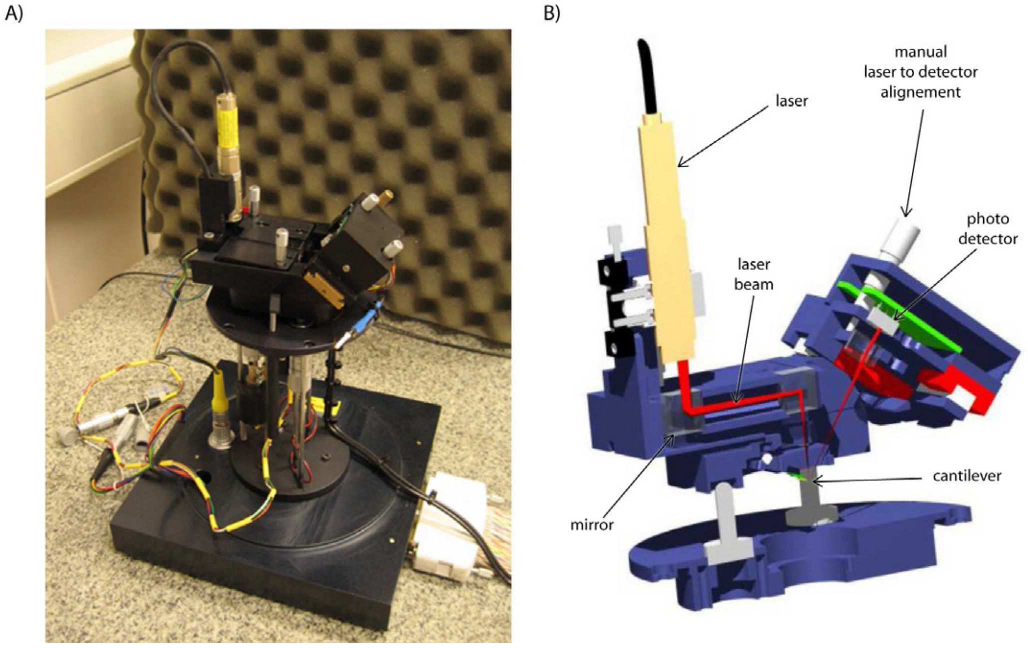

Figure 3.6: A) Photograph of Nanotec Atomic Force Microscope at Surface Science Laboratory. B) The cross-section of the AFM head.

Detection calibration

The photo-detector used in this microscope has frequency characteristics that cannot be reasonably well determined in the standard setup. Nevertheless, one assumption can be made. The microscope has been designed to use cantilevers with first resonant frequency up to 450kHz and we assume that the frequency spectra is approximately flat or at least there are no resonance peaks up to this frequency. Most of the measurements will be done in the first half of this frequency range. The photo-detector used for the cantilever position measurement has an unknown gain, that varies and has to be determined for each measurement to have a proper quantitative value of cantilever deflection. The simplest photo-detector calibration can be done by using the calibrated "z" scanner as reference for the position. After the cantilever is mounted onto the microscope's head, and the laser spot is positioned at its free end, the reflected laser beam has to be focused to the center of the photo-detector. These settings are done by hand and for each cantilever, the resulting photo-detector output voltage is different according to the quantity of lost light in the system. Now, the photo-detector output can be measured for a free cantilever far from the surface resulting in an average DC value which is considered as reference signal of the non deflected cantilever. Then, the cantilever is approached into a contact with a clean hard sample mounted on the scanner. The scanner position is adjusted the way that the photo-detector output remains the same as for a free cantilever. Then, the “z" scanner is driven by a reasonably slow (1-10Hz - without transient behavior) triangular signal with an amplitude chosen to achieve a vertical displacement of about $50nm$. The choice of a relatively small amplitude is necessary to stay in the linear range of detection and to avoid effects coming from the surface topography. Even for this small displacements, the detected magnitude is still significantly larger then the detection noise.

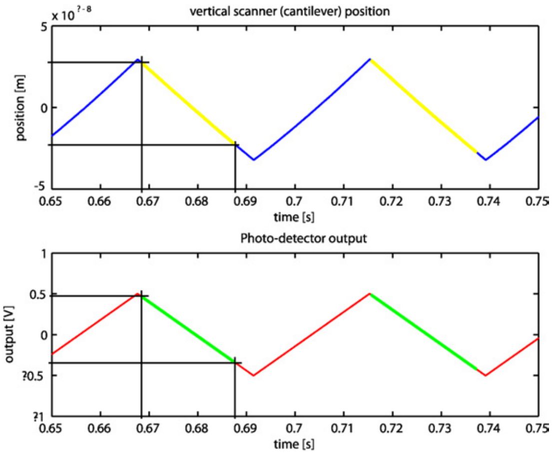

Figure 3.7: The graph on top shows a time sequence of the position of the vertical scanner (relative to zero deflection). The graph below shows the corresponding photo-detector output (offsetted to the zero for easier displaying). The yellow and green marked sections of the signals are the linear approximation of the signal sequence.

From the knowledge of the mechanical displacement of the scanner (cantilever in contact) and from the measured photo-detector output, the conversion constant (gain) between lever position in meters and photo-detector output in volts can be determined.
This calibration covers as well the conversion from the measured angle (see optical beam technique section 2.1.3) to the real cantilever displacement in vertical direction. The angle α at the cantilever's free end is corresponding to the vertical deflection z is a function of the lever length l, see [108].

$$\alpha = \frac{3z}{2l} \tag{3.68}$$

From the linear approximation shown in graph 3.7, the slopes of driving signal and photo-detector output can be easily determined. The photo-detector conversion constant can be directly calculated from these values.

$$k_{detector} = \frac{\Delta OUT}{\Delta z} = \frac{4.2[V/s]}{2.56 \cdot 10^{-6}[m/s]} \simeq 1.64 \cdot 10^{6} V/m \tag{3.69}$$

Optical beam - multi mode detection

Before approaching to the analysis of multi-mode response, a correction for higher mode detection has to be introduced. It has already been mentioned that the optical beam detection technique does not measure the real position of the cantilever but the deflection angle. In figure 3.2, can be seen how much increases the deflection angle with increasing harmonic mode, resulting in an apparently higher amplitude for higher harmonic modes.

The other difficulty is the dependence of the detection sensitivity on the position of the laser spot on the beam, see figure 2.11.
To make a reasonably simple correction of this problem, we assume that a laser spot always stays in the outmost 10% of the cantilever, where the beam can be linearized without introducing significant errors. This requirements is valid in most of the standard setups and it guarantees the highest possible position sensitivity. Then, for each harmonic mode, the deflection angle of the linearized free end can be calculated, see 3.2. The first harmonic mode is considered as reference and towards this angle an apparent magnification of higher modes of: $(\alpha_{n-th-mode}/\alpha_{1st-mode})$ is found. Introduced correction constant eliminates the apparent magnification according to the harmonic mode.

mode	$(a_iL)^2$	angle [deg]	apparent magnification [-]	correction constant [-]
1st	3.52	54.0	1	1
2nd	22.03	78.2	1.45	0.691
3rd	61.70	82.7	1.53	0.653
4th	120/91	84.8	1.57	0.637
5th	199.86	85.9	1.59	0.628
6th	298.56	86.7	1.61	0.623

Table 3.2: Multi-mode photo-detector correction

In real measurements, this correction has to be applied rather as a function of frequency than an harmonic mode. From equation 3.40, it is clear that the frequency of resonance peaks is function of $(a_iL)^2$ and that the $\sqrt{\frac{EI}{\bar{m}L^4}}$ just gives the scale. However, this correction can easily be described as function of $(a_iL)^2$, see figure 3.8. The exponential fit to the correction constant C_c can be written as:

$$C_c = 0.52exp\left(-0.119 \cdot (a_iL)^2\right) + 0.65exp\left(-188 \cdot 10^{-6} \cdot (a_iL)^2\right) \tag{3.70}$$

and, with the use of equation 3.40, this fit can be written as a function of frequency:

$$\begin{aligned} C_c &= 0.52exp\left(-0.119 \cdot 2\pi \cdot f \cdot \sqrt{\frac{\bar{m}L^4}{EI}}\right) \\ &\quad +0.65exp\left(-188 \cdot 10^{-6} \cdot 2\pi \cdot f \cdot \sqrt{\frac{\bar{m}L^4}{EI}}\right) \end{aligned} \tag{3.71}$$

The discussed correction is only valid for a free cantilever. In the case of a modification with a sphere, it has to be recalculated in the same manner as shown. Generally speaking, with increasing sphere mass, the increasing inclination angle at the free end, and apparent magnification gets more significant.

3.6.1 Cantilever identification

In chapter 3.7, a simulation of the amplitude modulation technique will be presented. These simulations have been done with the model of the soft cantilever CSC12/50 from UltraSharp, which technical parameters are in table 3.3. The identification results of cantilever's dynamic characteristics would be compared with our model to validate it.

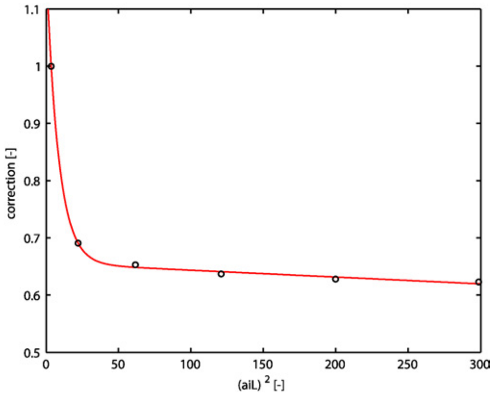

Figure 3.8: The correction constant as a function of $(a_i L)^2$ (black) and its fit (red).

Here, an identification of this cantilever will be performed from its response to thermal distortion measured with the Nanotec AFM. The cantilever is far from the surface and the only interaction exciting the cantilever are thermal noise and parasite mechanical vibrations. The measurement has been done in standard room conditions, the temperature was about 22°C. The spectral density of the cantilever position 100 times averaged is shown in figure 3.9. The measured spectra is fitted by a Lorentzian fit which correctly approximates spectral response of forced harmonic oscilator. It has been determined the resonance frequency, the damping coefficient and the effective spring constant from the fit for each harmonic mode shown in figure 3.10. The area of the Lorentzian fit corresponds to the position variance for a given harmonic mode. For earlier introduced second and higher harmonic modes, the detection correction has been applied, and the surface corresponding to the offset of the Lorentzian fit has been subtracted.

Description	**min**	**Typical**	**max**
Cantilever length, L, ±5μm	-	350	-
Cantilever width, w, ±3μm	-	35	-
Cantilever thickness, t, μm	0.7	1.0	1.3
Resonant frequency, kHz	7.0	10	14
Force constant, k, N/m	0.01	0.03	0.08

Table 3.3: Characteristics of the contact silicon cantilever CSC12/50 (cantilever E) provided by the manufacturer's data sheet (UltraSharp). The cantilever is made out of silicon with a material density of about 2330 kg/m^3 and a modulus of elasticity of 180 GPa.

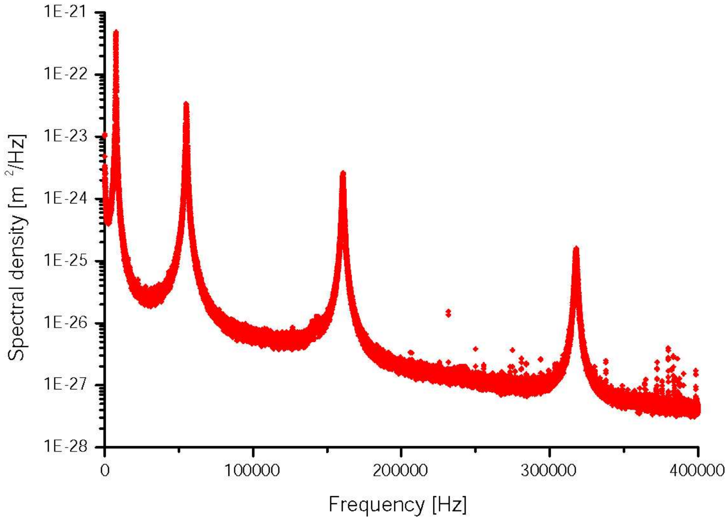

Figure 3.9: Spectral density of silicon cantilever CSC12/50 position excited by thermal noise. The first four harmonic modes can be seen. At very low frequencies, mechanical vibrations and electronic noise 1/f are visible, and at high frequencies small sharp spikes of electronic noise can be seen.

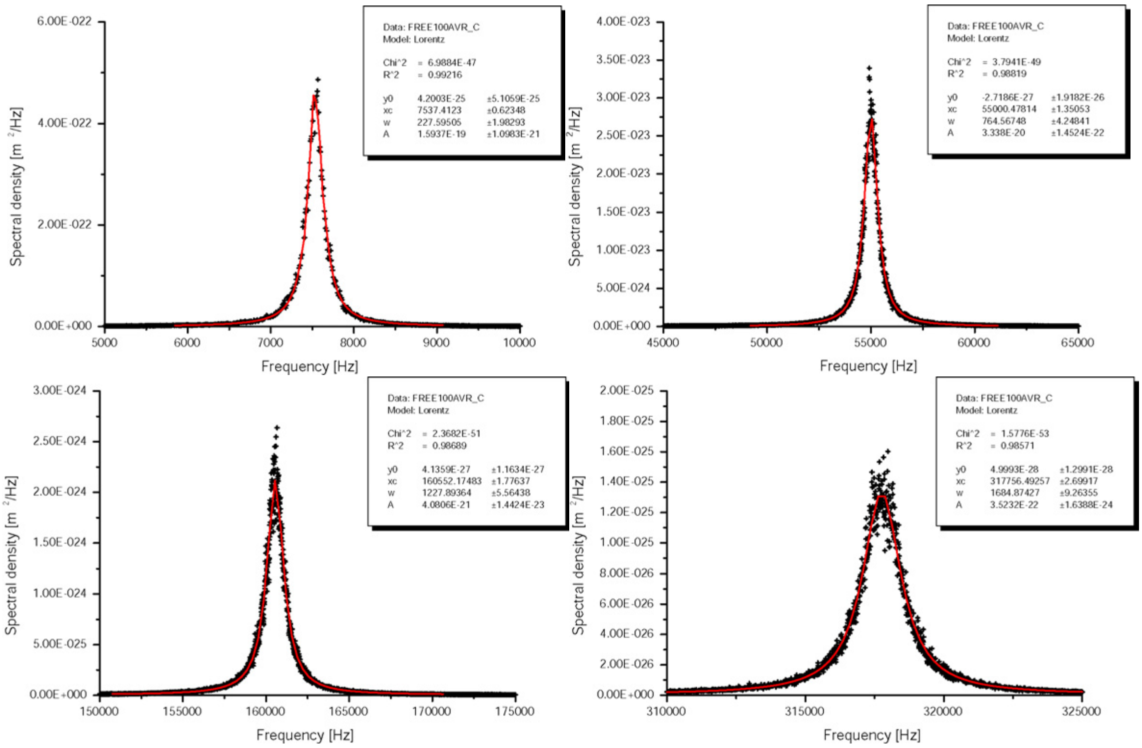

Figure 3.10: First four harmonic modes of silicon cantilever CSC12/50 being excited by thermal noise and their Lorentzian fits. Detailed properties of the fits are shown in the inserts of each harmonic mode.

harmonic mode	**1st**	**2nd**	**3rd**	**4th**
measured data				
frequency f [Hz]	7537.4	55000.4	160552	317756
width of fit γ [$kg\,m^{-1}s^{-1}$]	227.59	764.56	1227.89	1684.87
area [m^2]	1.594E-19	3.338E-20	4.080E-21	3.523E-22
Lorentzian fit offset	4.2E-25	-2.7E-27	4.1E-27	4.9E-28
calculated oscillator parameters				
corrected area [m^2]	1.594E-19	1.588E-20	1.741E-21	1.426E-22
spring constant k [N/m]	0.026	0.258	2.355	28.759
quality factor Q [a.u.]	33.1	71.9	130.8	188.6
mass m_{eff} [kg]	1.15E-11	2.16E-12	2.31E-12	7.21E-12

Table 3.4: Constants describing the properties of silicon cantilever CSC12/50 and the environment, determined from the measured spectral density of the cantilever position.

All values listed in the table 3.4 are obtained from the spectral density fits of the measured cantilever position. These results will be compared to the simulation results of the multi-mode cantilever model in the following section.

3.6.2 Identification of a cantilever with sphere

Most of experiments presented in chapter 5 concerning cold damping techniques will be effectuated with the standard contact cantilever from Veeco. Its technical parameters are listed bellow.

Description	min	max
length [μm]	515	535
width [μm]	25	35
thickness [μm]	1.5	2.5
resonant frequency [kHz]	17	20
force constant [N/m]	0.1	0.1

Table 3.5: Characteristics of the contact silicon cantilever Veeco MPP-32220, provided by the manufacturer's data sheet. This cantilever is made out of silicon with a material density of about $\rho = 2300 kg/m^3$ and a modulus of elasticity E=180GPa.

The cantilever used in our measurement is mechanically modified by a small polystyrene sphere mounted at its free end, see figure 3.11. The sphere radius is about $20\mu m$ and it is attached by epoxy glue. Then, the entire lever with the sphere is coated with a gold layer of 100 nm thickness, to achieve a maximal conductivity between the sphere and the chip. This modification of the system allows measure the surface interaction forces and the electrostatic force rather quantitatively than locally, because the intensity of the interaction force goes linear with the radius of the tip (Hamaker approximation). The main drawback is a loss in lateral resolution due to the sphere's diameter. However, this disadvantage does not have great importance, as our focus is to measure weak interaction forces and to treat the thermal noise distortion.

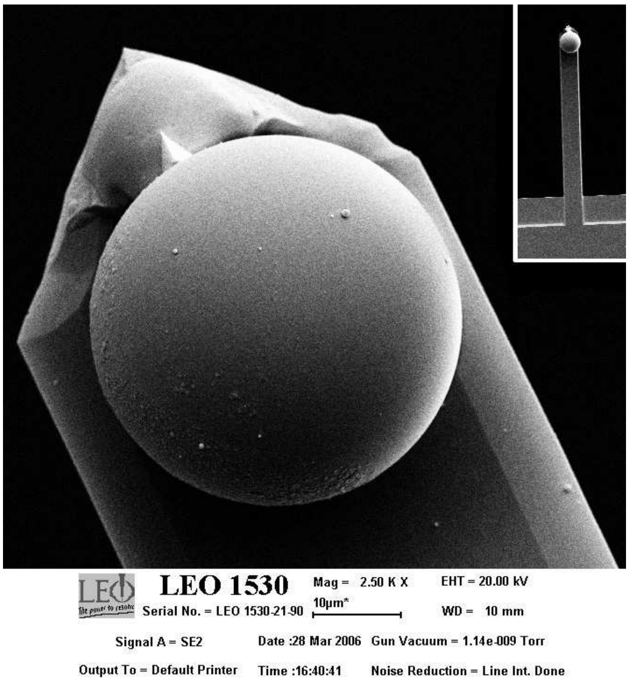

Figure 3.11: Scanning electron microscope image of the polystyrene sphere at the cantilever's end. The small image in the upper corner shows the entire lever.

The sphere's mass cannot be neglected. It changes the position of the resonance peaks. A new effective mass has to be introduced into our model to take into account this mass change. We can just add the sphere mass to the effective mass of the cantilever, as the image proposes that the sphere is placed at the very end of the cantilever:

$$m'_{eff} = m_{eff} + m_{sphere} = 0.24 \cdot l \cdot w \cdot t \cdot \rho + \frac{4}{3}\pi r^3_{sphere}\rho_{sphere} \tag{3.72}$$

where $r_{sphere} = 20\mu m$ is the sphere's radius and ρ_{sphere} is its material density with value for polystyrene of about $1050 kg/m^3$. The influence of the changed effective mass will be shown in the following paragraph.

The identification has to decouple the behavior of different parts of the system and it has to identify their characteristics. The main difficulty is that the parts of the system cannot be separated and measured independently, so that certain assumptions have to be made.

3.6.2.1 Time response

A direct and simple way to identify the system's dynamic is to use the input step response of the system. The cantilever has been brought into a position where the sphere-surface separation distance is in the order of tens of micrometers. The used surface has been coated with gold in advance to achieve maximum conductivity. A square electric potential of 10V with frequency of 40Hz is applied between the sphere and the sample. This period is sufficiently longer than the lever's settling time. The resulting electrostatic force excites the cantilever as it is required in step response identification, see figure 3.12. The photo-detector's output has been recalculated into the cantilever's position in meters and it has been verified that the vibration amplitude is not excessively large to keep the photo-detector response linear.

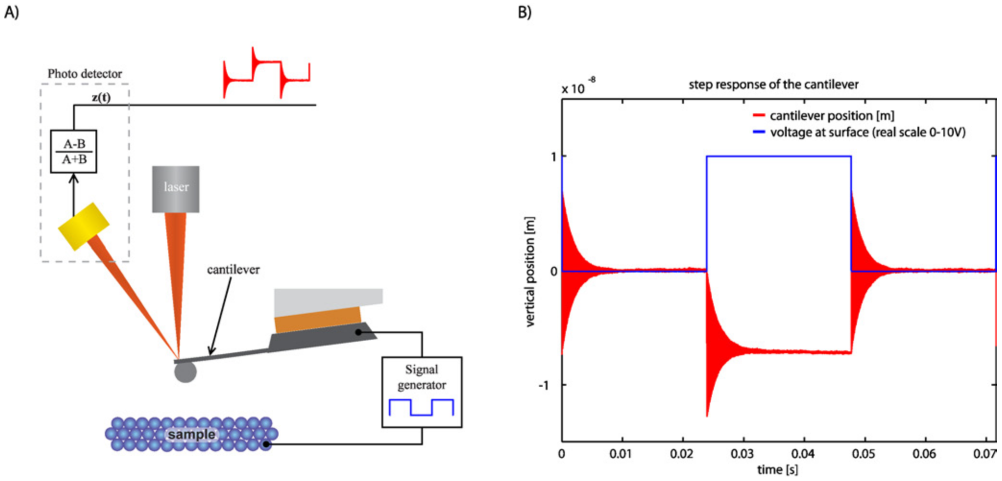

Figure 3.12: A) Indentification measurement schema. B) The blue curve is the electric potential between the two surfaces. The red curve is the cantilever's step response to electrostatic surface force.

From the measured time sequences, a part has been chosen where the cantilever is relaxing from an initial deflected position, bent towards the surface, back to its free position. The part of the signal where the cantilever is electrostatically attracted to the sample is lightly perturbed. This is due to the dependence of the electrostatic force on the separation distance between the two attracting surfaces. The relaxation part represents the motion of the cantilever releasing its potential energy without significant influence of residual charges on the sample's surface. This curve has been fitted with the approximation of a damped harmonic oscillator:

$$z(t) = A \cdot sin(\omega' t + \varphi) \cdot exp(-\gamma t) + z_0 \tag{3.73}$$

The measured signal has been offset and time shifted so that the parameters φ and z_0 are set to zero. These two parameters are mainly related to the measurement and they do not provide any information about system's dynamics. The parameters of amplitude A, resonance frequency ω and damping coefficient γ have been found with Matlab using the curve fitting tool. The measurement with its fit and the fitting error is shown in figure 3.13. The resulting vibration amplitude A only indicates a scale, it has no significant importance. The found resonant frequency $\omega' = 92500\, rad/s \Rightarrow f' = 14721\, Hz$ and damping coefficient $\gamma = 500.5\, kg/s$ leads to a quality factor $Q = \omega/\gamma = 184.8$.

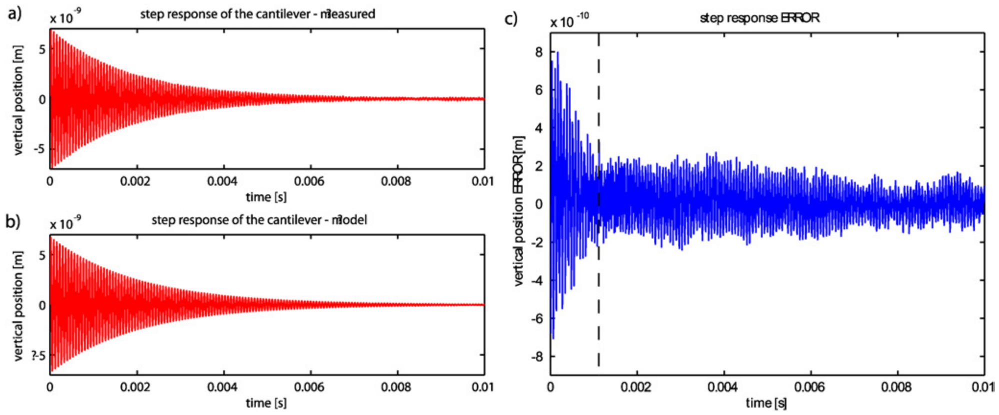

Figure 3.13: a) the measured lever position , b) the approximation found in Matlab and c) the estimation error. The vertical dashed line in c) approximately shows a point where the thermally induced cantilever vibration begins to be the main source of the fit error.

As can easily be seen, there is a shift in the resonant frequency compared to the value given by the manufacturer, see table 3.5 ($\Delta f_{min} = 2279\,Hz$ and $\Delta f_{max} = 5279\,Hz$). This is caused by the change in the lever's effective mass due to the sphere at the end. Now, we can calculate an approximate sphere mass from the measurement with:

$$\omega'^2 = \frac{k}{m'_{eff}} = \frac{k}{m_{eff} + m_{sphere}} \quad \Rightarrow \quad m_{sphere} = \frac{k}{\omega'^2} - m_{eff} = \frac{k}{\omega'^2} - \frac{k}{\omega^2} \tag{3.74}$$

For the cantilevers spring constant, the catalog value $k = 0.1\,N/m$ has been used. Then the sphere's mass is about $m_{sphere} = 2.9 \cdot 10^{-12} kg$ for a frequency shift of $\Delta f_{min} = 2279 Hz$ and $m_{sphere} = 5.35 \cdot 10^{-12} kg$ for a frequency shift of $\Delta f_{max} = 5279\,Hz$. The sphere mass obtained from time response is strongly dependent on the spring constant of the cantilever and, as will be shown later this constant may significantly differ from the value given by the catalog.

This step response identification is not suitable to identify higher harmonic modes with sufficient accuracy because of the high level of thermal noise masking the higher harmonic modes. The spectral analysis of the cantilever thermal noise response offers much better results for detecting all modes.

3.6.2.2 Frequency response

For higher accuracy, the frequency response identification can be used. This identification allows determine the higher harmonic modes of the cantilever. There are two approaches: one simpler approach is to use the frequency sweep using a lock-in amplifier with an actuator. Another possibility is to directly determine the cantilever characteristics directly from the thermal excitation. Here, the data analysis is more complex but the results provide information which is not influenced by the dynamic properties of the used driver.

Lock-in amplifier
This method is simple and it leads to a more accurate identification in comparison with the time response method. The setup used for this measurement is shown in figure 3.14. The cantilever, with and without sphere, has been excited by a function generator with selectable output frequency and the frequency sweep has been measured. From the measured lever position and from the known excitation signal, the phase shift and the amplitude have been detected, see figure 3.15.

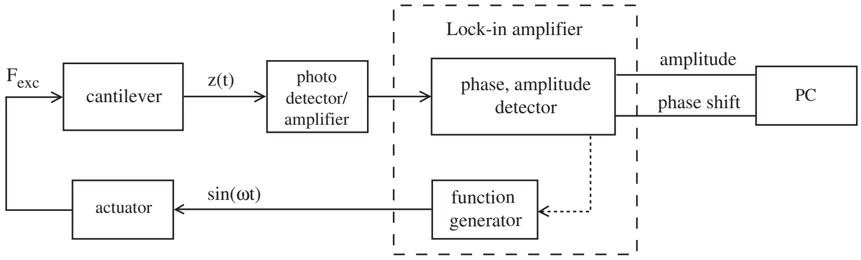

Figure 3.14: The cantilever is driven by an actuator on frequency set by an oscillator. Lever position is detected by a photo-detector and then compared with the known function generator signal inside the lock-in amplifier. The resulting phase and amplitude are saved by the data acquisition card.

In figure 3.15, the frequency shift caused by the mounted sphere can be easily seen. For both curves, a Lorentzian fit has been done to find the resonant frequency. For the free cantilever, the resonance frequency is $f = 20692Hz$ and, for the lever with sphere, a frequency of $f' = 14051Hz$ has been found. The frequency shift between the two levers is $\Delta f = 6641Hz$ which is a little bit higher than the frequency shift found with the step response identification. From the equation 3.74, the effective mass of the cantilever $m_{eff} = 5.9 \cdot 10^{-12} kg$ and the mass of the sphere $m_{sphere} = 6.9 \cdot 10^{-12} kg$ can be calculated.

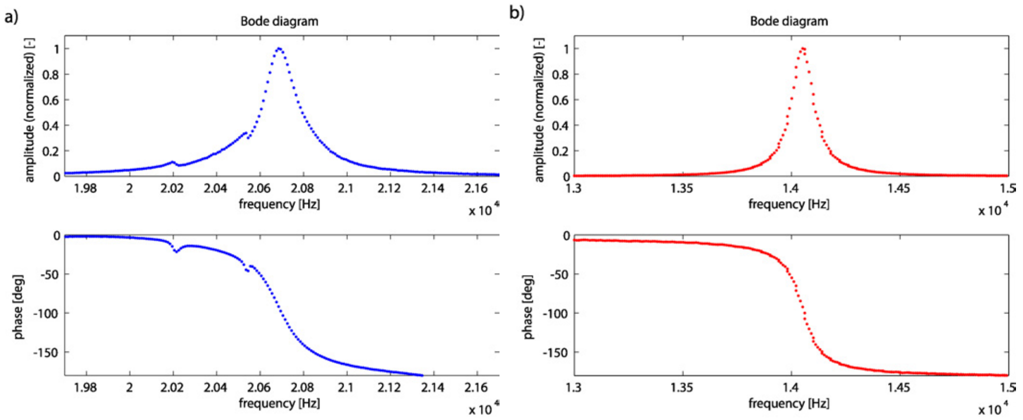

Figure 3.15: a) Bode diagram for an unmodified cantilever, b) Bode diagram for a cantilever with attached sphere.

In the previous paragraph, it has been already mentioned that the calculation of the sphere's mass is strongly dependent on the spring constant. The spring constant deviation is mainly caused by the inaccuracy in cantilever mechanical characteristics (length, width and thickness). To accurately determine this critical parameter, the thermal noise response identification will be used.

Spectral analysis of Brownian motion

The spectral analysis of the cantilever's thermal or Brownian motion provides information about all harmonic modes. It will be used to identify all harmonic modes of the cantilever. When the cantilever is far from the surface, the only interactions exciting the lever are thermal noise and parasite mechanical vibrations. Measurement has been done in standard room conditions at temperature about 22°C. The spectral density of the cantilever position, 100 times averaged, is shown in figure 3.16. From the measured spectra and from the Lorentzian fits the resonant frequency, the damping coefficient and the effective spring constant for each harmonic mode has been determined, see figure 3.17. The area of the

Lorentzian fit of the squared spectra corresponds to the position variance for a given harmonic mode. For the second and higher harmonic modes, the earlier introduced detection correction has been applied, and the surface corresponding to the Lorentzian fit offset from zero has been subtracted.

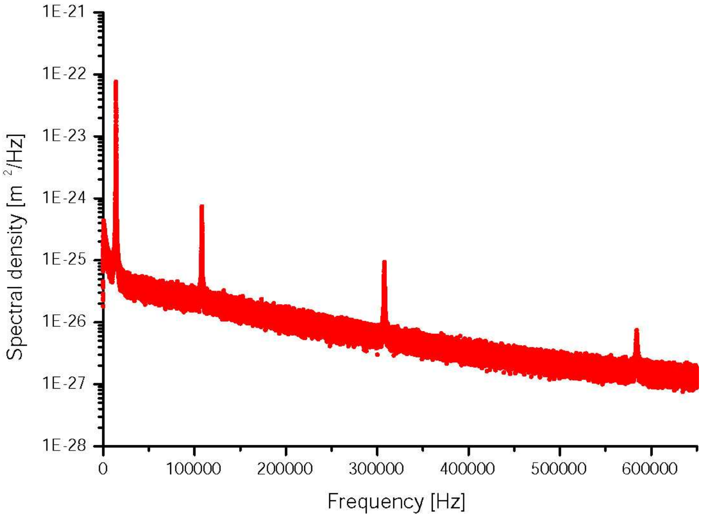

Figure 3.16: Spectral density of silicon cantilever MPP-32220 position being excited by thermal distortion. Spectra has been measured with mounted polystyrene sphere. The first four harmonic modes can be seen.

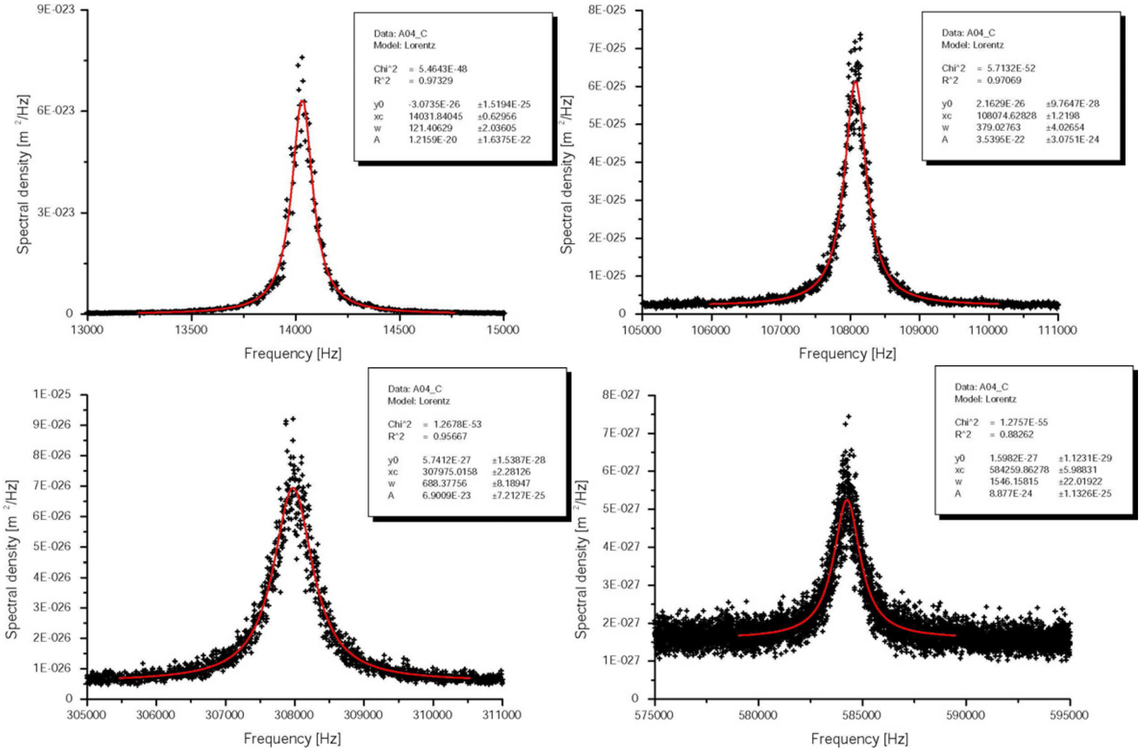

Figure 3.17: The first four harmonic modes of silicon cantilever MPP-32220 with the sphere excited by thermal noise and their Lorentzian fits. The detailed properties of the fit for each harmonic mode are shown next to the fit.

harmonic mode	**1st**	**2nd**	**3rd**	**4th**
measured data				
frequency f [Hz]	14031.84	108074.63	307975.02	584259.86
width of fit γ $[kg\, m^{-1} s^{-1}]$	121.41	379.03	688.38	1546.16
area $[m^2]$	1.22E-20	3.54E-22	6.90E-23	8.88E-24
Lorentzian fit offset	-3.07E-26	2.16E-26	5.74E-27	1.60E-27
calculated oscillator parameters				
corrected area $[m^2]$	1.216E-20	1.644E-22	2.779E-23	2.599E-24
spring constant k [N/m]	0.337	24.94	147.55	1577.87
quality factor Q [a.u.]	115.6	285.1	447.4	377.9
mass m_{eff} [kg]	4.34E-11	5.41E-11	3.94E-11	1.17E-10

Table 3.6: Constants describing properties of silicon cantilever MPP-32220 with mounted polystyrene sphere.

The obtained parameters fully describe the cantilever's dynamic properties and they take into account the influence of the mounted sphere in all harmonic modes. Due to the frequency properties of the thermal excitation, it is guaranteed that there is no influence of the driver's dynamic properties. In this case, the driver is the thermal energy which has flat power spectra density and all harmonic modes are excited evenly.

3.7 Simulation

In this section a numerical simulations of the earlier introduced multi-mode model will be presented and they will be compared to measurements of the soft cantilever CSC12/50 from UltraSharp. The simulations are performed in the Matlab/Simulink environment which provides all necessary tools for data analysis.

3.7.1 Higher harmonic modes

As a first step to verify the accuracy of the multi-mode model, a comparison of the system's frequency response has been done. The cantilever properties obtained from the measurements are shown in table 3.7. They will be used as reference values for the comparison with the proposed model. This data has been inserted into the earlier presented state space structure and the Bode diagram has been plotted in figure 3.18 (red curve). With the identical structure, a Bode diagram has been plotted for parameters being directly calculated from the cantilever's mechanical properties given by the manufacturer (table 3.7), see figure 3.18 (blue curve). The picture indicates that there is no complete agreement between the measurement and the model's resonance frequencies of higher harmonic modes. This deviation can be caused by inaccuracy of the lever's length, width and thickness. Equations 3.28 and 3.40 show that the resonant frequency is very sensitive to thickness variations. Exactly this parameter has the highest manufacturing inaccuracy, see table 3.3. To increase the accuracy of the proposed model, a weighted least square minimalization of the mode's resonant frequencies errors has been done, where the length, width and thickness have been used as free (adjustable) parameters. The weights used in this minimalization were chosen according to the modes contribution to the total cantilever displacement due to thermal excitation. For harmonic mode i, the displacement can be written as $\sqrt{\langle z_i^2 \rangle} = \sqrt{k_B T/k_i}$, where the random displacement is a simple function of parameter $1/\sqrt{k_i}$, and this parameter was used as weight. Further on, a test has been done with a weighting parameter $1/\sqrt[4]{k_i}$ attributing higher importance to higher harmonic modes in comparison to the weight $1/\sqrt{k_i}$. The results are presented in table 3.7 and the

Bode diagrams are shown in figure 3.18. Here, the green curve stands for a weight $1/\sqrt{k_i}$ and the yellow curve stands for a weight $1/\sqrt[4]{k_i}$.

Cantilever properties	**1. mode**	**2. mode**	**3. mode**	**4. mode**
Data obtained from measurement	-	-	-	-
Resonant frequency, [Hz]	7540	55000	160550	317760
Effective mass, [kg]	11.50E-12	2.16E-12	2.31E-12	7.21E-12
Spring constant, [N/m]	0.0260	0.2580	2.3550	28.7590
Dimensions from data sheet	-	-	-	-
l = 350E-6m, w = 35E-6m				
t = 0.7E-6m, $\rho = 2330 kg/m^{-3}$				
Resonant frequency, [Hz]	8280	51890	145310	284740
Effective mass, [kg]	4.795E-12	4.795E-12	4.795E-12	4.795E-12
Spring constant, [N/m]	0.0130	0.5098	3.9970	15.3479
Minimalization weight: $\sqrt{k_1}/\sqrt{k_i}$	1	0.159	0.057	0.029
l = 354.2E-6m, w = 35.1E-6m				
t = 0.67E-6m, ρ= $2359 kg/m^{-3}$				
Resonant frequency, [Hz]	7610	47700	133560	261710
Effective mass, [kg]	4.884E-12	4.884E-12	4.884E-12	4.884E-12
Spring constant, [N/m]	0.0112	0.4386	3.4391	13.2057
Minimalization weight: $\sqrt[4]{k_1}/\sqrt[4]{k_i}$	1	0.39	0.24	0.17
l = 355.6E-6m, w = 34.1E-6m				
t = 0.69E-6m, ro ρ= $2351 kg/m^{-3}$				
Resonant frequency, [Hz]	7810	48930	136990	268450
Effective mass, [kg]	4.926E-12	4.926E-12	4.926E-12	4.926E-12
Spring constant, [N/m]	0.0119	0.4655	3.6498	14.0148

Table 3.7: Computed cantilever parameters for different mechanical dimensions.

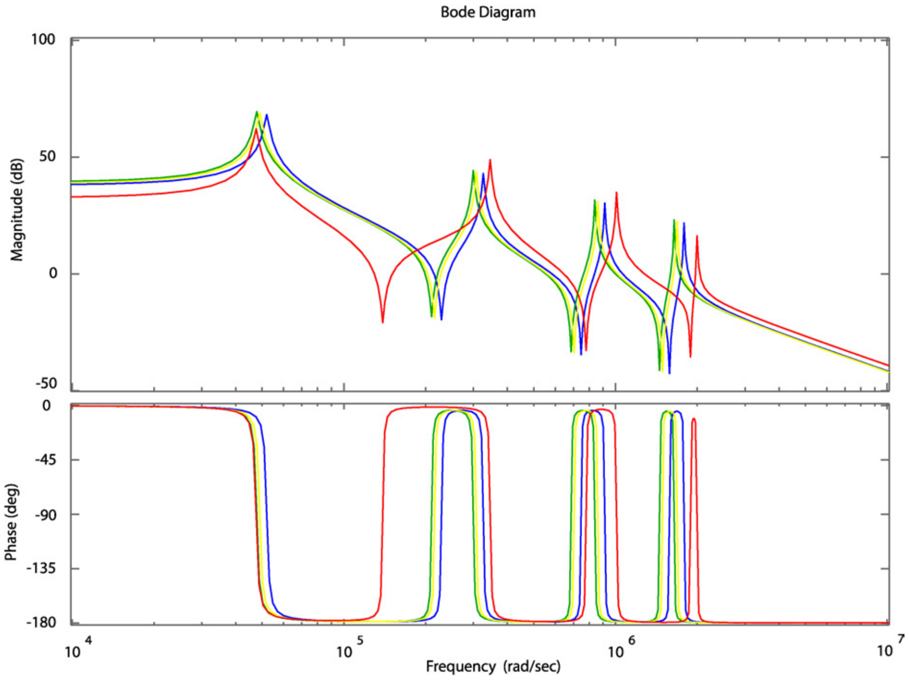

Figure 3.18: Bode diagram of the first four harmonic modes of the modeled cantilever with different parameters. red curve - parameters obtained from measurement, blue curve - parameters obtained from cantilever mechanical properties, green curve - weight $1/\sqrt{k_i}$ and yellow curve - weight $1/\sqrt[4]{k_i}$

The Bode diagram shows that the measured system does not strictly follow the distribution of resonance peaks in frequency it should, compared to the multi-mode model. The modes have certain deviation from their proper position according to beam theory. Especially the frequency gap between the first and the second harmonic mode is larger than predicted by theory and model. Secondly, the obtained spring constants differ to the values obtained from the thermal identification. These irregularities can be caused by many different factors: not exactly rectangular shape of the lever, not homogeneous material properties along the lever span and local structural damage.

Thermal noise excitation

The simulation of a thermally excited cantilever opens the great opportunity how to directly compare the measured spectra with the results obtained by simulation, without any further data treatment. Each harmonic mode of the cantilever model has been excited with an independent source of white noise. The correlation between the noise sources has to be close to zero to achieve the same conditions present in a real system because the thermal excitation of any two modes is completely uncorrelated. The spectral density of lever position has been determined from the simulated time sequences of the lever position, see figure 3.19. The shown spectra is the average over fifty independent spectra and it has been analyzed the same way as was shown in frequency identification section. Its Lorentzian fits are shown in figure 3.20 and the fit parameters are listed in table 3.8. Here presented simulation results can be compared to performed measurements shown in figures 3.9 and 3.10.

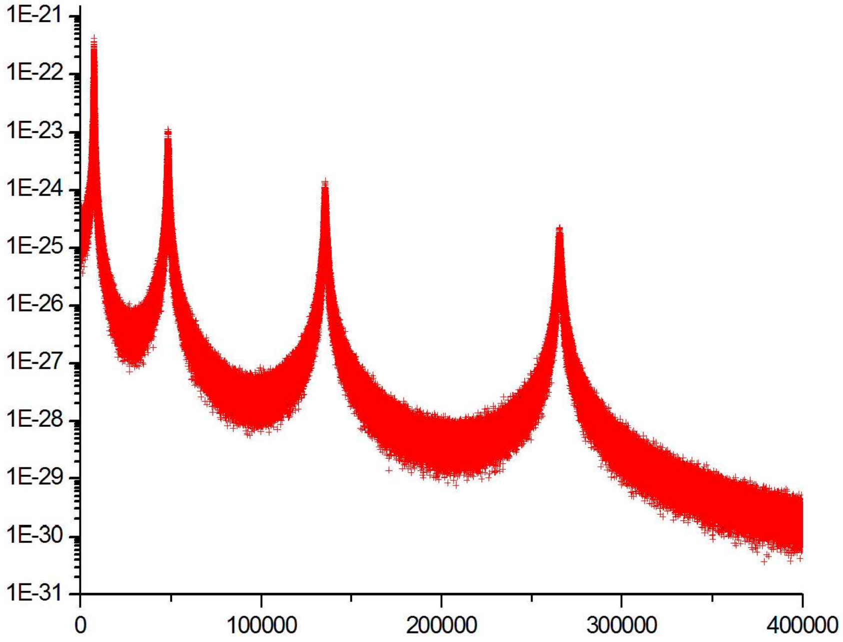

Figure 3.19: Simulated spectral density of soft cantilever CSC12/50 position being excited by thermal distortion. The first four harmonic modes are shown.

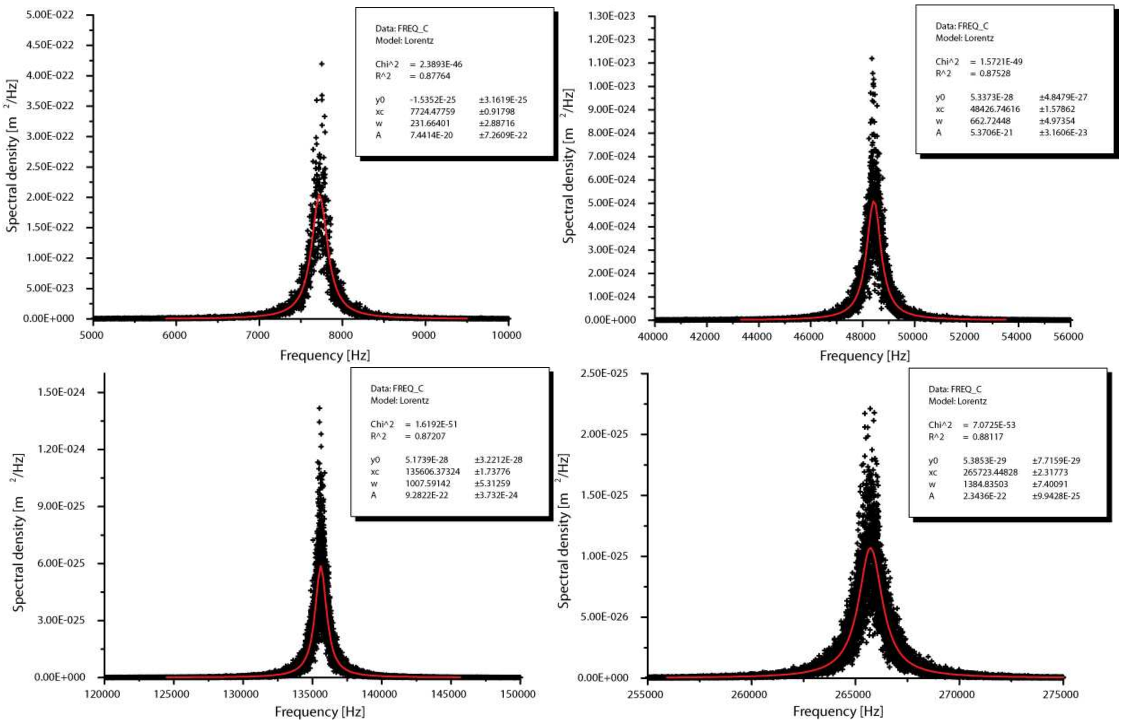

Figure 3.20: Simulated first four harmonic modes of soft cantilever CSC12/50 being excited by thermal noise together with their Lorentzian fits. The detailed properties of fit for each harmonic mode are shown next to the fit.

harmonic mode	**1st**	**2nd**	**3rd**	**4th**
Simulated data				
frequency [Hz]	7724.5	48427	135610	265720
width of fit γ [$kg\,m^{-1}s^{-1}$]	231.6	662.7	1007.6	1384.8
area [m^2]	7.44E-20	5.37E-21	9.28E-22	2.34E-22
Calculated oscillator parameters				
spring constant k [N/m]	0.0547	0.758	4.388	17.379
quality factor Q [a.u.]	33.34	73.07	134.59	191.88
mass m_{eff} [kg]	2.33E-11	8.2E-12	6.05E-12	6.24E-12

Table 3.8: Parameters of the cantilever obtained from the Lorentzian fits of the measured spectra of thermally excited soft cantilever CSC12/50.

The comparison between simulated data (figures 3.19, 3.20) and measured results (figures 3.9, 3.10) show two principal differences. The first: the position of the higher harmonic modes is offsetted to lower frequencies as it has been already observed in frequency response. The second difference is the cantilever spring constant. Its numerical value is different in comparison with the identified values. The position of the modes resonance frequencies and spring constants are in the beam theory strictly related to cantilever mechanical properties but measurement results do not preserve this relations. This can be caused by certain mechanical damage, coating or additional local mass pertubing the cantilever motion.

3.7.2 Interaction force and approach curve

The surface interaction model describing Van der Waals attractive forces and repulsive forces has been implemented into the model of the cantilever described above. The Hamaker approximation has been used for the interaction forces, equations 3.9 and 3.11. The cantilever's and the modeled sample important material properties for the simulated interaction are listed below.

Description	**Symbol**	**Value**
Effective stiffness, [Pa]	E_{eff}	10.2×10^9
Intermolecular distance, [m]	a_0	3.8e-10
Hamaker constant (Si-Si), [J]	A_H	1.865e-19
Tip radius, [m]	R	10e-9

Table 3.9: Parameters of the tip-surface interaction used for simulation.

The effective stiffness E_{eff} determines the full contact tip-surface stiffness and the repulsive interaction force is proportional to this parameter. The intermolecular distance a_0 determines the distance, where the repulsive interaction forces start to have a greater gradient than attractive forces, see figure 2.13. The Hamaker constant A_H describes the tip's and the sample's material properties. In this simulation, a silicon sphere is interacting with a flat silicon sample. The tip radius R is directly taken from the manufacturer's lever specification.

In a first step, the intensity of the interaction force as function of the separation distance has been calculated, see figure 3.21.

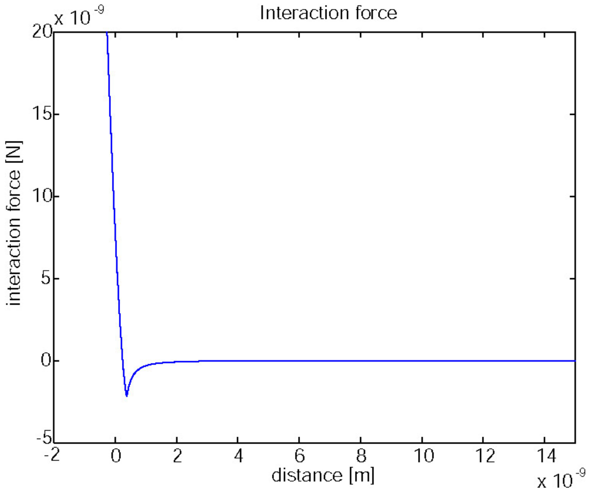

Figure 3.21: Surface interaction force as function of the separation distance.

In a second step, an approach curve has been simulated with the four mode cantilever model, see figure 3.22. The cantilever was not excited by any external signal and the displacements due to interaction forces are steady state results. The modeled surface was approaching towards the cantilever with constant speed $15 \cdot 10^{-9} m\, s^{-1}$ which guarantees that any transient effects are not present in this simulation. With decreasing tip-surface separation distance, the cantilever deflects towards the surface up to the point, where the interaction force gradient is larger than the gradient of the restoring force imposed by the cantilever's spring constant. At this point, the tip snaps into full mechanical contact, repulsive interaction. A small transient vibrations are visible right after the tip hits the sample. This model does not include any adhesion forces, which permits the visibility of the transient vibrations. The measured approach curves do not have these vibrations, because they dissipate very quickly due to intense adhesion damping. Nevertheless, this model is adequate for modeling non-contact operation modes. Simulations have been done for both, a cantilever excited and not excited by thermal noise. Figure 3.22 shows, that the system stays longer in static deflection without snapping to the surface in the case when it is not thermally excited. Difference of distances where cantilever snaps into contact is $2.2 \cdot 10^{-10} m$. This distance varies due to the stochastic behavior of thermal noise and induced lever deflection. To find this distance accuratly, the approach would has to be done with speed close to zero.

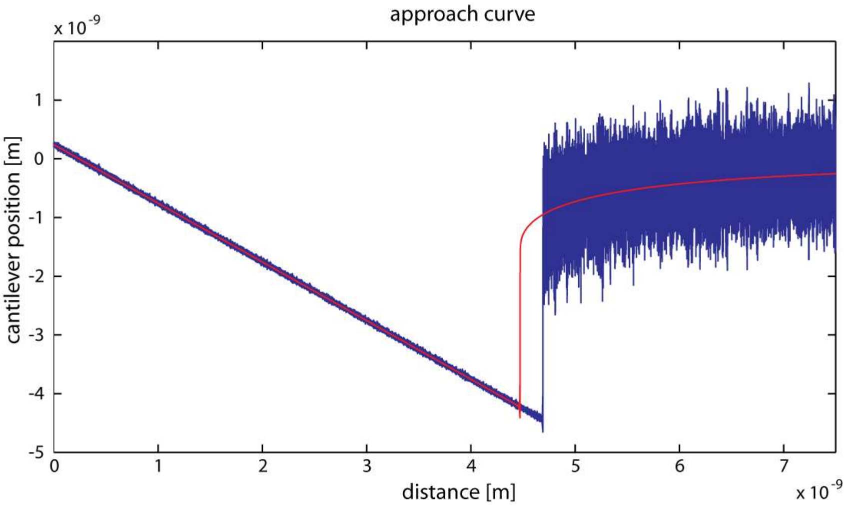

Figure 3.22: Simulated cantilever approach curve with thermally induced oscillation (blue curve) and without thermal excitation (red curve).

3.7.3 Amplitude modulation and Tapping mode

This simulation concentrates on two standard operation modes introduced in chapter 2.2 and explores the influence of higher harmonic modes to total cantilever displacement, while they are operated. A simulation has been performed using constant magnitude excitation signal with frequency chosen at the first resonance $\omega_{dri} = \omega_1$. The excitation has been applied onto the cantilever's free end as a force and vibrating cantilever has been simulated in varying separation distances from the surface. The approach speed to the surface has been chosen $80 \cdot 10^{-9} m\,s^{-1}$, so the cantilever stays in steady state and the transient behavior does not have significant influence. The used excitation intensity is 65 pN resulting in vibration amplitude of 190 nm at the cantilever's free end. This relatively large vibration amplitude has to be used because this cantilever is very soft ($k = 0.03N/m$). With a smaller amplitude, it would fall into full contact with the sample instead of operating in Tapping mode.

Figure 3.23 A) displays the envelope of the cantilever motion (blue curve) and the position of the surface (black curve). Figure 3.23 B) shows the phase shift between lever and driving signal during this simulation. In figure 3.24 the envelope of related interaction force is shown. When distance between cantilever base (zero lever position or mean position) and sample decreases, the tip begins to interact with the sample at its closest position towards the surface. All figures are divided into three numbered zones which correspond to different non-contact operation modes. Zone number 1, should theoretically begin at infinite separation distance between tip and lever base. In this zone, the system is limited by detection noise and thermal distortion, and the surface interaction cannot be measured. The zone's other end varies according to different levers and experimental setups. The phase shift between excitation signal and cantilever position at infinite separation distance is -90 degrees, and small variation occurs only due to distortion. Zone number 2 represents the standard Amplitude Modulation operation mode. Here, only attractive interaction forces are present. The cantilever vibration amplitude is changing as function of the surface interaction force magnitude. The phase shift decreases as well according to the intensity of the interaction. In this specific simulation, the maximal detectable interaction force with amplitude modulation mode is about 1nN. When the surface approach continues, the system enters unstable zone (not numbered) where the lever is randomly tapping and operating in amplitude modulation mode at the same time. After this transient zone, the tip begins to touch the sample every period and enters the Tapping mode, Zone number 3. The interaction forces have attractive and repulsive parts and, with continuously approaching surface the intensity increases up to the limit where the tip snaps to the sample and stays in contact (not shown in figures). Experimental results equivalent to this simulation can be found in [136] and additional simulation results in [134].

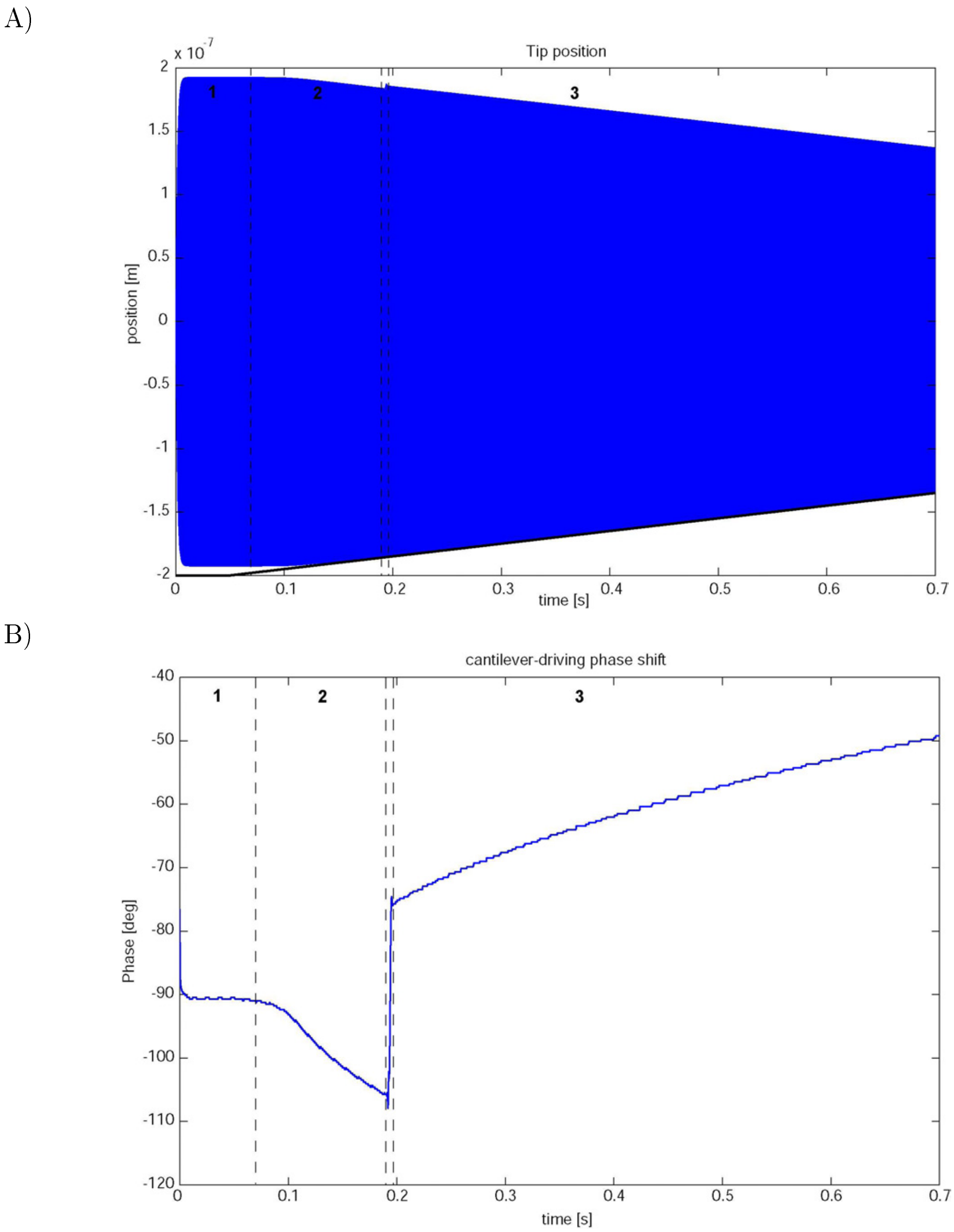

Figure 3.23: A) the cantilever's vibration envelope (blue) and the approaching sample (black). B) phase shift between driving signal and resulting cantilever position.

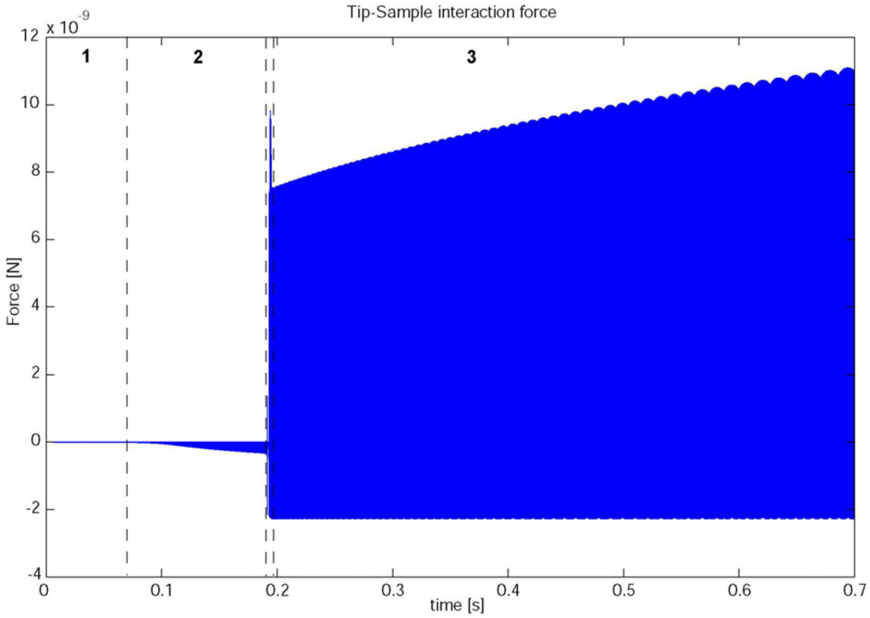

Figure 3.24: The interaction force influencing the tip as function of separation distance.

In the standard amplitude modulation mode, all interest is focused on the first harmonic and the change of its vibration amplitude. Despite the first mode carries the main deflection of the lever, all higher modes experience the same surface interactions and they indispensable contribute to the total lever deflection. To illustrate this fact, figure 3.25 separately shows the envelopes of the first four harmonic modes for presented simulations. The influence of the attractive and repulsive surface forces affects all harmonic modes.
The amplitude of first harmonic mode vibration decreases for smaller separation distances, while the amplitudes of higher harmonic modes increase. If we assume that there is no surface dissipation, then all missing energy from the first harmonic mode corresponding to amplitude decrease is transferred to higher harmonic modes. This effect can be easily followed in figure 3.25 zone 2.

The power spectra densities of the lever position in amplitude modulation mode for three different separation distances between lever base and sample is shown in figure 3.26 for 197 nm, in figure 3.27 for 195 nm and in figure 3.28 for 193 nm. Individual spectra of the first four harmonic modes for each of these separation distances are shown in these figures. In spectra of higher harmonic modes, a contribution of the cantilever thermal excitation resulting in Lorenzian peak at resonance frequency of given mode is clearly visible. First mode is strongly excited by external force at its resonance which completely masks Brownian motion caused by thermal excitation. Image of excitation signal is as well visible in higher harmonic modes as a sharp spike at excitation frequency $\omega_{dri} = \omega_1$. Increasing surface interaction force induces additional harmonics present at frequencies $\omega_n = n \cdot \omega_{dri}$ where $n = \mathbb{N}$.

1st harmonic mode

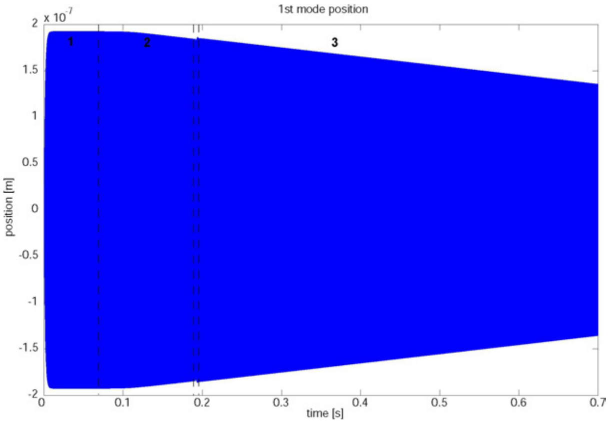

2nd harmonic mode

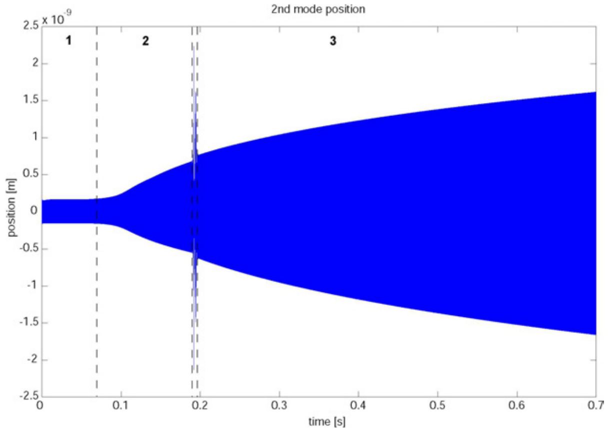

3rd harmonic mode

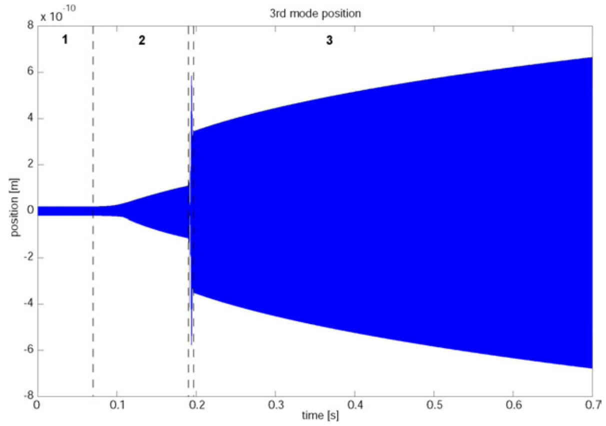

4th harmonic mode

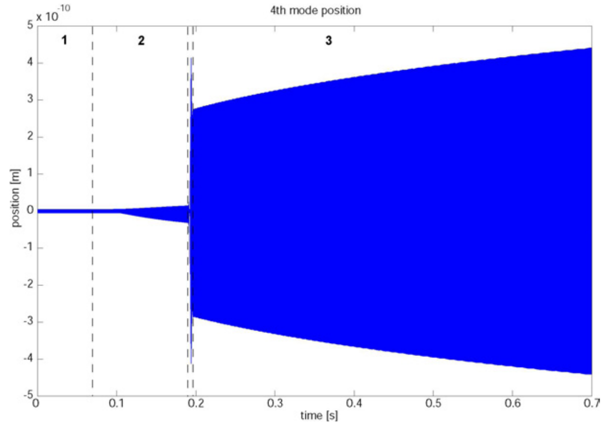

Figure 3.25: Vibration amplitudes of the first four harmonic modes during the approach to modeled surface.

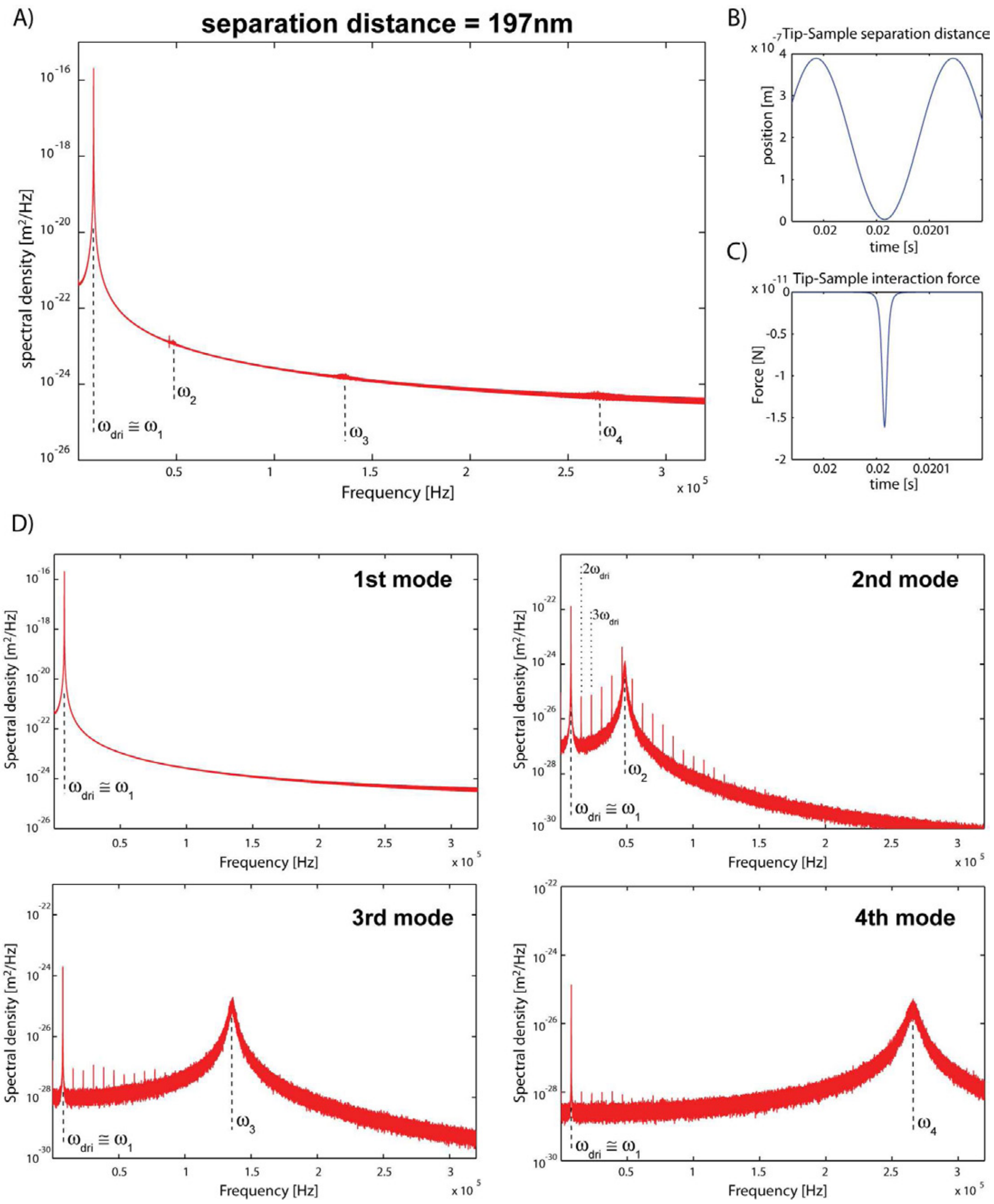

Figure 3.26: Frequency spectra of the cantilever position in amplitude modulation for separation distance 197nm. A) cantilever position spectra, B) tip sample separation distance time sequence, C) surface interaction force time sequence, D) separate spectra of the first four harmonic modes of the cantilever.

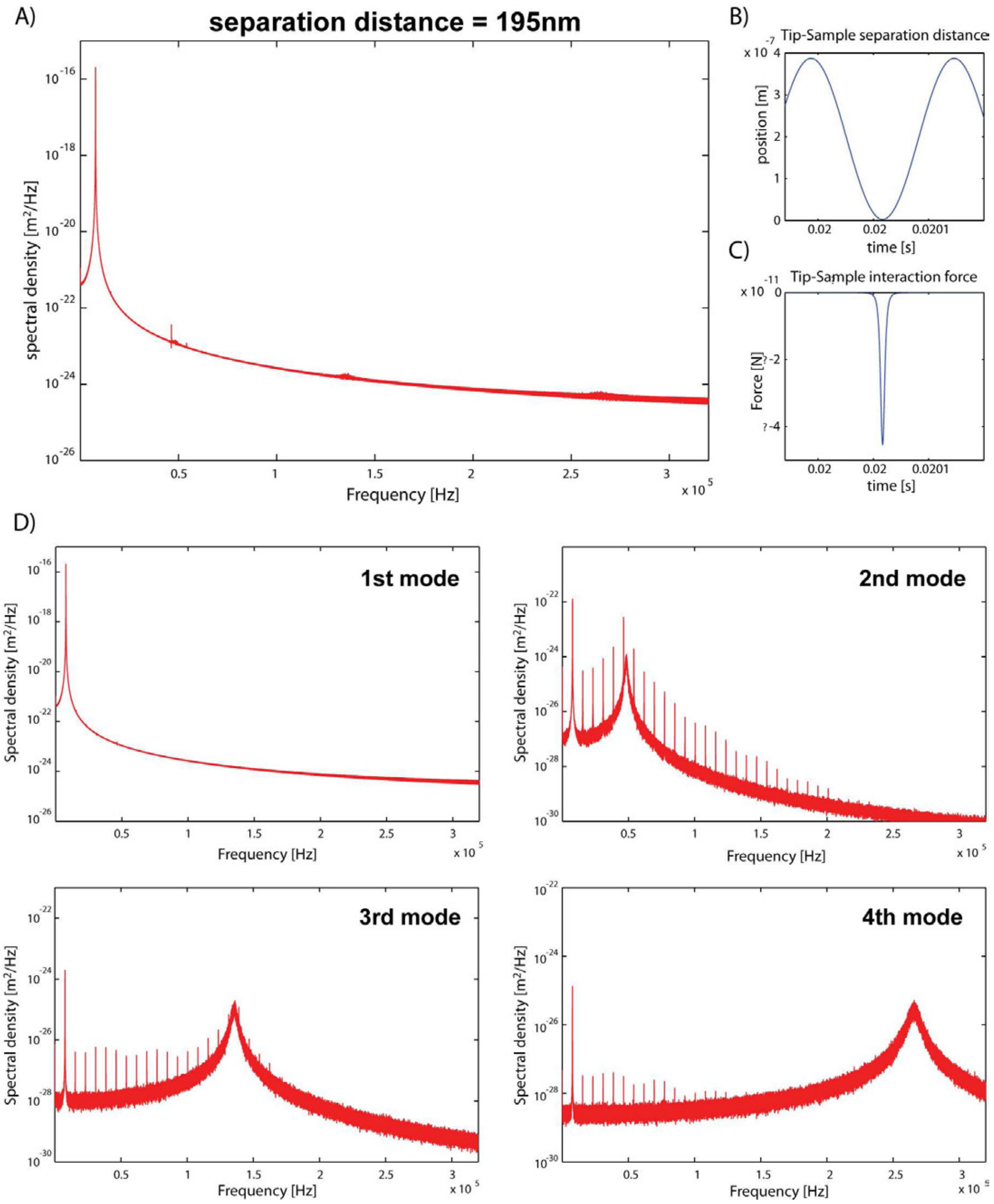

Figure 3.27: Frequency spectra of the cantilever position in amplitude modulation for separation distance 195nm. A) cantilever position spectra, B) tip sample separation distance time sequence, C) surface interaction force time sequence, D) separate spectra of the first four harmonic modes of the cantilever.

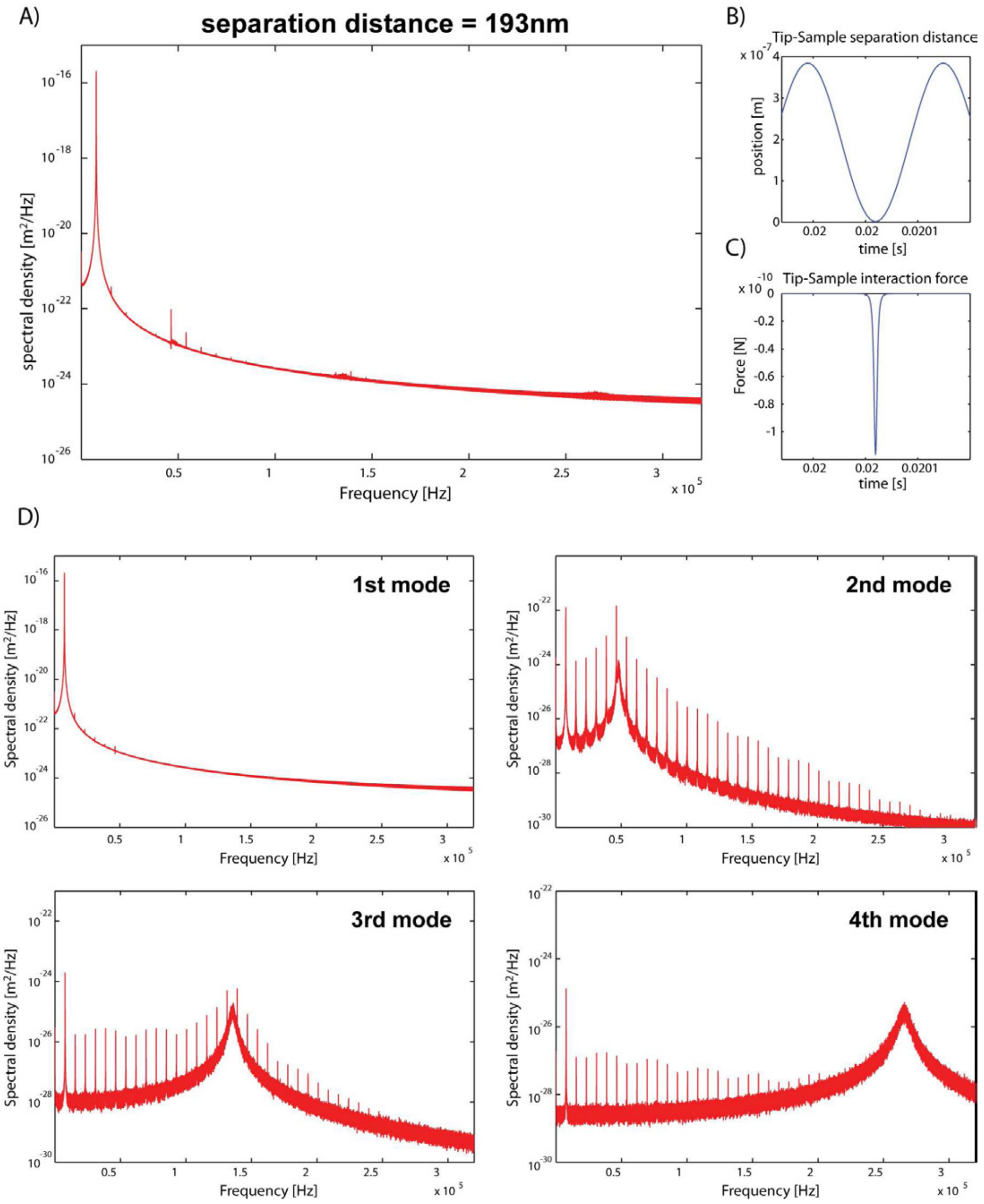

Figure 3.28: Frequency spectra of the cantilever position in amplitude modulation for separation distance 193nm. A) cantilever position spectra, B) tip sample separation distance time sequence, C) surface interaction force time sequence, D) separate spectra of the first four harmonic modes of the cantilever.

In Tapping mode, the influence of higher harmonic modes becomes even more significant in comparison with the amplitude modulation due to strong repulsive forces which are having broader frequency bandwidth. This force excites higher modes more effectively and their influence become not neglectable, see figure 3.25 zone 3. The power spectral densities are shown in figure 3.29 for separation distance 188 nm and in figure 3.30 for separation distance 180 nm. Individual spectra of the first four harmonic modes are shown bellow the figure of position sum for each of these separation distances.

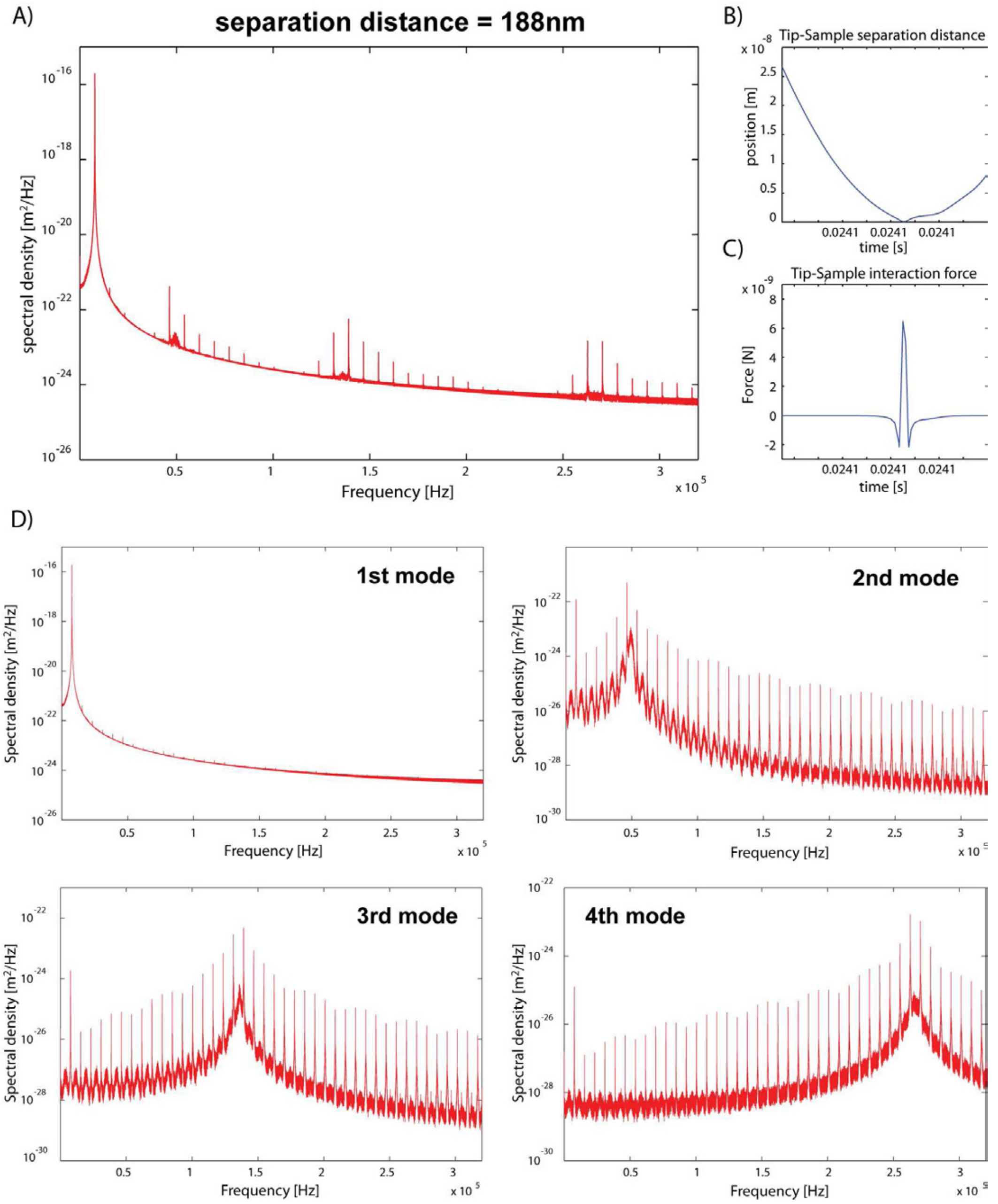

Figure 3.29: Frequency spectra of the cantilever position in Tapping mode for separation distance 188nm. A) cantilever position spectra, B) tip sample separation distance time sequence, C) surface interaction force time sequence, D) separate spectra of the first four harmonic modes of the cantilever.

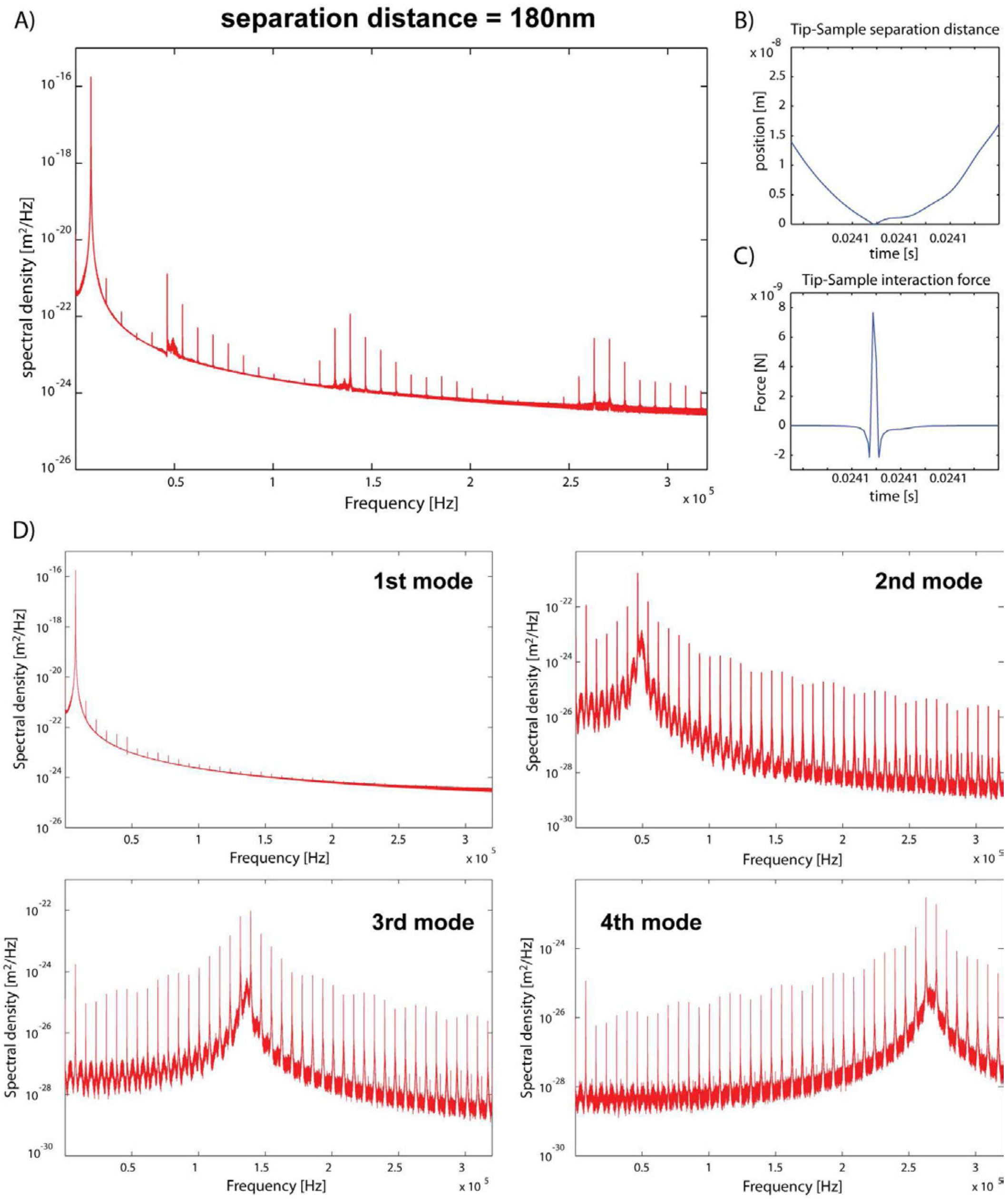

Figure 3.30: Frequency spectra of the cantilever position in Tapping mode for separation distance 180nm. A) cantilever position spectra, B) tip sample separation distance time sequence, C) surface interaction force time sequence, D) separate spectra of the first four harmonic modes of the cantilever.

The energy transfer to higher harmonic modes is visible in all of above presented simulation results. This behavior can be easily explained by well known properties of the surface interaction force and their influence on the cantilever. A model of the interaction force has been presented in section 3.1 and the Hamaker approximation of attractive interaction force can be written:

$$F_{vdW}(z_t) = -\frac{C_{vdW}}{z_t^2} \tag{3.75}$$

where C_{vdW} constant is incorporating all parameters (Hamaker constant, tip radius, ...) for a given model and z_t is the distance between tip and sample. If the system is approximated as undisturbed harmonic oscillator, the tip-sample separation distance can be written:

$$z_t(t) = z_c(t) + z(t) = z_c(t) + A_0 \cdot cos(\omega_{dri} t + \varphi) \tag{3.76}$$

then in dynamic operation mode with weak attractive interaction as an approximation of the resulting interaction force can be written:

$$F_{vdW}(t) = -\frac{C_{vdW}}{(z_c(t) + A_0 \cdot cos(\omega_{dri} t + \varphi))^2} \tag{3.77}$$

If the cantilever is maximally deflected towards the sample, the denominator is close to zero and attractive interaction force has a sharp peak, see figure 3.31 A). The maximum of the interaction force appears periodically with the same frequency as the first harmonic mode. The interaction is highly non-linear and its frequency spectra includes higher harmonic parts that are present at frequencies $\omega_n = n \cdot \omega_{dri}$ where $n = \mathbb{N}$, see figure 3.31 B). This interaction force with its spectra $S_{FF}(\omega)$ is then perturbing the cantilever with the transfer function $H(\omega)$ and resulting spectra of the cantilever position is:

$$S_{zz}(\omega) = |H(\omega)|^2 \cdot S_{FF}(\omega) \tag{3.78}$$

The interaction force spectra directly obtained from this simulation is shown in figure 3.31 C). There is small error between above mentioned model (equation 3.77) and simulated results. Trajectory of the tip in simulation is slightly deviated by the surface interaction in comparison with harmonic oscillator used above to explain this phenomena.

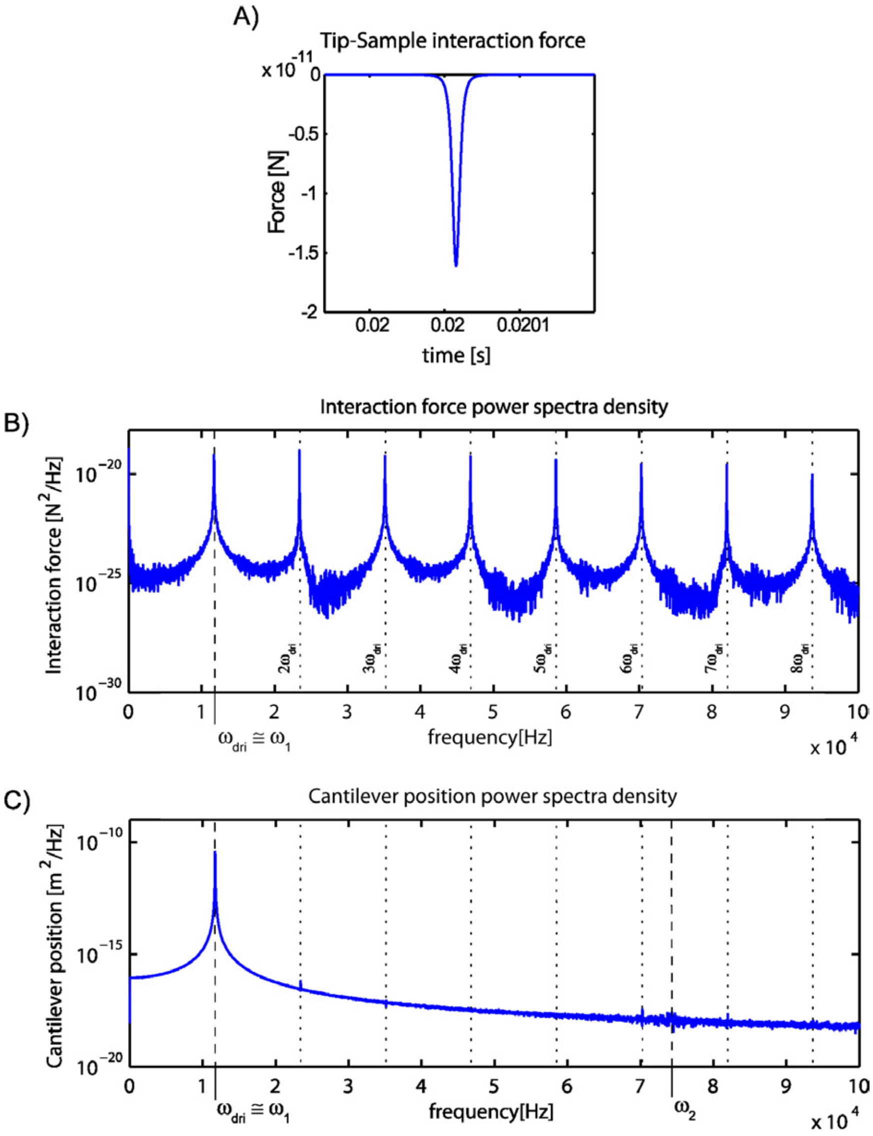

Figure 3.31: A) time sequence of the surface interaction force in amplitude modulation, B) power spectra density of the surface interaction force, B) power spectra density of the cantilever position

This is simplified explanation of the energy transfer to the higher harmonic modes during strong attractive interaction in amplitude modulation measurements.
In the Tapping mode not only attractive forces are present but as well repulsive forces. The frequency spectrum of the interaction force is even more complex and includes broader variation in the interaction force frequencies. High harmonic modes are in the tapping mode intensively perturbed by surface interaction, see figure 3.30.

Chapter 4

Observers

Observer techniques offer powerfull tools to treat signals with great variety of measurement noises and estimate system's internal states with improved precision. They as well offer the possibility to estimate states, that are not directly measurable but have great importance for control or measurement of given system. In this chapter a simulation results of observer aplication to the Atomic Force Microscopy will be presented. The simulations have been performed for the amplitude modulation technique, which has been analyzed earlier, and for a new static operation mode of the AFM.

4.1 Experiment noises

In a following text, the most fundamental experiment distortion induced by surrounding environment will be shortly mentioned. Then, all sources of detection and electronic noise will be presented to give a complete overview of the existing sources of experiment distortion. The distortions induced by surrounding environment are usually relatively strong, but with known techniques they can be effectively minimized to reach necessary condition for successful experiment. Detection and electronic noises usually have lower magnitude then thermal distortion of the cantilever and their influence is less significant. Thermally induced cantilever displacement, Brownian motion, is the main source of experiment distortion limiting microscope's force sensitivity.

Mechanical vibration

The experimental setup is always mechanically connected to the surrounding environment which provides a channel to transfer the mechanical distortion directly into the measurement. The origin of mechanical vibrations is mainly human activity in proximity to the microscope. Also natural vibrations are always present, but in usual conditions they are smaller than the ones induced by human (not considering the exceptions like an earthquake). Mechanical vibrations can be lowered by solid, robust, heavy and stable mechanical mounting of the microscope support. As a part of the support, has to be taken into the consideration as well the building where is the microscope used because usually has a significant influence on distortion intensity. The remaining vibrations which are still transferred to the system has to be eliminated by a passive or an active damping system usually placed between the mechanical support and the microscope itself. Modern active damping systems are capable to attenuate the vibrations and even to measure the residual vibrations intensity. Mechanical vibration are significant mainly at the low frequencies, below 100Hz. Higher frequency vibrations attenuate very fast and can be easily eliminated just by increasing the system's support mass.

A simple vibration measurement has been performed to verify the conditions in our laboratory. Vibrations have been measured during usual working hours and late at night when vibrations induced by human activity are minimized. The experimental setup is placed on a marble table (100x65x15 cm, 250 kg) which has four legs with integrated springs. To compare the efficiency of the used passive table, two additional measurements have been performed: first one directly at laboratory floor and second one at the top of active anti-vibration table (Halcyonics). The results for vertical vibration are shown for both tables in figure 4.1 A) for floor and figure 4.1 B). Figures show that during the day the vibrations around 2 Hz are twice as high as in the night. Passive table lowers the vibration amplitude above frequency 20 Hz, but vibrations at lower frequencies are rather amplified then damped. In figure 4.1 B) a new vibration peak around 15 Hz is visible which corresponds to the table resonance frequency. Active damping table is more efficient and lowers the vibrations above 2 Hz very efficiently. On the other hand, the frequencies below 2 Hz are amplified. In figure 4.1 C) and D) lateral vibration (X and Y axis) are shown.

Accustic vibration

The experiment is surrounded by air (moving molecules or fluid) that can carry *acoustic waves* affecting the measurement. Their influence can be distributed over larger bandwidth than the mechanical vibrations and their frequency can easily range up to tens of kilo hertz. In laboratory environment a wide variety of sources of this distortion exist, from running air conditioning, computer fans, to moving and speaking people. The influence of some of these sources can be minimized, however to function optimally the microscope has to be equipped with acoustic shielding.

Now we can consider the direct measurement distortions that usually come from the used measurement method and equipment. The very first distortion measurement which has been already introduced in chapter 3.2 was *thermal noise* and its description would not be developed any further. In this chapter, the presented description will focus directly on cantilever position detection using optical beam detection technique introduced in section 2.1.3 and noise related to this technique. Measurement noise in optical beam detection [108] can be divided into four parts:

Laser noise

The used light source (laser) is experiencing two kinds of fluctuations: *laser intensity noise* and *laser phase noise*. The phase noise is important for measurements using interferometric method but in the beam detection technique only the intensity noise is important. The laser operation is based on spontaneous light emission from active laser medium given external energy. Created light is trapped in optical cavity and regenerates more light from the active medium. This proces is very complex and many different effects can occur during operation. The laser manufacturers provide one general value of laser intensity fluctuation describing the sum of all different effects. The influence of the laser intensity noise can be lowered by dividing photo-detector signal for vertical and lateral deflection by the the sum of all detetectors segments, see section 2.1.3.

Optical path distortion

The light propagating trough any media is affected by different phenomenas (reflection, absorbtion, dispersion, diffraction, ...) that change its properties. In usual operation condition of Atomic Force Microscopy, this medium is air and in some biology applications it is water. The influence of this medium is randomly changing due to the constant motion of media particles due to flow and Brownian motion. This brings a random distortion to the measurement that is very difficult to describe mathematically. Another part of the *optical path distortion* is the optical parts used to focus and manipulate the light beam and their influence is usually static during the entire measurement.

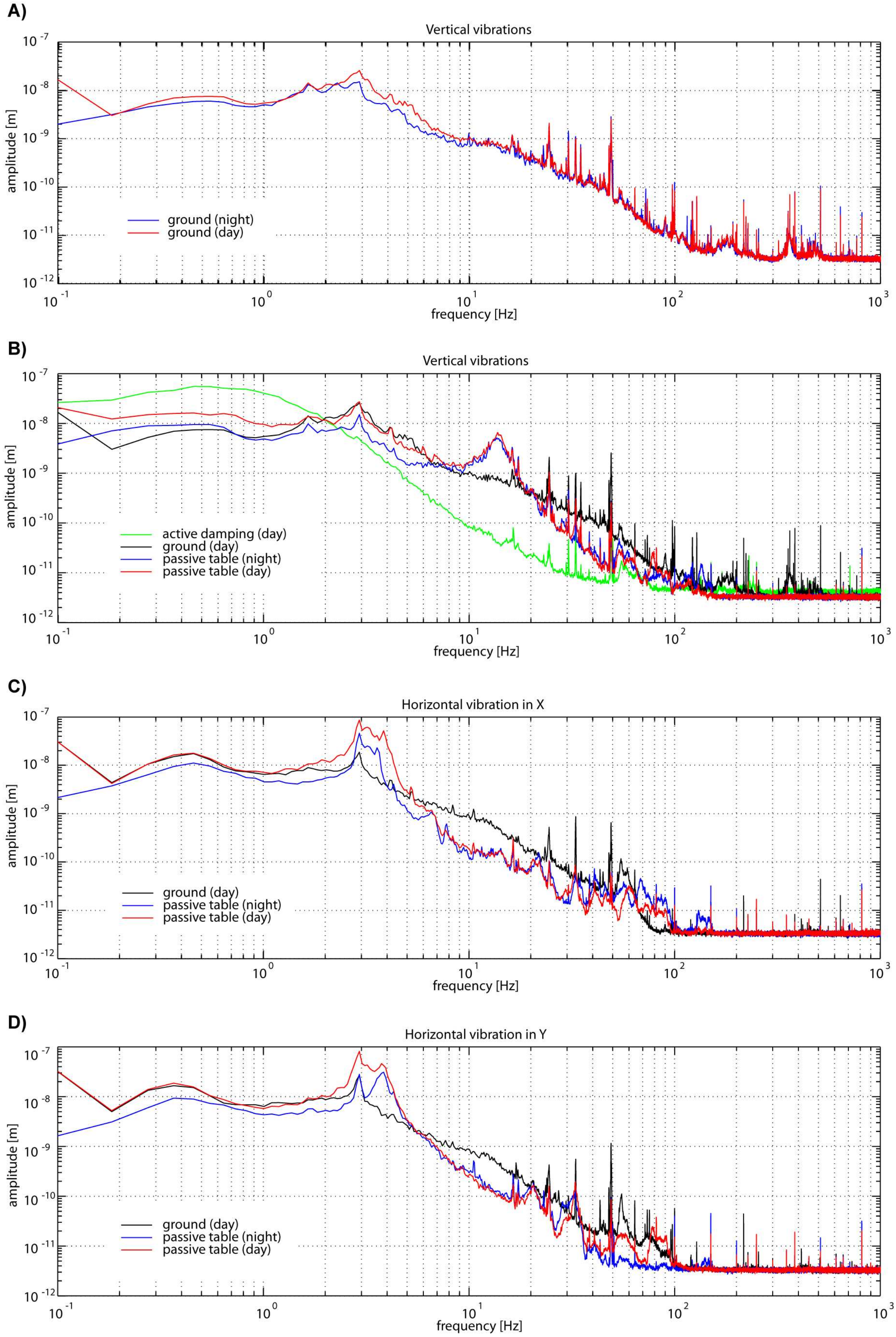

Figure 4.1: Mechanical vibration measured in Surface Science Laboratory - ESRF. Plot A) and B) show the spectral density of the vertical displacement (z axis), plot C) shows the lateral displacement in axis "x" and plot D) in axis "y".

Photo-detector - Shot noise
Laser spot position is detected by a photo-detector, more precisely photo-diodes which change their conductivity according to the quantity of incident light at the photo-sensitive surface. *Shot noise* is a type of photo-electronic noise that occurs due to finite number of particles (in this case photons) transporting the energy in the system. If the number of particles transporting the energy is sufficiently small the statistical fluctuations cause fluctuation of the output photo-current:

$$\left\langle \delta i^2_{PD-shot} \right\rangle = 2eGP_0\Delta f \tag{4.1}$$

where $e = 1.602 \cdot 10^{-19}$ C is the elementary charge, G is the photodetector conversion constant (A/W), P_0 is average optical power and Δf is the bandwidth of interest. This current fluctuation generates a voltage fluctuation on the load resistor R:

$$\left\langle \delta u^2_{PD-shot} \right\rangle = R^2 2eGP_0\Delta f \tag{4.2}$$

Electronic noise
In electronic devices, there are three main sources of noise related to flowing current and static voltage.
Shot noise - is a random fluctuation of electric current in electrical conductors. The current is carried by a limited number of elementary charges (electrons) which are moving through the conductor. In a short time period the charge is moving randomly and the total current is the mean value of the charge flow. Shot noise has a Poisson distribution and has “white noise" properties (flat power spectral density). The mean square variation of the current I around its average value produced by this noise is:

$$\left\langle \delta i^2_{E-shot} \right\rangle = 2e \left\langle I \right\rangle \Delta f \tag{4.3}$$

where $e = 1.602 \cdot 10^{-19}$ C is the elementary charge and Δf is the bandwidth of interest.
Thermal noise - often called Johnson noise after its founder. This noise is caused by the thermal agitation of the electrons and holes carrying electric charge in any conductor, causing fluctuation of total potential U. Like the shot noise, it has “white noise" properties (flat power spectral density). The mean square variation of the potential U is defined as:

$$\left\langle \delta u^2_{thermal} \right\rangle = 4k_BTR\Delta f \tag{4.4}$$

or the current fluctuation at the load resistor R is defined as:

$$\left\langle \delta i^2_{thermal} \right\rangle = 4k_BT\Delta f/R \tag{4.5}$$

where k_B is the Boltzmann's constant, T is the absolute temperature, R is the conductor resistance and Δf is the bandwidth of interest.
Flicker noise - also called “1/f" noise or pink noise. It is always present in active electronic devices and has various origins. At low frequencies the flicker noise magnitude is greater than the magnitudes of the white noises introduced earlier, but with increasing frequency decreases fast (one order per frequency decade) and white noises becomes dominant. The spectral density is defined by

$$\left\langle \delta i^2_{flicker} \right\rangle = K^2 I^2_{DC}\Delta f/f \tag{4.6}$$

where K is the system constant, I_{DC} is the direct current through the device, Δf is bandwidth of interest and f stands for frequency.

The presented sources of measurement noise have very complex relations and it is very difficult to estimate their contribution to the total amount of measurement distortion without extensive studies of the experimental setup. For the modeling and estimation purpose, these noises will be simplified and modeled by only single source of white noise. The magnitude of this noise is chosen higher in comparison to the results obtained with our microscope. The variance of the measurement noise is set to $\left\langle \nu_{measure}^2(t) \right\rangle = 25 \cdot 10^{-20}$ m for dynamic operation mode, and to $\left\langle \nu_{measure}^2(t) \right\rangle = 9 \cdot 10^{-20}$ m for the proposed static operation mode. The measurement noise for dynamic operation mode is set higher to take into the account a cantilever excitation which causes an additional perturbation. Both magnitudes are still significantly higher then the noises measured on the experimental set-up.

4.2 Observer introduction

In many cases, the controlled systems have more internal states then there are measurable outputs. The control of these states have a great interest in a wide variety of applications using the state space variables for the design and operation of the state space controller. The difficulty is that not necessary all states are measurable and can even be physically not existing. To be able to obtain internal states of a given system a state estimator commonly called *state observer* can be used.

The state observer can be defined as a program (or a device) that estimates states of the observed system that are unknown, from measured outputs of this system. An observer that estimates all states of the system is called *full-order state observer*. An observer that estimates additional variables is called *extended state observer*. The observer for its operation uses an internal model which output is compared with the measurement. Internal model states are “a copy" of the estimated system states. The observer includes a minimization algorithm which minimizes the error between the estimated output and the measurement. Details on the state observers can be found in [137, 138] and applications of state observers to non-linear systems are presented in [139, 140, 141].

Consider a dynamic time invariant system defined by:

$$\dot{\mathbf{x}} = \mathbf{A}\mathbf{x} + \mathbf{B}\mathbf{u} \tag{4.7}$$

$$\mathbf{y} = \mathbf{C}\mathbf{x} + \mathbf{D}\mathbf{u} \tag{4.8}$$

where $\mathbf{x}$ denotes the state vector, $\mathbf{y}$ is the measured output vector, $\mathbf{u}$ is the input vector, $\mathbf{A}$ is the dynamic matrix, $\mathbf{B}$ is the input matrix, $\mathbf{C}$ is the output matrix, $\mathbf{D}$ is direct transmission matrix. For the given system the state space observer can be constructed with approximated state vector **x’** and defined by matrices **A’**, **B’**, **C’**, **D’** and observer gain matrix $\mathbf{K}_e$. The constructed observer has matrices that approximate the estimated system but are not necessary exactly the same. The discrepancy between the original system and the model used in the observer depends on the accuracy of system identification and directly affects the estimated state vector from the measured data. The observer is defined by

$$\dot{\mathbf{x}}' = \mathbf{A}'\mathbf{x}' + \mathbf{B}'\mathbf{u} + \mathbf{K}_e(\mathbf{y} - \mathbf{C}'\mathbf{x}') \tag{4.9}$$

If we assume observer’s internal model to be identical to the estimated system (**A**=**A’**, **B**=**B’**, **C**=**C’**, **D**=**D’**) then the estimation error dynamics can be written

$$\dot{\mathbf{x}} - \dot{\mathbf{x}}' = \mathbf{A}\mathbf{x} - \mathbf{A}'\mathbf{x}' + \mathbf{K}_e(\mathbf{C}\mathbf{x} - \mathbf{C}'\mathbf{x}') = (\mathbf{A} - \mathbf{K}_e\mathbf{C})(\mathbf{x} - \mathbf{x}') \tag{4.10}$$

This equation can be reformulated using the observation error substitution $\mathbf{e} = \mathbf{x} - \mathbf{x}'$

$$\dot{\mathbf{e}} = (\mathbf{A} - \mathbf{K}_e\mathbf{C})\mathbf{e} \tag{4.11}$$

The estimation error will asymptotically converge to zero for any initial error vector $\mathbf{e}(0)$ only if the matrix $\mathbf{A}-\mathbf{K}_e\mathbf{C}$ is stable. The observer correction matrix $\mathbf{K}_e$ guaranties the observer stability and convergence speed. Its design is a dual problem to the design of the gain matrix for stable state space controller. The choice of desired observer eigenvalues is constrained by system stability and required convergence speed. The complete setup with system model and state space observer is depicted in figure 4.2.

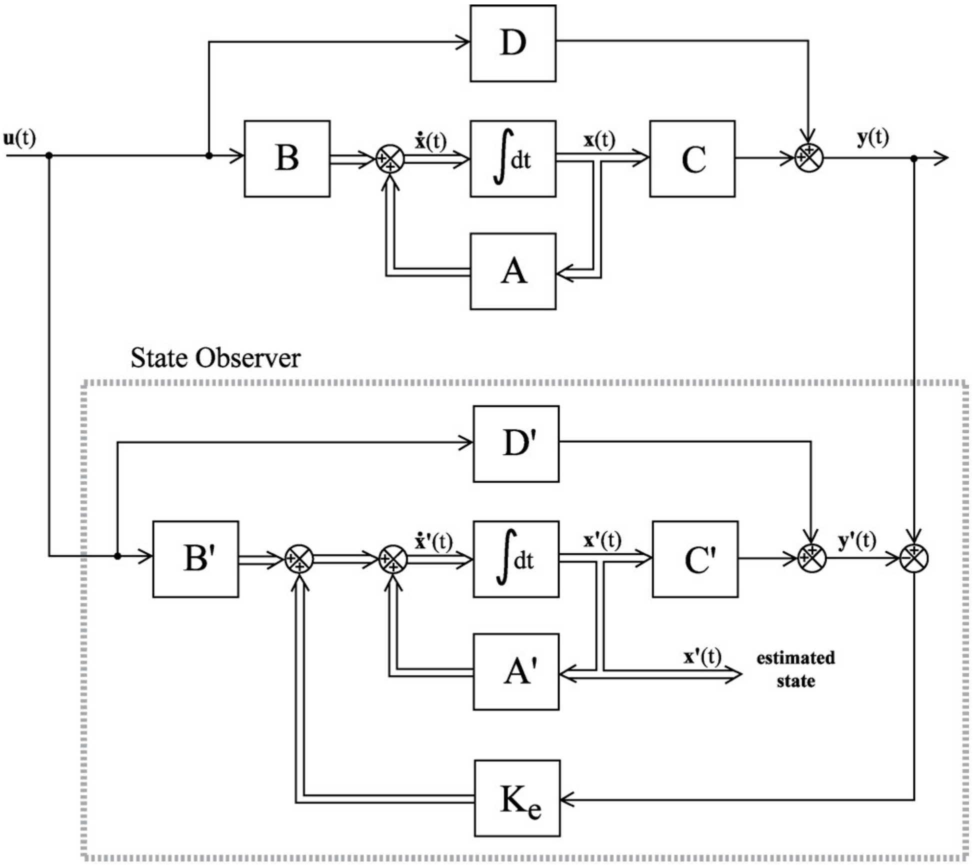

Figure 4.2: State observer operation - general schema.

The functionality of state observer has one more fundamental condition that has to be fulfilled. The observer exist only if the system is completely observable. The observability condition can be determined from a observability matrix **L** which is defined

$$\mathbf{L} = \begin{bmatrix} \mathbf{C}' \\ \mathbf{C}'\mathbf{A}' \\ \vdots \\ \mathbf{C}'\mathbf{A}'^{\mathbf{n-1}} \end{bmatrix} \tag{4.12}$$

The rank of the observability matrix L has to be equal to the system order n for the system to be completely observable. In the case that a rank is equal to m, which is smaller than n, the system has n-m unobservable states. If the system has one or more unobservable states, then an unique solution for the estimated system states for a given system input and output does not exist. The observability condition has to be always satisfied.

For the observer construction, it is convenient to transform internal model defined by **A'**, **B'**, **C'**, **D'** into the canonical form using the transformation base on observability matrix

$$\mathbf{T} = \mathbf{L} \tag{4.13}$$

The existence of the inverse matrix $\mathbf{T}^{-1}$ is guaranteed by the full observability of the given system. The new observer internal model matrices in canonical form (**A”**, **B”**, **C”**, **D”**) are defined:

$$\mathbf{A}'' = \mathbf{T}\mathbf{A}'\mathbf{T}^{-1} \tag{4.14}$$

$$\mathbf{B}'' = \mathbf{T}\mathbf{B}' \tag{4.15}$$

$$\mathbf{C}'' = \mathbf{C}'\mathbf{T}^{-1} \tag{4.16}$$

and the new state vector is

$$\mathbf{x}'' = \mathbf{T}\mathbf{x}' \tag{4.17}$$

The observer correction matrix $\mathbf{K}_e$ often called observer gain matrix can be now found as the solution of the equation

$$0 = -\Gamma\mathbf{K}_e - \mathbf{N}\mathbf{K}_e - \mathbf{K}_e\mathbf{N} + \mathbf{C}''^T\mathbf{C}'' \tag{4.18}$$

where $N_{i,j}$ is the anti-shift operator $N_{i,j} = \delta_{i,j-1}$, and Γ is a diagonal matrix defined by $\Gamma_{i,i} = \theta^i_{i,i}$. The free parameter $\theta = \theta_{i,i}$ has to be large enough to reach fast convergence to the solution and still maintaining the observer stability.

The presented state space observer with constant gain is relatively simple and has been chosen for purpose of easy implementation into Digital Signal Processor. With more complex observers with variable gain which is continuously adjusted during the operation, the implementation is very difficult due to large computation power demands on the real time system.

4.3 Dynamic mode - observer application

The Atomic Force Microscope is often used in dynamic operation mode and the cantilever is driven at its resonance frequency or in its close proximity, see section 2.2.2. The operation close to the resonance frequency is affected by Brownian motion which at this frequency region has significant amplitudes. Observer techniques offer great opportunity to improve signal to noise ratio in this standard operation mode. Great progress in the use of observer application to dynamic techniques has been done by *Sahoo, Sebastian* and their colleagues, which proposed transient sample detection [102, 142]. This technique is using observer innovations to sense sudden changes of surface topography, but it is unable to detect small gradients in surface topography. Other technique proposed by the same authors [103] detects a cantilever motion and controls (decrease/increase) the quality factor of the cantilever using observer in feedback loop. The capacitive detection of lever position enhanced by observer has been presented by *Napoli* [44] for AFM operated in standard dynamic mode.

Here presented work is using standard operation mode as well. On the other hand, proposed techniques are able to detect slow topography slopes and their application are not limited by the speed of topography changes. The observer application on the existing amplitude modulation technique has been tested for two different observer structures: state observer used to detect the cantilever vibration amplitude, and extended state observer capable to directly estimate the interaction force. Both observers use the same operation diagram shown in figure 4.3.

In the following simulations the same model as in section 3.7.3 is used, with parameters given in table 3.4. The cantilever is driven by an excitation signal $F_{dri}(t) = A_{drive} \cdot sin(\omega_{dri} \cdot t)$ with constant magnitude. The driving frequency is chosen $\omega_{dri} = 0.99 \cdot \omega_1$, where ω_1 is resonance frequency of cantilever first harmonic mode. The cantilever is driven by an excitation signal with constant magnitude resulting in cantilever free vibration amplitude equal 85 nm. The vibrating cantilever interacts with the surface force $F_{int}(t) = f(z(t) + z_c(t))$ where, $z(t)$ is actual cantilever deflection and $z_c(t)$ is the separation distance between the cantilever fixed end and the sample, see section 3.1. Parameter $z_c(t)$ is used to model the surface topography. It is a sum of two values: constant offset approximately equal to the cantilever vibration amplitude and a small periodic square signal (in order of nanometers). The constant value corresponds to the mean distance between cantilever fixed end and the surface. The added periodic signal stands for surface topography variation and its bandwidth is limited to tens of Hertz to be similar to the real topography. The numerical values of $z_c(t)$ are shown graphically for each simulation.

The cantilever model includes independent white noise sources for each harmonic mode to guaranty zero cross-correlation between thermally excited harmonic modes. Thus, a thermally distorted cantilever model accurately corresponds to the real physical system where all modes are uncorrelated. Measurement noise with variance $\langle \nu^2_{measure}(t) \rangle = 25 \cdot 10^{-20}$ m is added to the actual cantilever position $z(t)$. The chosen noise variation is larger than noise levels obtained with Nanotec experimental setup.

The obtained cantilever position $z_{measure}(t)$ and excitation signal $F_{dri}(t)$ are provided as inputs to the state observer or extended state observer. The observation error is calculated from the cantilever position without measurement noise and observer's output. This simulation setup is used for both versions of the state-space observers presented below.

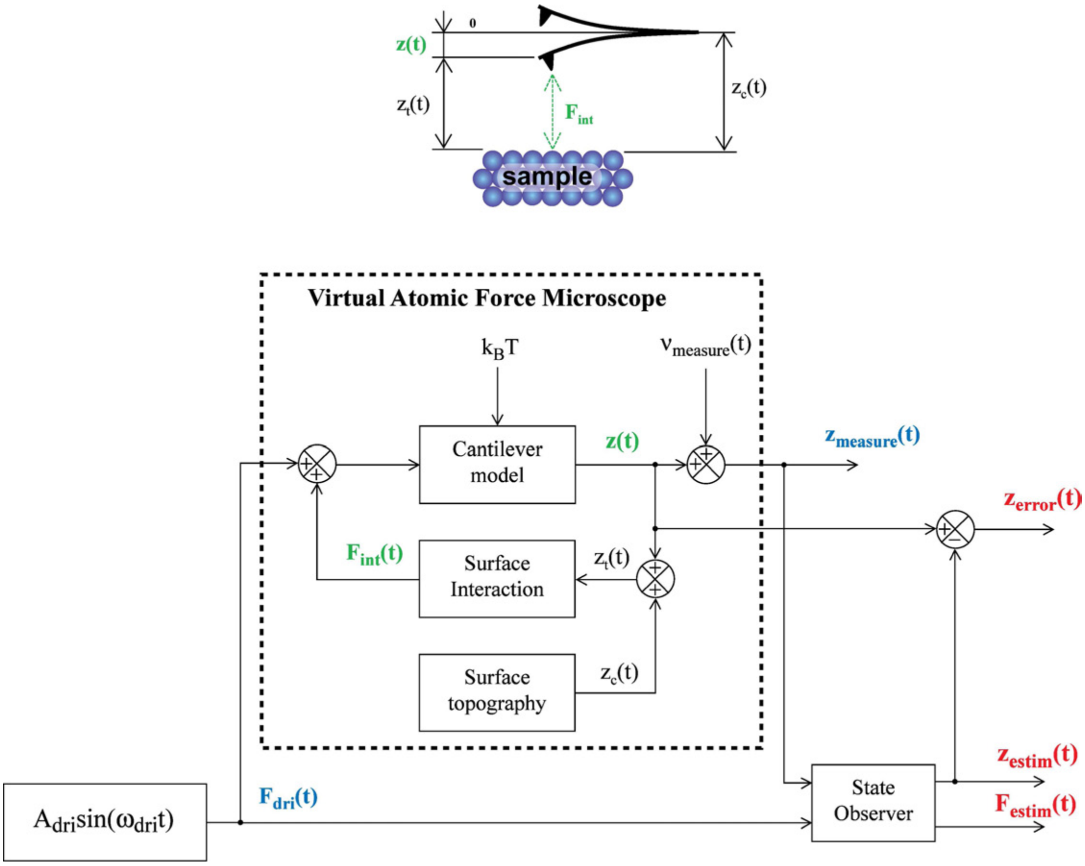

Figure 4.3: Virtual AFM and state-space observer simulation setup. Variables marked in green are accessible only in "virtual" AFM , variables marked in blue are known or measurable, red variables are results of the state observer.

The diagram in figure 4.3 will be used in all following observer simulations. The central part is the "virtual" atomic force microscope which is a model of the real experimental setup including measurement and thermal noise. The variables in green color are not accessible in a real experiment and our interest is to estimate their values with the proposed observers. The variables in blue are chosen by the user or they are easily measurable with the experimental setup and are used as observer inputs. The estimation results are in red color and will be compared with the values present in virtual (simulated) AFM, which are unknown in a real-time experiment.

4.3.1 State observer

The first test has been performed with constant gain state-space observer applied to simple and often used amplitude modulation mode, see section 3.7.3. The surface interaction force $F_{int}(t)$ modifies cantilever effective spring constant resulting in vibration amplitude modification. This general strategy of microscope operation has been maintained and the observer is only used to improve signal to noise ratio of the amplitude detection.

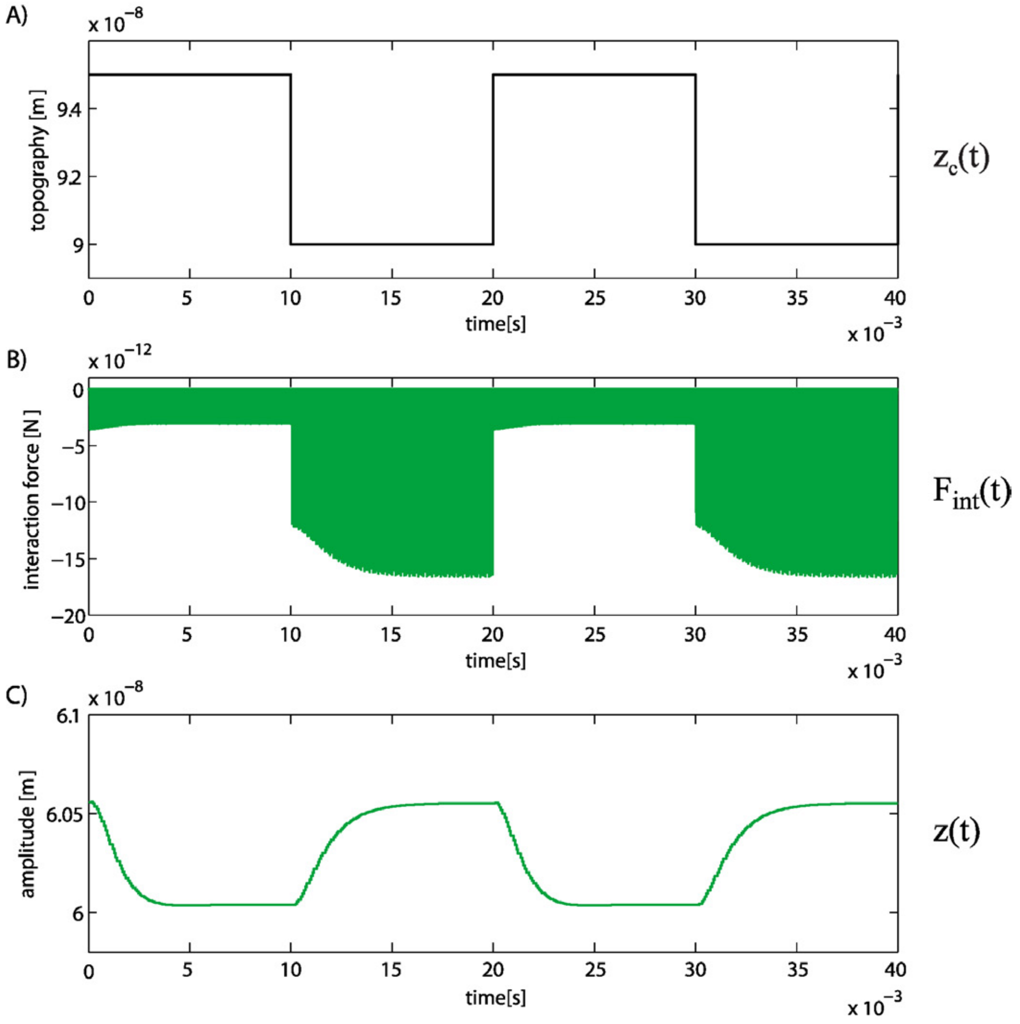

Figure 4.4: Ideal operation of amplitude modulation technique without any distortion. A) chip-sample separation distance (topography) $z_c(t)$. B) tip-surface interaction force $F_{int}(t)$. C) effective vibration amplitude $z(t)$.

The virtual AFM operation without any thermal distortion and measurement noise is shown in figure 4.4. The curves are theoretical and cannot be experimentally obtained. From figure 4.4 B) rather the envelope than the time sequence of the interaction force is visible. For detail of this force see for example figure 3.26. Figure 4.4 C) shows changing effective vibration amplitude according to the separation distance. The settle time is relativelly small and the final vibration amplitude is reached in less than five milliseconds due to relatively low cantilever quality factor.

The same simulation has been performed for the model including thermal distortion and measurement noise. The obtained results are shown in figure 4.5, A) is the separation distance $z_c(t)$, B) tip-surface interaction force $F_{int}(t)$ and C) measured vibration amplitude, blue curve.

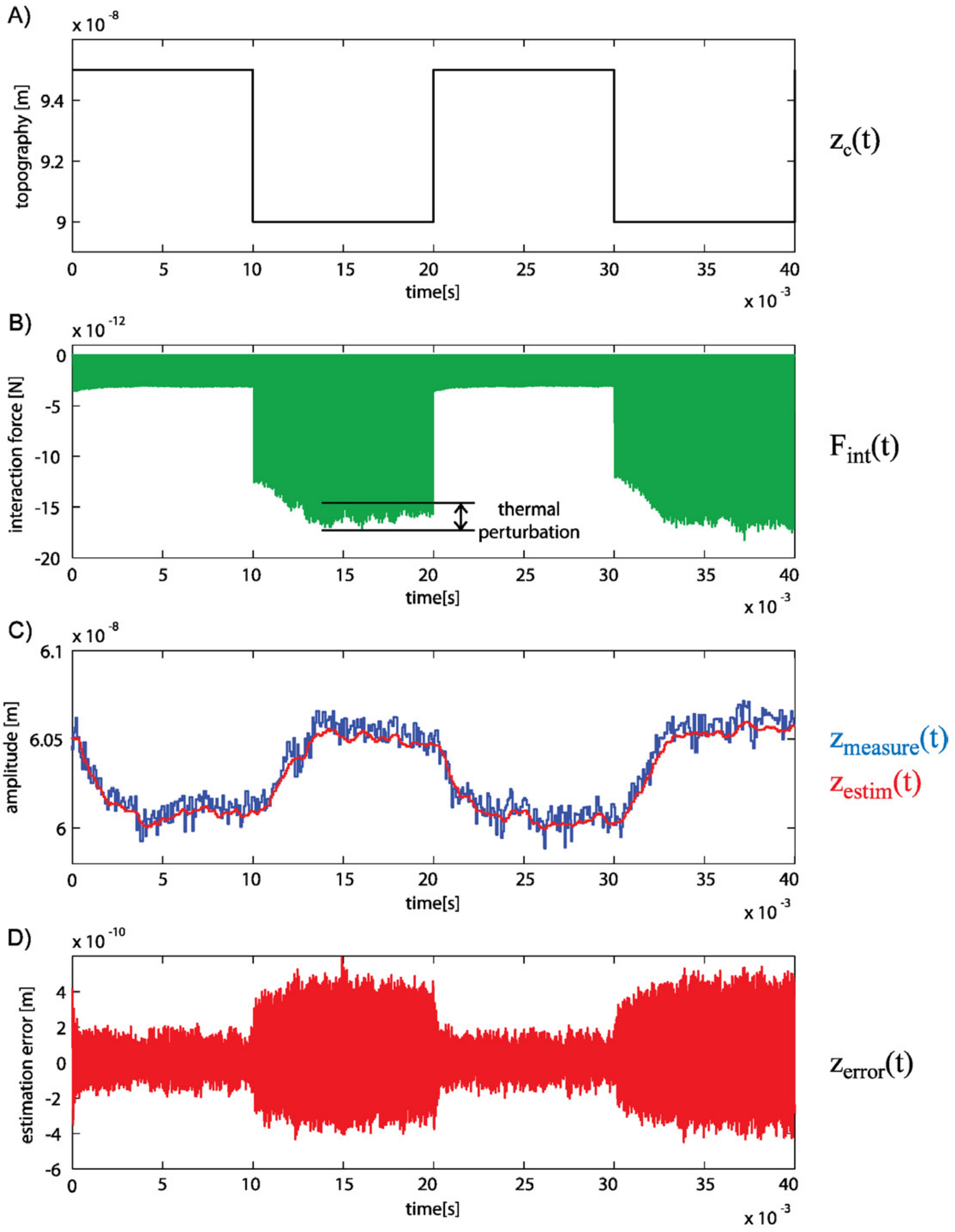

Figure 4.5: Amplitude modulation technique simulation with thermal distortion and measurement noise. A) chip-sample separation distance $z_c(t)$. B) tip-surface interaction force $F_{int}(t)$. C) effective vibration amplitude, blue curve - detected from noisy position measurement $z_{measure}(t)$, red curve - detected from estimated cantilever position $z_{estim}(t)$. D) position estimation error $z_{error}(t)$.

The state observer provides the possibility to adjust the observer gain allowing to reach the required functionality for particular needs. For this case, it has been found an observer gain θ equal to 10.1. This is a compromise between observation error and observer sensitivity to the measurement noise. The resulting effective vibration amplitude detected from the estimated cantilever position is shown in figure 4.5 C), red curve. A corresponding estimation error is shown in figure 4.5 D) and is calculated from cantilever

position without measurement noise $z(t)$. The estimation error reviels, that in presence of stronger interaction force, the observer is not able to minimize the error as efficiently as for weak interactions. This is caused by the high nonlinearity of the tip-surface interaction which cannot be easily followed by the linear observer. An estimation error improves if observer gain increases but the observer starts to follow a thermal noise.
Additional tests have been performed for higher levels of measurement noise. The designed observer was capable to eliminate this noise. From the estimated and measured vibration amplitude it is apparent that the observer does not sufficiently rejects the effects of thermal distortion. The observer is not able to distinguish between the effects of surface interaction and thermal distortion at resonance frequency, where the measurement is performed.

4.3.2 Extended state observer

The state observer introduced at the beginning of this chapter has been extended with an additional state representing searched tip-surface interaction force $F_{int}(t)$. Despite the high non-linearity of the surface interaction (see section3.7.3), the designed observer is linear to maintain the design simplicity. This observer gives the opportunity to directly estimate the interaction force instead of estimating the cantilever amplitude and calculate from it the interaction force. The estimated force is not a perfect copy of the force present in the real experiment which is non-linear. It is rather an image that has the same energetic influence on the moving cantilever resulting in an equivalent change in the vibration amplitude.

In section 3.5 was developed the state space representation of the cantilever model and from this equation the extended observer is formulated

$$m_{eff}\ddot{z}_i(t) + m_{eff}\gamma\dot{z}_i(t) + k_i z_i(t) - F_{estim}(t) = F_{\mathrm{dri}}(t) \tag{4.19}$$

where $F_{\mathrm{dri}}(t)$ is driving force and $F_{\mathrm{estim}}(t)$ is estimated tip-surface interaction

$$\ddot{z}_i(t) = -\frac{\omega_i}{Q_i}\dot{z}_i(t) - \frac{k_i}{m_{eff}}z_i(t) + \frac{F_{\mathrm{estim}}(t)}{m_{eff}} + \frac{F_{dri}(t)}{m_{eff}} \tag{4.20}$$

Now we can directly formulate the state space representation in standard form

$$\dot{\mathbf{x}}'(t) \quad = \quad \mathbf{A}'\mathbf{x}\text{'}(t) + \mathbf{B}\text{'}\mathbf{u}(t) \tag{4.21}$$

$$\mathbf{y}'(t) = \mathbf{C}\text{'}\mathbf{x}'(t) + \mathbf{D}\text{'}\mathbf{u}(t) \tag{4.22}$$

where $\mathbf{x}'(t)$ is the state vector, $\dot{\mathbf{x}}'(t)$ is derivation of the state vector, $u(t)$ is the input vector of driving force $F_{dri}(t)$ and $\mathbf{y}'(t)$ is the output vector of the cantilever model

$$\begin{bmatrix} \dot{x}_{11}(t) \\ \dot{x}_{12}(t) \\ \vdots \\ \dot{x}_{n1}(t) \\ \dot{x}_{n2}(t) \\ \dot{x}_{estim}(t) \end{bmatrix} = \begin{bmatrix} 0 & 1 & \dots & 0 & 0 & 0 \\ -\frac{k_1}{m_{eff}} & -\frac{\sqrt{k_1 m_{eff}}}{m_{eff}Q_1} & \dots & 0 & 0 & \frac{1}{m_{eff}} \\ \vdots & \vdots & \ddots & \vdots & \vdots & \vdots \\ 0 & 0 & \dots & 0 & 1 & 0 \\ 0 & 0 & \dots & -\frac{k_n}{m_{eff}} & -\frac{\sqrt{k_n m_{eff}}}{m_{eff}Q_n} & \frac{1}{m_{eff}} \\ 0 & 0 & \dots & 0 & 0 & 0 \end{bmatrix} \tag{4.23}$$

$$\times \begin{bmatrix} x_{11}(t) \\ x_{12}(t) \\ \vdots \\ x_{n1}(t) \\ x_{n2}(t) \\ x_{estim}(t) \end{bmatrix} + \begin{bmatrix} 0 \\ \frac{1}{m_{eff}} \\ \vdots \\ 0 \\ \frac{1}{m_{eff}} \\ 0 \end{bmatrix} \cdot u(t)$$

$$\mathbf{y}(t) = \begin{bmatrix} z_{estim}(t) \\ F_{estim}(t) \end{bmatrix} = \begin{bmatrix} 1 & 0 & \dots & 1 & 0 & 0 \\ 0 & 0 & \cdots & 0 & 0 & 1 \end{bmatrix} \times \begin{bmatrix} x_{11}(t) \\ x_{12}(t) \\ \vdots \\ x_{n1}(t) \\ x_{n2}(t) \\ x_{estim}(t) \end{bmatrix} \tag{4.24}$$

The estimated interaction force $F_{estim}(t)$ appears in the model as an additional state $x_{estim}(t)$. This state has no internal dynamics and is added to all other states as a force. The output vector has two components: the estimated cantilever position $z_{estim}(t)$ and the estimated interaction force $F_{estim}(t)$. The estimated position is compared to the measured cantilever position and used for the observer correction. The estimated interaction force is a result that cannot be compared to the real interaction force, because this force is not directly measurable in experimental conditions. However in simulation, it is possible to read out the interaction force and precisely validate the obtained results.

The proposed observer has been implemented using the simulation diagram shown in figure 4.3. The simulation has been performed for the model including all disturbances presented earlier. The cantilever is driven by excitation signal with constant magnitude resulting in cantilever free vibration amplitude equal 85 nm. If the driving frequency $\omega_{drive} = 0.99 \cdot \omega_1$, then the excitation is below the first resonance frequency. The cantilever fixed end is placed *92.5* nm above the surface with topography modeled as steps of ± 2.5 nm ($z_c = 92.5 \pm 2.5$ nm), see figure 4.6 A).

The observer gain was searched for to satisfy the requirements on measurement and thermal noise rejection. The observer becomes unstable for the gain of 18.8, but our requirements are met for a much lower value and the gain θ is set to 4.5. This gain is much lower than the one used in amplitude estimation which was 10.1. This results in larger cantilever position estimation error, see figure 4.6 B). The simulated and estimated vibration amplitude are not shown because the amplitude difference is very small compared to the vibration amplitude, and from the figure it is impossible qualify the difference. Nevertheless, this results underline the choice of low observer gain which maximally rejects the measurement noise. It will be shown later, that despite this position estimation inaccuracy, the interaction force estimation is still reasonably accurate.

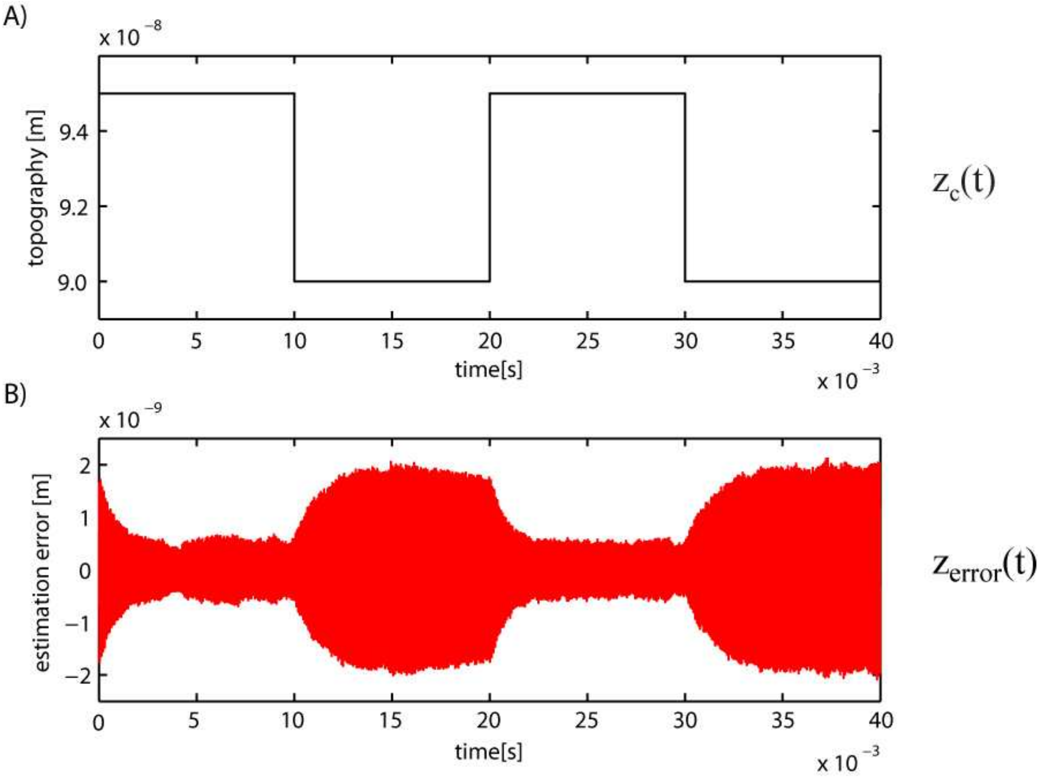

Figure 4.6: A) the distance between the cantilever fixed end and the surface $z_c(t)$ used to model surface topography. B) the estimation error of cantilever position $z_{error}(t)$ for a given topography.

The cantilever position spectral density obtained from simulated data is shown in figure 4.7 A), blue curve, and the spectral density of the estimated cantilever position is depicted on the same graph, red curve. These results have been simulated for a distance $z_c(t) = 90$ nm resulting in a relatively strong interaction and significant estimation error. The influence of higher harmonics induced by surface interaction is visible in the spectra of measured cantilever position. The spectra of the estimated cantilever position is completely missing these features for the chosen observer gain. These frequencies become apparent only if the gain is relatively high and as a consequence, a noise rejection becomes insufficient. Figure 4.7 B) shows the spectral density of tip-surface interaction force (green curve) and estimated interaction force (red curve). The observer is capable to sense displacement of the higher harmonics of the interaction force, but it is not able to estimate their full magnitude. This behavior is coming from the fact that the observer uses as input information the cantilever position, and in this signal the higher harmonics are attenuated by the cantilever transfer function. Then the observer with relatively low gain is not able to correctly follow this displacement.

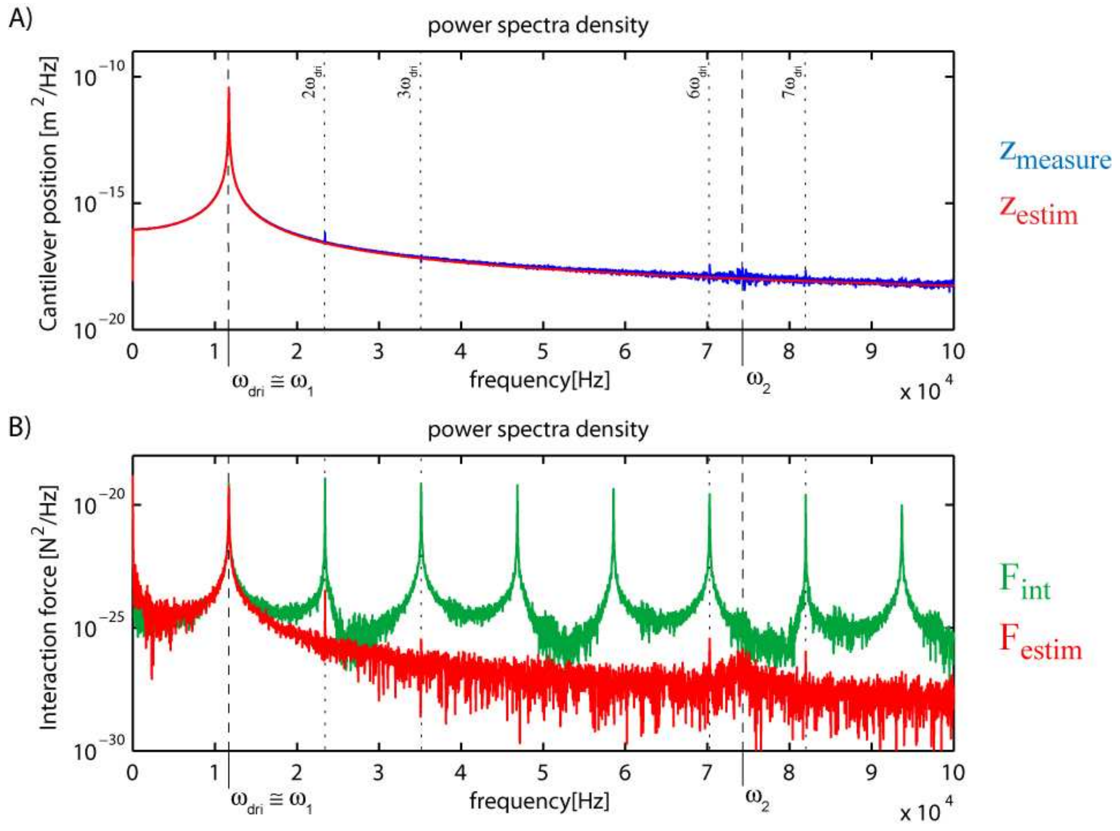

Figure 4.7: A) simulated cantilever position $z_{measure}$ power spectral density (blue curve) and estimated cantilever position z_{estim} spectra (red curve). B) interaction force F_{int} power spectral density obtained from the model (green curve) and estimated interaction force F_{estim} spectra (red curve).

Now the time sequences of the simulated and of the estimated interaction force according to the changing topography can be compared. Figure 4.8 A) shows topography modeled as chip sample separation distance $z_c(t)$. Figure 4.8 B) shows time sequence of the tip-sample interaction force $F_{int}(t)$, green curve, and the estimated interaction force $F_{estim}(t)$, red curve. In this graph, only the envelopes of both signals are visible. Figure 4.8 C) shows small section of the graph B) zoomed in. Here, the significant difference of the estimated and simulated interaction force is easily visible. The simulated force does not have any positive values and is highly non-linear. On the other hand, the estimated interaction force has sinusoidal shape, and only its mean value is shifted to negative values, and it has alternating sign of the interaction force.

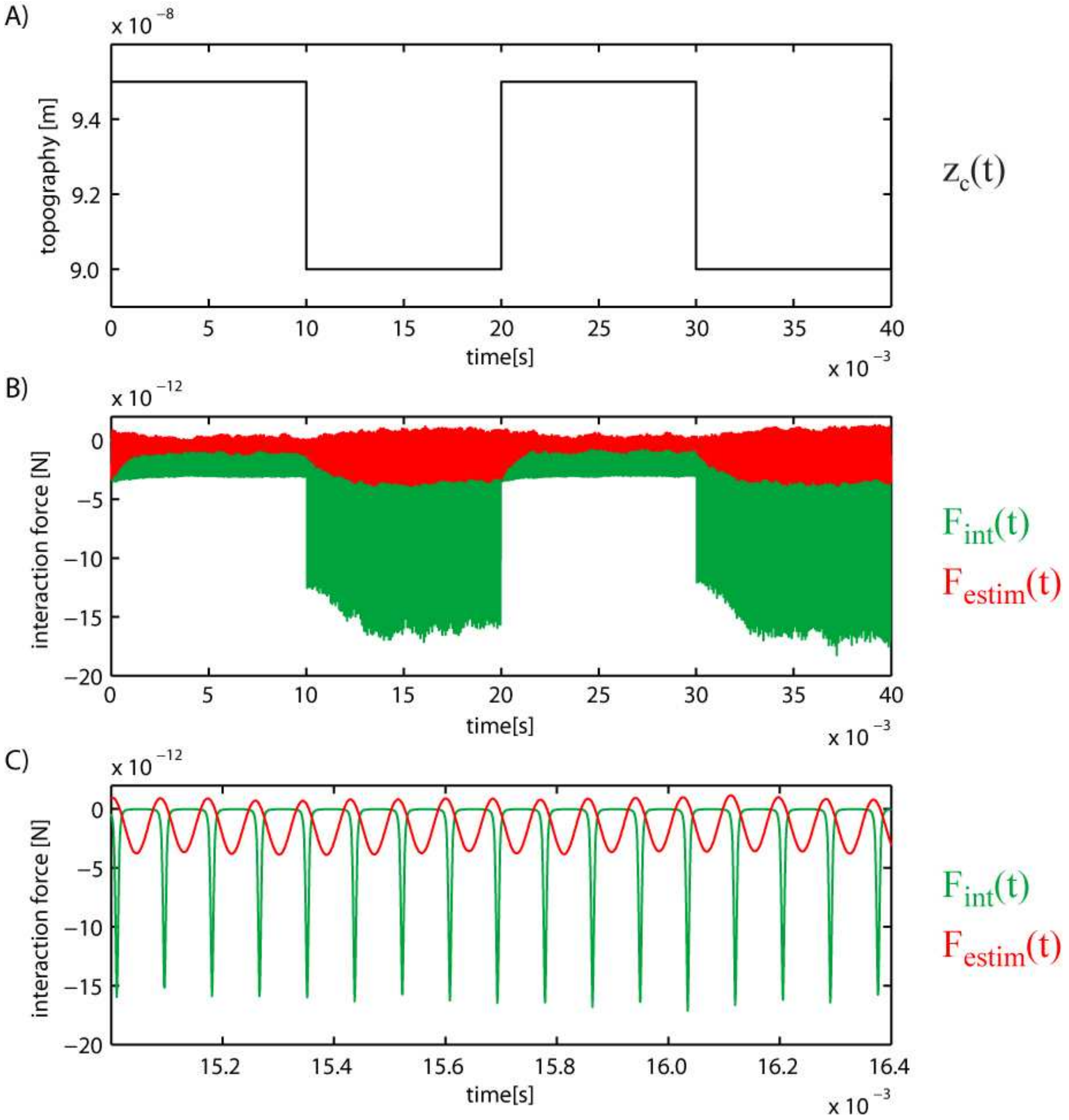

Figure 4.8: A)separation distance between cantilever fixed end and surface $z_c(t)$. B) time sequences of the interaction force obtained from the model $F_{int}(t)$ - green curve and estimated interaction force $F_{estim}(t)$ - red curve. C) displays zoom of interaction forces shown in B).

The relationship between the interaction force obtained from the model and the estimated interaction force is visible in figure 4.8 B). Topography changes are modifying the interaction intensity which is in certain form mirrored by the observer. Surface interaction is a highly non linear force affecting the harmonic oscillator. The resulting vibration amplitude modifications are only related to the root mean square (rms) value of the surface interaction, in other words, to the surface interaction energy modulating harmonic oscillator. To quantitatively evaluate the obtained results, it is necessary to calculate the rms values of both signals and compared them. A low pass filter has been used to obtain an approximation of the rms values of both interaction forces for time evoluting signal. The cut-off frequency of this filter has been set to 6 kHz, which is right below the cantilever's first harmonic mode (7.5 kHz), and significantly higher than the topography bandwidth. The obtained curves are shown in figure 4.9 A) modeled interaction force $F_{int}(t)$ - green curve, and estimated force $F_{estim}(t)$ - red curve. Figure 4.9 B) displays the rms interaction force estimation error. This graph shows that the observer is able to estimate *the effective* *interaction forces* as small as a half pico newton.

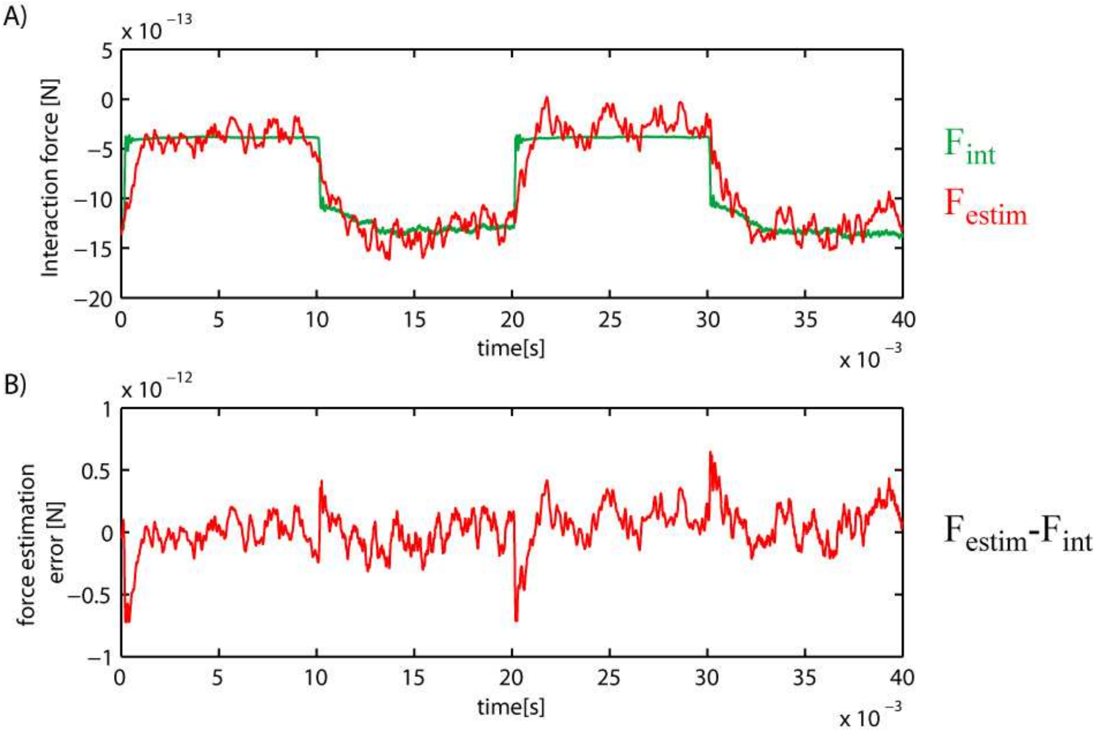

Figure 4.9: A) rms value of modeled tip-surface interaction force $rms(F_{int}(t))$ - green curve and estimated interaction force $rms(F_{estim}(t))$ - red curve. B) tip-surface interaction force estimation error.

The proposed technique makes possible to directly estimate the effective value of the interaction force in standard amplitude modulation technique. For the amplitude modulation technique, any analytical relation between vibration amplitude and interaction force does not exist. The observer is able to numerically estimate this force and obtain its rms approximation. There is no need to precisely know the relation between the amplitude and the interaction force any more.

4.4 Static deflection observer

An other possible application of the extended state observer for surface interaction force detection can be static non-contact force measurement. The first publications dedicated to static non-contact measurements have been published by *Gannepalli* and his colleagues [51, 52, 53]. These publications propose the position measurement of the thermally excited cantilever at its free resonance frequency, and a detection of frequency shift induced by the surface interaction. The obtained frequency shift is then fed into the vertical scanning control loop to control tip-surface separation distance constant. The authors have shown the ability to maintain tip-sample separation distance constant for long periods of time without snapping to the contact.

The succesfull observer application to position detection of a microsystem has been presented by *G. Besancon* and his colleagues [141]. The publication demonstrates the possibility to eliminate thermal perturbations and the detection "back action" of a micro electromechanic system at room temperature.

Here presented work concentrates on direct tip-surface interaction force detection (estimation) from the measured cantilever position [143, 144]. The proposed technique uses a measurement bandwidth below the frequency of the first harmonic mode. The force is estimated from the position signal in low frequencies but it is necessary to detect cantilever position at higher frequencies. The observer is using the position information of multiple harmonic modes to estimate the interaction force. Each harmonic mode is perturbed by independent source of thermal noise and these noises have a zero cross-correlation function. This permits the observer to eliminate the thermal perturbations more efficiently than a simple low pass filter. This technique is new AFM operation mode able to measure an interaction force at its original frequency bandwidth without frequency or amplitude modulation. It is essential to use cantilevers with very low spring constant and low quality factor to reach maximal sensitivity. This cantilever choice increases measurement sensitivity and minimizes settling time which limits measurement speed. In dynamic operation mode low quality factor brings difficulties to lever excitation and frequency shift detection. The simulation is performed with the same schema as was presented in observer application to standard dynamic operation mode, see figure 4.3. The only difference is that excitation signal $F_{dri}(t)$ is set to zero (no driving). The cantilever is only excited by thermal distortion and surface interaction force $F_{int}(t)$. Surface interaction force is estimated from the measured lever position containing measurement noise. Two different applications are presented: detection of an interaction force smaller than 1 pN and detection of a surface topography of one Angstrom with interaction force smaller than 20 pN.

4.4.1 Pico Newton detection

Free thermally excited cantilever is brought into interaction with a modeled surface. The separation distance $z_c(t)$ between the cantilever fixed end and the surface is set to 20 nm. The topography is modeled by random ±4 nm steps with frequency 30 Hz and its bandwidth is limited to 1 kHz. The obtained topography model has similar properties as a real experimental topography. The interaction force bandwidth is dependent on the scan speed, on the size and on the sample rugosity and in usual applications does not exceeds 1 kHz. This as well eliminates transient behavior of the cantilever and its harmonic modes. White noise with variance $\langle \nu^2_{measure}(t) \rangle = 9 \cdot 10^{-20}$ m was added to the simulated cantilever position $z(t)$ as measurement noise. The chosen noise variation is higher than noise levels obtained with Nanotec experimental setup. The obtained cantilever position $z_{measure}(t)$ is provided as an input to extended state observer. All presented simulations were done with measurement noise, but from some figures this noise has been removed to better demonstrate the intensity of the thermal distortion.

The same extended state observer as in dynamic operation mode has been used. In this static case the driving signal input of the observer is set to zero. The observer gain θ was chosen according to the fact that the entire system is operated in static mode and surface interaction of interest is in low frequencies. The gain has been set to 3.3 to maximally profit from the static detection and improved signal to noise ratio.

Figure 4.10 A) shows a cantilever position time sequence while its tip is in interaction with modeled surface. The shown graph is without any measurement noise to demonstrate how intense distortion is induced by thermal agitation during the measurement. The cantilever is slightly deflected towards the sample but this displacement is completely masked by thermal distortion. Figure 4.10 B) shows the estimated cantilever position $z_{estim}(t)$ with visible steps of about 1 pm corresponding to topographical changes.

Figure 4.10 C) shows the estimation error (measurement noise has been removed). The main interest of observer application is to eliminate thermal distortion which limits the force sensitivity. For this reason, a presented estimation error is calculated from the cantilever position without measurement noise and estimated cantilever position. This is possible only in the simulation and it gives opportunity to better evaluate observer capabilities. Nevertheless, the measured cantilever position $z_{measure}(t)$ provided as an input to the observer includes measurement noise specified earlier. Figure 4.10 D) shows power spectral density of the estimation error. The measurement noise would represent in this spectra only a flat floor of minimal detectable cantilever displacement. From this graph, it is visible that the observer very efficiently rejects thermally induced mechanical vibrations of cantilever's harmonic modes.

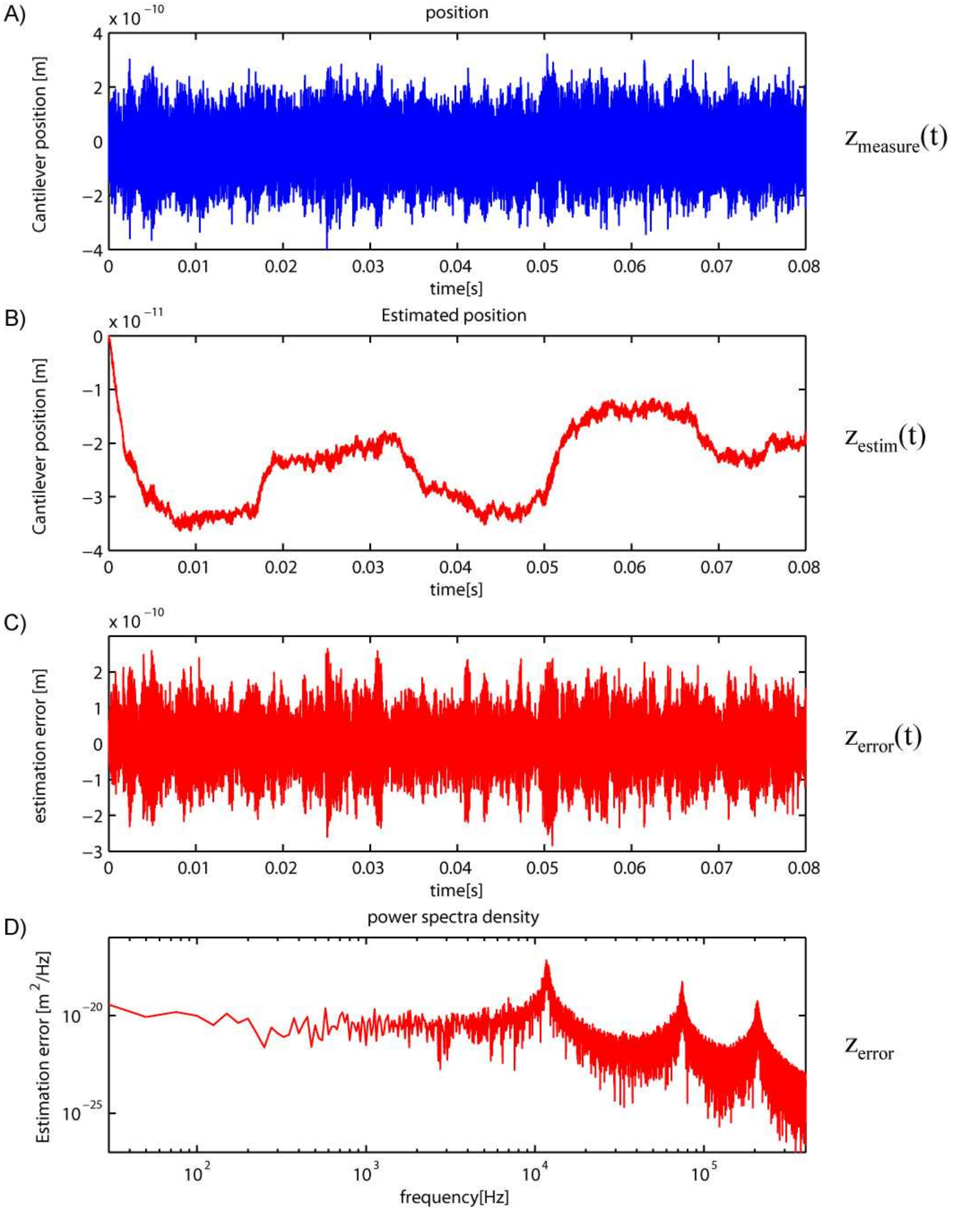

Figure 4.10: Pico newton force estimation, A) cantilever position time sequence (measurement noise removed). B) estimated cantilever position $z_{estim}(t)$. C) position estimation error $z_{estim}(t) - z(t)$. D) power spectra density of estimation error.

In figure 4.11 A) the modeled surface topography $z_c(t)$ is shown. Figure 4.11 B) shows the model interaction force $F_{int}(t)$ - green curve and the estimated interaction force $F_{estim}(t)$ - red curve, corresponding to the variable topography. The force $F_{int}(t)$ is not directly accessible value in real experiment but with our model this signal can be extracted and directly compared with the estimated value. A small variation of interaction force $F_{int}(t)$ is visible, mainly caused by changing position of thermaly perturbed cantilever. The interaction force estimation error equals to $F_{estim}(t) - F_{int}(t)$ and is shown in figure 4.11 C). The reached interaction force accuracy with this observer is about a half pico

Newton. The observers convergence time is about $5ms$. System speed can be increased by increasing the observer gain, but in this simulation the main challenge was the detection of an interaction force with magnitude smaller than $1pN$.

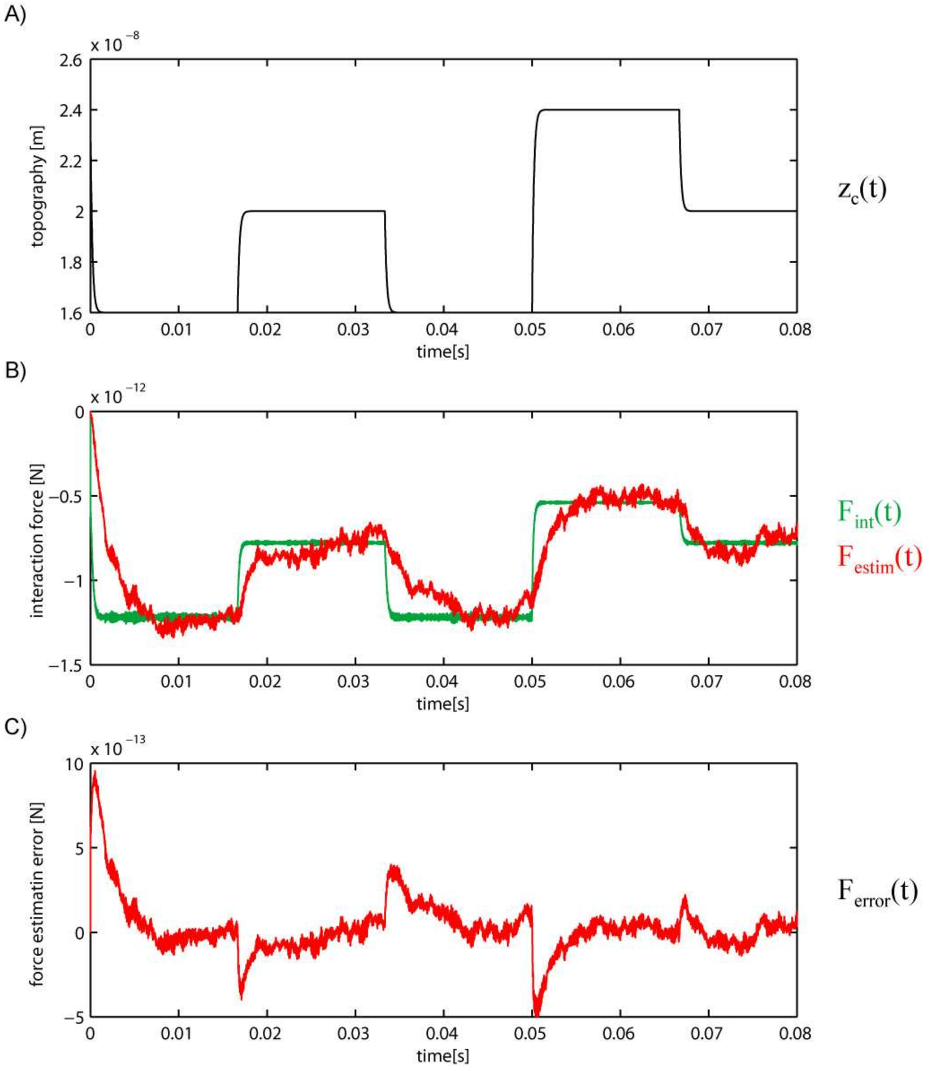

Figure 4.11: Pico newton force estimation. A) simulated topography $z_c(t)$. B) model interaction force $F_{int}(t)$ - green curve and estimated interaction force $F_{estim}(t)$ - red curve. C) interaction force estimation error $F_{estim}(t) - F_{int}(t)$.

Figure 4.12 A) shows the power spectral density of the simulated cantilever position $z_{measure}(t)$ - blue curve, and the estimated cantilever position $z_{estim}(t)$ - red curve. Both spectra include a measurement noise to display values directly comparable with the real experimental data. The modeled measurement noise has magnitude which makes it almost impossible to see third harmonic mode. The displayed spectra are identical in lower frequencies but in higher frequencies the observer attenuates cantilever displacement caused by the thermal excitation. Figure 4.12 B) shows power spectral density of the simulated interaction force $F_{int}(t)$ - green curve, and the estimated interaction force $F_{estim}(t)$ - red curve. The spectra of the estimated force is very close to the simulated force which is unknown value in an experiment. There is a slight discrepancy between the signals around cantilever harmonic modes. The observer is able to efficiently eliminate the thermal distortion of the cantilever position and at the same time relatively accurately follow the unknown interaction force.

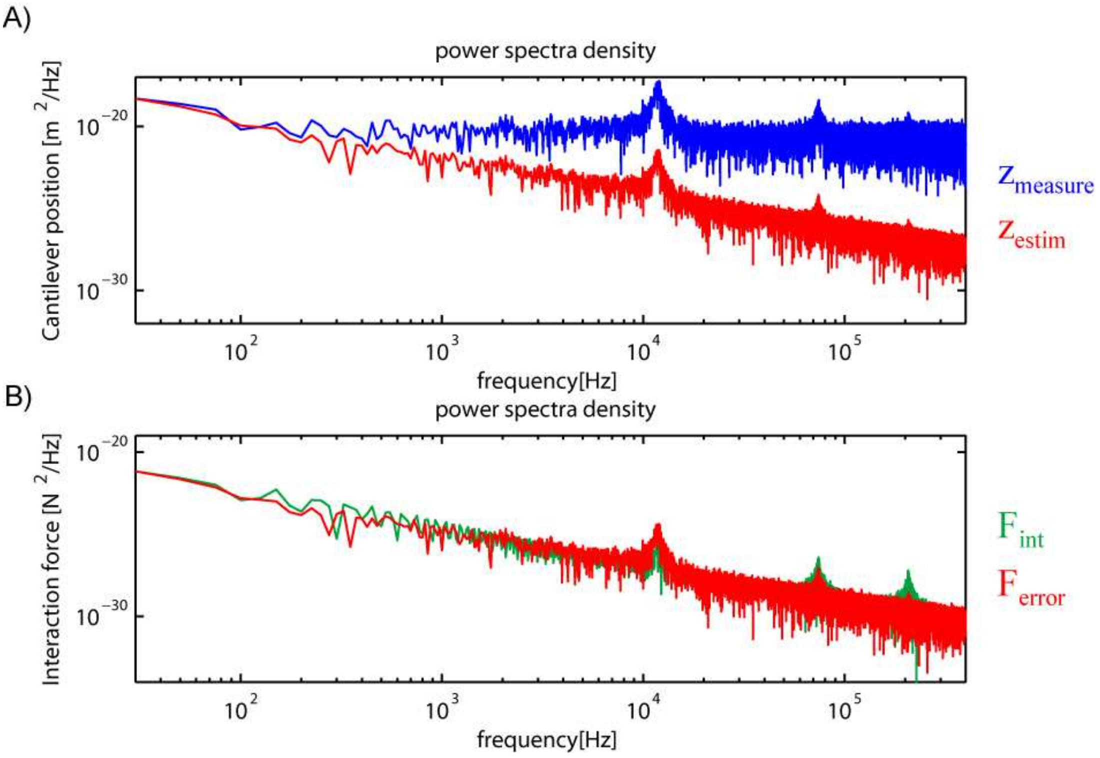

Figure 4.12: A) power spectral density of simulated cantilever position $z_{measure}(t)$ - blue curve and estimated cantilever position $z_{estim}(t)$ - red curve. B) power spectral density of simulated interaction force $F_{int}(t)$ - green curve and estimated interaction force $F_{estim}(t)$ - red curve.

4.4.2 Angstrom topography detection

This simulation follows the same general schema presented for pico newton detection. Free thermally excited cantilever is brought into interaction with the modeled surface. The separation distance between the cantilever fixed end and the surface is set to 4.9 nm which is significantly closer then in the case of pico newton detection. The topography $z_c(t)$ is modeled by random ±0.1 nm steps with frequency 30 Hz and bandwidth limited to 1 kHz. This eliminates the transient behavior of the cantilever which in such a proximity to the surface can cause snapping to it. The cantilever position $z_{measure}(t)$ including measurement noise with variance $\langle \nu^2_{measure}(t) \rangle = 9 \cdot 10^{-20}$ m is provided as an input to the extended state observer. The observer gain was chosen according to the fact that the entire system is operated in static mode and the surface interaction of interest is in low frequencies. The gain θ is set to 3.3 as in the previous section.

Figure 4.13 A) shows the cantilever position time sequence without any measurement noise to demonstrate thermal distortion of the cantilever during the measurement. The cantilever is visibly deflected towards the sample by 0.45 nm but topographical changes are completely masked by thermal distortion. Figure 4.13 B) shows the estimated cantilever position $z_{estim}(t)$, and figure 4.13 C) shows the estimation error without measurement noise. Nevertheless, the measured cantilever position $z_{measure}(t)$ provided as an input to the observer includes the measurement noise specified earlier. Figure 4.13 D) shows a power spectral density of the estimation error.

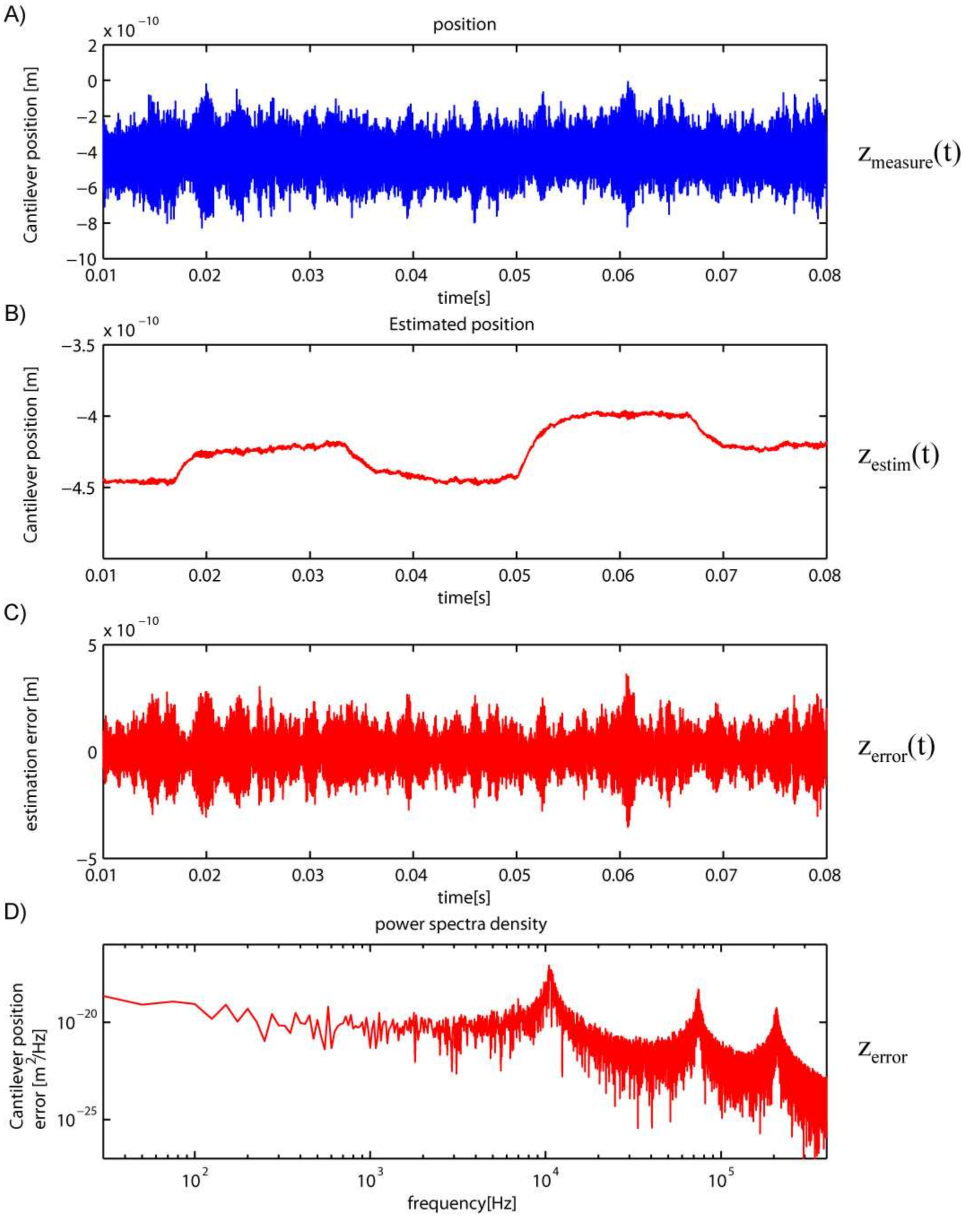

Figure 4.13: Angstrom topography detection, A) cantilever position time sequence without measurement noise. B) estimated cantilever position $z_{estim}(t)$. C) position estimation error $z_{estim}(t) - z(t)$. D) power spectral density of estimation error.

In figure 4.14 A) the modeled surface topography is shown. Figure 4.14 B) shows model interaction force $F_{int}(t)$ - green curve, and estimated interaction force $F_{estim}(t)$ - red curve, corresponding to the changing surface topography. The interaction force $F_{int}(t)$ has relatively large intensity variations in comparison with the previous simulation (see figure 4.11). A relatively small cantilever displacement caused by thermal excitation causes force variation that is comparable with the force variation caused by topography changes. This behavior is a result of the nonlinear dependance of the interaction force on the distance and is significant at very short distances, see figure 2.13. The observer successfully rejects these distortions and converges to the correct force value. This can be used to calculate direct surface topography, which variation is 0.1 nm in this simulation. The interaction force does not exceed 20 pN in this simulation which is a relatively low intensity to be able to measure so small surface topography. The interaction force estimation error $F_{estim}(t) - F_{int}(t)$ is shown in figure 4.14 C).

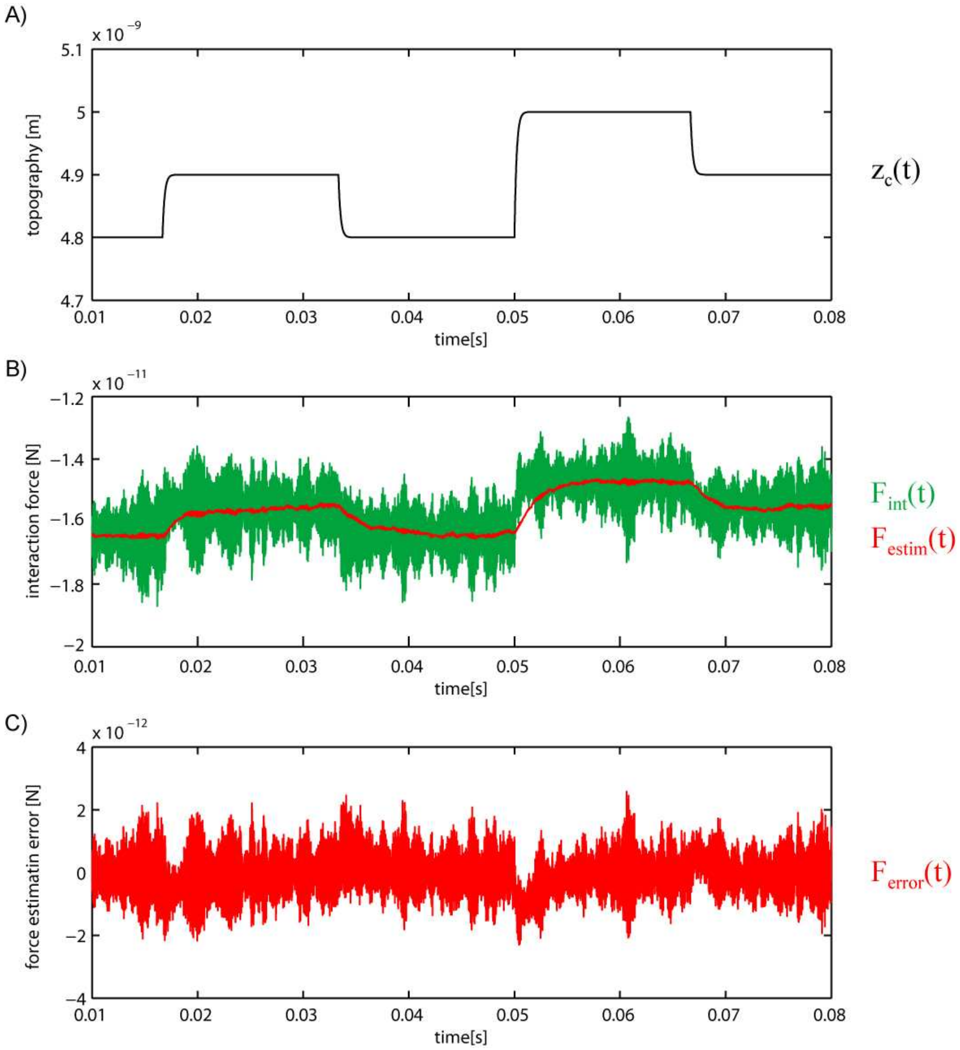

Figure 4.14: Force estimation during the angstrom topography detection simulation. A) simulated topography $z_c(t)$. B) model interaction force $F_{int}(t)$ - green curve, and estimated interaction force $F_{estim}(t)$ - red curve. C) interaction force estimation error $F_{estim}(t) - F_{int}(t)$.

Figure 4.15 A) shows the power spectral density of the simulated cantilever position $z_{measure}(t)$ - blue curve, and the estimated cantilever position $z_{estim}(t)$ - red curve. Both spectra include a measurement noise to display values directly comparable with the real experimental data. The modeled measurement noise has magnitude that makes it almost impossible to see third harmonic mode. The displayed spectra are identical in lower frequencies but in higher frequencies the observer attenuates a cantilever displacement caused by thermal excitation. Figure 4.15 B) shows the power spectral density of the simulated interaction force $F_{int}(t)$ - green curve, and the estimated interaction force $F_{estim}(t)$ - red curve. The spectra of estimated force is equal to simulated force at low frequencies where is the searched topography located. Therefore at higher frequencies the observer rejects thermally induced force variation and improves the force estimation accuracy. All the force variations caused by thermal agitation of the cantilever are attenuated in estimated force $F_{estim}(t)$. The modeled interaction force $F_{int}(t)$ has magnitude variation caused by the thermal agitation comparable with the force changes induced by the topography. The estimated force $F_{estim}(t)$ efficiently attenuates the effects of thermal agitation and preserve only the changes caused by the surface topography.

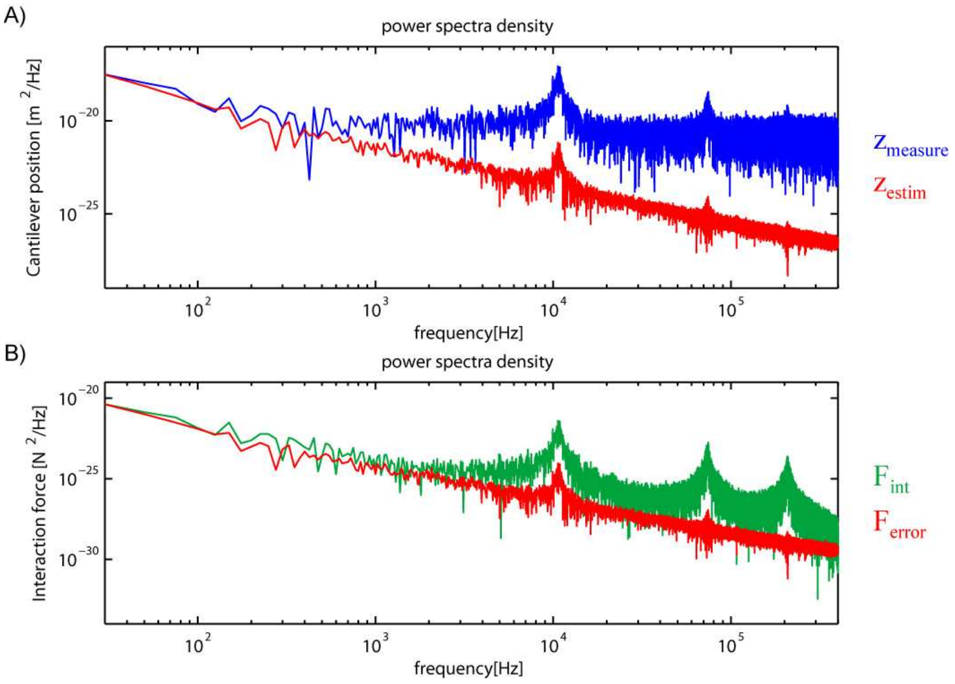

Figure 4.15: Angstrom topography detection. A) power spectra density of simulated cantilever position $z_{measure}(t)$ - blue curve, and estimated cantilever position $z_{estim}(t)$ - red curve. B) power spectra density of simulated interaction force $F_{int}(t)$ - green curve, and estimated interaction force $F_{estim}(t)$ - red curve.

Chapter 5

Cooling mode AFM

5.1 Damping/Cooling in AFM - introduction

Many publications have been presented on the subject of a damping of a macro, micro and nano objects. Wide range of possible applications of this fundamental technique enormously diversify the existing publications: from attenuation of the mechanical vibration in macro structures as buildings and bridges, the vibrations of a smaller mechanical and electromechanical structures as machines, motors and so on. A great interest has been given to the vibration treatment of the nano systems with increasing development of the nano technology. Many works on the subject of micro/nano structures mechanical vibration damping have been published in recent years. These vibrations are very often induced by thermal excitation due to the small size of these objects and authors use word “cooling" instead of “damping" to precisely describe obtained results. Here the same terminology will be used and the state of art will be based only on the publications focusing on the micro and nano systems. The publications can be divided into two parts according to the used actuation method to cool a given system:

Optical radiation pressure
The force used to stabilize the cantilever position is induced by a light source in the form of radiation pressure which is focused onto the cooled object. This technique can be further divided into two different operation versions:

- A passive damping based on changing cavity pressure due to actual position of damped object. Used light source has constant intensity and the damping system does not include active control loop. The cavity preasure is changing according to the changing distance between the objects craeting the optical cavity. To increase the efficiency of the damping, it is necessary to increase the power of the light source and without any further tuning the system effective temperature will decrease. This technique is often called *self-cooling* and has been published by many authors [145, 146, 147] for applications in atomic force microscopy.

- The second technique is actively changing the radiation pressure according to the cantilever displacement. A feedback loop detects cantilever position and actively modulate the laser intensity to minimize the cantilever displacement. This technique has been implemented to stabilize the position of the cavity mirrors [148, 149] and to control mechanical vibrations of the oscillators and levers [150, 151]. The ability to reach sub-kelvin effective temperature of the cantilever has been presented in [152]. The quantum limitation of the thermal agitation cooling has been presented in [153].

Electro-mechanical actuation
This approach is usually used with a feedback control loop which actively attenuates the

mechanical vibration of a given system. The application of this method varies from the one-electron oscillators [154], the gravitational wave detectors [155] to the nano-mechanical resonators. The nano oscillator cooling has been done with the magnetic actuation [156] but very often the electrostatic force is used for the ease of application. A doubly clamped beams with the electro-mechanic cooling have been presented in [157, 158, 159] and the author shown the performance of this technique.

The work resented is using an electro-mechanical actuator in the feedback loop to attenuate thermally induced vibrations of the cantilever. The choice of the actuator and the controller will be explained in the following text. Now will be introduced “Cold damping" theory which is the theoretical framework of the proposed operation mode of the Atomic Force Microscope.

5.2 Cold damping theory

The thermal noise and the fluctuation-dissipation theorem have been introduced in section 3.2. A theoretical description for the cold damping theory will be developed with the help of these results.

The power spectral density of the fluctuating force at the system input i, in the thermal equlibrium with the bath of temperature T is described by the Nyquist Theorem

$$S_{ii}(\omega) = 4k_B T\gamma m_{eff} = S_{F_L}(\omega) \tag{5.1}$$

where k_B is Boltzmann constant and γ is the system damping. Coupling of a system to the thermal bath is often described with the help of Langevin force F_L which is applied on the system input. $S_{F_L}(\omega)$ stands for the spectral density of this force. The cantilever position variance can be written

$$\left\langle z^2(t)\right\rangle = \frac{k_B T}{k} \tag{5.2}$$

Dynamic response of the lever single harmonic mode in complex plane to Langevin force is

$$\hat{z}_i(\omega) = \frac{\hat{F}_L}{m_{eff}(\omega_i^2 - \omega^2 + \mathbf{i}\gamma\omega)} = \hat{Z}_i(\omega)\cdot\hat{F}_L \tag{5.3}$$

$$\left|\hat{Z}_i(\omega)\right|^2 = \frac{1}{m_{eff}^2\cdot\left[(\omega_i^2-\omega^2)^2+\gamma^2\omega^2\right]} \tag{5.4}$$

Spectral density of the lever displacement induced by thermal excitation at the temperature T, can be written as

$$S_{z_i z_i}^T(\omega) = S_{ii}\cdot\left|\hat{Z}_i(\omega)\right|^2 = \frac{4k_B T\gamma}{m_{eff}}\frac{1}{(\omega_i^2-\omega^2)^2+\gamma^2\omega^2} \tag{5.5}$$

The cooling mechanism is using the measured lever position and through the feedback loop is applying onto the cantilever properly adjusted damping force $F_{damp}(\omega)$. Lets assume that the damping force is proportional to the actual speed of the lever motion as follow

$$\hat{F}_{damp}(\omega) = \mathbf{i}m_{eff}\gamma\omega g\cdot\hat{z}_i(\omega) \tag{5.6}$$

where g is the gain of the feedback loop. The resulting cantilever position equals:

$$\hat{z}_i(\omega) = \hat{Z}_i(\omega)\left(\hat{F}_L(\omega)+\hat{F}_{damp}(\omega)\right) \tag{5.7}$$

By substitution of equations 2.4, 2.5 and 5.6 into equation 5.7 the lever position has a form

$$\hat{z}_i(\omega) = \frac{\hat{F}_L(\omega)}{m_{eff}} \frac{1}{\omega_i^2 - \omega^2 - \mathbf{i}\gamma\omega(1+g)} = \hat{Z}_i(\omega, g) \cdot \hat{F}_L(\omega) \tag{5.8}$$

Then the spectral density of the cantilever position is

$$S^T_{z_i z_i}(\omega) = S_{ii} \cdot \left|\hat{Z}_i(\omega)\right|^2 = \frac{4k_B T\gamma}{m_{eff}} \frac{1}{(\omega_i^2 - \omega^2)^2 + \gamma^2\omega^2(1+g)^2} \tag{5.9}$$

This equation shows that the damping part of the cantilever motion equation contains the feedback loop gain. With increasing feedback gain, the damping coefficient of the oscillator is increasing and the random displacement is attenuated. It is important to notice that the resonance frequency is not affected (shifted) by applied damping force.

At the resonance frequency or in its close proximity $\omega \approx \omega_i$ the spectral density is directly related to the loop gain

$$S^T_{z_i z_i}(\omega_i) \approx \frac{4k_B T\gamma m_{eff} Q^2}{k^2(1+g)^2} \tag{5.10}$$

At very low frequencies and close proximity to zero $\omega \ll \omega_i (\approx 0)$, the spectral density independent on the loop gain and depends only on the spring constant of the cantilever

$$S^T_{z_i z_i}(\omega_i) \approx \frac{4k_B T\gamma m_{eff}}{k^2} \tag{5.11}$$

The effective damping γ_{damp} and the effective temperature T_{damp} of the damped oscillator can be now introduced by

$$\gamma_{damp} = (1+g) \cdot \gamma \qquad T_{damp} = \frac{T}{(1+g)} \tag{5.12}$$

The correctness of these definitions can be easily verified with the help of Langevin force exciting the harmonic oscillator

$$S_{F_L}(\omega) = 4k_B T_{damp}\gamma_{damp} m_{eff} = 4k_B \cdot \frac{T}{(1+g)} \cdot (1+g) \cdot \gamma m_{eff} = 4k_B T\gamma m_{eff} \tag{5.13}$$

This as well verifies that the system has always the same energy $k_B T/2$ and stays in the thermal equilibrium.

5.3 New AFM operation mode

All existing techniques used to operate atomic force microscope have been introduced in the first chapter. With some generalization we can say that there are only two techniques: the static contact operation mode, see figure 2.2 and the dynamic non-contact operation mode, see figure 2.3. It has been said that: the contact mode is harsh onto the surface and requires strong surface interaction, the non-contact is less invasive to the sample but requires to keep the cantilever vibrating. The interaction force is obtained from the frequency or the amplitude shift induced by the interaction. The first publications in direction to operate the microscope in the static non-contact mode have been published by Gannepalli and his colleagues [51, 52, 53]. The word “static" in these publications means rather as a “non artificially excited" cantilever operation mode. The interaction force is obtained from the frequency shift induced by the surface interaction on the thermally excited cantilever. The authors have shown the ability to maintain the tip-sample separation distance constant for a long periods of the time just by keeping the desired frequency shift constant. The snapping of the tip to the sample is prevented by displacing the sample bellow thermally excited cantilever. The name given to this technique is: thermally driven non-contact atomic force microscopy.

I would like to introduce a new operation mode which is non-contact and truly static. To achieve such a functionality, it is necessary to attenuate, as much as possible, the thermally induced cantilever displacement and detect the static interaction force induced onto the cantilever tip by the surface. Other important difficulty to be overcomed is the cantilever snapping to the sample which is critical for the measurement stability and a possibility to operate with any desired interaction force intensity.

The used controller cannot be acting only as in cold damping technique to eliminate the snapping phenomena. It has to control static position/deflection of the cantilever. Lets introduce a new stabilization force $F_{stab}(\omega)$ which is applied through the feedback loop onto the cantilevers free end. The stabilization force has a part for static force that is proportional to the cantilever actual position and a damping part proportional to the actual speed of the lever motion

$$\hat{F}_{stab}(\omega) = (m_{eff}s + \mathbf{i}m_{eff}\gamma\omega g) \cdot \hat{z}_i(\omega) \tag{5.14}$$

where s is the static gain of the feedback loop and g is the gain for the derivative part. Then the cantilever position is

$$\hat{z}_i(\omega) = \hat{Z}_i(\omega)\left(\hat{F}_L(\omega) + \hat{F}_{stab}(\omega)\right) \tag{5.15}$$

With the help of equations 2.4, 2.5 and 5.6, it can be shown that the lever position has a form

$$\hat{z}_i(\omega) = \frac{\hat{F}_L(\omega)}{m_{eff}} \frac{1}{\omega_i^2 - s - \omega^2 - \mathbf{i}\gamma\omega(1+g)} = \hat{Z}_i(\omega, g) \cdot \hat{F}_L(\omega) \tag{5.16}$$

The spectral density of the cantilever position then has a form

$$S^T_{z_i z_i}(\omega) = S_{ii} \cdot \left|\hat{Z}_i(\omega)\right|^2 = \frac{4k_B T\gamma}{m_{eff}} \frac{1}{(\omega_i^2 - s - \omega^2)^2 + \gamma^2\omega^2(1+g)^2} \tag{5.17}$$

The influence of the derivative gain g has been explained earlier. Newly introduced static force is shifting the resonance frequency of the cantilever to lower frequencies and modifying dynamic properties of the system.

At the resonance frequency or in its close proximity, $\omega \approx \omega_i$, the spectral density related to both loop gains is

$$S^T_{z_i z_i}(\omega_i) \approx \frac{4k_B T\gamma m_{eff} Q^2}{k^2(1+g)^2 - s m_{eff} Q^2} \tag{5.18}$$

Lets take a look on the spectral density of the cantilever motion in low frequencies where $\omega \ll \omega_i (\approx 0)$. The spectral density is dependent only on the static loop gain s and the spring constant of the cantilever

$$S^T_{z_i z_i}(\omega) \approx \frac{4k_B T\gamma m_{eff}}{(k - s m_{eff})^2} \tag{5.19}$$

Cooling mode operation description

Figure 5.1 shows a simple drawing of the cooling mode operation and figure 5.2 shows the regulation scheme describing proposed operation mode. For easier understanding the scheme can be divided into two lops: the cantilever stabilizing loop (marked red) and the set-point loop (marked green). Both loops will be introduced separately and the complete function became apparent from their description.

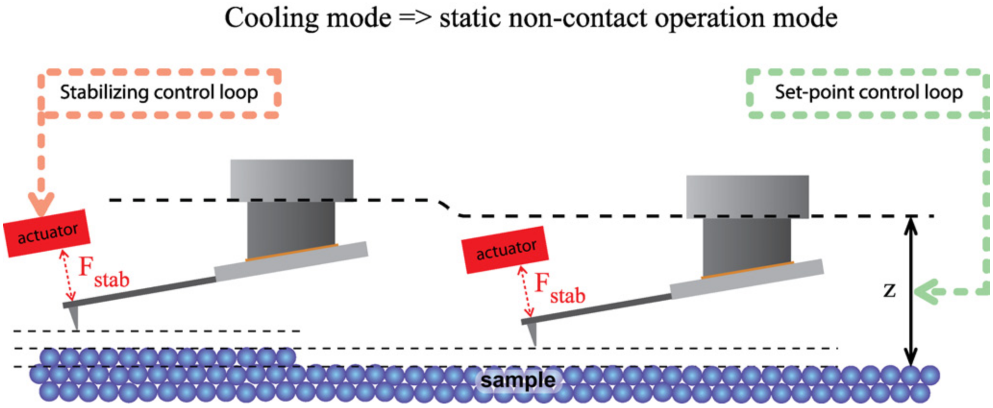

Figure 5.1: The cooling mode operation. Stabilizing control loop - marked red, Set-point control loop - marked green.

The stabilizing loop damps/attenuats Brownian motion of the cantilever and the static deflection induced by the surface interaction. A lever position is measured by the photodetector and fed into the stabilizing controller that generates a damping signal. This signal is amplified and applied onto the cantilever through the electrostatic actuator. Further on, the stabilizing controller output signal will be called the "stabilizing effort" to stress its force background. The stabilizing controller has to be high order discrete controller able to operate in a broad frequency bandwidth. These specifications are necessary to damp multiple harmonic modes of the cantilever. Theoretical description of this loop has been given above and the controller design will be explained in chapter 5.9.

The meaning of the measurement set-point has been explained for the standard operation techniques in section 2.1 and here has the same meaning. In the standard contact operation mode a set-point is equivalent to the static deflection of the lever and in the dynamic operation mode equals to the frequency or the amplitude shift. By choosing the set-point value (desired value of the set-point controller) the required tip-surface interaction intensity can be selected. The set-point controller drives a piezo-electric scanner displacing the sample below the tip, so that the interaction intensity remains constant while scanning. The set-point in the cooling mode "stabilizing effort" needed to keep the lever in undeflected position which can be, with the knowledge of the actuator constant, directly converted into the measured force. Thus the surface interaction is measured in its original frequency bandwidth as in the standard contact (static) operation mode, but the tip does not touch the studied specimen. In the standard non-contact (dynamic) operation mode, the surface force modulates the properties of the harmonic oscillator (lever) and this detuning is then detected.

The functionality of the selective low-pass filter used in the set-point control loop has a complex relationship to the measured force and will be explained later. For now, it would be sufficient to assume that the cut-off frequency is chosen just bellow the resonance peak of the first harmonic mode. So we take into account only the low frequency (static) interaction force and all damping signal at the high frequencies is filtered out.

Figure 5.2 depicts optional frequency analyzer, which possible applications will be explained later in section 5.5.

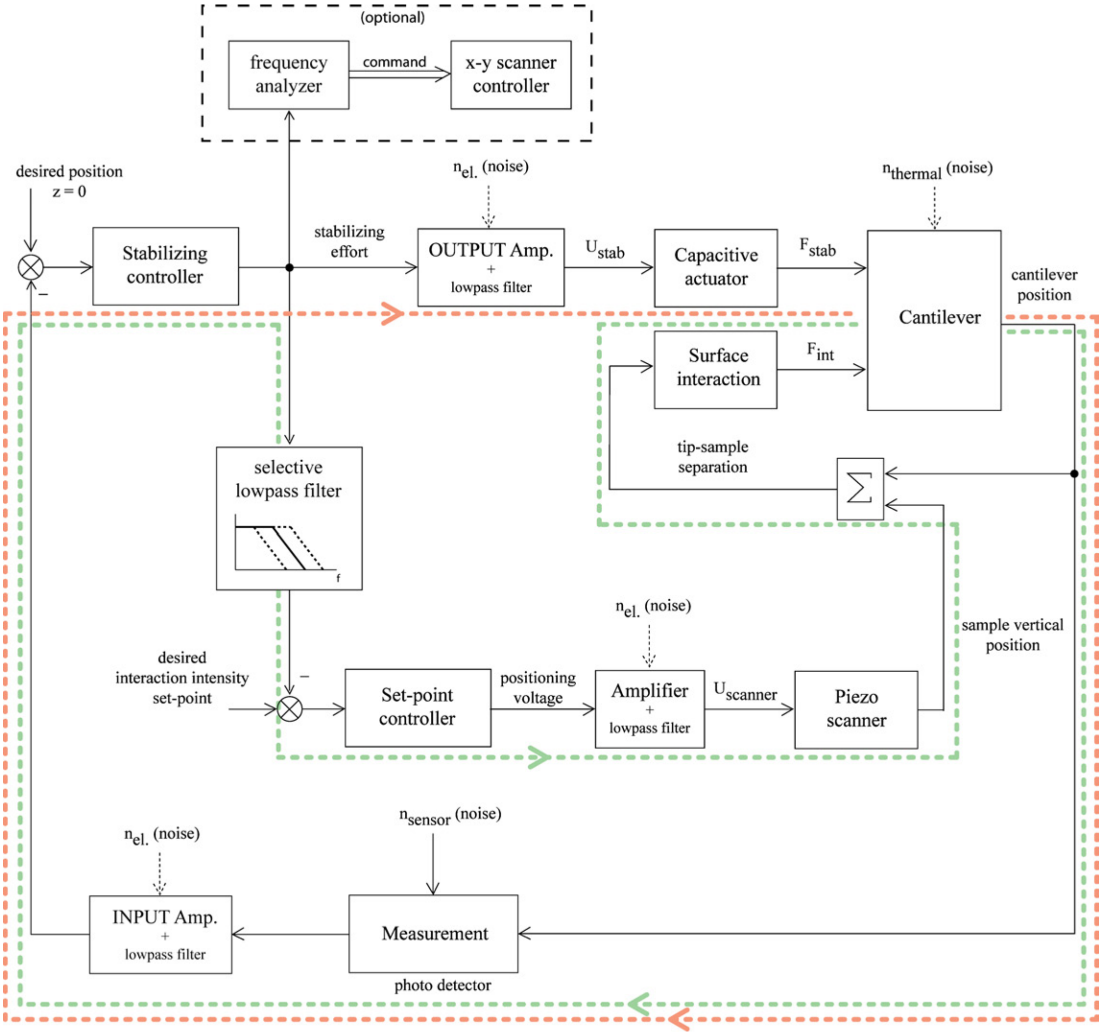

Figure 5.2: The cooling mode operation schema with control loops. Stabilizing control loop - marked red, Set-point control loop - marked green.

The function of the new operation mode for atomic force microscope can be summarized:
The stabilizing controller simultaneously attenuates any cantilever displacement without distinguishing the difference between the thermal distortion and the tip-surface interaction in a broad frequency range. The set-point controller uses the low frequency part of the stabilizing effort (below first resonance), compares it with the desired interaction intensity and displaces the sample in a vertical direction to reach the desired value. Let us call this new mode: “**cooling mode**". A 3D computer image of the mechanical realization of the cooling mode with simplified control loops equivalent to presented scheme are shown in figures 5.7 and 5.9.

Remark: The amplifiers used in the cooling mode schema include a low pass filters which only eliminate high frequency noise and don’t have any direct significance for the control loops functionality. The filters are inserted in this schema to be coherent with the real experimental setup where the filters eliminate a parasite high frequency electric noise induced by used electronics, digital to analog converters and discrete controller, for details see section 5.8.1.

5.4 Comparison with existing modes

Further enlisted advantages are rather a comparison to the existing operation modes and more advantages can be probably found when this mode will be used in different applications and measurements. They are based on theoretical expectations and deeper experimental verification has to be performed.

Lower effective temperature - The fundamental function of the stabilizing controller is to damp cantilever displacement caused by the thermal agitation. This damping can be as well presented as decreasing the effective quality factor of the system. This damping attenuates the amplitude of the thermally induced cantilever displacement. For comparison, in the dynamic operation self-excitation mode the thermal distortion is sensed by the position detector and through the feedback system is re-injected as a driving signal. If the quality factor decreases to lower thermal vibrations, the gain of the feedback loop increases to be able to maintain the vibration amplitude constant, and the signal to noise ration stays unchanged. Moreover, in the cooling mode, the attenuation of the cantilever vibrations decreases the surface interaction noise caused by random cantilever displacement in close proximity to the surface.

Direct force measurement - The interaction force and the thermal excitation are simultaneously counterbalanced by the feedback loop. With the knowledge of the actuator gain (conversion: tension to force) the controller output voltage (stabilizing effort) can be directly converted to the searched force. If the regulation error has been kept in certain limits during the measurement, then the stabilizing force is equal to the tip-surface interaction force with the accuracy given by regulation error.

The interaction force is measured in its **original spectra range** and is not modulating harmonic vibration of the cantilever as it is done in the standard non-contact operation mode. The spectra of the measured interaction force is a function of the studied sample rugosity and the scanning speed. The sample topography is unknown value but the scanning speed can be selected by user, so that the interaction force bandwidth stays in a certain frequency range.

The measurement is performed in **well defined tip-surface separation distance**. The standard non-contact operation mode integrates the tip-surface interaction force over the entire trajectory of the cantilever harmonic motion. The detected force is then an effective force (averaged force) for the entire motion range. More precisely, the frequency or the amplitude modulation modes detect the interaction force gradient and not the force intensity directly. This behavior is very complex, due to highly non-linear shape of the interaction force. Some details about this complex relationship have been presented in section 3.7.3. The cooling mode is maintaining the tip steady and the interaction is measured from one separation distance during the entire measurement. This significant difference is graphically explained in figure 5.3. In the figure the vibration amplitude of the standard dynamic mode is relatively small ($\approx 5nm$) while in usual application is much larger.

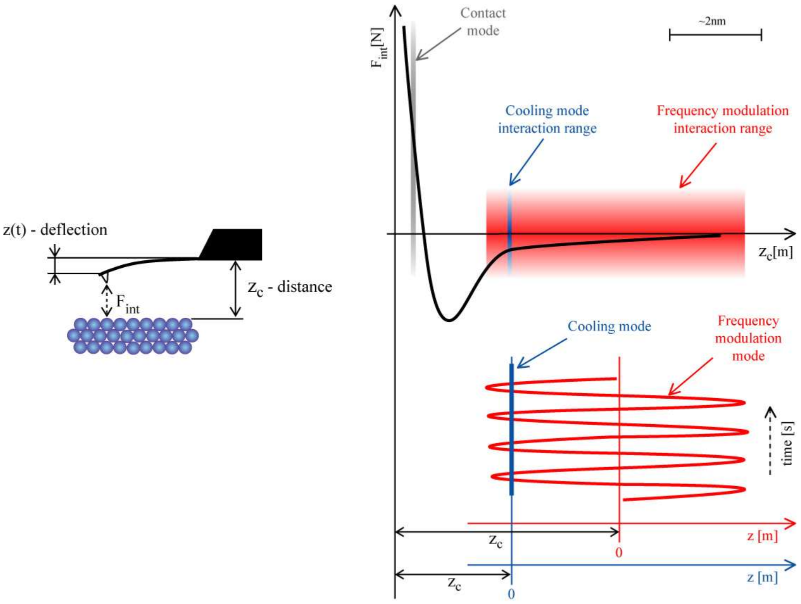

Figure 5.3: Comparison of the dynamic operation mode and proposed cooling mode. red - the tip position in the non-contact (dynamic) operation mode, gray - contact (static) operation mode, blue - cooling mode

Experiment stability - the approach-retract curve has been introduced in chapter 2.2. This non-linear behavior is completely eliminated due to the elimination of any cantilever displacement. If the approach-retract curve with the cooling mode is performed, the cantilever position remains zero, and only the required stabilizing effort changes with decreasing separation distance. The feedback loop is changing the effective spring constant of the cantilever, and by selecting the static gain high enough, the lever can be completelly prevented to snap onto the sample during the approach.
Figure 5.4 shows the approach-retract curves: standard one on the left, and other with the cooling mode on the right. While in the standard mode the interaction force is counterbalacedalanced with a restoring force of the cantilever spring, in the cooling mode is contra-balanced by the stabilizing force from the actuator. In the curve of the standard mode, are two significant points: “snap on" - where the gradient of the interaction force is larger than the gradient of the restoring force, and the lever snap onto the sample; “snap off" - where the spring restoring force is large enough to overcome the capillarity forces induced by the surface water. The cooling mode has two significant points as well: biggest interaction force gradient - this moment is the most critical for the controller to stabilize the lever position. Here the smallest displacement induces a large changes in the interaction force which can lead to instability and snapping to the sample. Second important point is when the tip reaches the thin film of water that is always present at the surface. At this moment, the capillarity force starts to pull the lever towards the surface and the stabilizing force has to suddenly increase its magnitude to contra-balanced this force. This behavior disappears if the cantilever and sample are immersed in a liquid medium, and the approach-retract curve won’t have any hysteresis.

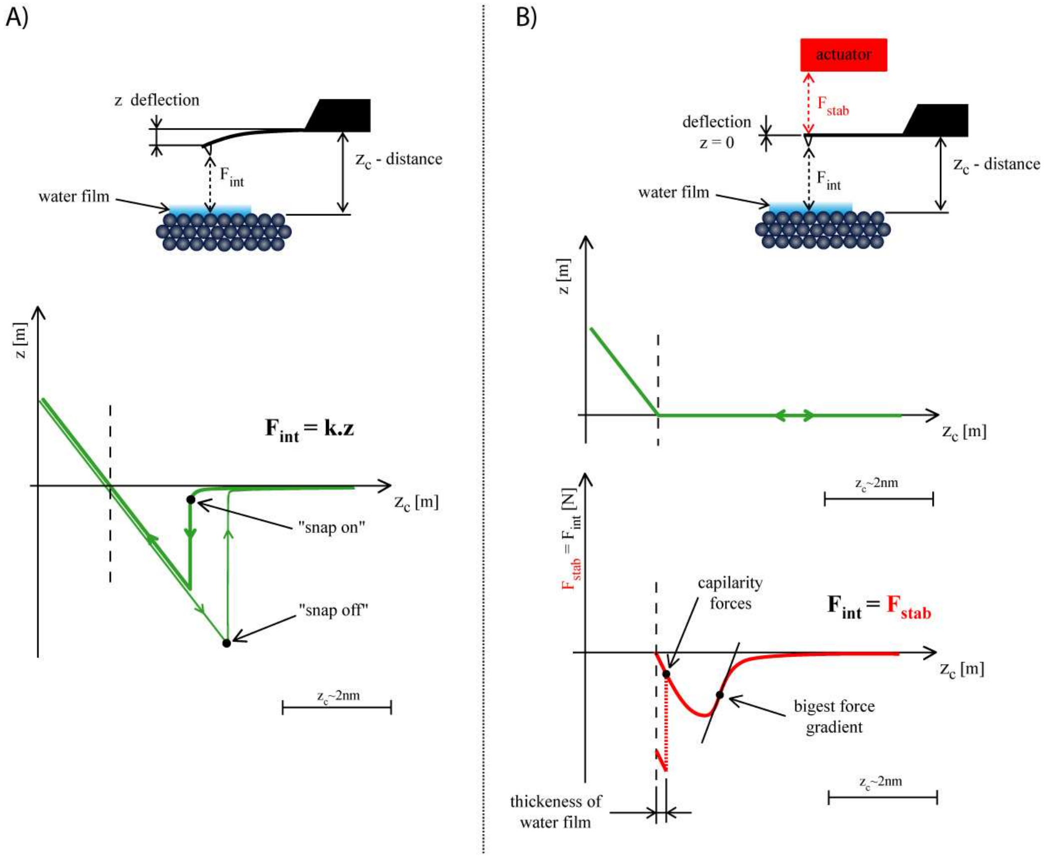

Figure 5.4: Approach-retract curve A) standard behavior with snapping to the sample B) the cooling mode approach curve without snapping to the sample.

The cooling mode is able to operate at **any desired level of the interaction force** intensity if the stability requirements are met. The surface interaction force can be attractive (Van der Waals) or a combination of attractive and repulsive forces. The force intensity depends only on the users choice.

An important property of the proposed system is **a broader operation bandwidth**. The time response to a sudden change of the interaction force is much faster than in the dynamic operation mode due to the active damping of the cantilever and a static operation. The dynamic mode settling time is a function of the quality factor and the resonance frequency. The quality factor of the cantilever is lowered by the feedback loop and the measurement off the resonance frequency is performed. The system can be operated at higher speeds of the lateral scanning without a lost of topographical information. More details about the measurement bandwidth will be given in section 5.5.

The last property to be mentioned here is the capability to **operate in a liquid media**. The standard non-contact operation mode requires to keep the cantilever vibrating at its resonance frequency. The excitation of the cantilever becomes a great difficulty if the lever is immersed into a liquid. The resonance frequency is shifted to the lower fequencies, and the quality factor significantly decreases due to viscosity of the liquid. The driver has to use a larger amplitude to maintain the cantilever vibration constant. The harmonically moving driver and the cantilever are inducing vibrations into the liquid media which interfere with the surface interaction force, and lower the force resolution. Some techniques, how to improve the cantilever driving and detection at the new resonance frequency, has been proposed in [50]. The cooling mode does not induce a vibration into the surrounding media, due to its steady operation, and required stabilizing force is approximately the same like in the air operation. The viscosity of the surrounding media even improves the damping ability of the feedback loop and helps attenuate the Brownian motion. The interaction force is measured in relatively low frequency bandwidth where the influence of the liquid viscosity is less significant, which leads to a better force sensitivity.

5.5 Measurement bandwidth

In the introduction to Cooling mode, the measurement bandwidth has been very shortly mentioned. The Cooling mode operates the cantilever in completely static manner which increases the measurement bandwidth in a comparison to the dynamic operation mode. Before getting any further, it is important to distinguish between the measurement bandwidth and the interaction force bandwidth which is directly related to the topography. The *measurement bandwidth* depends on the experiment setup and usually is given by the dynamic response of the cantilever to the interaction force. The *interaction force bandwidth* depends on the rugosity of the sample and on the tip motion speed above it. The sample is the object of our study and its properties are unknown. In many cases the sample topography can be at least predicted. On the other hand, the scanning speed is fully in the user control and can be set to any desired values.

There exists a great interest to perform the topography measurements on a maximal possible speed to minimize the influence of the thermal drifts. In the biology there is an additional motivation: to be able to observe a real-time evolution of a living biological sample (cell, bacteria, ...). The Cooling mode can be operated in two different regimes: a high accuracy measurement, and a large bandwidth measurement. The operation regime is defined by the scanning speed chosen by the user. The frequency analyzer shown in figure 5.2 detects the bandwidth where the interaction force is present and sets the lateral scanning speed to keep the interaction force bandwidth in limits chosen by the user. The selective low pass filter, which is inserted in the set-point control loop (figure 5.2), reduces the response bandwidth of this loop to the frequency that is directly related to the desired interaction bandwidth. Thus, the disturbances caused by the thermal excitation of the cantilever higher harmonic modes and a high frequency electronic noise can be isolated.

5.5.1 Force accuracy measurement

The lateral scanning speed is set so that the interaction bandwidth stays below the cantilever first resonance peak. This can be done manually or with the help of the spectra analyzer which detects the interaction force bandwidth from the stabilizing effort. The selective filter in the set-point loop is set to transfer only a low frequency band to the set-point controller.

Figure 5.5 A) shows a frequency spectra of three main parts that contribute to the detected cantilever position signal in the open loop. The thermally excited cantilever displacement is the red curve, blue curve is an electrical and a detection noise, and green curve is the interaction force applied to the cantilever. These parts of the signal are not visible separately but as a sum measured by the photo-detector and fed to the stabilizing controller input. For the open loop this signal is shown in figure 5.5 B). Here used photo-detector signal representation is only approximative and a real spectra could vary according to the experimental setup. If the control loop is closed and the stabilizing controller is well tuned, then the cantilever displacement caused by the thermal excitation and the interaction force will be attenuated as is shown in figure 5.5 C). The spectra is not equal to zero because a complete attenuation of the cantilever displacement is not possible in a real experiment due to the re-injected measurement noise. The frequency spectra of the electrical signal at the stabilizing controller output is shown in figure 5.5 D). The stabilizing controller is able to actuate at the cantilever modes resonances more efficiently due to the modes quality factors. The effort needed to attenuate any displacement is Q times smaller than to attenuate the same displacement magnitude off the resonance. The resulting controller output signal accurately corresponds to the interaction forces applied to the cantilever tip and the influence of thermal distortion at resonance is well suppressed.

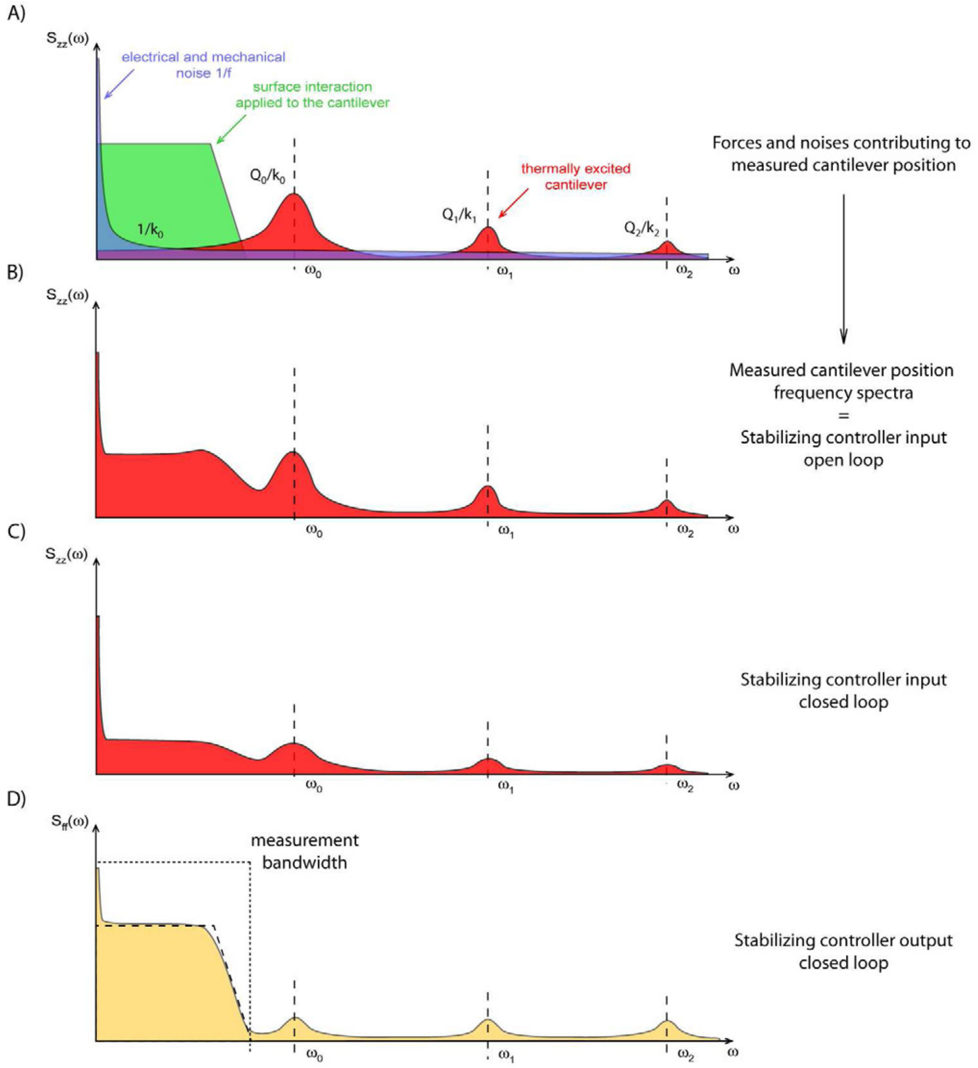

Figure 5.5: Frequency spectra of the cooling mode in force accuracy measurement regime.

5.5.2 Large bandwidth measurement

Some users need to measure the surface topography as fast as possible to obtain a real time data of the surface evolution. This need is met with the second operation regime. The lateral scanning is set very fast which results in the interaction force bandwidth covers even multiple harmonic modes of the cantilever. The functionality of the cooling mode is the same as in the force accuracy measurement. Figure 5.6 A) shows all parts contributing to the measured cantilever position, B) shows the frequency spectra of the measured cantilever position in an open loop and figure 5.6 C) in a closed loop. A significant difference is visible in the frequency spectra of the stabilizing controller output 5.6 D). The interaction force has a broad bandwidth and directly interacts with the cantilever at its resonance. The first harmonic mode is now present in the measurement bandwidth and the thermally induced distortion is added to the interaction force and sensed together by the set-point control loop, compared to the force accuracy measurement.

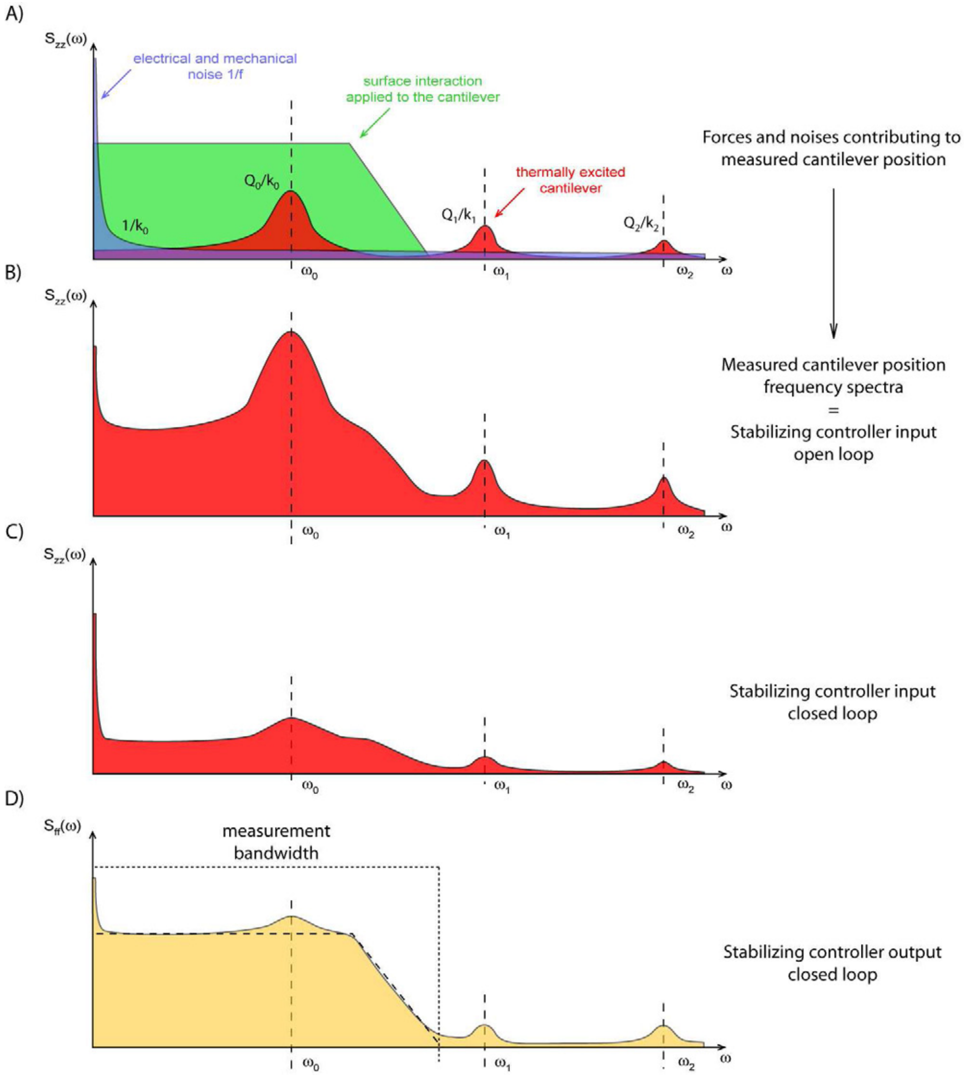

Figure 5.6: Frequency spectra of the cooling mode in large bandwidth measurement regime.

The measurement bandwidth is not limited by the cantilever settling time but rather by the stability of the control loop attenuating the cantilever displacement. With the increasing scanning speed perturbations with a high frequencies are generated which require a fast stabilizing controller to attenuate them. This as well demands a controller with a large gain which leads to the difficulties with the robustness and the system stability. If the interaction force is relatively large, the cantilever is directly in the zone where, in free conditions, would snap to the sample. This zone puts a great requirements on the stabilizing loop to attenuate the cantilever motion and to maintain the system stability.

Remarks:

- The surface interaction force and the stabilizing electrostatic forces are both simultaneously applied to the cantilever. Both of them are interacting with the same dynamic system but with opposite orientation of the force. As a consequence, the dynamics properties of the cantilever are not significantly contributing to the measurement. The cantilever dynamics properties are mainly visible through the residual cantilever displacement caused

by the thermal agitation which has not been completely attenuated, see section 5.6.
- The stabilizing controller is lowering the effective quality factor of the cantilever. This results in spreading the cantilever displacement caused by thermal excitation into a broader frequency range and its smaller amplitude around resonance frequencies. This can be interpreted as follows: the system has a new effective temperature (apparent temperature) that is decreasing the amplitude of thermally induced cantilever displacement at its resonance.

5.6 Force sensitivity

The thermal agitation is the biggest source of the distortion in Atomic Force Microscopy and its amplitude is significantly higher than the amplitude of the measurement noise. The measurement noise is assumed to be zero (spectral density of measurement noise $S_{z_{meas}z_{meas}}(\omega) = 0$) to simplify following calculations and the thermal excitation will be the unique source of system's distortion. Despite the measurement noise is always present in a real experiment, it is not the main force sensitivity limitation and can be lowered with a known techniques.
The thermal distortion will be represented by Langevin force with a spectral density $S_{F_L F_L}(\omega)$. This force is applied to the cantilever model simplified to the first harmonic mode. The obtained results are valid for all higher harmonic modes in the same way like for the first one. A cantilever's harmonic mode i transfer function, see section 2.1.2, in complex plane is

$$\hat{Z}_i(\omega) = \frac{1}{m_{eff}(\omega_i^2 - \omega^2 + \mathbf{i}\gamma\omega)} \tag{5.20}$$

Cantilever position spectral density induced by Langeving force is

$$S_{z_i z_i}(\omega) = \left|\hat{Z}_i(\omega)\right|^2 \cdot S_{F_L F_L} \tag{5.21}$$

There are two possibilities to minimize the thermally induced cantilever displacement $S_{z_i z_i}(\omega)$:

- Change dynamics properties of the oscillator → modify $\left|\hat{Z}_i(\omega)\right|^2$ by increasing damping coefficient γ. This results in decrease of the thermally induced displacement and its distribution into a broader frequency bandwidth.
- Change intensity of the thermal distortion → modify $S_{F_L F_L}$: Langeving force is a linear function of the systems temperature T and with decreasing temperature is the amplitude of thermally induced vibrations also decreased.

Presented cooling mode operation is concentrating on the possibility how to artificially modify the cantilever dynamics properties defined by its transfer function $\hat{Z}_i(\omega)$ and through this attenuate system's thermal distortion.

Previous section shown two possibilities of Cooling mode operation: Force accuracy measurement and Large bandwidth measurement. A simple comparison between the system sensitivity operating at the resonance frequency and off the resonance is necessary to evaluate proposed operation modes. Lets assume that the minimal detectable force of the system equals to the force noise induced by Langeving force $F_L(\omega)$.

The force noise induced by the thermal excitation for the measurement performed at the resonance frequency $\omega \approx \omega_i$ equals:

$$F_{min}(\omega_i) = \frac{k_i}{Q_i} \cdot z_i(\omega_i) \tag{5.22}$$

where k_i is the spring constant and Q_i is the quality factor of the cantilever's harmonic mode i. The minimal detectable force spectral density can found with the help of equation 5.21 and equals:

$$S_{F_{min}F_{min}}(\omega_i) = \frac{k_i^2}{Q_i^2} \cdot S_{z_i z_i}(\omega_i) = \frac{k_i^2}{Q_i^2} \cdot \left|\hat{Z}_i(\omega_i)\right|^2 \cdot S_{F_L F_L} = 1 \cdot S_{F_L F_L} \tag{5.23}$$

For the measurement performed at the low frequencies, $\omega \ll \omega_i(\approx 0)$, the minimal detectable force spectral density is

$$F_{min}(0) = k_i \cdot z_i(\omega) \tag{5.24}$$

$$S_{F_{min}F_{min}}(0) = k_i^2 \cdot S_{z_i z_i}(0) = k_i^2 \cdot \left|\hat{Z}_i(0)\right|^2 \cdot S_{F_L F_L} = 1 \cdot S_{F_L F_L} \tag{5.25}$$

From the obtained results it is easy to see that the force sensitivity equals for operation at the resonance frequency or bellow the resonance. The cooling mode has the same force sensitivity in the entire frequency spectra. The proposed force accuracy measurement has a better sensitivity due to a slow scan speed and possible averaging of the stabilizing force over certain time period. Therefore the force noise level induced by Langevin force stays the same in both operation modes.

The main functionality of the cooling mode is to eliminate any displacement of the cantilever. The stabilizing controller loop applies force $F_{stab}(\omega)$ to contra-balance external forces: Langevin force $F_L(\omega)$ and surface interaction force $F_{int}(\omega)$ to keep cantilever position $z_i(\omega)$ equal to zero.

$$0 \approx z_{i-error}(\omega) = \hat{Z}_i(\omega) \cdot (F_L(\omega) + F_{int}(\omega) + F_{stab}(\omega)) + \eta_{measure}(\omega) \tag{5.26}$$

In all real experiments a detection/measurement noise $\eta_{measure}(\omega)$ is present and $z_{i-error}(\omega)$ is a residual cantilever displacement caused by noise re-injection. For an ideal case the stabilizing force can be written

$$F_{stab}(\omega) = -F_L(\omega) - F_{int}(\omega) + \frac{z_{i-error}(\omega)}{\hat{Z}_i(\omega)} - \frac{\eta_{measure}(\omega)}{\hat{Z}_i(\omega)} \tag{5.27}$$

This equation shows that the cantilever dynamics properties are not important in the cooling mode measurement of the interaction force because $F_{stab}(\omega) = -F_L(\omega) - F_{int}(\omega)$. The stabilizing force has to be equal to all external forces if the cantilever stays non deflected $0 \approx z_{i-error}(\omega)$. The highest detectable frequency of the surface interaction is limited by the control loop speed and not by the cantilever settling time.

Only the detection noise depends on the cantilever transfer function. For the measurement at the resonance frequency $\omega \approx \omega_i$ it can be written

$$F_{stab}(\omega_i) = -F_L(\omega_i) - F_{int}(\omega_i) + \frac{k}{Q} \cdot (z_{i-error}(\omega) - \eta_{measure}(\omega_i)) \tag{5.28}$$

and for the measurement at the low frequencies $\omega \ll \omega_i(\approx 0)$

$$F_{stab}(0) = -F_L(0) - F_{int}(0) + k \cdot (z_{i-error}(\omega) - \eta_{measure}(\omega_i)) \tag{5.29}$$

To improve the measurement sensitivity and to minimize the influence of the measurement noise, it is possible to choose cantilever with a very small spring constant k. This causes a decrease of the cantilever resonance frequency. Therefore the cooling mode is not affected by this change and influence of the measurement noise would linearly decrease with the spring constant.

5.7 Electrostatic actuation

The proposed cooling mode creates a new requirements onto the used actuator to achieve desired functionality. These needs cannot be fulfilled with a standard bimorph (piezoelectric) driver which holds the cantilever fixed end (the chip). A new actuator has to be introduced to directly interact with the lever free end, to act directly at the place where is mounted a sharp probe interacting with the surface. The actuation at the free end using electrostatic force from the measured sample has been used by *Rugar* [158] for the thermal noise squeezing application and an electromagnetic free end drivers have been presented in [160, 49, 156, 50].

For this stabilizing application an electrostatic actuator placed above the cantilever has been chosen. The main advantage of this technique is that the applied electrostatic force can be relatively easily focalized only at the free end of the cantilever. The choice of the actuators geometry plays important role for the correct system functionality. Furthermore, the area where is the electrostatic force applied is strongly dependent on distance between plates. The added actuator (the fixed plate) has been design and manufactured with thickness and width in order of tens of micrometers. If the separation distance between fixed plate and cantilever is in order of tenths of micrometers we can say that the force is applied at the area approximately equal to the plates cross section. Other advantage of electrostatic actuator in comparison with electromagnetic actuation is small frequency dependence in bandwidth demanded by this application. It will be shown that the frequency dependency of applied electrostatic force can be neglected.

The electrostatic actuator is able to apply only an attractive force onto the cantilever which is not electricaly charged. The surface interaction forces in the non-contact operation mode are attractive with an opposite force vector orientation, which makes an electrostatic actuator suitable for this application. An electrostatic stabilization force is described by equation:

$$F_{stab}(t) = \varepsilon A \frac{(U_{offset} + U(t))^2}{2 \cdot (d_{act} + z(t))^2} \tag{5.30}$$

where ε is the environment permittivity, A is a surface of the actuator plates, U_{offset} is applied offset voltage, $U(t)$ is applied voltage by the stabilizing control loop, d_{act} is the distance between plates and $z(t)$ is the cantilever displacement.

The difficulties appear if we try to damp thermally induced vibrations which are displacing the cantilever in both directions (Langevin force has a changing sign). In this case the control loop is not able to act correctly in one half of the cantilever displacement range. This problem can be easily overcome if we apply a constant voltage U_{offset} between the cantilever and the actuator. If the offset voltage is set larger then a maximal value of the stabilizing signal $max(U(t))$ and if the damping signal is added to the offset, resulting voltage never changes the sign and the actuation is always correct.

The cantilever is deflected towards the actuator which slightly improves the actuation effectivity due to decreased distance between the plates. Other motivation to operate the system with offset voltage is the linearization of the force applied by the actuator. If $U_{offset} > U(t)$ then the response of the actuator can be linearized around the operation point U_{offset}.

Further on, an other assumption can be introduced: the fixed distance between the cantilever and the actuator is much larger than the cantilever displacement due to the thermal agitation $d_{act} \gg z(t)$. Under these assumptions the equation for stabilizing force can be simplified to:

$$F_{stab}(t) \approx \varepsilon A \frac{U_{offset}^2 + 2 \cdot U_{offset} \cdot U(t)}{2 \cdot d_{act}^2} \tag{5.31}$$

This solution can be easily implemented into the linear time invariant model which will be used for the stabilizing controller design and the cooling mode simulation. Reached discrepancy between a chosen actuator model and an experimental setup is sufficiently low to design entire control loop in a linear regime.

The first generation of the electrostatic actuator, which has been constructed and experimentally tested at SSL, is shown in figure 5.7. Both regulation loops needed to operate proposed cooling mode are displayed in the same figure. This schema corresponds to the schema shown in figure 5.2. The active surface of the actuators electrodes is placed above the cantilever between the fixed end and a half of the cantilever length, see the insert in figure 5.7. This organization has been chosen to maintain the ability to detect the cantilever free end with a laser and a photo-detector and relatively easy manufacturing. A photographs of this mechanical setup from an optical microscope are shown in figure 5.8. The photographs reveal that the actuator's plate is relatively narrow with a big error in the geometry, despite the effort to simplify the manufacturing process. The aluminum part is coated by gold to increase the conductivity. A small square of mica is glued on top of it as an isolator and then a chip with a cantilever is placed on it. An electrical connection is done with a silver paint which attaches used wires, see figure 5.8 A).

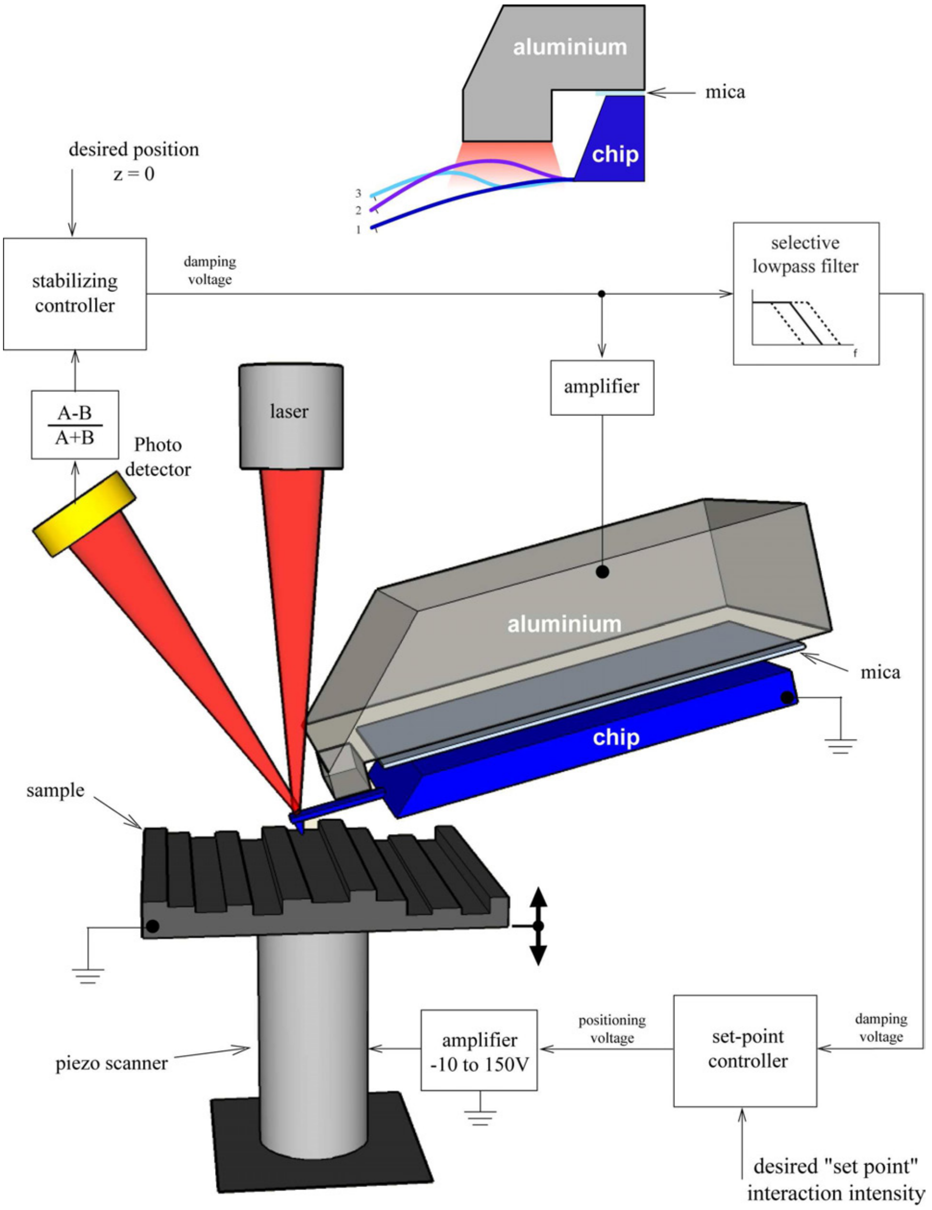

Figure 5.7: The cooling mode experimental setup with both control loops. Image shows the mechanical realization of the electrostatic actuator first generation.

The main difficulty of the actuator first generation is the inability to actuate with a correct sense (direction) for all harmonic modes which results in the system instability. The cantilever position is detected at the free end, but the actuator is placed close to the fixed end. The stabilizing force is applied inaccurately due to the different deflection shapes of a harmonic modes and the system is unable to correctly actuate on multiple harmonic modes. Lets compare the first and the second harmonic mode from the insert in figure 5.7. If the first harmonic mode is deflected towards the sample, the control loop has to apply an electrical signal to lift it up. But, if the second harmonic mode is deflected towards the sample and the required action close to the fixed end is to push it down due to the shape of this harmonic mode. In other words, the two modes have an opposite sign of the actuation. For higher harmonic modes the relation in this geometry is even more complicated and the actuator functions on some cantilever sections with correct sense and on some sections incorrectly.

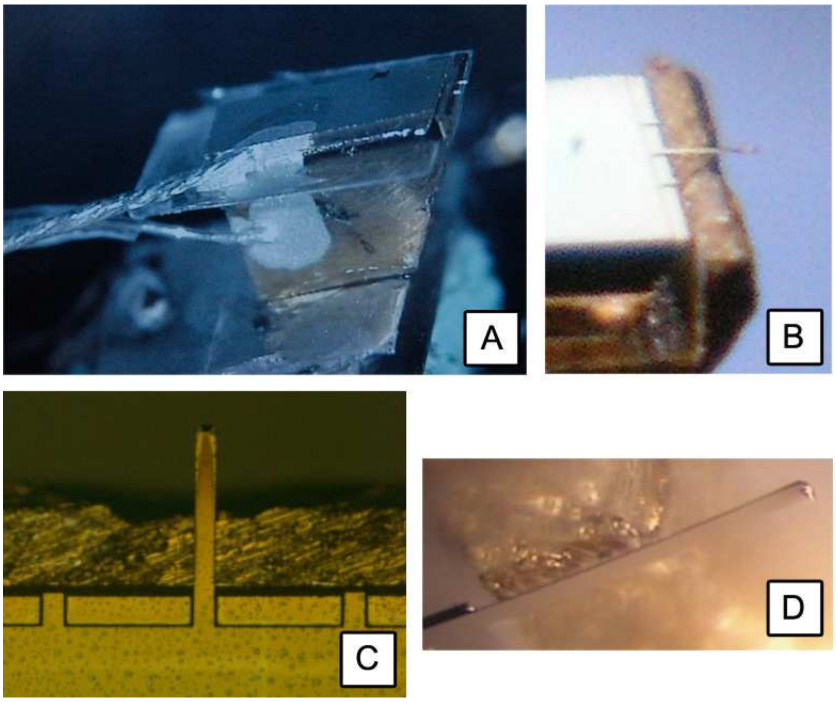

Figure 5.8: The first generation of a laboratory made electrostatic actuators. A) complete image of the actuator with a cantilever and an electrical connections. B) detail of the inserted mechanical part under the cantilever. C) and D) details of two different cantilevers and the actuator below them.

To eliminate problems that were mentioned for the actuator first generation three condition has to be met:

- measurement of the cantilever position and the actuation has to be performed at the same place or in a close proximity
- the actuation has to be done at the free end of the cantilever, ideally at its extremity.
- the actuation has to be done on very small segment of the cantilever length.

Satifying these three conditions permit to actuate on all harmonic modes of the cantilever with correct phase.

The actuator has been redesigned according to these requirements and the **second generation** of the system has been developed, see figure 5.9. The actuator electrode is placed above the cantilever free end and the laser spot of the position detection is aligned right next to it. The position cannot be measured at the free end of the beam any more, but is measured, at least, in a last quarter of the cantilever length. This guaranties that the detector is able to sense the first three harmonic modes without being to close to a peaks of the deflected beam where it loses its sensitivity, see section 2.1.3.
The experimental realization is shown in figure 5.10. The main mechanical part is made out of aluminum, equipped with an electrical connector and coated by gold. The entire actuator is then coated by isolating polymer (Parylene, www.paryleneinc.com). A small square of mica is glued and a chip with a cantilever is placed on its top.

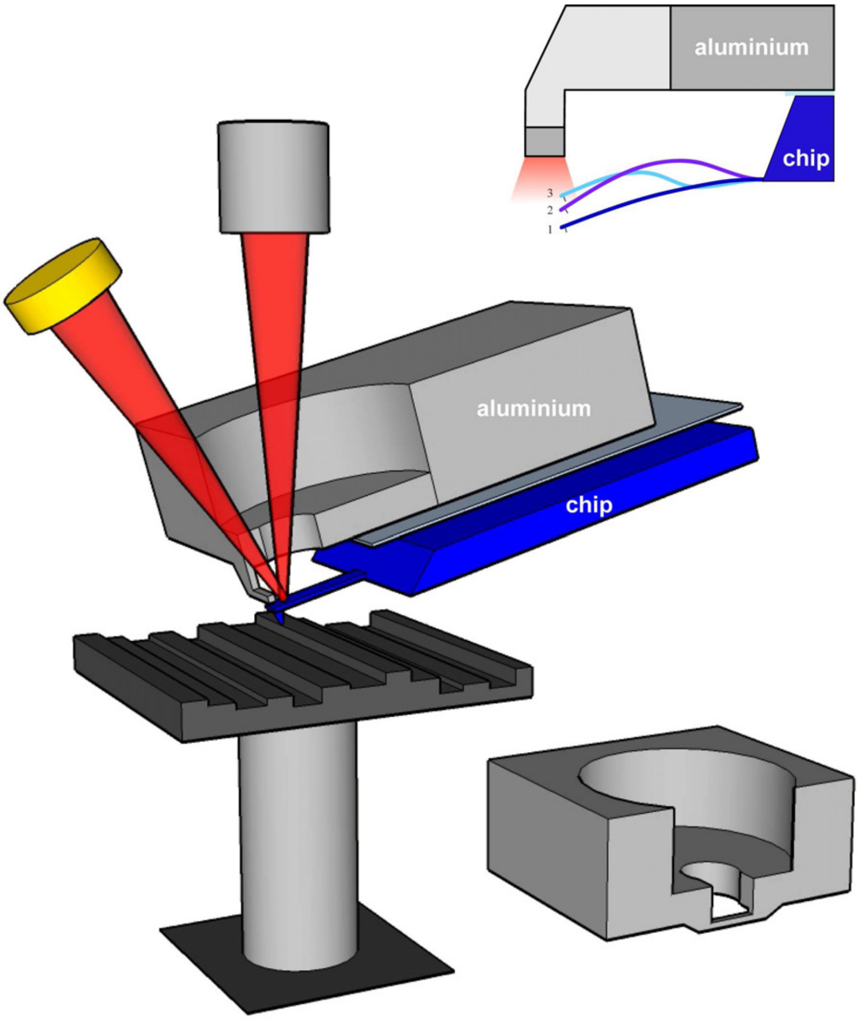

Figure 5.9: Mechanical realization of the second generation electrostatic actuator.

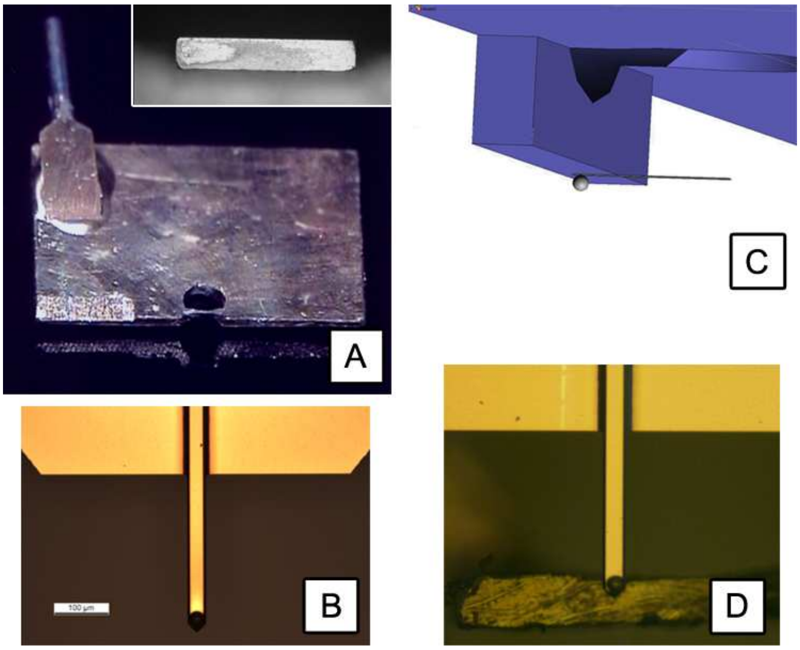

Figure 5.10: The second generation of laboratory made electrostatic actuators build at the SSL. A) a fixed part of the actuator with a connector before coating; in the insert is detail of the actuator surface. B) detail of the cantilever with metalized sphere at its end. C) 3D drawing of the cantilever and the actuator. D) image of the cantilever with the actuator below it.

5.8 Experimental setup analysis

The experiment setup is based on a commercial atomic force microscope Nanotec introduced in section 3.6 and shown in figure 3.6. This instrument is relatively open compare to other commercial microscopes and allows tho user to directly access many signals. A data can be collected from the selective outputs of the provided electronic or directly measured from the flat cable between the electronics and the AFM head. This access point gives an opportunity to obtain a data from the photo detector without any preliminary filtering.

5.8.1 Stabilizing control loop identification

The stabilizing control loop is the most important part of the proposed operation mode. The experimental setup is based on a standard commercial microscope which has been modified to test the cooling mode. This gives many constrains for the choice of used actuator and a controller. An addition active parts are introduced to be able to connect the entire control loop together. A precise analysis of each given or chosen block has to be made to achieve optimal functionality. Each block has to satisfy certain requirements usually given by the neighboring blocks. Figure 5.11 shows all parts of the stabilizing loop drawn as a blocs corresponding to a separated physical instruments which this loop includes. There are six distinctive electrical and mechanical blocs: photo-detector, controller input amplifier, discrete controller, controller output amplifier, actuator and cantilever. Some of these blocs can be identified independently without any extensive measurements but certain blocs can be easily identified only coupled to some of their neighbors.

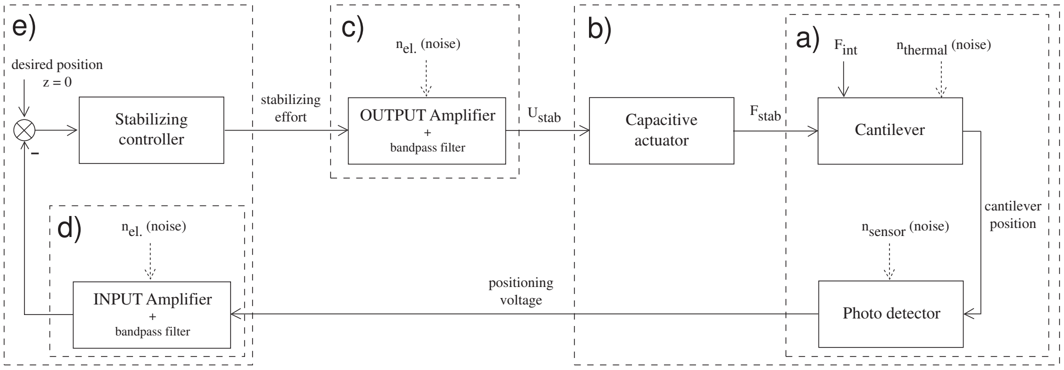

Figure 5.11: Schema of the stabilizing control loop with a separate function blocs.

The identification of this loop can be divided into parts to better evaluate the systems properties. The cantilever dynamics properties cannot be identified without use of the photo-detector. The identification of the photo-detector properties alone is a very difficult and extensive task. This is the reason why they are always analyzed together as an unique block, see figure 5.11 a). The results of the cantilever thermal noise identification are shown in section Section 3.6 and any further analysis is not necessary. The electrostatic actuator dynamics properties and its coupling to the lever can be evaluated only with the lever and the photo-detector together, figure 5.11 b). The actuator properties can be extracted by a comparison of these two identification results.
The identification of an electrical components is easier and they are all custom designed to fulfill needed requirements. The input and the output amplifiers can be analyzed separately, see figure 5.11 c) and d). The discrete controller will be identified with connected input amplifier which guarantee the required input signal conditioning (offset, differential input), see figure 5.11 e).

5.8.2 Amplifiers design and identification

Two amplifiers with integrated bandpass filter are used in the stabilizing control loop. Their general functionality is to convert electrical signals and connect an active blocs that are pre-defined and cannot be modified. Both amplifiers have been designed and constructed at the Surface Science Laboratory with a standard electronic components. Their identification has been performed with the lock-in amplifier Signal Recovery model 7280. This instrument is a DSP based wide bandwidth lock-in amplifier capable to operate at frequencies up to 2MHz. It provides a direct interface with a PC to easily read out and process obtained data.

The input amplifier (figure 5.11 d)) converts the voltage provided by the single ended photo-detector to the discrete controller differential input. Other important functionality is to offset the output signal to 3.5V to fulfill the requirement of the analog to digital converters at the controller input. The amplifier includes a band pass filter to eliminate an electronic distortion high above the frequencies of our interest. The very low frequencies of the signal are attenuated as well to minimize the influence of the experimental setup mechanical instability. More precisely, the drifts introduced by the mechanical modifications necessary to actuate at the cantilever free end. These changes are essential for the cooling mode operation and are achieved by mounting the actuator between the chip holder and the chip with a cantilever.
The amplifier is based on the chip THS4130 from Texas Instrument which consists of one fully-differential amplifier optimized for a preamplifier applications for the analog to digital converters, see figure 5.12. The amplifier has been designed and a passive components were

chosen with the help of the application note provided by the manufacturer. The amplifier was constructed as a band pass filter with a low cut-off frequency 10Hz and a high cut-off frequency 250kHz. The photo-detector output signal from the thermally excited cantilever has an amplitude about 20mV. The amplifier gain was chosen 35 to obtain controller input maximal amplitude $\pm 0.7V$ which corresponds to 70% of the input range. This gives certain reserve in amplitude to do not saturate the input converter if there are some random amplitude spikes. All given specifications were the desired properties of the amplifier but the real parameters are slightly different and has to be identified. This discrepancy is caused by the limited accuracy of the passive components used for the amplifier construction.

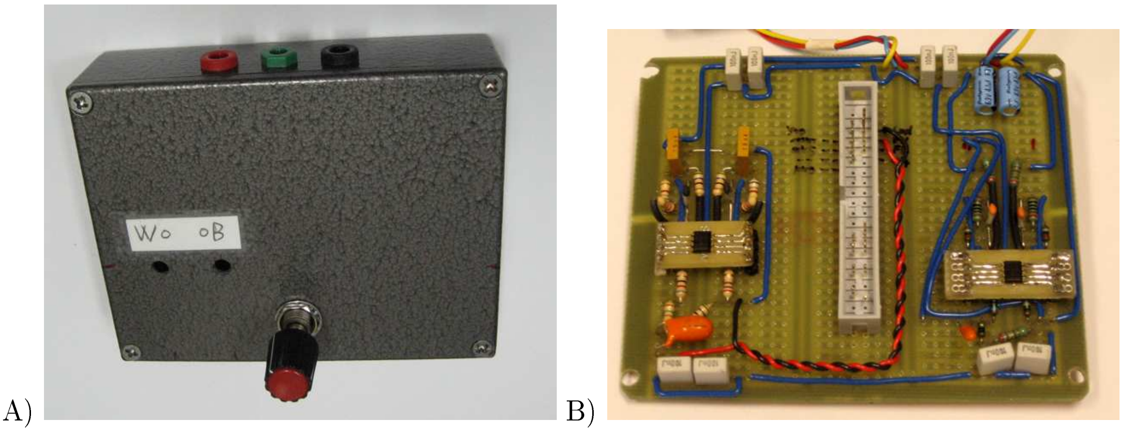

Figure 5.12: A) Enclosed “laboratory made" input amplifier. B) The detail of the input amplifier electronic.

The identification has been performed with the above mentioned lock-in amplifier for both amplifier outputs (inverted and regular). The sweep frequency has been chosen from 1Hz to 1MHz to cover the entire operation band with a large reserve at both ends. Obtained results for the inverted output are shown in figure 5.13 A) and for the regular output in figure 5.13 C). Both Bode diagrams have significant deformations at the frequencies 50Hz and 100Hz. These features are not coming from the input amplifier but are caused by the lock-in amplifier. Most probably it is a cross talk between the power network supplying the instrument and the measured signal. A simple measurement with a generator and an oscilloscope at these two frequencies has been done and shown that the system does not have any amplitude drop as was measured by the lock-in.
The measured spectral response shows that the cut-off frequencies of the implemented band pass filter are shifted compare to the desired values. The low cut-off frequency equals 14Hz instead of 10Hz and the high cut-off frequency equals 195kHz instead of desired 250kHz. Measured amplifier gain is 34 for 20mV input signal (red curve in figure 5.13 A) and blue in figure 5.13 C)). A simple test for different input amplitudes has been performed to verify amplifier gain. The amplifier has a constant gain for the input amplitudes above 15mV. If the input is below this limit, the amplifier gain decreases. Figure 5.13 A) - green curve and figure 5.13 C) - yellow curve show new amplifier gain 25 if 10mV input voltage is applied. This behavior has to be taken into account for a quantitative explanation of the obtained results but it does not change the control loop frequency properties.
Other important feature of the input amplifier is to offset the output signal to 3.5V. The amplifier has been designed with a potentiometer which allows to manually select the output offset in a range 1 to 5V. Both amplifier outputs should have exactly the same offset but the measurements shown that they have offset deviation of 180mV. This results in an apparent DC offset of the controller input that has to be subtracted numerically in the controller after the conversion to a discrete signal.

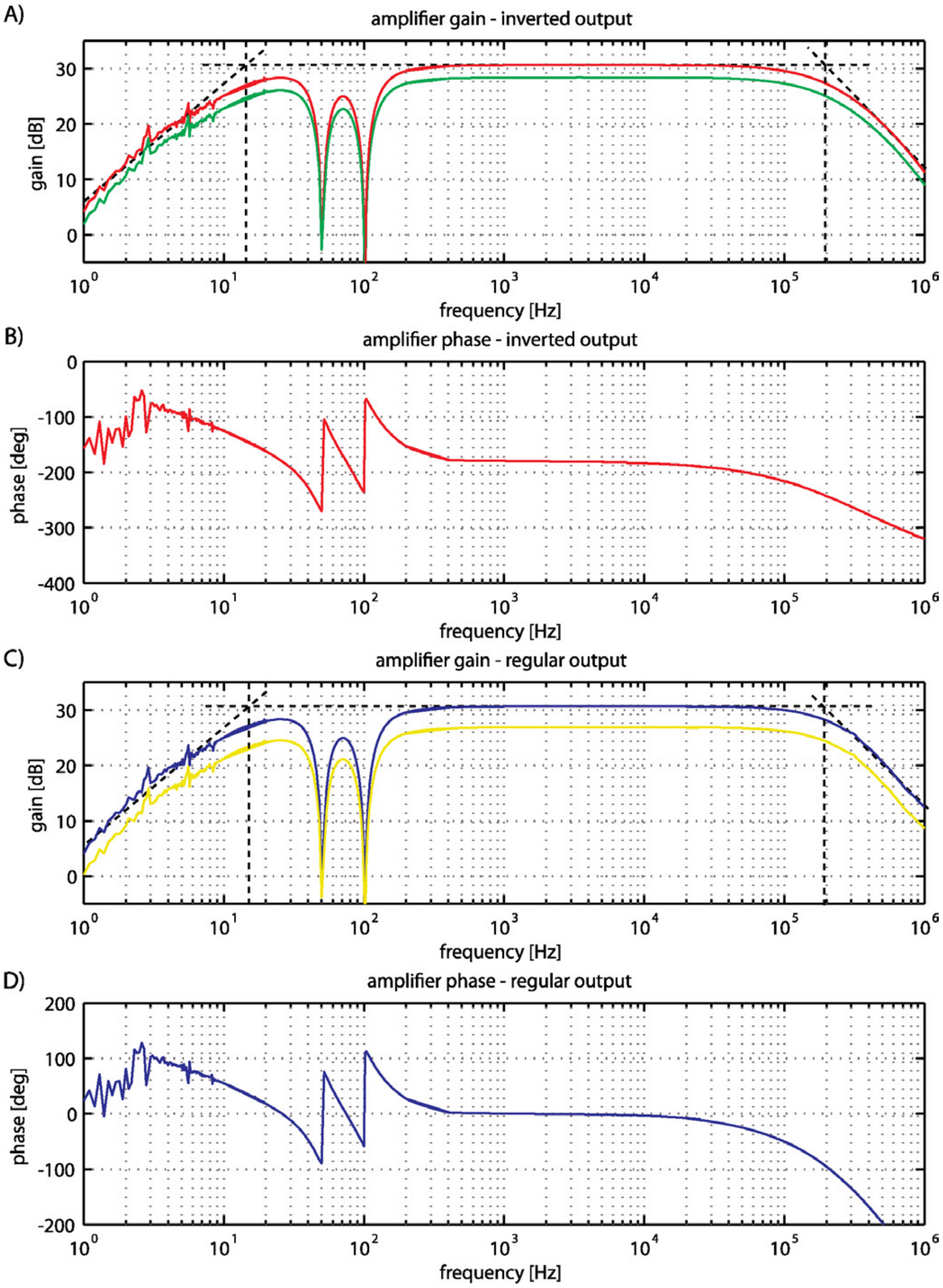

Figure 5.13: Bode diagrams of the input amplifier; A) red curve - the inverted output gain for 20mV input and green for 10mV. B) the inverted output phase. C) blue curve - the regular output gain for 20mV input and yellow for 10mV. D) the regular output phase.

The obtained results of the input amplifier identification have to be converted into a transfer function that can be easily used in Matlab/Simulink environment for a controller design. The Bode diagram shown in figure 5.13 corresponds to a dynamic system with a transfer function:

$$H_{in-amp}(s) = \frac{Ks}{(T_1 s + 1)(T_2 s + 1)} = \frac{0.3875s}{(11.4 \cdot 10^{-3} s + 1)(8.16 \cdot 10^{-7} s + 1)} \tag{5.32}$$

The output amplifier (figure 5.11 c)) is used as a manually selective gain of the control loop to ease the system testing. Other important functionality is to offset the controller output signal to a desired value to be able to operate the electrostatic actuator in a region where it can be easily linearized. The actuator linearization has been introduced in section 5.7.

The designed amplifier is a cascade of two operational amplifiers embedded on one integrated circuit OPA2604 from Burr-Brown, see figure 5.14. The first amplifier offsets the input voltage to a selectable value in a range from 0.5 to 1.8V. This output voltage offset has been later set to 1.1V which is larger value than the maximal voltage $\pm 1V$ at the discrete controller output. Further more, the controller is designed to have at least 30% reserve to its maximal output voltage to guarantee that the output discrete to analog converters will not numerically overflow. This achieves that after passing the first operational amplifier, the signal is in a range from 0.4V to 1.8V. The second cascade amplifier multiplies this signal with a manually selectable gain in a range 1 to 8. The amplification is performed with already offsetted signal which guaranties that there is no change of the signal polarity and the actuator operates in a regime where it can be linearized. The resulting output signal offset is changing according to the selected gain which modifies the actuator internal gain due to the quadratic relationship between the applied force and used actuator voltage. The increased offset causes as well a bigger cantilever deflection towards the static actuator plate which weakly increases the actuator efficiency. These two behaviors do not have any significance for the frequency response of the system and stay constant once the amplifier gain is set.

The entire amplifier is designed as a band pass filter with the low cut-off frequency 10Hz and attenuation 20dB per decade. The high bandwidth limitation was done by two filters designed with the cut-off frequencies 350kHz and 1MHZ and attenuation 20dB per decade each.

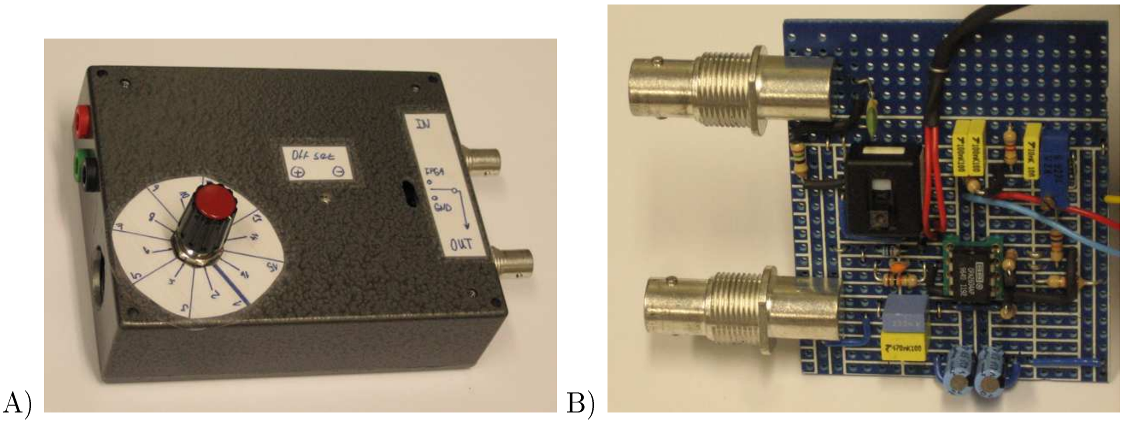

Figure 5.14: A) Enclosed "laboratory made" output amplifier. B) The detail of the output amplifier electronic.

The output amplifier identification was performed by a sweep measured with a lock-in amplifier and manual measurement by frequency points with an oscilloscope. From the manual measurement the incorrect result given by the lock-in amplifier at the frequencies 50Hz and 100Hz can be verified, see figure 5.15. The identification was done with the smallest possible amplifier gain because higher gains are meant only for the testing. A simple verification was performed for some higher amplifier gains and the frequency responses corresponded to the response at the minimal gain. The obtained spectra for both techniques are shown in figure 5.15, blue curve for the lock-in and red curve for the manual measurement. The identified high pass filters cut-off frequency equals 16Hz with attenuation 20dB. The low pass filter has the frequency response in which is very difficult to distinguish two independent cut-off frequencies and even experience certain parasite effects. The Bode diagram has been fitted with only one low pass filter with cut-off frequency 950KHz and attenuation 40dB to reach a simple and reasonably accurate transfer function for this amplifier. The resulting transfer function is:

$$H_{out-amp} = \frac{Ks}{(T_1 s + 1)(T_2 s + 1)^2} = \frac{0.0129s}{(9.95 \cdot 10^{-3} s + 1)(1.67 \cdot 10^{-7} s + 1)^2} \tag{5.33}$$

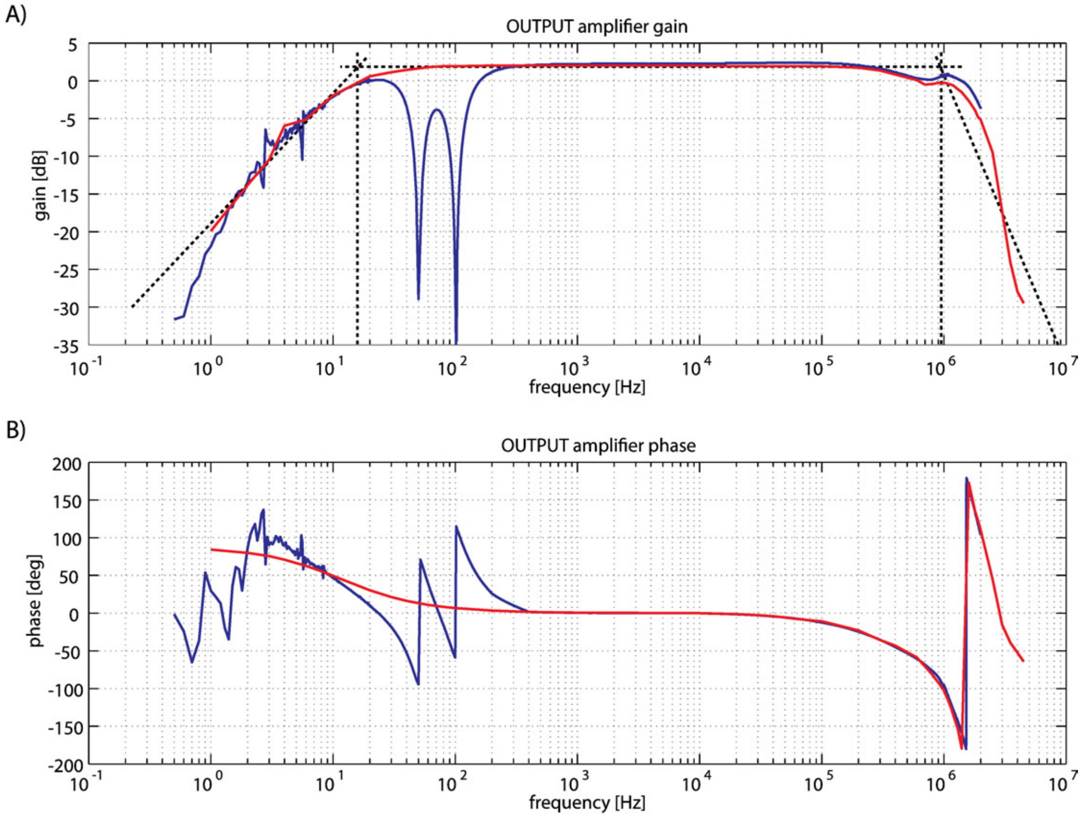

Figure 5.15: The output amplifier Bode diagrams. A) amplifier gain; red curve measured manually and blue curve measured with the lock-in. B) amplifier phase.

The amplifier gain is manually selectable by a potentiometer implemented into the second amplifier cascade. It is not possible accurately describe the gain evolution according to the potentiometer position, because there is not any accurate reading of the selected potentiometer position. Only an approximate measurement of this relation has been done to demonstrate the systems properties and application possibilities. The potentiometer has been equipped with a numbered scale and for each position on this scale the output signal has been measured. A harmonic signal with frequency 10kHz and effective amplitude 100mV has been used as the amplifier input. The obtained relation between the potentiometer position and the gain is shown in figure 5.16 A). The potentiometer movement in positions between 1 and 3 has a little influence at the output and the gain stays equal to 1.3. When the position is in range from 3 to 5.5 the gain is a linear function of the potentiometer position. Further increasing of the gain causes the amplifier saturation due to a large signal offset which reaches 6V, see figure 5.16 B). The maximal measured amplifier gain is about 6.5.

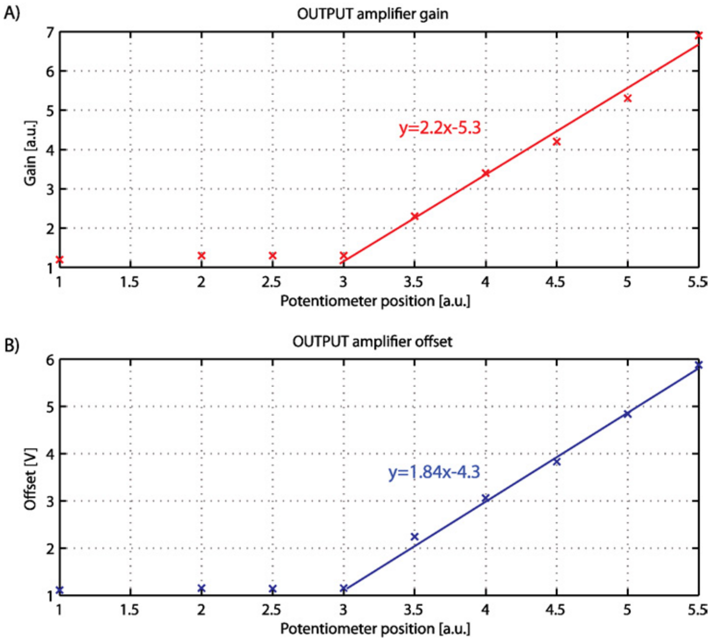

Figure 5.16: A) The amplifier gain evolution with changing potentiometer position. B) The output offset evolution with a changing potentiometer position.

5.8.3 Actuator identification

The capacitive actuator was introduced in section 5.7. Here presented identification results are only for the actuator second generation with mounted Veeco MPP-32220 cantilever. This generation has significantly better functionality and will be used in all following simulations and experiments. The identification is done in two steps: quantitative and frequency domain analysis. In both cases the entire chain of blocks consisting of: electrostatic actuator, cantilever and photo-detector shown in figure 5.11 b) will be identified. The actuator cannot be identified separately but with the knowledge of the cantilever and the photo-detector properties we can precisely determine the actuator's properties. The photo-detector measures the position of the cantilever during the identification process, and its gain and frequency properties has to be taken into account. The electrostatic actuator uses two plates for its operation: the fix one and the another plate is the cantilever itself, which is the controlled plant at the same time. The identification is then performed for actuator and plant together and their properties has to be separated afterwads.

Quantitative analysis
The aim of this identification is to precisely determine actuator's gain. In other words, to found a constant which gives accurate relation between applied voltage and resulting electrostatic force. The identification has been done with the output amplifier, figure 5.11 c), and a laboratory function generator. The amplifier is used to offset the identification signal to chosen operation point and performed the identification in the standard operation conditions. The first step was to determine the photo-detector calibration constant with the procedure presented in section 3.6. The measured photo-detector output will be converted to the position with the help of this constant. The found photo-detector conversion constant $k_{detector} = 1.48 \cdot 10^6 \mathrm{V/m}$.

A triangular signal of amplitude 1Vpp and frequency 70Hz at the amplifier input has been used for the identification, see figure 5.17 A). The amplifier gain is set to 4 and the obtained output voltage is displayed in figure 5.17 B). This signal is directly applied to the actuator. The measured cantilever position, already converted to meters, is shown in figure 5.17 C). A large triangular displacement is caused by the electrostatic actuator, and small vibrations present in the measurement are the cantilever thermal vibrations. The applied electrostatical force can be determined from the measured cantilever position and its spring constant, which has been identified in section 3.6.2.2. The calculated actuator force applied to the cantilever is shown in figure 5.17 D).

The actuator gain has been determined from direct comparison of curves B) and D) in figure 5.17. To achieve better accuracy, the yellow marked sections of both signals have been linearized and from their slopes the actuator gain $k_{actuator} = 3.69 \cdot 10^{-10}$ N/V was directly calculated.

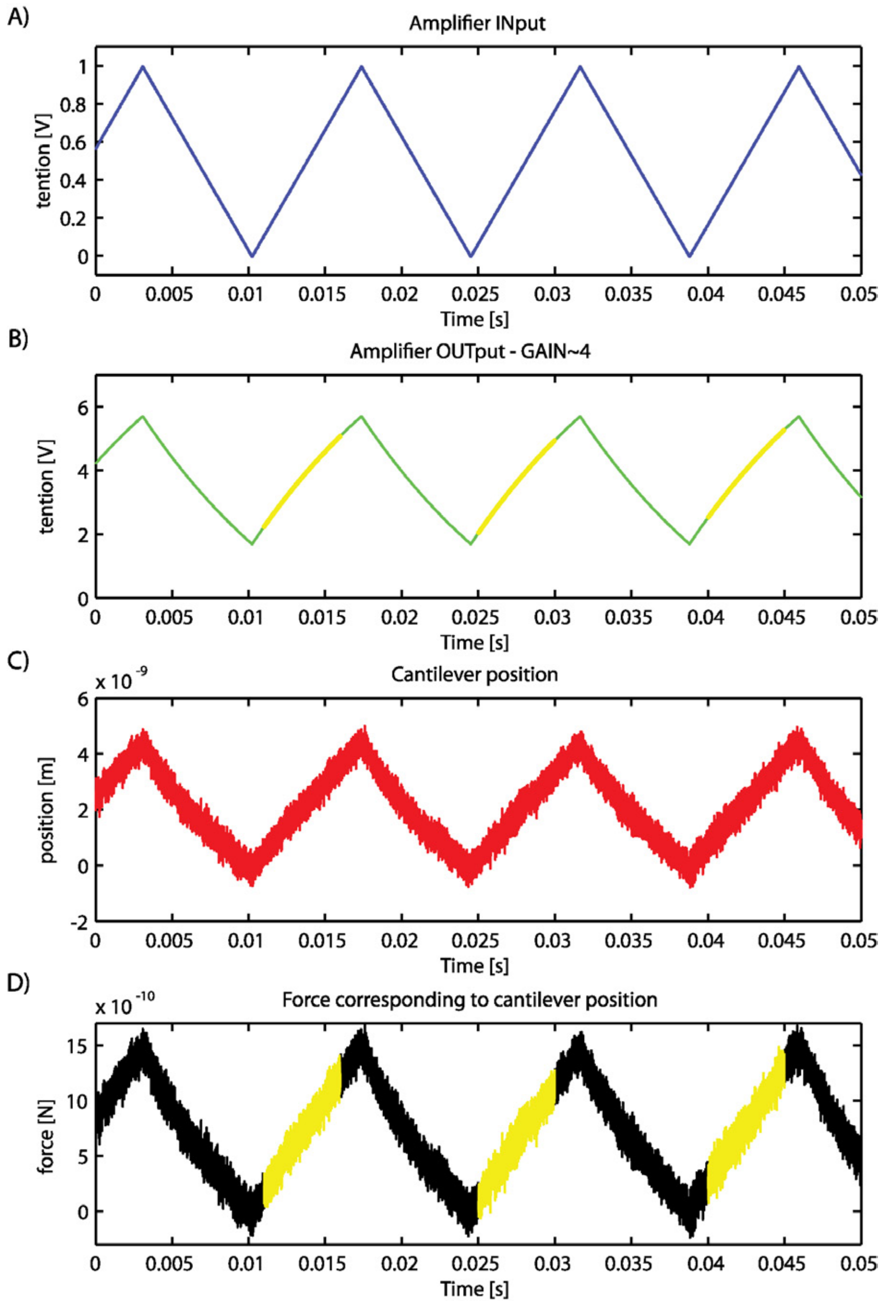

Figure 5.17: A) The output amplifier triangular input. B) The amplifier output voltage. C) The measured cantilever position. D) A calculated force corresponding to the measured cantilever position.

Frequency domain analysis

This part of the identification should reveal the electrostatic actuation frequency properties. The main difficulty is to decouple the frequency properties of the cantilever and the influence of the electrostatic actuator. The identification has been performed with the lock-in amplifier Signal Recovery model 7280. The measurement was set up according to the schema shown in figure 5.11 b). Two independent measurements were done: the lock-in amplifier output was directly applied to the electrostatic actuator and in the second measurement the output amplifier between the lock-in and the actuator, see figure 5.11 b) and c) was used. The comparison between these two measurements allows to identify the influence of the output amplifier on the regulated system.

The figure 5.18 shows the Bode diagram of the regulated system up to frequency 200 kHz which is the general measurement bandwidth including the first two resonance peaks of the cantilever. Blue dashed curve stands for the direct excitation of the system with the lock-in amplifier, and red curve shows results obtained with the inserted output amplifier. Both curves contain a disturbance coming from the lock-in amplifier at the frequencies 50 and 100 Hz. The measurements show that the influence of the output amplifier is visible only at the low frequencies where the excitation signal is attenuated. The rest of the spectra is matching with very small discrepancies.

The actuation influence at the cantilever's resonance frequencies should be visible from the comparison of the amplitude spectra in figure 5.18 and the thermally excited cantilever displacement spectra shown in figure 3.16. The resonance peaks frequencies in both measurements are matching, and the actuator is not detectably changing the systems frequency properties in the measurement bandwidth. Only a small disturbance is present after the second resonance peak at a frequency about 155 kHz.

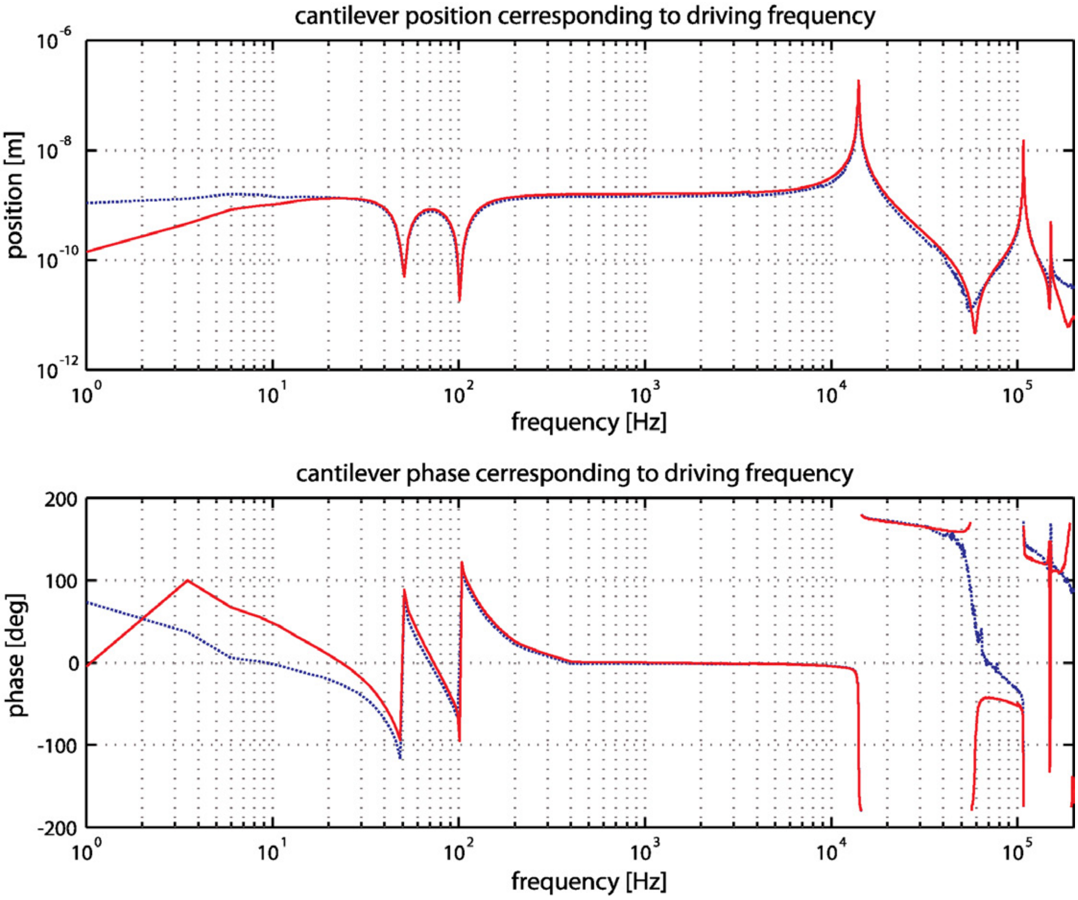

Figure 5.18: Bode diagram of the cantilever frequency response to the electrostatic actuation for the bandwidth up to 200kHz. Blue curve - the excitation voltage is directly applied to the actuator. Red curve - the output amplifier is used at the actuators input.

The most interesting result of this measurement is the amplitude drop present at the frequency about 60 kHz. This significant decrease of the vibration amplitude is caused by the destructive interference of the two neighboring harmonic modes. This behavior cannot be observed in the thermal noise measurements due to independent, random and uncorrelated thermal excitation of each harmonic mode. Therefore this behavior has been predicted by a model based on the beam theory [161, 162] presented in section 3.3. For example, see figure 3.18 where is this amplitude decrease visible (attention: plotted Bode diagrams are for different cantilever).
To further investigate the system properties in higher frequencies, a spectra has been measured up to 800 kHz. This bandwidth covers the first four harmonic modes of the used cantilever, and is shown in figure 5.19. The spectra measurement has been performed in a small sections of the entire bandwidth which caused many discontinuities of the measured phase shift. The actuator induces two minnor peaks at about 155 and 270 kHz and at the higher frequencies its spectra is flat. On the other hand, the influence of the output amplifier at the frequencies above 155 kHz is clearly visible.

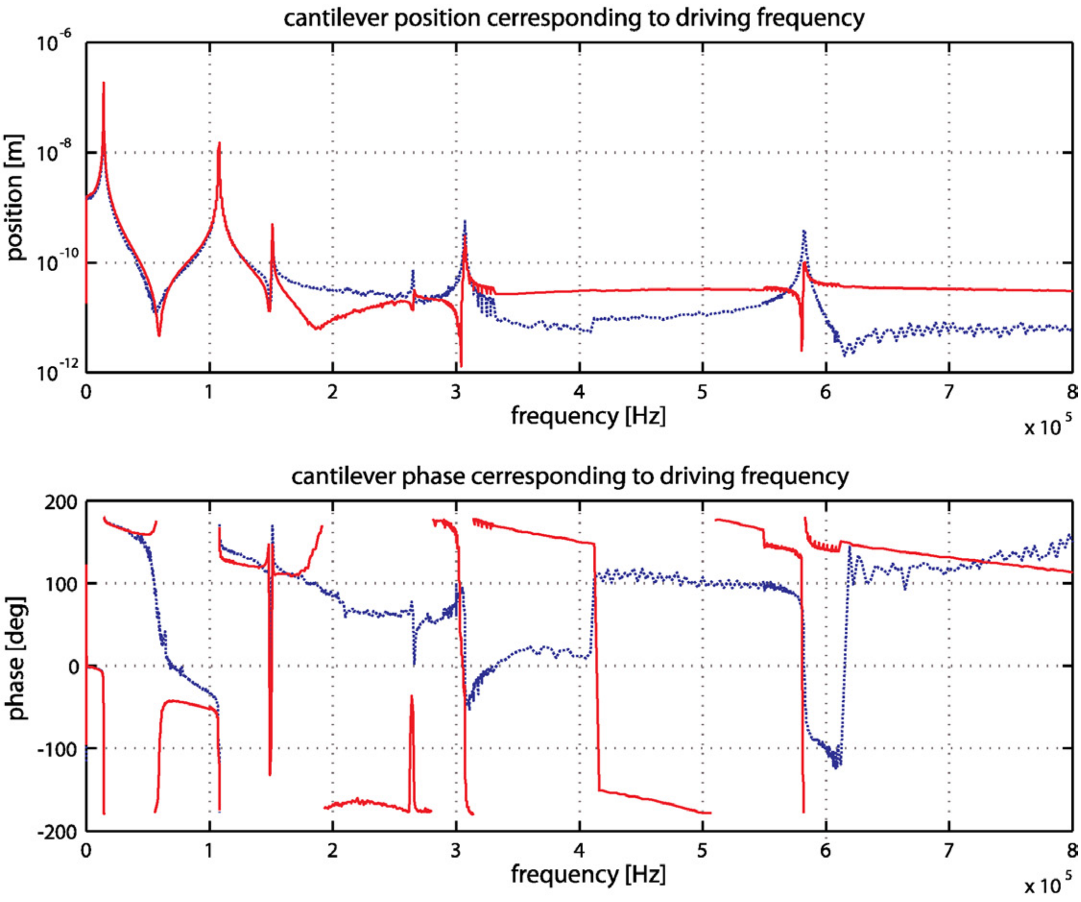

Figure 5.19: Bode diagram of the first four harmonic modes of the cantilever response to the electrostatic actuation. Blue curve - the excitation voltage is directly applied to the actuator. Red curve - the output amplifier is used at the actuator input.

From the obtained identification results can be concluded that the electrostatic actuator can be approximated only by a simple constant $k_{actuator}$. This simple model will be used for the stabilizing controller design and the cooling mode simulations. The actuator dynamics properties are insignificant in a comparison with the cantilever dynamics properties inside the measurement bandwidth. Furthermore, the influence of the output amplifier is more significant than the actuator's influence in the regulated system.

5.8.4 Real-time controller design and identification

The choice of the real-time controller technology has been made according to the requirements for its operation speed, easy modification of controller structure and possibility to implement a controller of higher order than standard PID/PSD. The real-time stabilizing controller used in the cooling mode experimental setup is a discrete controller based on the Fully Programable Gate Array (FPGA) chip from Xilinx (www.xilinx.com). This technology provides desired technical parameters, and its modularity and flexibility makes it well suited for this application. A modular system from Hunt Engineering (www.hunteng.co.uk) with already developed lowest level of a function code to minimize needed development time has been used. A customized code to provide desired functionality is developed on the top of these procedures and libraries. The modular system consists of a carrier board HEPC9 which is inserted into computer's PCI slot, see figure 5.20 A). This board has two main functionalities; docking up to four function modules, and providing communication between them and PC. These function modules can be chosen according to users' needs and in our case the module HERON-IO2 has been used, see figure 5.20 B). The module consists of two input analog/digital and two output digital/analog converters, FPGA chip with 1 million gates, source of common clock, clock dividers, PROM memory, JTAG programming channel and additional circuits for the communication with other modules or the PC. All these parts are implemented onto a single printed circuit that represents one module planted onto the HERON carrier board. Further details about used technology are out of scope of this thesis and can be found at the site of the manufacturer www.hunteng.co.uk.

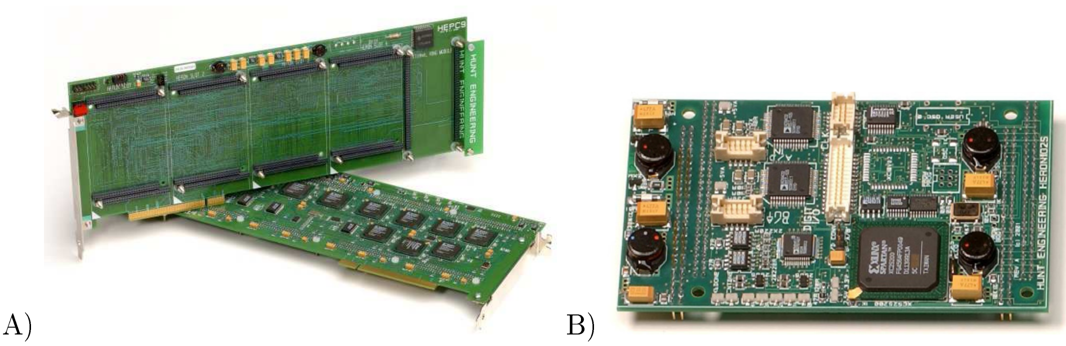

Figure 5.20: A) HEPC9 carrier board. B) HERON-IO2 input/output FPGA module.

A discrete controller has been implemented into the HERON-IO2 module with a FPGA chip as a code written in the hardware description language VHDL. The code has been developed in collaboration with Ondrej Kotaba, Brno University of Technology during his masters stage at the UJF/LAG. All details about different functions of the developed code are described in his diploma thesis [163]. The HERON modular system offers a possibility to develop a Graphical User Interface (GUI) ran on the hosting PC that can directly communicate and modify controllers numerical constants, set sampling rate, chose input and output channels and other features. The GUI has been developed by Pavel Bohacik, Technical University of Ostrava in C++ with a use of the HERON API functions during his Erasmus stage at UJF/LAG. The technical details and description of separate parts of the GUI has been summarized in the stage report [164]. The technical development performed with these students has been necessary to build a complete experimental setup. Precise description of this development with all technical details is out of scope of this thesis and for further information see given references.

The presented FPGA based real-time controller is used as the stabilizing controller in the feedback loop shown in figure 5.11 e). The controller is presented as one block but it can be further divided into a set of sub-blocks which characterize the system more precisely, see figure 5.21. The analog to digital converter at the FPGA input converts a differential analog input signal to a discrete signal of 12 bits with maximal sampling rate 125MHz. This data is synchronously passed to the FPGA chip with internal maximal clock 100MHz. The FPGA uses external clock of 100MHz which can be later, inside the FPGA, divided according to applications needs. All signal processing is performed in the FPGA and the resulting discrete signal is passed to the digital to analog converter with 14 bits resolution and maximal conversion clock 125MHz. The HERON system allows user to operate the entire system asynchronously or synchronize the input and the output converters with the clock selected in the FPGA. This option is used in our setup because it is easier to work with and there is no loss of information due to discrete data re-sampling.

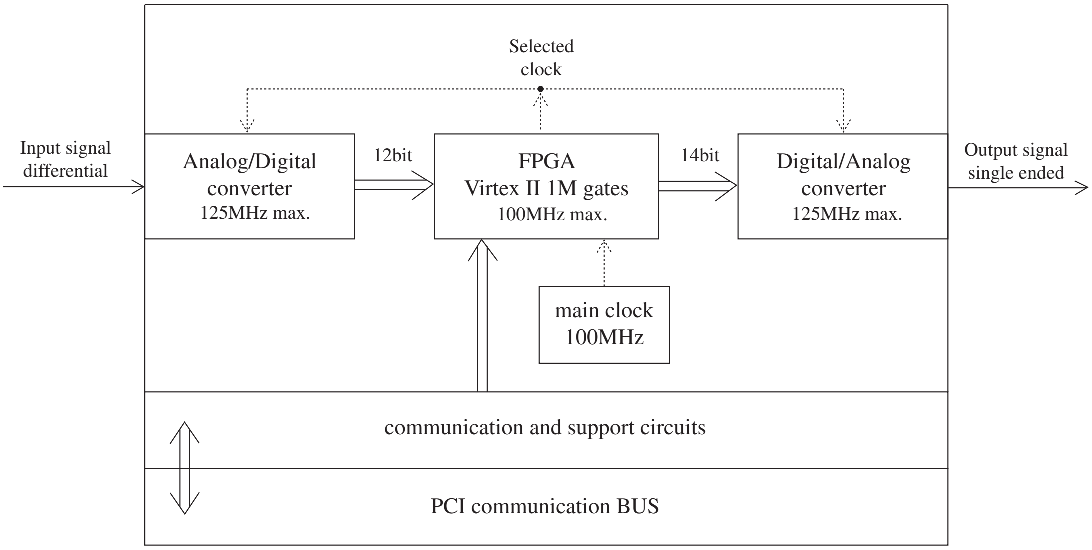

Figure 5.21: Discrete real-time controller internal blocs schema.

A short description of the code implemented into the FPGA has to be given before approaching to the controller identification. Two main function blocks are implemented into the FPGA: Phase Lock Loop (PLL) and discrete regulator. The first block is used only in standard AFM operation mode which is not focus of the cooling mode experiment [163] and only the discrete controller will be used. Detailed controller implementation is shown in figure 5.22. The implementation is based on a standard FPGA function hardware blocs which are integrated on the chip: time delay z^{-1}, numerical shifter → and numerical multiplier ×. These blocs are routed together, with the help of VHDL, to form desired functionality.

The controller can be further divided into three separate parts: input signal treatment H_{reg1}, regulators dynamics H_{reg2} and output signal treatment H_{reg3}. Their mathematical description is:

$$H_{reg1} = \frac{input}{2^{d_a}} + bias_{input} \tag{5.34}$$

$$H_{reg2} = \frac{\frac{b_0+b_1z^{-1}+...+b_7z^{-7}}{2^{n7}}}{1+\frac{a_1z^{-1}+...+a_7z^{-7}}{2^{m7}}} \tag{5.35}$$

$$H_{reg3} = \frac{H_{reg2}out \cdot c_b}{2^{d_b}} + bias_{output} \tag{5.36}$$

where basic functionality of H_{reg1} and H_{reg3} is to divide or multiply signals and add desired offsets. The H_{reg1} block helps to adapt regulator input. This block is used to eliminate the input signal offset caused by the unbalanced differential input. The H_{reg3} block functionality is mainly to multiply or divide regulator output to guarantee that the output digital to analog converter will not numerically overflow. Regulators dynamics is implemented in the H_{reg2} block. This is a standard discrete transfer function used in control theory. The parameters b_{0-7} and a_{1-7} are the regulators constants, 2^n and $2^m$are optional constants dividers. The complete regulator transfer function has a form:

$$H_{reg} = H_{reg1} \cdot H_{reg2} \cdot H_{reg3} \tag{5.37}$$

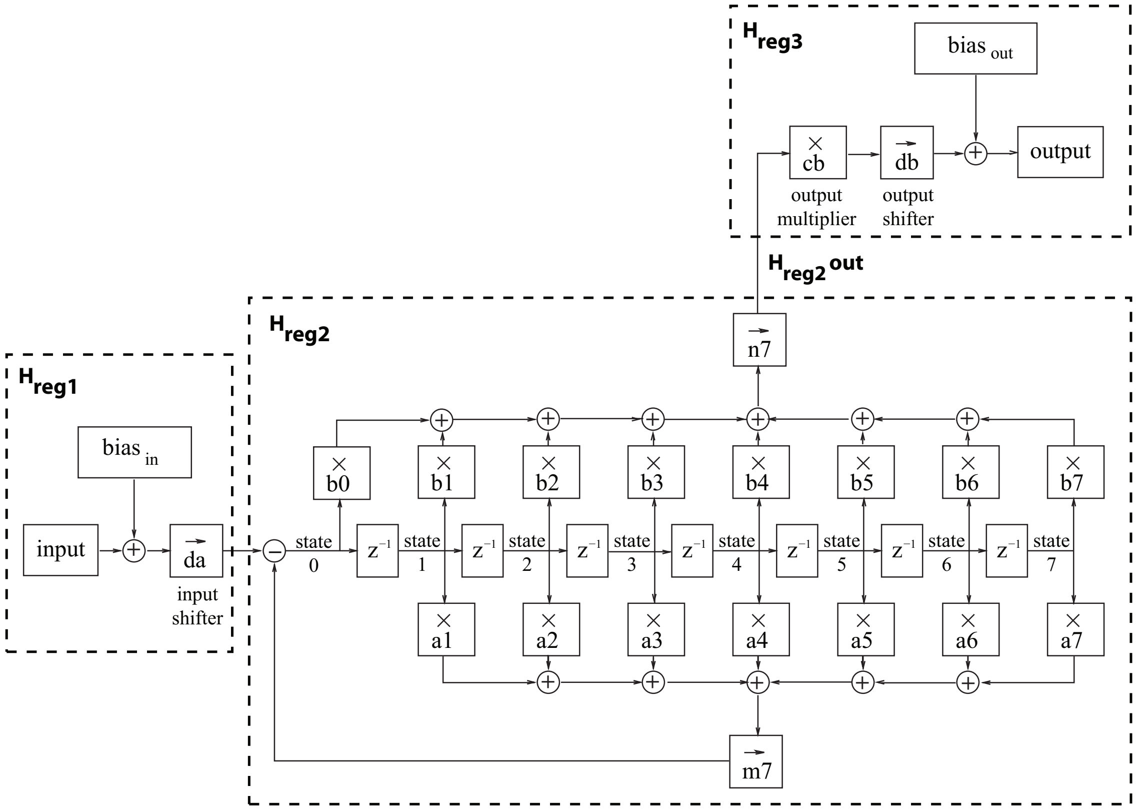

Figure 5.22: The discrete controller implementation into the FPGA processor.

The identification of the discrete controller depends on used regulators constants. The regulator is set to have only constant gain with no internal dynamics to be able to identify system's parasite dynamics. All parameters are set to zero except b_0 and c_b which are set to one. In this configuration the system should have, in ideal case, the transfer function equal to one. The HERON-IO2 module consist of the discrete elements: A/D converter, FPGA and D/A converter. All these blocks have a sampling rate that significantly influence the controller frequency response. The identification has been performed with the sampling rate 50 MHz as the common clock for all three discrete elements.

The discrete controller cannot be identified without the input amplifier because there is not lock-in amplifier with differential outputs. The obtained results are the convolution of the input amplifier and the controller dynamics properties. The influence of the controller dynamics can be distinguished by comparison with the identification results of the input amplifier, figure 5.13. The lock-in amplifier sweep is set the same way like in the input amplifier identification in section 5.8.2 to achieve same conditions of the measurement. The measured frequency spectra is shown in figure 5.23. It is impossible to see the difference of this Bode diagram in comparison with figure 5.13. This result verifies that the controller electronic is well designed to do not modified the passing signal at the frequency range of our interest. If the sampling rate is set low (below 800 kHz) the discrete operation of the system starts to influence the passing signal and generates many sub-harmonics perturbing the output (this measurement is not shown). The designed discrete controller has the sampling rate always higher than 1 MHz which permits us to assume that the controller has no parasite frequency behavior. The controller parasite behavior is neglectable and the parasite transfer function can be set to 1. Later, the controller will include a transfer function defined by parameters b_{0-7} and a_{1-7} which will be designed in section 5.9. The Bode diagram would vary according to chosen regulator's parameters.

The only change that has been detected during the identification, is an increase of the signal noise and the output voltage offset. The added noise has not been identified separately and in the simulations all electronic noise is simulated with only one source of white noise. The output voltage offset has been already discussed in the identification of the input amplifier. It is caused by unbalanced differential input. This offset has been removed with the digital selectable offset implemented into the FPGA.

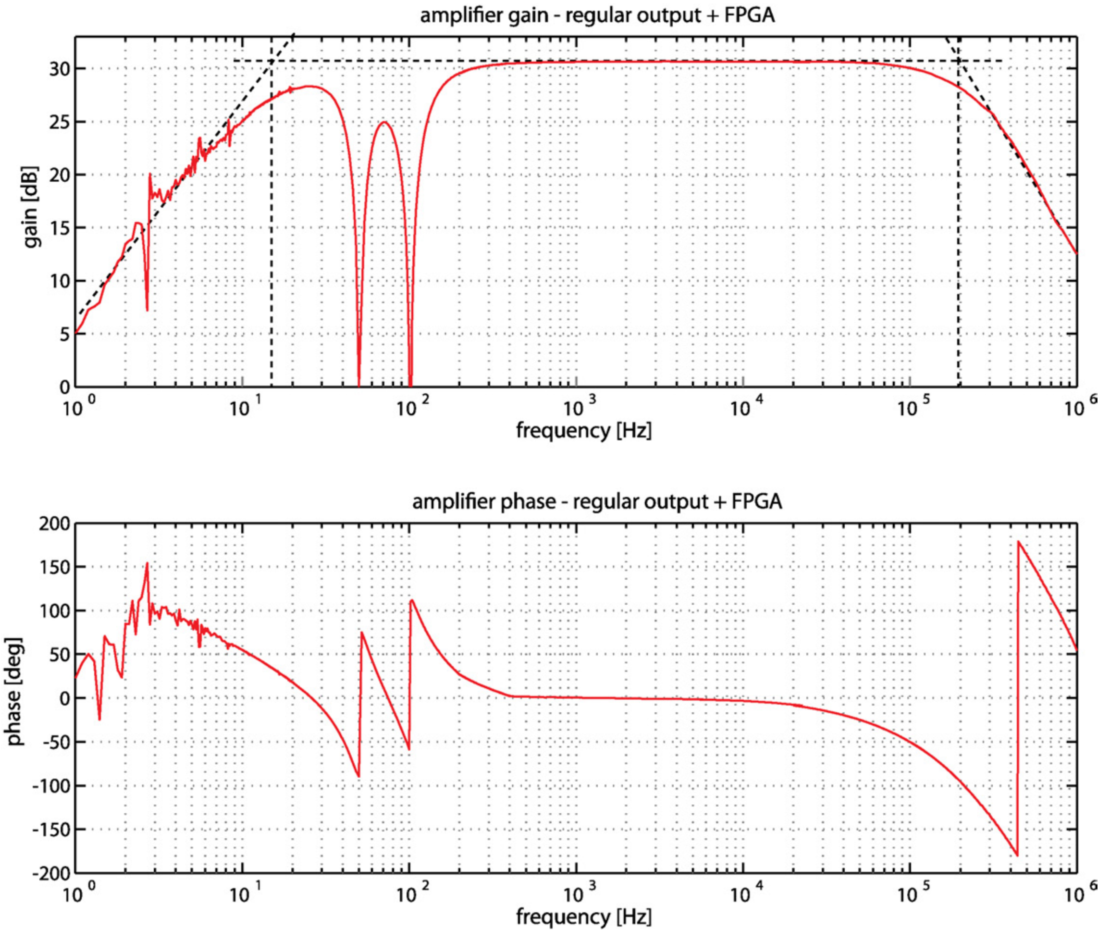

Figure 5.23: The Bode diagram of the discrete controller coupled to the lock-in amplifier trough the input amplifier.

5.9 Controller design

The entire stabilizing loop is carefully identified in the section above. These results allow to create sufficiently precise model of the stabilizing control loop and design a controller which would satisfy desired closed loop properties. The stabilizing loop includes amplifiers that impose strong constraints on the achievable closed loop results. The most significant limitations of the stabilizing loop are the high pass filters implemented in both amplifiers. This results in floating of the entire stabilizing loop without having fixed zero signal. Despite this drawback, these filters are necessary due to systems mechanical instability. The fluctuations in low frequencies have significant values and would heavily perturb the stabilizing loop operation. These difficulties are caused by the mechanical modifications necessary to implement the electrostatic actuator at the cantilever free end.

The required closed loop properties/functionality can be summarized as follow:

- The main functionality of the designed controller is to maximally attenuate any cantilever displacement, whatever is the origin. The controller does not have to distinguish between the thermal perturbations or the surface interaction forces.
- The controller has to operate on a large bandwidth to attenuate simultaneously multiple cantilever harmonic modes.
- There is not direct requirement for the controller tracking capabilities which simplifies controller design. The desired cantilever position value will be set constant during the cooling mode operation.
- The Atomic Force Microscopes are extremely sensitive instruments which results in presence of a significant noise levels that perturb the system. The sources of a different noises and their approximate amplitudes have been analyzed at the beginning of the section 4.1. These operation distortions will be modeled by noise sources implemented in the simulation presented in section 5.10. The controller has to be designed robustly to be able to overcome the presence of these noises in the control loop and maintain the system stability.
- Further robustness requirements are coming from the inaccuracy of the cantilever model used for the controller design. The simulation presented in section 3.3 and the identification in section 3.6 revealed the possible cantilever model discrepancies depending on the manufacturing accuracy and additional cantilever modifications (coating, mounting a sphere, ...). The designed controller has to be able to cope with this discrepancy and remain in a stable operation.
- The last requirements are the technical limitations of the experimental system. The real time controller implemented into the FPGA has a limited size of the discrete transfer function. The highest possible regulator order is eight with maximal sampling frequency 50 MHz.

The requirements for the controller robustness suggest H_∞ technique [165, 166] or a pole placement technique [167]. The pole placement technique combined with the frequency response sensitivity functions shaping [168, 169] has been chosen for the controller design. It is well suited for multimode oscillatory systems, and their control and oscillations attenuation. Further more, the designer can chose the order of the controller at the beginning of the design process. This has great importance for possible experimental validation of designed controller on a real time system that has limited order of implemented discrete controller. The H_∞ methods usually lead to high order controllers witch has to be later decimated to required order.

The pole placement technique permits to design a controller by shaping the closed loop sensitivity functions. Their shapes are adjusted by choice of the controllers poles and zeros. The closed loop system including the controlled plant and the regulator is shown in figure 5.24. The plant representing the regulated system is defined by the transfer function with row vector A and B. The sensor transfer function has been added to the standard schema and is represented by row vectors D_1 and D_2. The controller is divided into three distinctive part R, S and T where each of them is an independent vector of coefficients. The desired value of the plant output is denoted as r(t) and in this application will equal to constant (zero). Other two important variables present in this schema are the plant input u(t) and the plant output y(t). The schema includes two sources of perturbation: the plant input perturbation du(t) and the plant output perturbation dy(t).

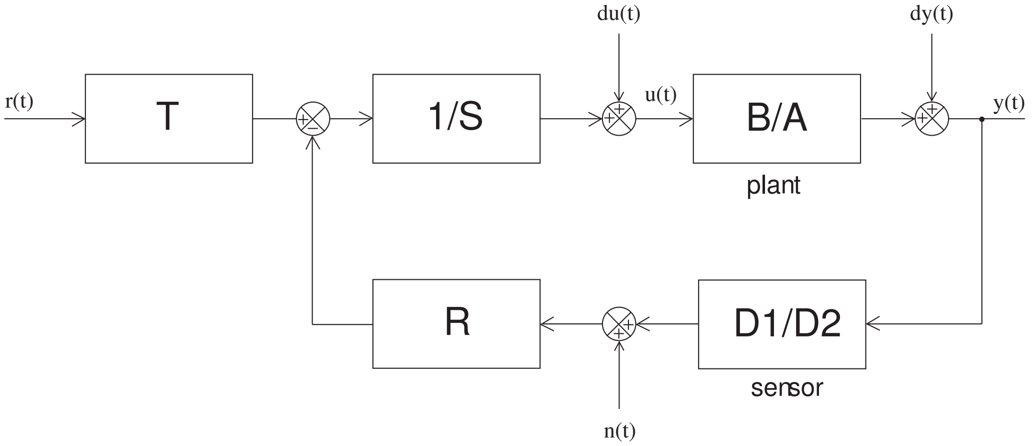

Figure 5.24: Closed regulation loop with an RST controller.

The effects of the perturbations present in the control loop can be analyzed through the sensitivity functions. Furthermore, these function are used for analysis of the system robustness to the modeling error. The shape of these functions assures the system performance and the ability to reject disturbances. Three disturbances are present in the loop: output disturbance, input disturbance and measurement noise. The influence of these disturbances on closed loop system performance can be analyzed with three sensitivity functions:

The **output sensitivity function** is the transfer function between the output disturbance dy(t) and the plant output y(t).

$$S_{y\,dy}(\omega) = \frac{A(\omega)\cdot S(\omega)\cdot D_2(\omega)}{A(\omega)\cdot S(\omega)\cdot D_2(\omega) + B(\omega)\cdot R(\omega)\cdot D_1(\omega)} \tag{5.38}$$

The **input sensitivity function** is the transfer function between the output disturbance dy(t) and the plant input u(t).

$$S_{u\,dy}(\omega) = \frac{-A(\omega)\cdot R(\omega)\cdot D_1(\omega)}{A(\omega)\cdot S(\omega)\cdot D_2(\omega) + B(\omega)\cdot R(\omega)\cdot D_1(\omega)} \tag{5.39}$$

The **noise sensitivity function** is the transfer function between the measurement noise n(t) and the plant output y(t).

$$S_{y\,n}(\omega) = \frac{-B(\omega)\cdot R(\omega)\cdot D_2(\omega)}{A(\omega)\cdot S(\omega)\cdot D_2(\omega) + B(\omega)\cdot R(\omega)\cdot D_1(\omega)} \tag{5.40}$$

The sensitivity functions permit to determine the closed loop system performance. A robustness margins can be deployed to quantitatively evaluate the closed loop system robustness [137, 167]. The amplitude margin and the phase margin are well known from the linear control systems design. These two margins can be directly determined from the Nyquist plot or from the Bode diagram of the open loop transfer function. They are often used for a controller design in the frequency domain and to determine the system stability. These margins do not completely satisfy the requirements for the robust controller design. The modulus margin and the delay margin are introduced to better evaluate the robustness of the designed controller. All four of these margins determine the system stability and permit to design a stable controller for given application.

The **gain margin** ΔG is the inverse of the magnitude of the open loop transfer function $|H_{OL}(\omega)|$ at the frequency $\omega_{-180deg}$ where the phase equals to -180 degrees. In terms of decibels: $\Delta GdB = -20log\left|H_{OL}(\omega_{-180deg})\right|$.

The **phase margin** $\Delta\Phi$ is the amount of additional phase shift at the gain crossover frequency required to bring the system to the edge of instability. The gain crossover frequency ω_c is the frequency where the magnitude of the open loop transfer function $|H_{OL}(\omega)|$ equals to one.

The **modulus margin** ΔM is the inverse of the maximum modulus of the output sensitivity function $S_{y\,dy}(\omega)$. The modulus margin is defined as a radius of a circle placed at critical point [-1, j0] of the Nyquist plot which is touching the Nyquist plot of the open loop $|H_{OL}(\omega)|$. In terms of decibels: $\Delta MdB = \left|1 + H_{OL}(\omega)\right|_{min} dB = (\left|S_{y\,dy}(\omega)\right|_{max})^{-1}dB = -\left|S_{y\,dy}(\omega)\right|_{max} dB$

The **delay margin** $\Delta\tau$ can be obtained from the phase margin and represent a time delay that will introduce a phase lag resulting in the system instability. $\Delta\tau = \Delta\Phi/\omega_c$. This margin has a great importance for the systems with time delay or with multiple vibration modes.

The presented margins have to have certain values to achieve robust controller design:

- $\Delta M \geq -6dB$, minimum -8dB
- $\Delta\tau \geq T_s$, minimum $0.75T_s$, where T_s is the discrete controller sampling rate.
- The gain margin and the phase margin are predefined by the modulus margin $\Delta M \geq -6dB$ and equal: $\Delta G \geq 6dB$ and $\Delta\Phi > 29deg$.

The stabilizing controller has been designed in the Matlab environment with the help of the control toolbox. The stabilizing control loop model used for the controller design is shown in figure 5.11. The loop has been implemented into the Matlab and the transfer functions of each block have been set according to the identification results obtained in section 5.8. The photodetector and the input amplifier transfer functions are inserted into the vectors D_1 and D_2. The output amplifier, actuator and cantilever transfer functions have been implemented into the plant row vectors A and B.

The design has been performed for the cantilever Veeco MPP-32220 indentified in section 3.6. The cantilever mechanical parameters provided by manufacturer are shown in table 5.1. The thermal identification revealed that the real properties are different due to the mounted sphere and the manufacturing inaccuracy, see table 3.6. In our model, the mass of the sphere mounted at the cantilever free end has been set to $5 \cdot 10^{-12}kg$. New cantilever parameters have been found to better match the thermal identification results, see table 5.1. These parameters have been incorporated into the multimode model presented in section 3.5 and transformed to a simple transfer function inserted into the control loop.

It has been already mentioned that the controller has to be robust to be able to cope with the model discrepancy. To test model discrepancy robustness, the cantilever thickness will be used as a parameter which will be modified ±20%. The resonance frequencies and the spring constants of the cantilever with these modifications are shown in table 5.1.

Description	data sheet min	data sheet max	thickness−20% blue curve	thermal ident. black curve	thickness+20% red curve
length [μm]	515	535	515	515	515
width [μm]	25	35	39	39	39
thickness [μm]	1.5	2.5	2.24	2.8	3.36
resonant freq. [kHz]	17	20	11.02	14.05	17.08
force constant [N/m]	0.1	0.1	0.15	0.29	0.52

Table 5.1: The characteristics of contact silicon cantilever Veeco MPP-32220 used for the controller design.

The controller design has been performed manually in a graphical design tool named “rltool" in the Matlab. This tool allows to design a controller by placing the poles and the zeros directly into a root-locus or an open loop Bode diagram of the control loop. This is performed manually and achieved results can be displayed in a wide variety of Bode plots, Nyquist plots, root-locus diagrams and step responses. All margins determining the controller robustness can be directly shown in this graphical environment.

The regulated micro system is operating with less than nanometer displacements y(t) and pico newtons of the interaction force dy(t). On the other hand, the controller at its output u(t) operates with hundreds of milivolts which drive the electrostatic actuator. From this simplified overview it is visible that there is multiple order difference between the measured values ($\approx 10^{-9}$m) and the applied signals ($\approx 10^{-1}$V). This puts additional requirements on the tools that can be used for the controller design if is required to design the controller for the plant in its original scale. The control toolbox "rltool” is able to work with the system at the original scale without difficulties and the design has been performed without system rescaling. The sensitivity functions shown at the end of this section are in the original scales.

The open loop Bode diagram of the stabilizing control loop is shown in figure 5.25. The black curve stands for the cantilever matching the thermal identification results, the blue curve is for the lever with the thickness lowered by 20% and the red curve is for the thickness increased by 20%. The crosses stand for the poles and the circles for the zeros of the open loop (for these three cantilever thicknesses). From the Bode diagram, it is visible the significant change of the system sensitivity at frequencies bellow the first resonance (200-30k rad/sec) caused by the changing cantilever thickness. This underlines the advantages to use very soft cantilever for the cooling mode measurements.
The green crosses and circles represent the poles and the zeros of the designed controller. They have been placed manually to achieve maximal attenuation of the cantilever harmonic modes and maintaining the loop stability. The position of the poles and the zeros have been set with the help of the root-locus diagram which will be shown later. The designed controller gain and a list of poles and zeros are shown in figure 5.26. The controller parameters shown in this figure will be used in all simulations of Cooling mode operation presented in this chapter.
The measurement bandwidth of the stabilizing loop is given by the transfer functions of the amplifiers with integrated band pass filters. The group of poles placed at higher frequencies is used to attenuate all noises above the measurement bandwidth.

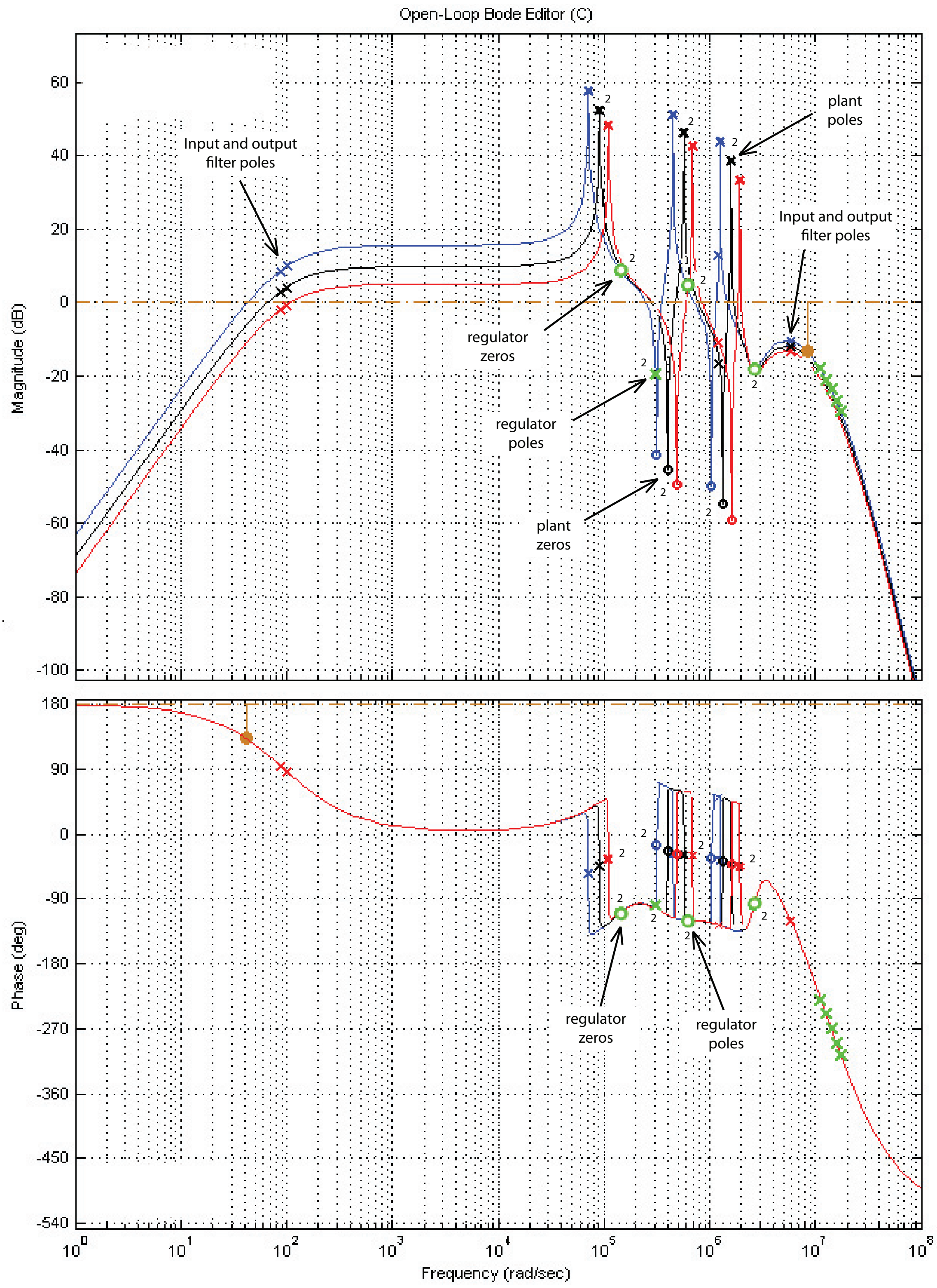

Figure 5.25: An open loop Bode diagram. black curve - cantilever matching the thermal identification, blue curve - thickness lowered by 20%, red curve - thickness increased by 20%. A cross stands for a pole and a circle for a zero of the open loop transfer function. Small index “2" next to the poles and zeros signify that they are complex.

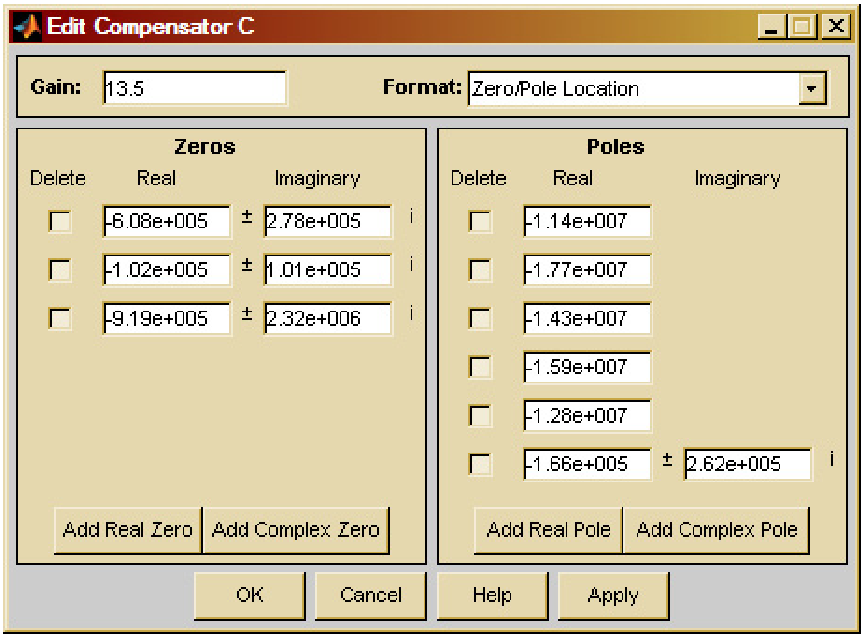

Gain: 13.5

Format: Zero/Pole Location

Zeros

Delete	Real		Imaginary	
☐	-6.08e+005	±	2.78e+005	i
☐	-1.02e+005	±	1.01e+005	i
☐	-9.19e+005	±	2.32e+006	i

Poles

Delete	Real		Imaginary	
☐	-1.14e+007			
☐	-1.77e+007			
☐	-1.43e+007			
☐	-1.59e+007			
☐	-1.28e+007			
☐	-1.66e+005	±	2.62e+005	i

Figure 5.26: A screen shot of the “rltool" with the controllers gain, poles and zeros. The regulator using these parameters is used for all following simulation.

The controller gain has been set relatively low to obtain maximal robustness and to be able to later use the manual gain that is implemented into the output amplifier. The resulting gain and phase margins are listed in table 5.2. These margins are far above the robustness requirements stated earlier.

	gain margin ΔG [dB]	phase margin $\Delta\Phi$ [deg]
thickness−20%	13.1	-48.1
thermal ident.	14.8	46.1
thickness+20%	16.2	45.5

Table 5.2: The gain margin and the phase margin obtained with designed controller.

The root-locus diagram of the closed control loop have to be shown before approaching to the sensitivity functions and further investigation of the modulus margins. The root-locus diagram shown in figure 5.27 does not display the group of a high frequency poles which are above the measurement bandwidth. They are not directly contributing to the cantilever vibration attenuation. The shown zoom at the lower frequency part includes the entire measurement bandwidth with the first three cantilever harmonic modes. This diagram uses the same notation for the poles and the zeros as in the open loop bode diagram. The cantilever poles and zeros are complex. They are placed at the complex axis of the root-locus diagram. The magenta squares in the diagram represents position of the poles in the closed loop operation. Shown closed loop poles are for the same gains like in the Bode diagram.

The root-locus diagram allows to easily evaluate the cantilever harmonic modes attenuation/damping. The grey triangle represents a zone where the closed loop damping coefficient is 0.5 or higher. The cantilevers closed loop poles need to be placed inside this triangle for the system to have such damping coefficient. The diagram shows that the first two harmonic modes are in close proximity to this triangle and if the loop gain is increased they would be inside. The third harmonic mode damping is relatively weak due to the influence of the amplifiers band pass filters.

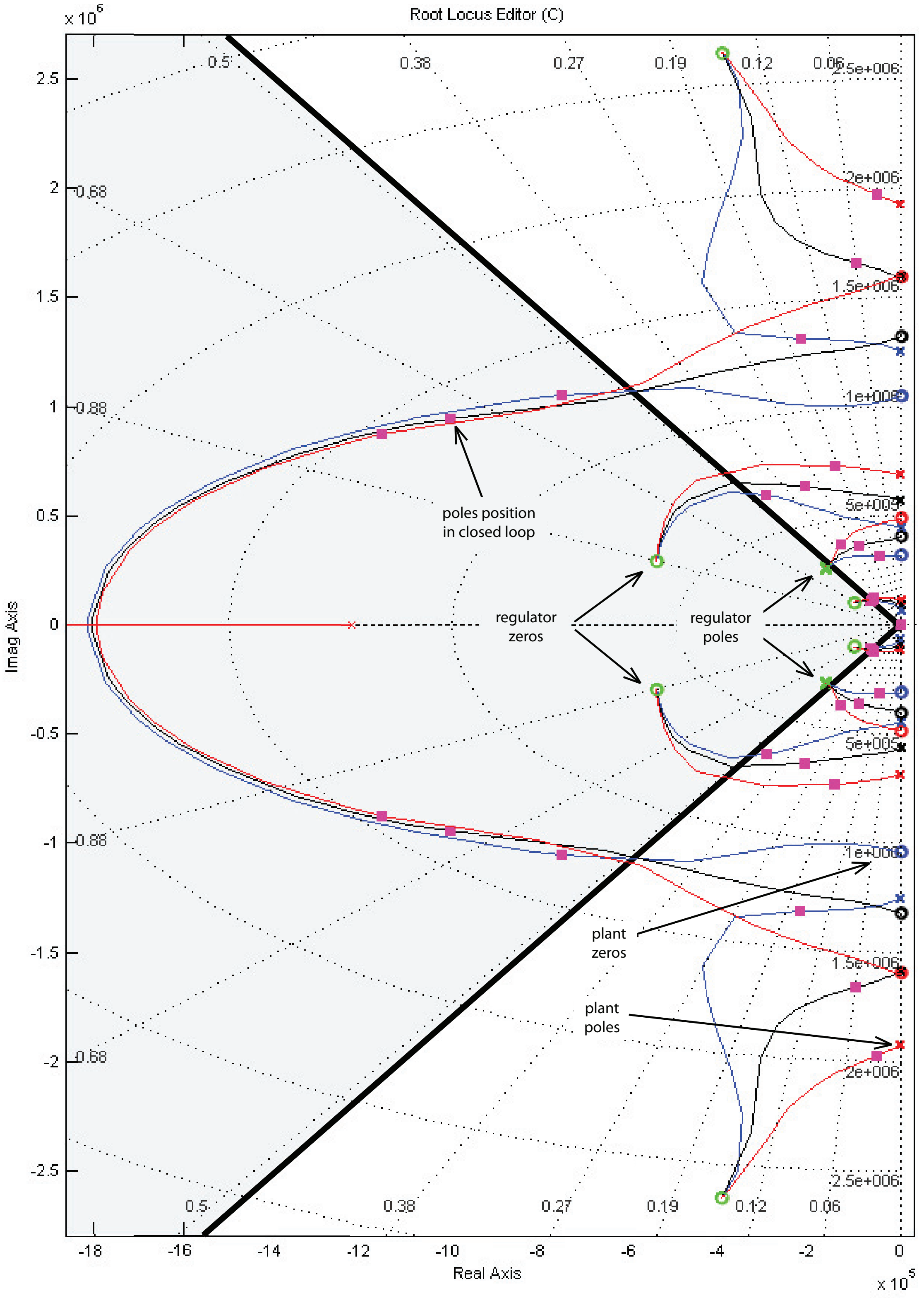

Figure 5.27: The closed control loop root-locus diagram. This diagram only shows the measurement bandwidth with the cantilever harmonic modes and the most significant regulators poles and zeros. The high frequency poles placed outside of this diagram zoom are not displayed. The magenta squares represent the closed loop systems poles.

There is a large reserve in the controller gain and if the closed loop gain is increased, the damping coefficient of the loop would increase. On the other hand, the weak gain improves the system robustness to the measurement noise. The controller will be used in this form and additional gain increase will be performed by the output amplifier.

The sensitivity functions have been introduced at the beginning of this section. The most important from the robustness point of view is the output sensitivity function shown in figure 5.28. The modulus margin of the control loop for the designed controller can be determined directly from the bode diagram. The modulus margin required for a robust design $\Delta M_{min} = -6dB$ is marked directly into the bode diagram. The achieved modulus margin equals $-|S_{y\,dy}(\omega)|_{max} = -3dB$ for the cantilever matching the thermal identification results (black curve). The sensitivity functions for the cantilevers with modified thickness are shown in the same bode diagram. The smallest modulus margin was obtained for the thickness decreased by 20% (blue curve) and equals -4dB. This is still under the robustness margin limitation.

The sensitivity function gives an information about how intensively are certain frequencies attenuated. In the diagram three significant drops in the amplitude corresponding to the three resonance peaks of the cantilever are visible. The stabilizing loop is able to attenuate output disturbances at these frequencies very efficiently. The flat part bellow the first resonant frequency corresponds to a frequency range where most of the surface interaction force will be present. The attenuation in this range is about 12dB.

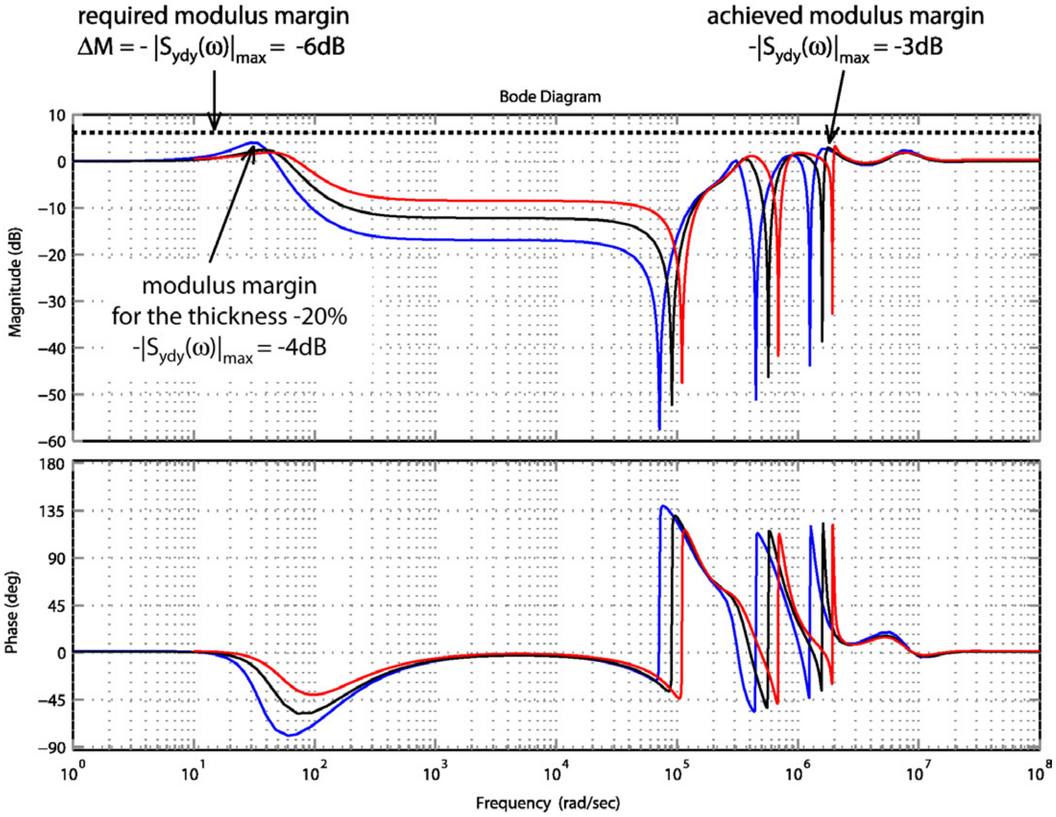

Figure 5.28: Output sensitivity function. black curve - cantilever matching the thermal identification, blue curve - thickness lowered by 20%, red curve - thickness increased by 20%.

The noise sensitivity function is shown in figure 5.29. The detection noise n has the biggest influence at the edges of the measurement bandwidth. The detection noise is well attenuated at the frequencies outside of the measurement bandwidth. The influence of the cantilever resonance peaks is not significantly visible due to sufficient controller robustness. Only the third harmonic mode has a small peak in the measurement noise response. The amplitude drops present between the resonance peaks correspond to the destructive interference of two neighboring cantilever harmonic modes and this attenuation is coming from the cantilever itself and not from the stabilizing control loop.

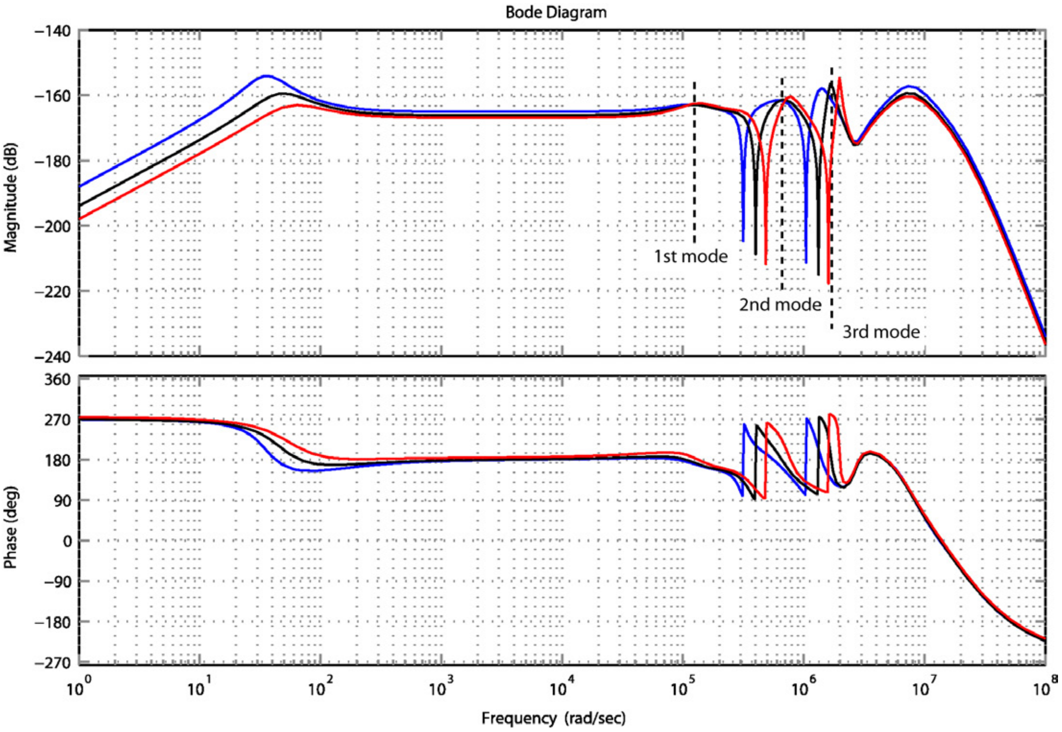

Figure 5.29: Measurement noise sensitivity function with marked position of the cantilever resonance peaks.

The input disturbance sensitivity is shown in figure 5.30. This can be interpreted as an approximate cantilever closed loop response to the thermal agitation. In the real system Langeving force is not applied through a band pass filter as it is done in our case. Here used plant model includes output amplifier band pass filter which is filtering the input perturbations!

The amplitudes of all harmonic modes are attenuated as required. Only the third harmonic mode has a visible resonance peak. The Bode diagram amplitude is decreasing with raising frequency due to the increasing effective spring constants of the higher harmonic modes. The same behavior is visible for example in figure 3.18, which shows a Bode diagram of a free cantilever (attention: plotted Bode diagrams are for different cantilevers). The cantilever multi-mode model used for controller design has only first three harmonic modes. In a real system Bode diagram the higher harmonic modes with slowly decreasing amplitudes for raising frequency will be present. The shown Bode diagram is missing these modes and its amplitude sharply falls with increasing frequency.

The input disturbance has the strongest influence at low frequencies and especially at the low edge of the measurement bandwidth. If the regulator gain is increased, the entire Bode diagram would decrease its amplitude. On the other hand, if a softer cantilever is used, the entire input disturbance sensitivity function would increase its amplitude.

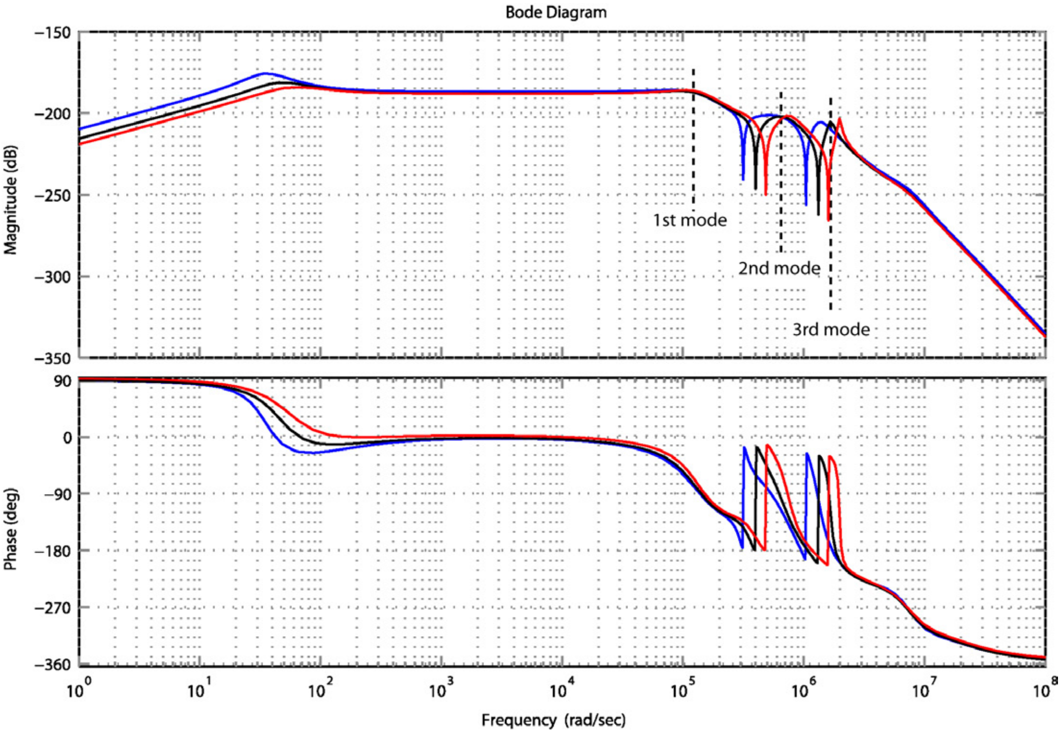

Figure 5.30: Input disturbance sensitivity.

The cooling mode does not have any requirements on the desired cantilever position *r(t)* tracking, because it is set to constant value during the system operation and usually equals zero. This is the reason why the vector T of the RST controller is set to gain 1 without any additional desired value conditioning. The sensitivity function between desired value *r(t)* and measured output *y(t)* is shown in figure 5.31.

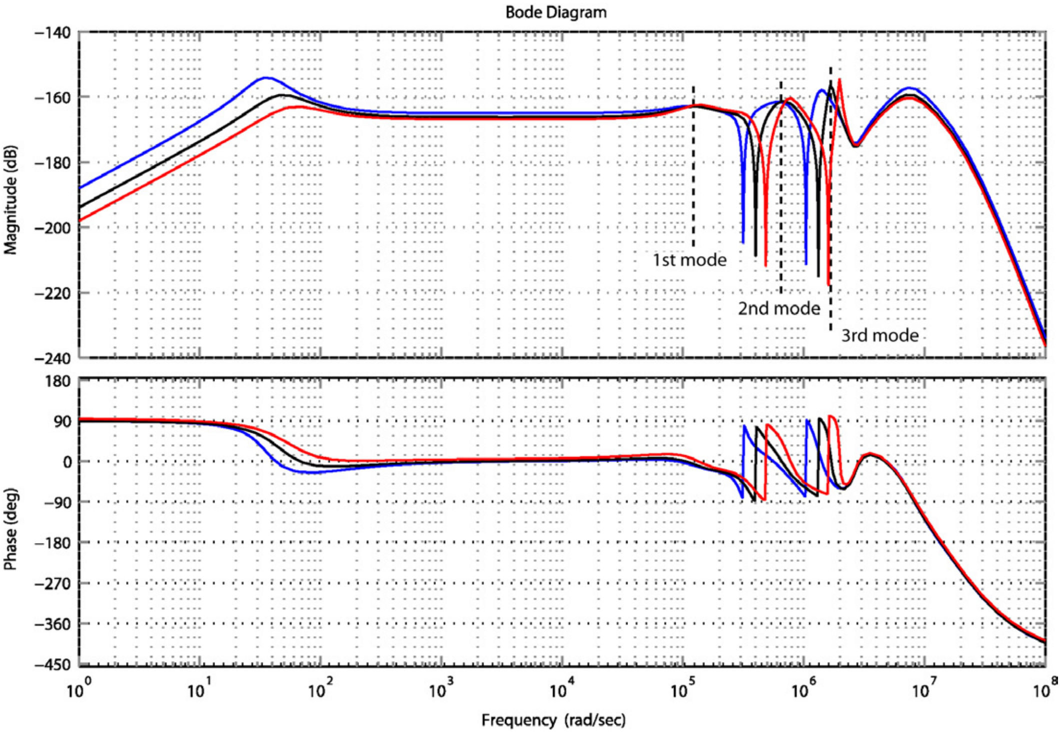

Figure 5.31: Desired value sensitivity function.

5.10 Cooling mode - Simulation

A numerical simulation of the cooling mode stabilizing control loop has been performed to verify proposed measurement mode. In section 3.7 and in chapter 4 the advantages of evaluating proposed techniques in simulation have been demonstrated. This approach offers great opportunity to directly compare detection or measurement results with modeled force which is known value. This is the main motivation to perform complete simulation of the real experimental setup identified in section 5.8.

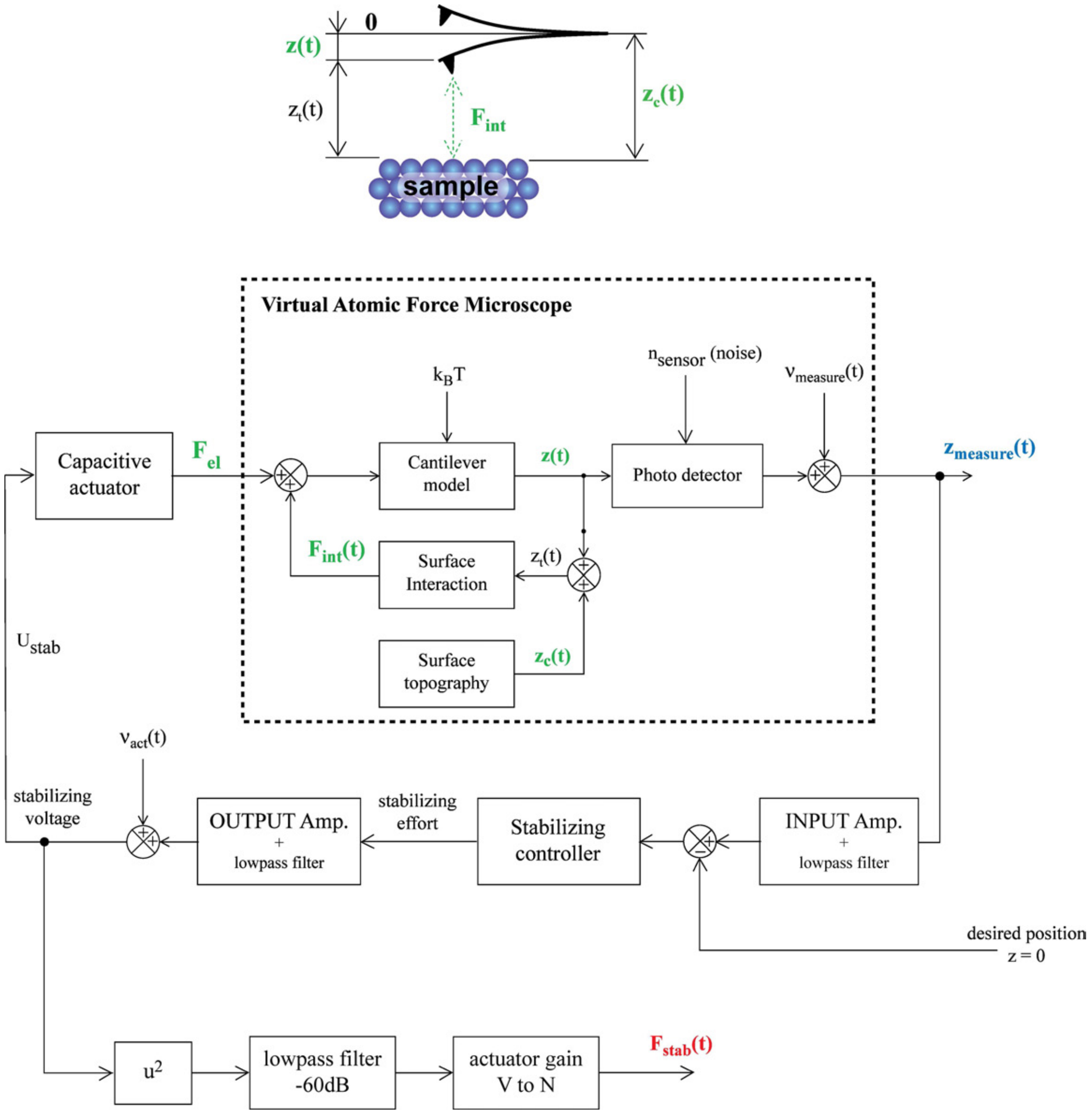

Figure 5.32: General cooling mode simulation schema.

The simulations have been performed in Matlab/Simulink environment with a numerical model of the entire experiment. General schema used for all following simulations is shown in figure 5.32. The central part of this schema is a virtual Atomic Force Microscope. The used model includes the photo-detector contrary to the observer simulations presented in chapter 4 to incorporate the transfer function of the position to electrical tension conversion. The schema as well includes the external stabilizing control loop consisting all individual electronic components (amplifiers and filters) that have to be used to combine the Nanotec AFM with the HERON controller. Their internal transfer functions correspond to values identified earlier. The controller response signal is converted with the actuators mathematical model based on known system mechanical properties into a force and applied to the cantilever.

The capacitive actuator is modeled as a non-linear system with internal function specified by equation 5.30. Some parameters of this equation cannot be directly measured on mechanical setup and only approximate values have been used at the beginning. The surface of the plates is defined by the cantilever width, which is well known and the actuator width, which is only estimated. The distance between the plates has been measured with an optical microscope with very low accuracy. A simple identification of the model have been performed to verify good correlation between the model and the real actuator. The tension used at the actuator input was the same as in real measurement and detected cantilever position was compared with the identification measurement, section 5.8.3. The comparison results shown certain discrepancy between the model and the experiment. The mechanical parameters: actuator width and plates distance had to be manually adjusted to achieve equivalent response. In table 5.3 original approximate mechanical parameters of the electrostatic actuator and adjusted parameters to match the identification are shown.

mechanical property	original	adjusted
cantilever width (w) [μm]	35	39
actuator width (w_{act}) [μm]	35	70
plates distance (d_{act}) [μm]	25	16

Table 5.3: Mechanical parameters of the electrostatic actuator model.

Adjusted actuator's response fits the identification results performed for triangular signal of amplitude 1.8V to 5.8V, see figure 5.17. Therefore, the identification amplitude range is higher than visioned operation range 0.4V to 1.8V. The identification measurement has been performed at this higher range to measure the cantilever displacement heavily perturbed by thermal and detection noise, see figure 5.17 C). The identification results can be easily transferred to desired tension range with the help of the adjusted electrostatic actuator model. The model response in the range 0.4V to 1.8V can be then easily linearized to find a new actuator gain. In figure 5.33 model response with its linear fits for the identified input voltage range and the desired operational range is shown. The equations of the linear fits are displayed for both ranges. The actuator gain measured in section 5.8.3 equals to $3.7 \cdot 10^{-10} N/V$. The actuator gain in the operation voltage range is lower due to the non linearity of equation 5.30 and equals $9.3 \cdot 10^{-11} N/V$.

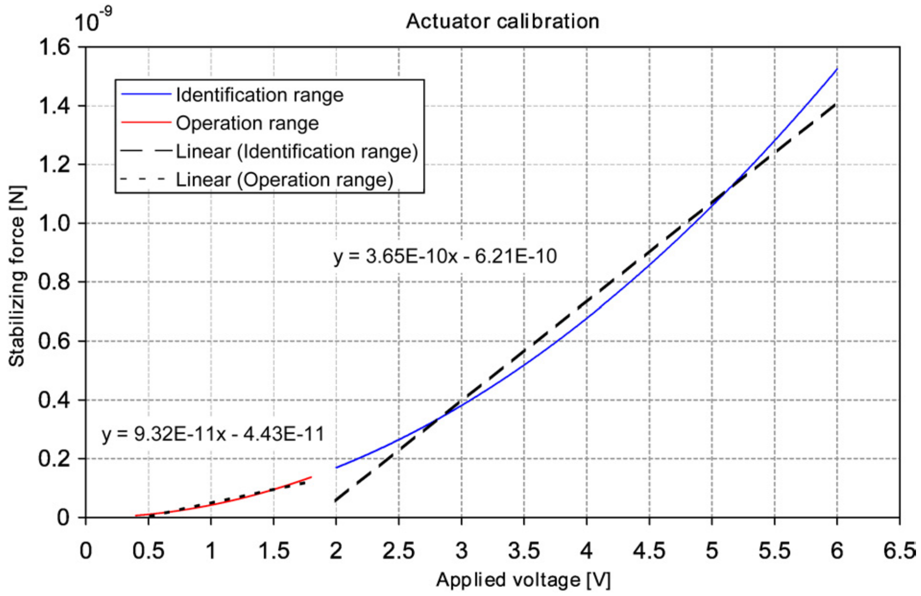

Figure 5.33: Linearization of the electrostatic actuator in identification and operation range.

Numerical simulation of the stabilizing control loop has been performed with accurate model of the entire experimental setup shown in figure 5.32. Both amplifiers have an internal transfer functions identified in section 5.8.2 and the output amplifier offsets the controller voltage to desired 1.1V and has gain 1.3. The cantilever model is based on the parameters obtained by identification in section 3.6.2. Used controller was designed for identical cantilever in previous section. In figure 5.34 time sequence of free thermally excited cantilever - open control loop is shown. The vibration amplitude varies according to the systems random perturbations, and shown time section is only an example. The cantilever is statically deflected about 2.5 nm by output amplifier offset voltage 1.1V and randomly vibrates around this equilibrium point.

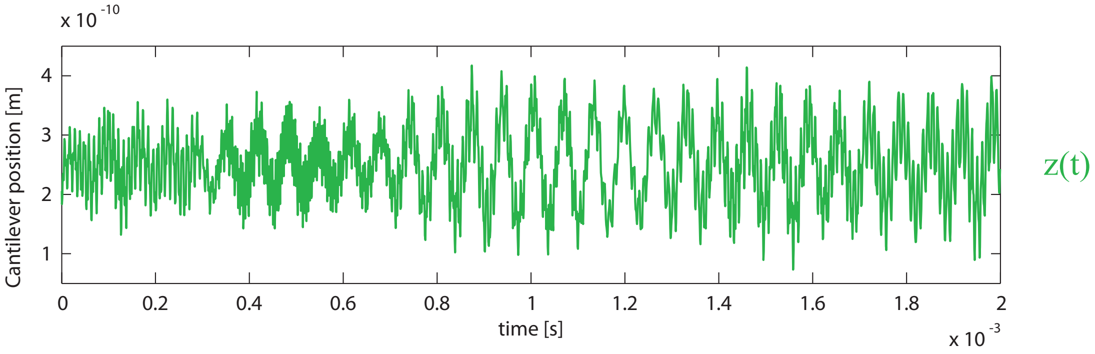

Figure 5.34: Free cantilever thermal vibrations.

Surface interaction

Next step is to approach to the modeled surface, introduce surface interaction force and observe cantilever response. There are two possibilities to operate the lateral scanner according to the measurement bandwidth introduced in section 5.5. For the moment only fast lateral scanning will be presented. The topography is modeled as distance $z_c(t)$ between the cantilevers fixed end and the surface. This distance has constant part of 5nm with added 5nm square signal of frequency 2kHz. The entire topography is bandwidth limited to 30kHz to achieve more realistic properties of surface, see figure 5.35 A). The free cantilever interacts with this modeled surface with relative weak interaction force displayed in figure 5.35 B) where small variation of the interaction force caused by thermal agitation are visible. Resulting cantilever position is shown in figure 5.35 C). The influence of the interaction force is visible from the cantilever displacement. The interaction bandwidth is large and covers the cantilever first harmonic mode. This results in possible excitation of the first harmonic mode by the interaction force. The induced vibrations amplitude depends on the presence of some topography sub-harmonic in close proximity to the cantilever resonance peak.

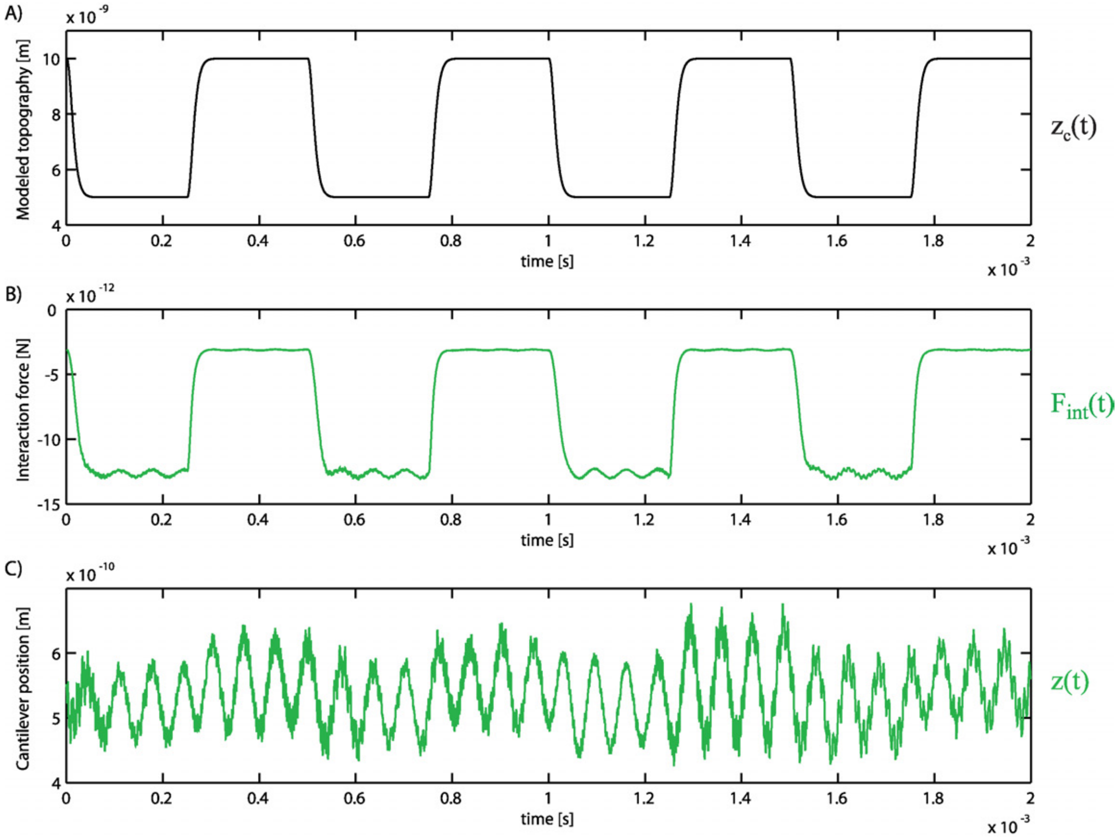

Figure 5.35: A) Modeled sample topography. B) Tip-sample interaction force. C) Cantilever displacement caused by surface interaction and thermal perturbation.

Thermal vibration attenuation

The cold damping theory has been introduced in this chapter beginning. A numerical simulation of the thermally excited cantilever displacement damping with the feedback loop will be shown. The cantilever is placed far away from the modeled surface $z_c(t) \rightarrow \infty$ and any surface interaction force is not present. The stabilizing control loop is closed as shown in figure 5.32, and a spectral density of the lever displacement is calculated. Three independent noise sources are present in this simulation: thermal, measurement and actuation noise. Thermal noise model has been presented in section 3.4 and is simulated according to this theoretical description. The measurement/detection noise variation $\langle \nu_{measure}^2(t) \rangle = 1 \cdot 10^{-22} m$ which is higher then result obtained during measurements with Nanotec AFM. The choice to perform the simulation with higher measurement noise is to test the performance and robustness of the designed controller. *The actuation noise*, more precisely stabilizing control loop electronic noise, variation was set to $\langle \nu_{act}^2(t) \rangle = 1 \cdot 10^{-6} V$. To clearly demonstrate the effects of active damping on cantilever displacement, multiple spectra have been simulated for different gains of stabilizing controller. In figure 5.36 black curve represents spectra of free thermally excited cantilever which is our reference to evaluate cooling results. The same graph shows cantilever spectra for different stabilizing controller gains in a range from 0.1 to 1.8. This gain was manually selected and controller output signal has been multiplied by this constant. In real-time measurement this would be achieved by selectable gain of the output amplifier.

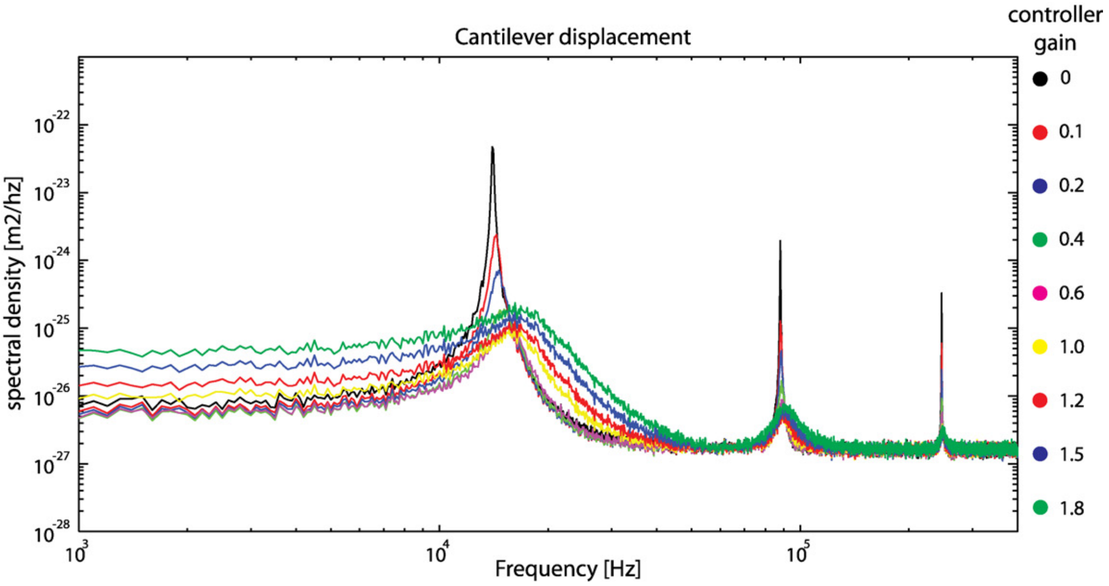

Figure 5.36: Spectral density of the first three harmonic modes cooled by the stabilizing control loop. The regulator gain is marked next to the spectra.

This graph clearly demonstrate the ability of the stabilizing control loop to effectively damp multiple harmonic modes of the cantilever. The first and the second harmonic mode are placed inside the band pass of the input amplifier and their attenuation is already significant for relatively low controller gains. The third harmonic mode is slightly behind the cut-off frequency of the band pass filter resulting in weaker attenuation of random displacement. Nevertheless, all three harmonic modes are attenuated three orders of original amplitude at the maximal controller gain. The detailed spectra sections for each harmonic mode are shown in figures 5.37, 5.38 and 5.39.
The presented spectra show that all three harmonic modes are shifted to higher frequencies with increasing controller gain. The designed controller is not purely derivative to be able to attenuate static cantilever deflection and that is the origin of the harmonic modes frequency shift. The frequency of attenuated harmonic modes is not really important in this system, because it is operating statically and the interaction is detected in its original frequency bandwidth. Therefore, the frequency shift cannot exceed certain limit which would cause the controller instability. The range of possible frequency shift is given by the controller robustness and can be chosen at the stage of controller design.

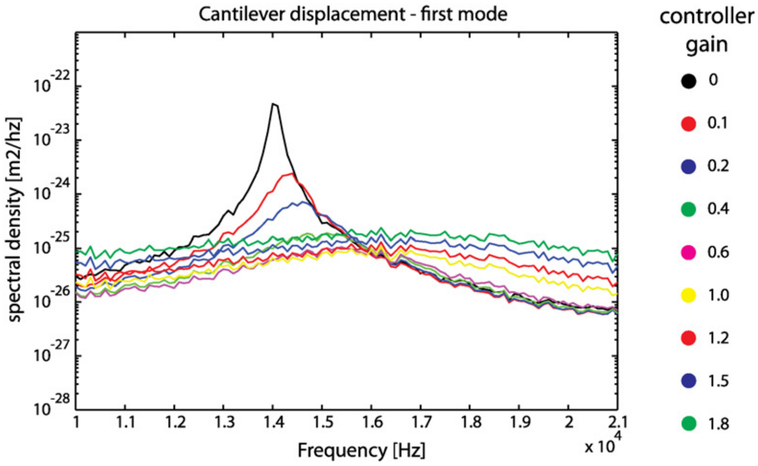

Figure 5.37: The first harmonic mode spectral density for different controller gains.

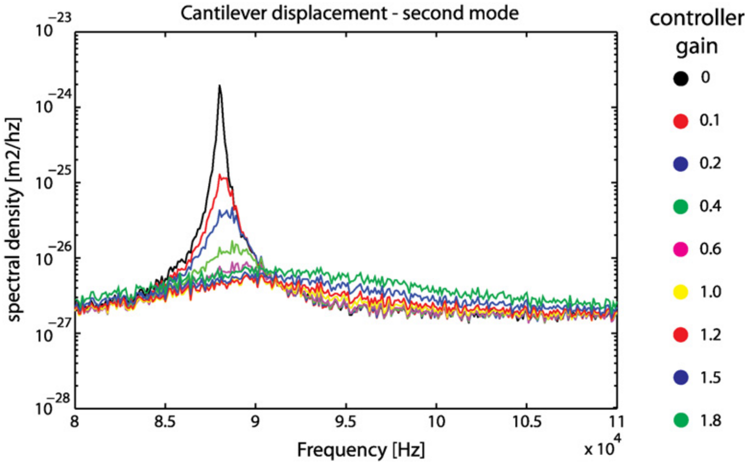

Figure 5.38: The second harmonic mode spectral density for different controller gains.

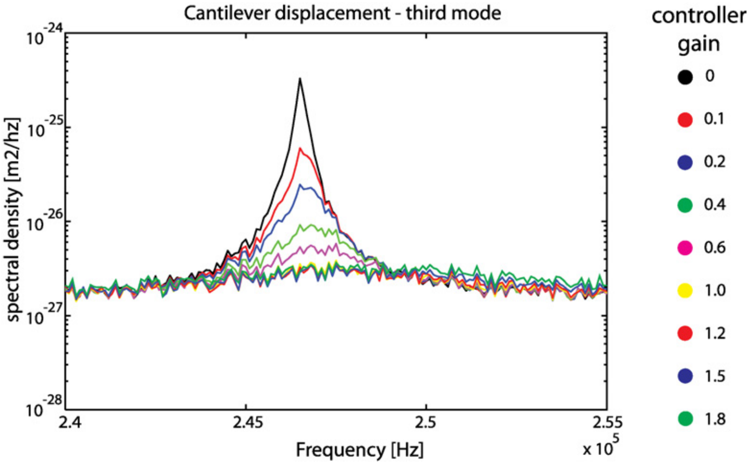

Figure 5.39: The third harmonic mode spectral density for different controller gains.

The spectra in figure 5.36 shows that for higher controller gains the low part of the frequency spectra starts to have higher amplitudes than in undamped (free) case. The amplification of low frequency displacement become significant for the gains higher than

1. This is caused by the measurement and the actuation noise which are re-injected into the electro-mechanical system. The presence of the measurement and the actuation noise in the simulation was mentioned earlier in this section. For high controller gains, their amplitude became comparable with Brownian motion of the damped cantilever. The controller amplifies this noise and applies it on the cantilever as a force causing excitation instead of the lever motion attenuation. This determines a limit to the maximal thermal displacement attenuation which cannot be overcome until the noises amplitudes are lowered. Detailed analysis of the limits in the reduction of Brownian motion has been presented and experimentally demonstrated by *Guillaume Jourdan* [170].

Figure 5.40 shows power spectral density of the stabilizing force $F_{stab}(t)$ for different controller gains. The floor of the spectra is given by the measurement and the actuation noise. The first three harmonic modes are visible for lower gains, but with increasing controller gain the amplitude of harmonic modes became comparable with the noise level. The first harmonic mode reached its maximal vibration attenuation at the gain equal to one and any further gain increase does not influence its thermal vibration level. The second and third mode reached its maximal attenuation later. For the second mode it is at the gain about 1.2. The attenuation maximum for third mode was not reached.

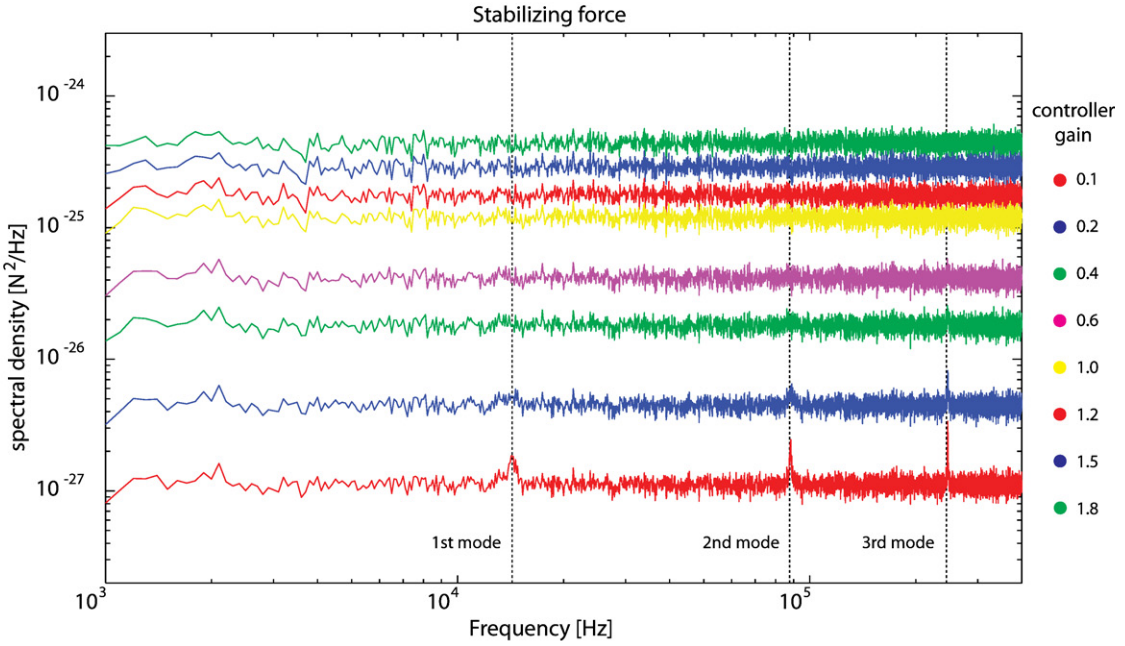

Figure 5.40: Power spectral density of the stabilizing force with the controller gain marked aside.

Large bandwidth measurement - simulation

In section 5.5 a large bandwidth measurement of the surface topography (interaction force) with the cooling mode was theoretically presented. A numerical simulation of this measurement with the experimental system model has been performed. The simulation was performed with closed stabilizing control loop shown in figure 5.32. The stabilizing controller gain was set to 1.5 which is sufficiently large to achieve desired attenuation of Brownian motion and the interaction force. The topography is modeled as distance $z_c(t)$ between the cantilever fixed end and the surface. This distance has constant part of 5 nm with added 5 nm square signal of frequency 2 kHz. The entire topography is bandwidth limited to 30 kHz to achieve more realistic surface properties, see figure 5.41 A). The corresponding interaction force $F_{int}(t)$ applied onto the cantilever is shown in figure 5.41 B). The used interaction force model is for a sharp silicon tip with radius 10 nm and flat silicon surfaces. The residual displacement of the cantilever $z_{measure}(t)$ caused by insufficient damping and counterbalancing the interaction force is shown in figure 5.41 C).

The stabilizing force needed to achieve these results has a large bandwidth with significant amplitudes at frequencies above the first harmonic mode which mask important surface interaction features at lower frequencies. In figure 5.41 D) stabilizing force $F_{stab}(t)$ with limited bandwidth to 30 kHz is shown. Dotted curve in the same graph is the result obtained with low past filter with cut-off frequency 50 kHz. This bandwidth limitation is set the same as the interaction force bandwidth. The stabilizing force is calculated from the stabilizing voltage of the output amplifier. This signal is squared as in equation 5.30 and multiplied by the actuator gain found from the actuator linearization. The stabilizing force has a constant value of about 165 pN corresponding to static deflection caused by the output amplifier offset voltage. The measured interaction force appears as a variation of the stabilizing force from this DC offset. From the graph, it can be determined that this stabilizing force variation equals about 5 pN. On the other hand, from the figure 5.41 B) it can be determined that the interaction force variation equals 9.5 pN. The missing 4.5 pN are in the residual cantilever displacement which was not completely eliminated by the controller. This displacement has amplitude about 12 pm and if is this number multiplied by the cantilever spring constant 0.298 N/m we will find force 4.17 pN corresponding to the missing value.

It has to be noted that the cooling mode is able to follow the interaction forces with large bandwidth without loosing the high frequency information. The standard non contact AFM operation mode appears as low pass filter that can only follow the low frequency changes, see for example the amplitude modulation simulated in section 4.3. The influence of the cantilever settle time is suppressed by the static operation mode and the active feedback that increases system damping. The cooling mode maximal measurement bandwidth is not limited by the cantilever dynamic and is directly determined by the stabilizing control loop.

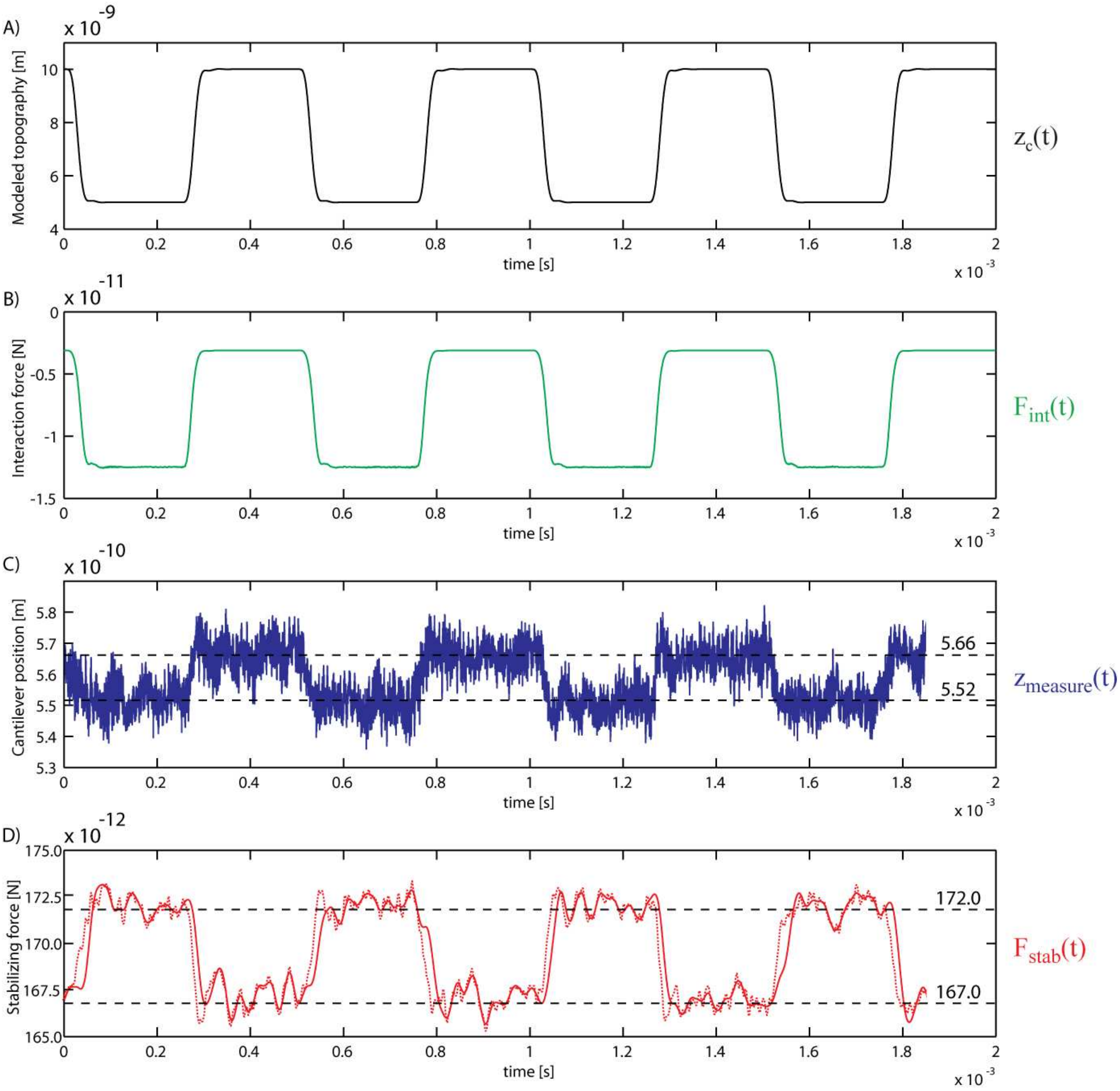

Figure 5.41: Large bandwidth measurement simulation. A) Modeled sample topography. B) Tip-sample interaction force. C) Residual cantilever displacement caused by the surface interaction and the thermal perturbation. D) The stabilizing force calculated from the stabilizing voltage.

Other possibility how to evaluate the performance of the cooling mode is to analyze a frequency spectra of the signal time sequences shown in figure 5.41. Figure 5.42 A) shows frequency spectra of the surface interaction force $F_{int}(t)$. This signal does not have any measurement noise (theoretical) and the lowest spectra value (the spectra floor) is given by calculation inaccuracy. Figure 5.42 B) shows the power spectra density of the residual cantilever deflection. The influence of the interaction force is clearly visible in this spectra and underlines that the stabilizing controller gain was not high enough to completely eliminate the lever displacement caused by the interaction force. On the other hand, the amplitude of the cantilever harmonic modes excited by the thermal agitation has very low amplitudes. Figure 5.42 C) shows the stabilizing force power spectral density calculated form the output amplifier output. This spectra is a bandwidth limited and is matching the modeled surface interaction spectra. The effort needed to counterbalance the thermal vibration of the first harmonic mode is very weakly visible around the frequency 15.3 kHz. Both graphs B) and C) are calculated from the signals with the measurement and the actuation noise which gives a floor (a background) to these spectral densities.

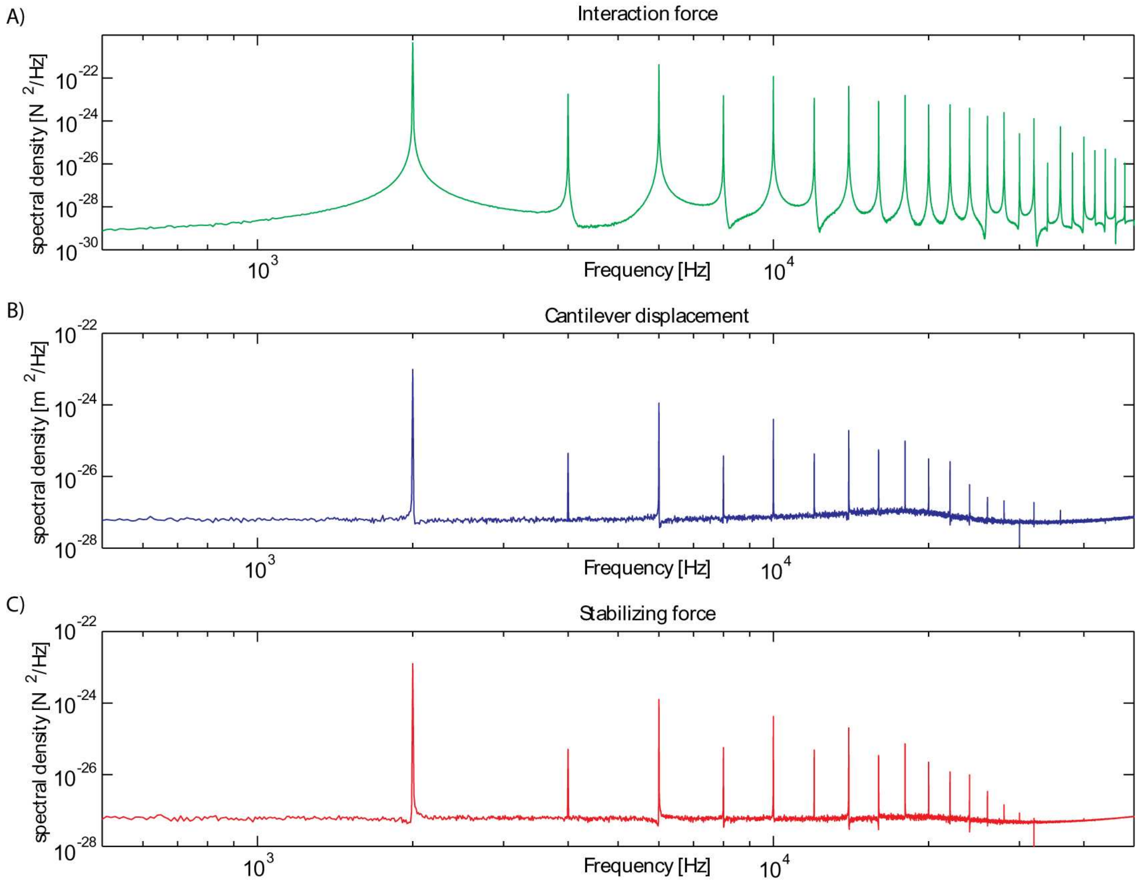

Figure 5.42: Large bandwidth measurement simulation. A) The surface interaction force spectra. B) The cantilever residual displacement spectra. C) Spectra of the stabilizing force calculated from the stabilizing voltage.

The same simulation as the one performed above has been done for different topography frequencies to further investigate the limitation of possible measurement speeds. There is many possibilities of the surface topography shapes and scanning speeds which determines the measurement bandwidth. Here, only one example would be shown, which is significant result that clearly set apart the cooling mode operation from the standard non-contact operation modes. The simulation has exactly same properties as previously performed one, only the square topography frequency is set higher then the first cantilever harmonic mode. The modeled cantilever has resonance frequency 15.3 kHz and used square topography has frequency 17 kHz and is bandwidth limited to 70 kHz. It is absolutely impossible to sense such high frequencies in the standard dynamic operation mode. The system speed is limited by the cantilever dynamic and all features of the surface would be lost. The chosen topography has other important property that makes the simulation very difficult. The frequency is in close proximity of the cantilever resonance which causes that the system is getting excited by the surface interaction and tend to oscillate. This simulation is an example of a “really bad" choice of the scanning speed in contrast with the cantilever properties. It has been mentioned earlier that in the cooling mode the systems dynamic is not given by the cantilever but by the stabilizing control loop.

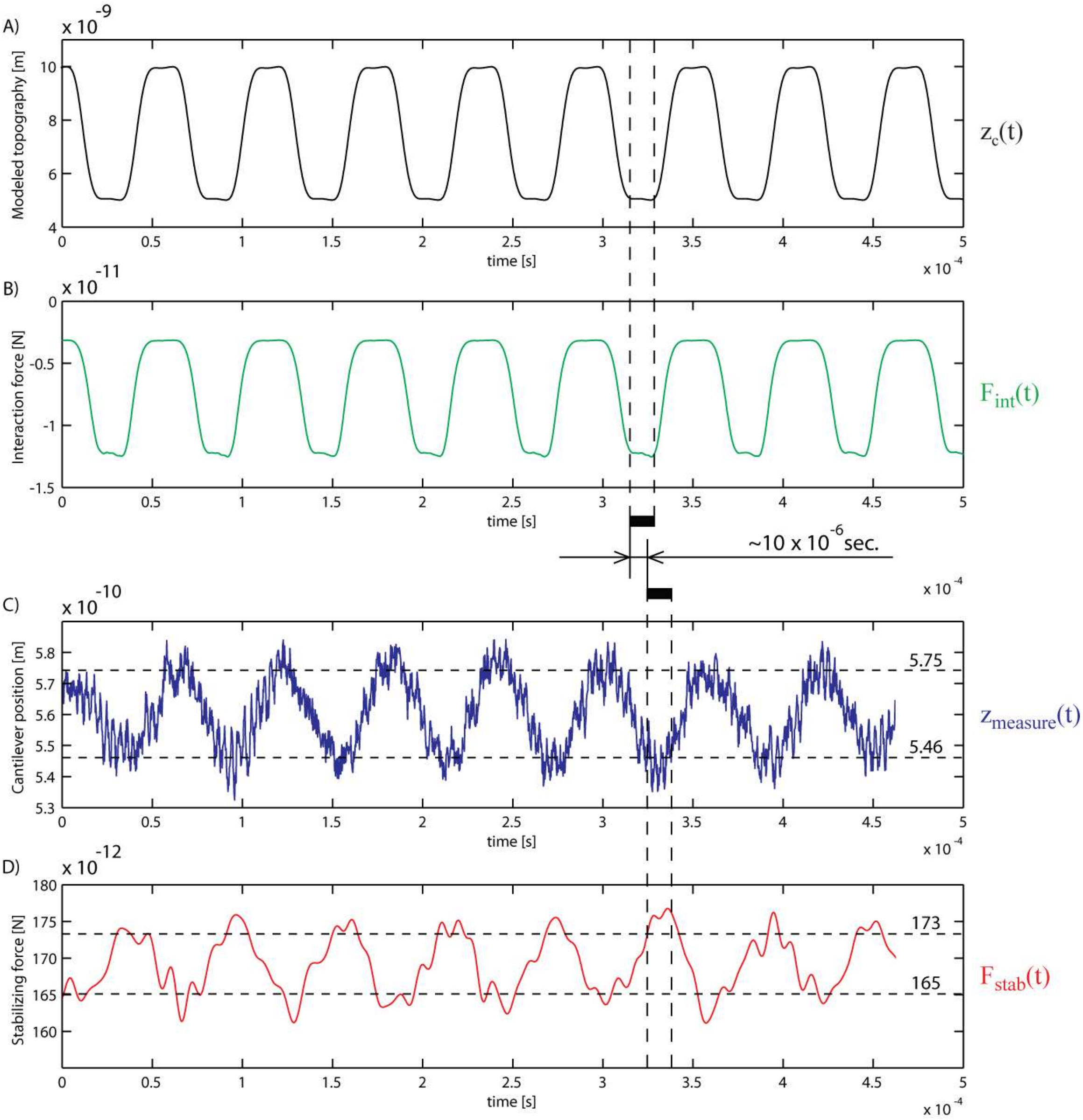

Figure 5.43: Large bandwidth measurement simulation. A) Modeled sample topography. B) Tip-sample interaction force. C) Residual cantilever displacement caused by the surface interaction and the thermal perturbation. D) Stabilizing force calculated from the stabilizing voltage.

Figure 5.43 shows the obtained simulation result. The graph A) displays the topography and B) the surface interaction force. From figure 5.43 C) is visible that the residual cantilever displacement is larger then in the previous simulation. For topography of 2 kHz this displacement was about 14pm, and in this simulation equals 29 pm. The stabilizing controller does not have sufficiently high gain to attenuate this displacement. Figure 5.43 C) shows the stabilizing force with limited bandwidth to 70 kHz. The shape of the surface interaction force despite strong perturbations of this signal is still visible. The time delay between the interaction force and counterbalancing stabilizing force in this simulation becomes not neglectable compare to the interaction force period and equals $10 \cdot 10^{-6} s$. This delay was neglectable in the previous simulation with 2 kHz topography. The time delay suggest that the system operates in a transient mode and the stabilizing loop is not sufficiently fast. The value of detected interaction force equals about 8 pN but the residual cantilever deflection corresponds to another 8.7 pN. The sum of these two forces is higher then the interaction force applied by the surface model to the cantilever. This all underlines the fact that the controller has difficulties to correctly counterbalance the interaction force and eliminate any lever displacement. The achieved results show that it is possible to operate the cooling mode at very high scan speeds, despite all difficulties. Such a fast measurement would be possible with improved stabilizing control loop and actuator. This simulation should be considered as the worst possible case due to conditioning of the cantilever and the surface properties.

Force accuracy measurement - simulation

The last simulation focuses at the measurement accuracy. More precisely, it tries to explore the force sensitivity limitation of the cooling mode. The choice of using exact model of the experimental setup is already giving significant limitations coming from the noise levels imposed by used electronic and detection system. Other limitation is the cantilever spring constant. For the experiment a cantilever with spring constant 0.298 N/m has been used, identified in section 3.6. The reason to use this lever was its exceptional length $525\mu m$ which allowed to perform the necessary mechanical modifications to place the electrostatic actuator at its free end. This cantilever is relatively soft but there exist levers with a spring constants ten times lower. This would give enormous advantage for this simulation because the measurement noise would be less significant in comparison with the deflection caused by the thermal excitation and the interaction force. The theoretical limitation of the force sensitivity has been shown in section 5.6 and is related to the energy given to the system by surrounding thermal bath. Here explored limits are given by the detection and actuation noise rather than Brownian motion.

The simulation is performed in exactly same configuration as already presented simulations. The distance $z_c(t)$ between the cantilever fixed end and the surface is set larger to achieve interaction forces in order of piconewtons. This distance has constant part of 10 nm with added 5 nm square signal representing the surface topography. The entire simulation is performed slower to comply with the conditions suggested by theoretical introduction in section 5.5. The topography has frequency 200 Hz and is bandwidth limited to 3 kHz to achieve realistic properties of the surface, see figure 5.44 A). The resulting interaction force alternates between 1.4 pN and 3.1pN, see figure 5.44 B). The residual cantilever displacement shown in figure 5.44 C) still includes displacement caused by the surface interaction but its amplitude is smaller than the maximum of the thermal vibrations. Stabilizing force shown in figure 5.44 D) is bandwidth limited to 3 kHz. The force detected from the stabilizing effort is 0.9 pN and corresponds to approximately half of the real force amplitude (1.7 pN). The missing 0.8pN are hidden in the residual cantilever displacement.

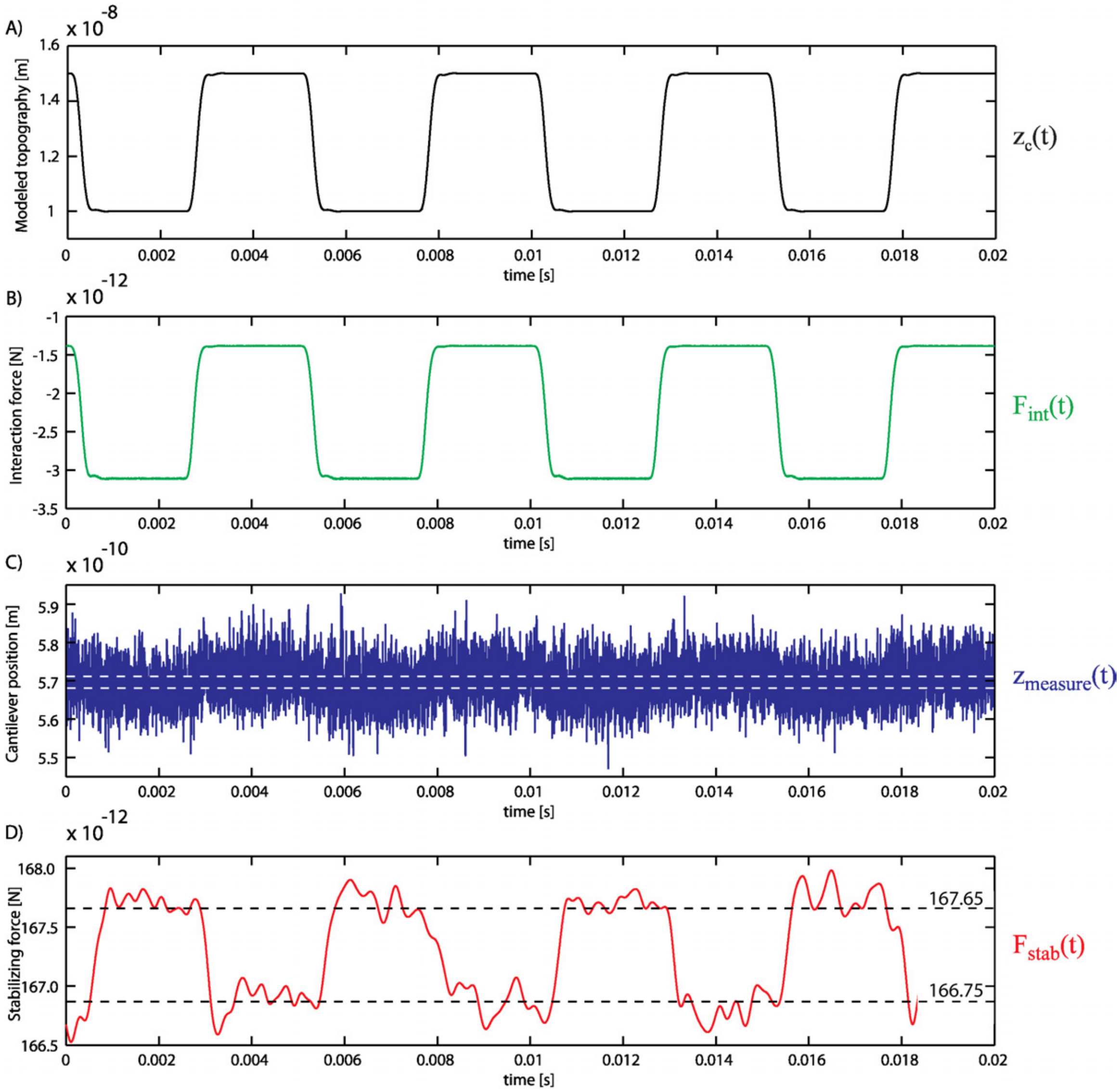

Figure 5.44: Force accuracy measurement simulation. A) Modeled sample topography. B) Tip-sample interaction force. C) Residual cantilever displacement caused by the surface interaction and the thermal perturbations. D) The stabilizing force calculated from the stabilizing voltage.

The power spectral densities of the interaction force, the residual cantilever displacement and the stabilizing force are shown in figure 5.45. The measurement and actuation noise have comparable values with the deflection caused by the surface interaction force. The spectra of the cantilever residual deflection shown in figure 5.45 B) is missing all interaction features above 20 kHz because they are masked by the detection and actuation noise. The stabilizing control loop is not able to detect and attenuate this higher part of the interaction force spectra.

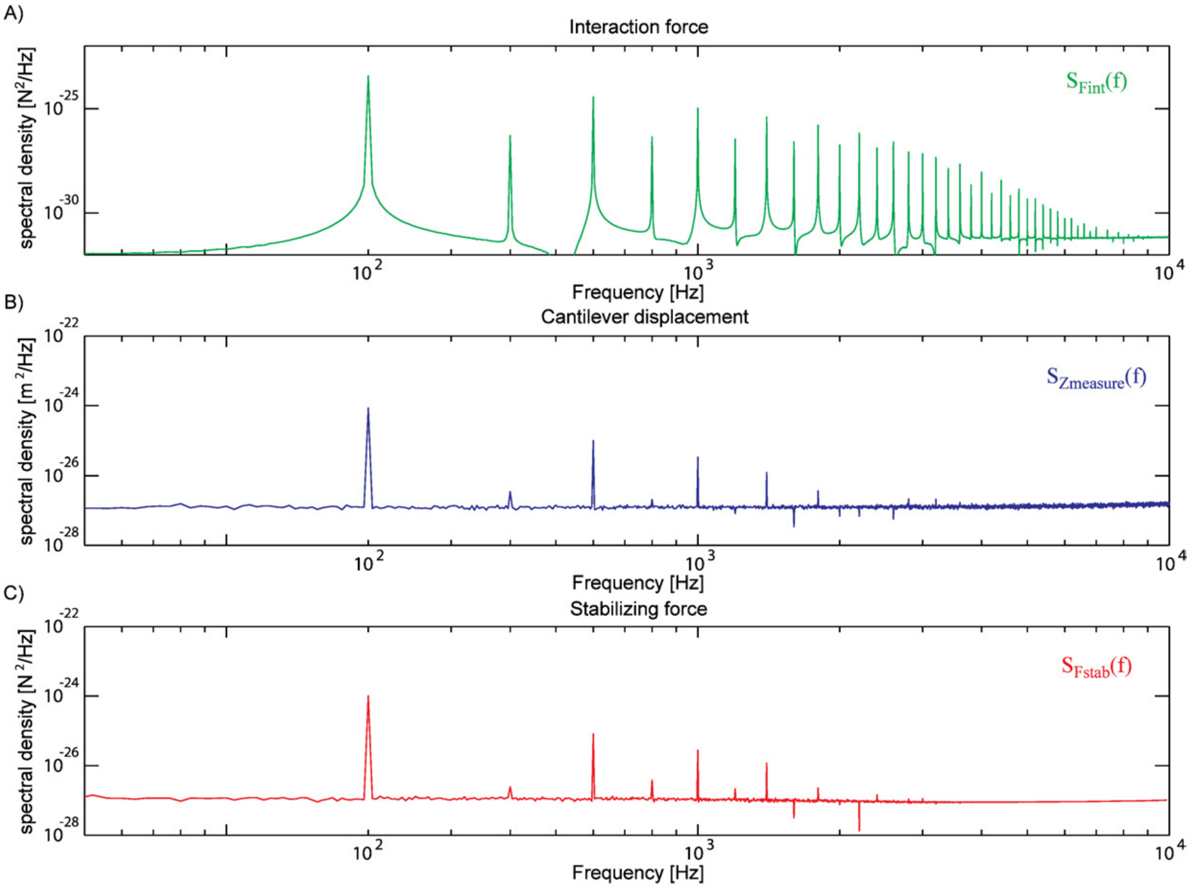

Figure 5.45: Force accuracy measurement simulation. A) The surface interaction force spectra. B) The cantilever residual displacement spectra. C) Spectra of the stabilizing force calculated from the stabilizing voltage.

Approach-retract curve

The aproach-retract curve simulation has been performed with the cooling mode to further validate its functionality and possible applications. This simulation reveals the cooling mode capability to counterbalance a strong surface interaction forces and maintain the cantilever in undeflected position. The approach-retract curve is simulated for the chip sample separation distance in a range from 20 nm to 1.5 nm. The separation distance is measured between the cantilever fixed end and the modeled surface. If the separation distance is smaller than 1.5 nm the stabilizing control loop is unable to maintain the cantilever stability and the lever snaps to the surface. To simulate the entire approach-retract curve as it has been presented in figure 5.4, it is necessary to increase the actuator gain. In other words, to increase the area of the actuator plates and decrease the separation distance between them, see section 5.7.

The presented simulation results are for the system as it has been identified without any additional modifications. The approach-retract curve cannot be simulated at very low frequencies due to the high pass filters implemented in the amplifiers. This is the reason why the simulation was performed at the frequency 100Hz. The cantilever is approaching the sample on a parabolic trajectory to minimize the influence of all transient behaviors during this simulation. The obtained results are shown in figure 5.46. The graph A) shows the surface interaction force $F_{int}(t)$ dependency on the separation distance. The graph B) shows this dependency for the electrostatic force $F_{el}(t)$ which is obtained directly from the actuator output. The electrostatic force has at the large separation distance offset 1.65 pN caused by the voltage offset 1.1V of the output amplifier. This counterbalancing force is not calculated from the output amplifier voltage as in the previous simulations, because the linearization is not valid at this large forces range. A precise non-linear converter describing the actuator properties would have to be used to obtain the counterbalancing force from the output amplifier voltage.

The residual cantilever displacement is shown in figure 5.46 C). The cantilever is deflected 5.7Å by the output amplifier offset voltage at the large separation distances. This static deflection decreases due to the surface interaction force during the approach-retract curve. The stabilizing loop in not able to fully counterbalance the surface interaction forces and the cantilever is deflected towards the surface at small separatioin distances.

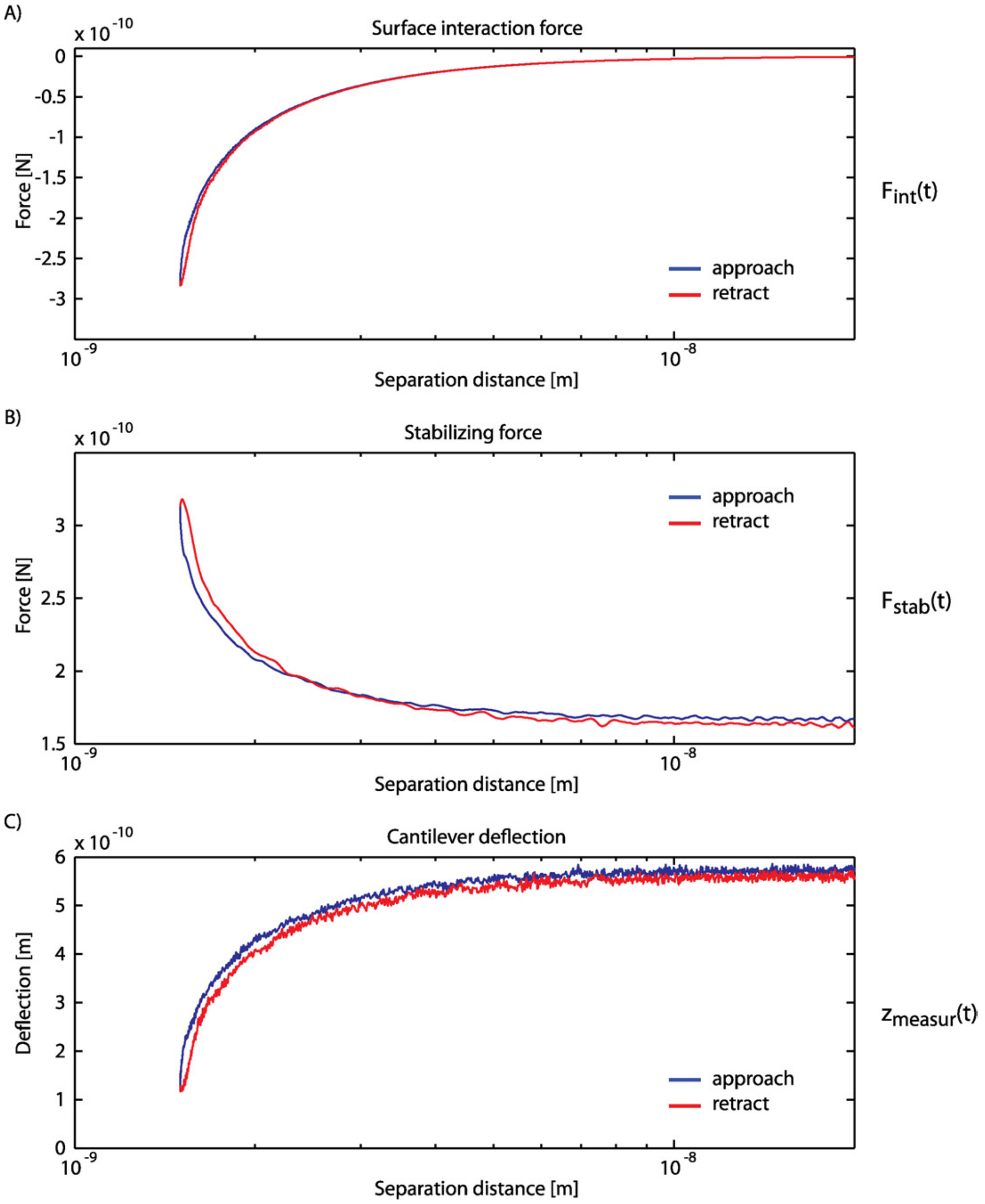

Figure 5.46: Approach retract curve. A) The surface interaction force. B) The actuator counterbalancing electrostatic force. C) The residual cantilever displacement.

5.11 Preliminary measurement results

The last step to verify proposed cooling mode technique is to experimentally validate the simulation results. The experimental setup with Nanotec AFM and all necessary electronic has been described and identified earlier in this chapter. The stabilizing control loop schema is shown in figure 5.11 and 3D image of the same loop with shown mechanical parts is in figure 5.7.
The damping experiment has been performed with the cantilever Veeco MPP-32220 mounted on the electrostatic actuator as it has been described earlier. The regulator designed in section 5.9 has been discretised with the help of Matlab control toolbox and inserted into the real-time regulator. The discrete regulator implemented into the HERON card has technical problems that have not been solved before this thesis manuscript has been finished. The real-time regulator is numerical overflowing if the inserted discrete regulator has higher order then one. This numerical overflow completely saturate the output digital to analog converter. The system could not be used in the same form as it was designed.

A simple temporary real-time regulator had been found to be able to obtain some real-time measurement data. The regulator was found according to the real-time system stability and have not been designed standard way. It is only a “test regulator" and the real-time experiment has to be repaired before performing any consistent and fully relayable measurement with well designed controller.
The controller structure is shown in figure 5.22 and the test regulator is defined by constants: $b_0 = 1$, $n_7 = 0$, $a_1 = 350$, $m_7 = 10$, $d_a = 0$, $c_b = 1$, $d_b = 0$. All the other constants are set to zero. This can be written as a discrete equation: $output(k) = \frac{b_0}{2^{n_7}} \cdot (input(k) - \frac{a_1}{2^{m_7}} \cdot input(k-1)) = 1 \cdot (input(k) - 0.342 \cdot input(k-1))$ using the same notation as the block diagram in figure 5.22. The sampling rate of the FPGA and its synchronous converters has been set to 325 kHz.

Figure 5.47 shows experimental results of the cantilever active damping. Graph A) displays power spectral density of thermally excited cantilever. The measurement has significantly stronger measurement noise in comparison with noise levels measured in section 3.6. The electrostatic actuator implemented into Nanotec AFM is the cause of this measurement noise increase. The laser is aligned very close to the actuator fixed plate and part of the laser beam is reflected by the actuator and this light is perturbing the photo detector. Further on, only a small part of the beam is reflected from the cantilever to the photo-detector and this causes additional decrease in signal to noise ration. The spectra has many additional spikes that have not been observed before the microscope modification.

The spectra in figure 5.47 A) shows only first two cantilever harmonic modes because higher harmonic modes are invisible due to high levels of the detection noise. Figure 5.47 B) and C) show frequency zoom of the first and the second harmonic mode. The black curve is the power spectra density of thermally excited free cantilever in open loop. The colored curves stands for cantilever motion with different gains of the closed stabilizing control loop. The manual gain of the output amplifier has been used to change the closed loop gain. The shown attenuation maximum is the curve where the resonance peak of the first harmonic mode equals to the low frequency re-injected noise.

It is not possible to measure the potentiometer position and only approximate minimal and maximal values are shown next to the graph. The positions in between have been set the way that the measured spectra are well distributed in this range and clearly demonstrate different attenuation levels. The curves are indexed from 2 to 11 for easy orientation in the following analysis. The free cantilever spectra has index 1.

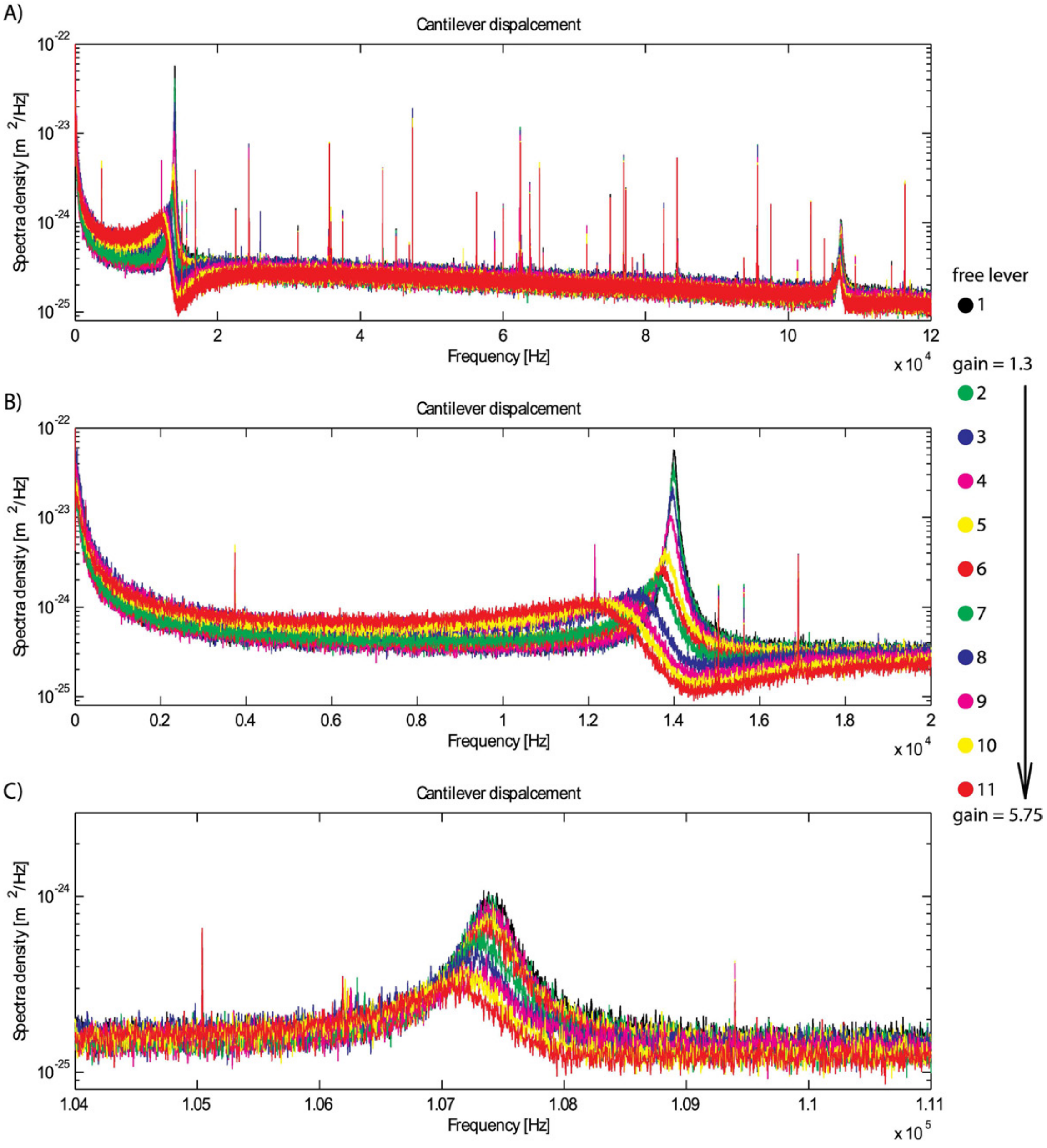

Figure 5.47: The real-time measurement of the cantilever multimode active damping. A) Cantilever position power spectral density for different stabilizing control loop gains. B) The first harmonic mode detail. C) The second harmonic mode detail.

The simplest way how to quantitatively evaluate the efficiency of the active cooling/damping is to observe the changes in resonance peaks heights and their quality factors. The resonance peaks of both harmonic modes have been fitted with Lorentzian fit for all measured damping levels. These fits provide quantitative information and can be easily compared. Figure 5.48 A) shows the fits heights and B) shows the quality factors for both cantilever harmonic modes. The lateral axis represents the index of different closed loop attenuation level. The first harmonic mode spectra were fitted only up to index 8 because all higher damping levels strongly deformed the resonance peak and it can not be correctly fitted with Lorenzian.

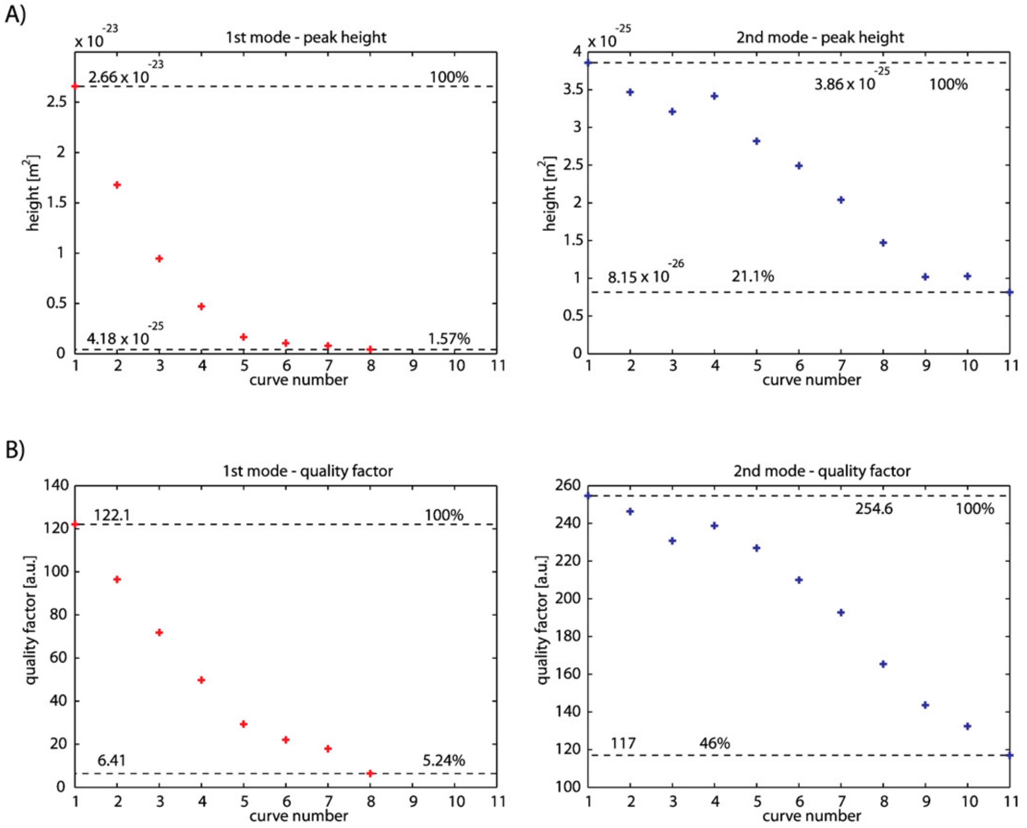

Figure 5.48: The cantilever damping for different gains of the stabilizing control loop. A) Lorenzian fits heights. B) Calculated quality factor.

The maximal achieved attenuation of the cantilever Brownian motion is summarized in table 5.4. The first harmonic mode achieved significant decrease 98.43% of thermally induced displacement. The second harmonic mode did not achieved such a results but Brownian motion attenuation almost reached 80%.

	free cantilever	maximal damping	attenuation
peak height $[m^2]$			
1st mode	2.66e-23	4.28e-25	98.43%
2nd mode	3.86e-25	8.15e-26	78.9%
quality factor [a.u.]			
1st mode	122.1	6.41	94.76%
2nd mode	254.6	117	54%

Table 5.4: Quantitative results of the thermally excited cantilever damping.

The thermal perturbations are permanently present in all AFM measurement. It is direct function of the thermal bath temperature T surrounding the cantilever. The theoretical introduction given at the beginning of this chapter has introduced a term "effective temperature". This temperature can be calculated from the position variance of actively attenuated cantilever. The effective temperature is another way how to evaluate obtained experimental data and can be calculated from the Lorenzian fits.

The effective spring constants of both harmonic modes have been calculated from the free cantilever spectra with the help of equation 3.24. The spring constant of the first harmonic mode equals 0.417 N/m and for the second mode 7.97N/m. These two constants were used to recalculate position variance into the effective temperature for different cooling levels. Obtained effective temperatures are shown in figure 5.49. The first harmonic mode reached effective temperature 52.2 K and the second mode 135.1 K at the cooling maximum.

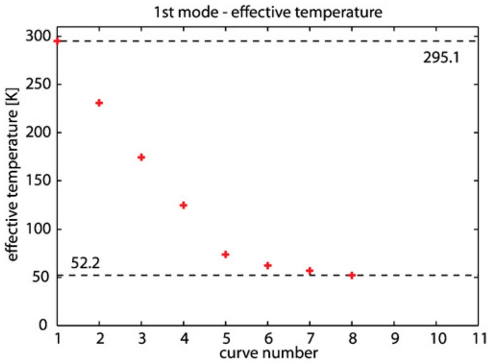

Figure 5.49: The effective temperature of the first two harmonic modes for different levels of cooling.

An active cooling of the cantilever motion causes a frequency shift of both harmonic modes that is clearly visible in figure 5.47. The resonance peaks are shifted towards lower frequencies due to used controller. In the simulation with high order controller presented earlier were all harmonic modes shifted towards higher frequencies. The evolution of measured resonance frequency as a function of different damping levels is shown in figure 5.50.

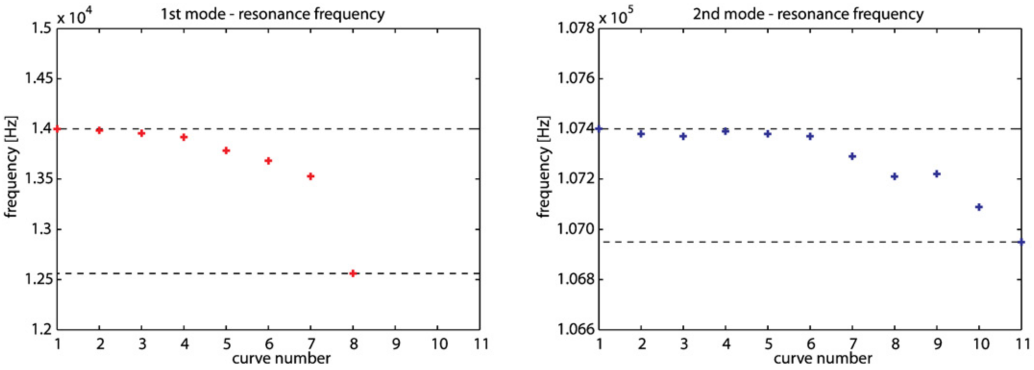

Figure 5.50: The resonance frequency shift for both harmonic modes.

The experimental verification of the cooling mode could not been advanced any further until the technical problems with the FPGA real-time controller are solved. The presented results are obtained with temporary regulator and should be considered as preliminary results!

Chapter 6

Conclusions and Perspectives

The work presented in this thesis has given a new vision on how to operate the Atomic Force Microscope (AFM) and to improve its accuracy by application of different control strategies. This thesis is the interface between the physics of surface with its instrumentation and advanced control techniques. Obtained results rely on the exchange between these two fields of science that have allowed a new approach to Atomic Force Microscopy to be proposed. The introduction of control to physical experiments with AFM permits problems that are not necessary solvable by improvements of experiment design to be addressed. The most important of these problems is the spontaneous perturbation of micro mechanical system used as force sensor by thermal agitation. This phenomena is well known as Brownian motion. If there is any reason that limits the possibility of using AFM at very low temperatures, this fundamental measurement perturbation cannot be eliminated. This thesis tries to address these thermal perturbations and propose new methods on how to improve the accuracy of AFM at ambient temperature.

The results can be summarized into three distinctive parts:

- Cantilever modeling
- Observer application to AFM
- New AFM operation mode

Great attention has been given to the modeling of the cantilever as a multimode dynamic system. This modeling approach permits complex dynamic behavior of thermally excited cantilever to be well understood. Furthermore, it allows the cantilever response to an attractive or strong repulsive interaction force to be deeply understood.

Chapter 3 presents the possibility to construct a precise cantilever multimode model based on information obtained from the measurement of free, thermally-excited cantilever motion. The cantilever identification based on thermal excitation has been presented and the obtained model has been compared with measurement results. Secondly, the cantilever model has been presented, based on its mechanical properties without any further identification. This model shows a certain discrepancy with measurement data but allows very simple approximation of system behavior to be obtained. To minimize its error, a numerical minimalization method has been presented that permits new mechanical parameters of the cantilever for the model to be estimated, to better correspond to the measured spectra of system response to thermal agitation.

Developed models have been used to study cantilever behavior in dynamic non-contact and Tapping operation mode. When the oscillating cantilever approaches a measured surface, the forces acting on the cantilever tip modulate its motion. The interaction force is strongly non-linear which causes agitation of multiple cantilever harmonic modes at the same time. This has been demonstrated by simulation. This contributes to the decrease of the first harmonic mode vibration amplitude, even if the interaction force is not dissipative. The energy of the freely vibrating cantilever is stored around its first resonance frequency. When the system is perturbed by non-linear force, some energy is transferred to higher harmonics and original vibration amplitude decreases.

These modeling results have been a necessary step to propose new force detection techniques based on the state space observer. Proposed models have been used as the? observers internal models. The state space observer is able to mirror the measured system and estimate its internal states, despite the fact that they are not directly measurable.

This functionality has been used for the standard amplitude modulation technique. The constructed observer has at (as?) its input the measured cantilever position and estimates actual position of all harmonic modes of the cantilever. This permits accuracy of the vibration amplitude detection to be improved.

A modified detection system has been proposed to further explore the possibilities of the observer capability to directly estimate the surface interaction forces. The standard state space observer has been extended with new state representing the unknown interaction force. The observer can estimate the cantilever position as before, but has a new state which represents the interaction force. It is important to realize that the real interaction force is strongly non-linear but the used observer is linear. This is the reason why the estimated interaction force does not accurately match the shape of the real force, but it estimates an energy that is necessary to achieve a corresponding deviation from the original resonance frequency of the system. If the effective values of real and estimated interaction force are compared, it is/can be demonstrated that the proposed force estimation technique has an accuracy better than 0.5pN.

Another proposed observer based technique for AFM is an interaction force measurement with non-excited cantilever in attractive interaction with the studied surface. This non-contact measurement technique is detecting the interaction force statically without cantilever excitation at its resonance frequency. It was demonstrated that a resolution better than 1 pN can be achieved.

The main result of this thesis is a definition of new AFM operation mode which has been named: "Cooling mode". This mode is further developing the idea of measuring the surface interaction force in non-contact regime with non-excited cantilever. This measurement approach brings many exciting possibilities to make fast imagery in liquid media.

The AFM has been modified to operate in this mode and an electrostatic actuator has been added to the existing system to actuate directly at the cantilever free end. The cantilevers thermally-induced vibration is dampened/cooled through the active feedback loop, with the help of this actuator. The stabilizing control loop is at the same time counterbalancing the surface interaction forces to maintain the cantilever in non-deflected (zero) position. The interaction force is detected directly from the "effort" needed to stabilize the cantilever in a non-deflected position. The force measurement is performed at a well-defined constant distance from the surface and non linear behavior of interaction force does not apply. The force is measured in the original interaction bandwidth. There is no frequency or amplitude modulation necessary. The dynamic properties of the cantilever are suppressed and the measurement can be performed at very high speeds. This mode is well suited for operation in liquid media due to the static operation. The Cooling mode has been tested in the simulation and preliminary measurement verification has been done. Therefore, a profound experimental validation was not performed due to technical problems, and further verification of the Cooling mode operation at high speeds and in liquid media has to be done.

The Cooling mode has great industrial potential and has been protected by patent number FR06/04674. The Cooling mode will be further developed and tested in a framework of a new project called Small Infinity. This project will transfer developed technology into the commercial product which can be used by researchers in different domains.

This thesis demonstrates the great opportunity to apply advance control systems to the physics experiments and this way vitally contribute to their further development. The control techniques show strong potential in nanotechnology where they permit certain difficulties that cannot be overcome by experiment design to be eliminated. The Brownian motion treated in this thesis is one example from a long list of challenges that nano-science faces. Generally speaking, it can be said that nano positioning and manipulation is one area of nano science that cannot be done without active control systems.

Bibliography

[1] G. Binning, H. Rohrer, C. Gerber, and E. Weibel, "Surface studies by scanning tunneling microscopy," *Phys. Rev. Lett.*, vol. 49, pp. 57–61, 1982.

[2] G. Binning, C. F. Quate, and C. Gerber, "Atomic force microscope," *Phys. Rev. Lett.*, vol. 56, pp. 930–934, 1986.

[3] D. Sarid and V. Elings, "Review of scanning force microscopy," *J. Vac. Sci. Technol. B*, vol. 9 (2), pp. 431–437, 1991.

[4] P. K. Hansma and J. Tersoff, "Scanning tunneling microscopy," *J. Appl. Phys.*, vol. 61 (2), pp. R1–R23, 1987.

[5] G. Binning and H. Rohrer, "Scaning tunneling microscopy-from birth to adolescence," *Reviews of Modern Physics*, vol. 59, pp. 615–629, 1987.

[6] C. M. Mate, G. M. McClelland, R. Erlandsson, and S. Chiang, "Atomic-scale friction of a tungsten tip on a graphite surface," *Phys. Rev. Lett.*, vol. 59, pp. 1942–1946, 1987.

[7] R. Erlandsson, G. M. McClelland, C. M. Mate, and S. Chiang, "Atomic force microscopy using optical interferometry," *J. Vac. Scl. Technol. A*, vol. 6, pp. 266–270, 1988.

[8] O. Marti, J. Colchero, and J. Mlynek, "Combined scanning force and friction microscopy of mica," *Nanotechnology*, vol. 1, pp. 141–144, 1990.

[9] G. Meyer and N. M. Amer, "Simultaneous measurement of lateral and normal forces with an optical-beam-deflection atomic force microscope," *Appl. Phys. Lett.*, vol. 57, pp. 2089–2091, 1990.

[10] Y. Martin, C. C. Williams, and H. K. Wickramasinghe, "Atomic force microscope-force mapping and profiling on a sub 100-a scale," *J. Appl. Phys.*, vol. 61, pp. 4723–4729, 1987.

[11] J. E. Stern, B. D. Terris, H. J. Mamin, and D. Rugar, "Deposition and imaging of localized charge on insulator surfaces using a force microscope," *Appl. Phys. Lett.*, vol. 53, pp. 2717–2719, 1988.

[12] Y. Martin and H. K. Wickramasinghe, "Magnetic imaging by "force microscopy" with 1000 a resolution," *Appl. Phys. Lett.*, vol. 50, pp. 1455–1457, 1987.

[13] D. W. Pohl, W. Denk, and M. Lanz, "Optical stethoscopy: Image recording with resolution lambda/20," *Appl. Phys. Lett.*, vol. 44, pp. 651–653, 1984.

[14] E. Betzig, P. L. Finn, and J. S. Weiner, "Combined shear force and near-field scanning o tical microscopy," *Appl. Phys. Lett.*, vol. 60, pp. 2484–2486, 1992.

[15] E. Betzig, J. Trautman, T. Harris, and J. Weiner, "Breaking the diffraction barrier: Optical microscopy on a nanommetric scale," *Science*, vol. 251, pp. 1468–1470, 1991.

[16] Y. Martin, D. W. Abraham, and H. K. Wickramasinghe, "High-resolution capacitance measurement and potentiometry by force microscopy," *Appl. Phys. Lett.*, vol. 52, pp. 1103–1105, 1988.

[17] M. Nonnenmacher, M. P. OBoyle, and H. K. Wickramasinghe, "Kelvin probe force microscopy," *Appl. Phys. Lett.*, vol. 58, pp. 2921–2923, 1991.

[18] D. DeVecchio and B. Bhushan, "Use of a nanoscale kelvin probe for detecting wear precursors," *Rev. Sci. Instrum.*, vol. 69, pp. 3618–3624, 1998.

[19] J. M. R. Weaver and W. Abraham, "High resolution atomic force microscopy potentiometry," *J. Vac. Sci. Technol. B*, vol. 9 (3), pp. 1559–1561, 1991.

[20] C. C. Williams and H. K. Wickramasinghe, "Microscopy of chemical-potentional variations on an atomic scale," *Nature*, vol. 344, pp. 317–319, 1990.

[21] P. K. Hansma, B. Drake, O. Marti, S. A. C. Gould, and C. B. Prater, "The scanning ion-canductance microscope," *Science*, vol. 243, pp. 641–643, 1989.

[22] D. Rugar, H. J. Mamin, P. Guethner, S. E. Lambert, J. E. Stern, I. McFadyen, and T. Yogi, "Magnetic force microscopy: General principles and application to longitudinal recording media," *J. Appl. Phys.*, vol. 68, pp. 1169–1183, 1990.

[23] I. Giaever, "Energy gap in superconductors measured by electron tunneling," *Phys. Rev. Lett.*, vol. 5, pp. 147–148, 1960.

[24] U. Durig, J. Gimzewski, and D. W. Pohl, "Experimental observation of forces acting during scanning tunneling microscopy," *Phys. Rev. Lett.*, vol. 57 (19), pp. 2403–2406, 1986.

[25] M. Tortonesse, R. C. Barrett, and C. F. Quate, "Atomic resolution with an atomic force microscope using piezoresistive detection." *Appl. Phys. Lett.*, vol. 62 (8), pp. 834–836, 1993.

[26] S. Akamine, R. C. Barrett, and C. F. Quate, "Improved atomic force microscope images using microcantilevers with sharp tips," *Appl. Phys. Lett.*, vol. 57 (3), pp. 316–318, 1990.

[27] O. Wolter, T. Bayer, and J. Greschner, "Micromachined silicon sensors for scanning force microscopy," *J. Vac. Sci. Technol. B*, vol. 9 (2), pp. 1353–1357, 1991.

[28] R. Erlandsson, G. McClelland, C. Mate, and S. Chiang, "Atomic force microscopy using optical interferometry," *J. Vac. Sci. Technol.*, vol. 6, pp. 266–270, 1988.

[29] M. J. Cunningham, S. T. Cheng, and W. W. Clegg, "A differential interferometer for scanning force microscopy," *Meas. Sci. Technol.*, vol. 5, pp. 1350–1354, 1994.

[30] C. Schönenberger and S. F. Alvarado, "A differential interferometer for force microscopy," *Rev. Sci. Instrum.*, vol. 60, pp. 3131–3134, 1989.

[31] D. Rugar, H. Mamin, R. Erlandsson, J. Stern, and B. Terris, "Force microscope using a fiber-optic displacement sensor," *Rev. Sci. Instrum.*, vol. 59, pp. 2339–2340, 1988.

[32] D. Rugar, H. J. Mamin, and P. Guethner, "Improved fiber-optic interferometer for atomic force microscopy," *Appl. Phys. Lett.*, vol. 55 (25), pp. 2588–2590, 1989.

[33] M. Vogel, C. Mooser, K. Karrai, and R. J. Warburton, “Optically tunable mechanics of cantilevers,” *Appl. Phys. Lett.*, vol. 83 (7), pp. 1337–1339, 2003.

[34] G. Meyer and N. M. Amer, “Novel optical approach to atomic force microscopy,” *Appl. Phys. Lett.*, vol. 53, pp. 1045–1047, 1988.

[35] ——, “Erratum - novel optical approach to atomic force microscopy,” *Appl. Phys. Lett.*, vol. 53, pp. 2400–2402, 1988.

[36] T. Itoh and T. Suga, “Development of a force sensor for atomic force microscopy using piezoelectric thin films,” *Nanotechnology*, vol. 4, p. 218, 1993.

[37] T. Itoh, C. Lee, , and T. Suga, “Deflection detection and feedback actuation using a self-excited piezoelectric pb(zr,ti)o3 microcantilever for dynamic scanning force microscopy,” *Appl. Phys. Lett.*, vol. 69, pp. 2036–2038, 1996.

[38] G. Abadal, Z. J. Davis, B. Helbo, X. Borrise, R. Ruiz, A. Boisen, F. Campabadal, J. Esteve, E. Figueras, F. Perez-Murano, and N. Barniol, “Electromechanical model of a resonating nano-cantilever-based sensor for high-resolution and high-sensitivity mass detection,” *Nanotechnology*, vol. 12, pp. 100–104, 2001.

[39] T. E. Schaffer, “Force spectroscopy with a large dynamic range using small cantilevers and an array detector,” *J. Appl. Phys.*, vol. 91, pp. 4739–4746, 2002.

[40] M. Stark, B. N. Bercu, F. Marchi, J. Chevrier, and S. Huant, “Marking the difference: Interferometric detection vs optical beam deflection in afm,” *AIP 2003 Conference Proceedings*, vol. 696, pp. 385–391, 2003.

[41] G. Binning and D. P. E. Smith, “Single-tube three-dimensional scanner for scanning tunneling microscopy,” *Rev. Sci. Instrum.*, vol. 57 (8), pp. 1688–1689, 1986.

[42] C. J. Chen, “Electromechanical deflections of piezoelectric tubes with quartered electrodes,” *Appl. Phys. Lett.*, vol. 60 (1), pp. 132–134, 1992.

[43] G. Schitter, A. Stemmer, and F. Allgöwer, “Robust 2dof-control of a piezoelectric tube scanner for high speed atomic force microscopy,” *American Control Conference, Denver, Colorado*, vol. -, pp. 3720–3725, 2003.

[44] M. Napoli, B. Bamieh, and K. Turner, “Mathematical modeling, experimental validation and observer design for a capacitively actuated microcantilever,” *American Control Conference, Denver, Colorado*, pp. 3732–3737, 2003.

[45] M. Napoli and B. Bamieh, “Design of a decoupling controller for electrostatically coupled microcantilevers based on current measurement,” *American Control Conference, Boston, Massachusetts*, pp. 3134–3139, 2004.

[46] C. Huang, Y. Y. Lin, and T. A. Tang, “Study on the tip-deflection of a piezoelectric bimorph cantilever in the static state,” *Journal of micromechanics and microengineering*, vol. 14, pp. 530–534, 2004.

[47] B. Rogers, D. York, N. Whisman, M. Jones, K. Murray, J. D. Adams, T. Sulchek, and S. C. Minne, “Tapping mode atomic force microscopy in liquid with an insulated piezoelectric microactuator,” *Rev. Sci. Instrum.*, vol. 73, pp. 3242–3244, 2002.

[48] B. Rogers, T. Sulchek, K. Murray, D. York, M. Jones, L. Manning, S. Malekos, B. Beneschott, J. D. Adams, H. Cavazos, and S. C. Minne, “High speed tapping mode atomic force microscopy in liquid using an insulated piezoelectric cantilever,” *Rev. Sci. Instrum.*, vol. 74, pp. 4683–4686, 2003.

[49] W. Han, S. M. Lindsay, and T. Jing, “A magnetically driven oscillating probe microscope for operation in liquids,” *Appl. Phys. Lett.*, vol. 69, pp. 4111–4113, 1996.

[50] A. Buguin, O. D. Roure, and P. Silberzan, “Active atomic force microscopy cantilevers for imaging in liquids,” *Appl. Phys. Lett.*, vol. 78, pp. 2982–2984, 2001.

[51] A. Gannepalli, A. Sebastian, J. P. Cleveland, and M. V. Salapaka, “Thermal noise response based control of tip-sample separation in afm,” *American Control Conference, Boston, Massachusetts*, pp. 3122–3127, 2004.

[52] A. Gannepalli, A. Sebastian, M. V. Salapaka, and J. P. Cleveland, “Thermal noise response based static non-contact atomic force microscopy,” *NSTI-Nanotech*, vol. 3, pp. 159–162, 2004.

[53] A. Gannepalli, A. Sebastian, J. Cleveland, and M. Salapaka, “Thermally driven noncontact atomic force microscopy,” *Appl. Phys. Lett.*, vol. 87, p. 111901, 2005.

[54] J. K. H. Horber and M. J. Miles, “Scanning probe evolution in biology,” *Science*, vol. 302, pp. 1002–1005, 2003.

[55] F. Ohnesorge and G. Binning, “True atomic resolution by atomic force microscopy trough repulsive and attractice forces,” *Science*, vol. 260, pp. 1451–1456, 1993.

[56] S. P. Jarvis, H. Yamada, S. I. Yamamoto, H. Tokumoto, and J. B. Pethica, “Direct mechanical measurement of interatomic potentials,” *Nature*, vol. 384, pp. 247–249, 1996.

[57] F. J. Giessibl, S. Hembacher, H. Bielefeldt, and J. Mannhart, “Subatomic features on the silicon (111)-(7x7) surface observed by atomic force microscopy,” *Science*, vol. 289, pp. 422–425, 2000.

[58] B. Anczykowski, D. Kruger, K. L. Babcock, and H. Fuchs, “Basic properties of dynamic force spectroscopy with the scanning force microscope in experiment and simulation,” *Ultramicroscopy*, vol. 66, pp. 251–259, 1996.

[59] B. Anczykowski, B. Gotsmann, H. Fuchs, J. Cleveland, and V. Elings, “How to measure energy dissipation in dynamic mode atomic force microscopy,” *Applied Surface Science*, vol. 140, pp. 376–382, 1999.

[60] B. Anczykowski, D. Kruger, and H. Fuchs, “Cantilever dynamics in quasinoncontact force microscopy: Spectroscopic aspects,” *Phys. Rev. B*, vol. 53 (23), pp. 15 485–15 488, 1996.

[61] R. Garcia and A. S. Paulo, “Attractive and repulsive tip-sample interaction regimes in tapping-mode atomic force microscopy,” *Phys. Rev. B*, vol. 60 (7), pp. 4961–4967, 1999.

[62] B. Anczykowski, B. Gotsmann, H. Fuchs, J. Cleveland, and V. Elings, “How to measure energy dissipation in dynamic mode atomic force microscopy,” *Applied Surface Science*, vol. 140, pp. 376–382, 1999.

[63] A. S. Paulo and R. Garcia, “Tip-surface forces, amplitude, and energy dissipation in amplitude-modulation tapping mode force microscopy,” *Phys. Rev. B*, vol. 64, p. 193411, 2001.

[64] Q. Zhong, D. Inniss, K. Kjoller, and V. B. Elings, “Fractured polymer/silica fiber surface studied by tapping mode atomic force microscopy,” *Surface Science*, vol. 290, pp. L688–L692, 1993.

[65] N. A. Burnham, O. P. Behrend, F. Oulevey, G. Gremaud, P.-J. Gallo, D. Gourdon, E. Dupas, A. J. Kulik, H. M. Pollock, and G. A. D. Briggs, “How does a tip tap?” *Nanotechnology*, vol. 8, pp. 67–75, 1997.

[66] G. Y. Chen, R. J. Warmack, A. Huang, and T. Thundat, “Harmonic response of near-contact scanning force microscopy,” *J. Appl. Phys.*, vol. 78 (3), pp. 1465–1469, 1995.

[67] G. Y. Chen, R. J. Warmack, T. Thundat, D. P. Allison, and A. Huang, “Resonance response of scanning force microscopy cantilevers,” *Rev. Sci. Instrum.*, vol. 65, p. 2532, 1994.

[68] U. Dürig, O. Züger, and A. Stalder, “Interaction force detection in scanning probe microscopy - methods and applications,” *J. Appl. Phys.*, vol. 72, pp. 1778–1798, 1992.

[69] T. R. Albrecht, P. Grtitter, D. Horne, and D. Rugar, “Frequency modulation detection using high-q cantilevers for enhanced force microscope sensitivity,” *J. Appl. Phys.*, vol. 69, pp. 668–673, 1991.

[70] F. J. Giessibl, “Atomic resolution of the silicon (111)-(7x7) surface by atomic force microscopy,” *Science*, vol. 267, pp. 68–71, 1995.

[71] A. Passiana, G. Muralidharan, S. Kouchekian, A. Mehta, S. Cherian, T. L. Ferrell, and T. Thundat, “Dynamics of self driven microcantilevers,” *J. Appl. Phys.*, vol. 91, pp. 4693–4700, 2002.

[72] U. Durig, “Conservative and dissipative interactions in dynamic force microscopy,” *Surface and Interface Analysis*, vol. 27, pp. 467–473, 1999.

[73] ——, “Relations between interaction force and frequency shift in large amplitude dynamic force microscopy,” *Appl. Phys. Lett.*, vol. 75, pp. 433–435, 1999.

[74] ——, “Interaction sensing in dynamic force microscopy,” *New Journal of Physiscs*, vol. 2, pp. 5 1–12, 2000.

[75] F. J. Giessibl, “Forces and frequency shifts in atomic-resolution dynamic-force microscopy,” *Phys. Rev. B*, vol. 56, pp. 16 010–16 015, 1997.

[76] J. E. Sader and S. P. Jarvis, “Accurate formulas for interaction force and energy in frequency modulation force spectroscopy,” *Appl. Phys. Lett.*, vol. 84, pp. 1801–1803, 2004.

[77] R. Smith, A. Hatch, and T. De, “Model development for piezoceramic nanopositioners,” *Decision and Control, 2003. Proceedings. 42nd IEEE Conference*, vol. 3, pp. 2638–2643, 2003.

[78] A. Hatch, R. Smith, and T. De, “Experimental implementation of a model-based inverse filter to attenuate hysteresis in an atomic force microscope,” *Decision and Control, 2004. CDC. 43rd IEEE Conference*, vol. 3, pp. 3062– 3067, 2004.

[79] G. Schitter, F. Allgöwer, and A. Stemmer, “A new control strategy for high-speed atomic force microscopy,” *Nanotechnology*, vol. 15, pp. 108–114, 2004.

[80] G. Schitter and A. Stemmer, “Identification and open-loop tracking control of a piezoelectric tube scanner for high-speed scanning-probe microscopy,” *IEEE transactions on Control Systems Technology*, vol. 12, pp. 449–454, 2004.

[81] Y. Xu and P. H. Meckl, “Time-optimal motion control of piezoelectric actuator: Stm application,” *American Control Conference, Boston, Massachusetts*, pp. 4849–4854, 2004.

[82] S. Tien, Q. Zou, and S. Devasia, “Control of dynamics-coupling effects in piezo-actuator for high-speed afm operation,” *American Control Conference, Boston, Massachusetts*, pp. 3116–3121, 2004.

[83] A. Daniele, S. Salapaka, M. Salapaka, and M. Dahleh, “Piezoelectric scanners for atomic force microscopes: Design of lateral sensors, identification and control,” *American Control Conference, San Diego, California*, pp. 253–257, 1999.

[84] D. Croft and S. Devasia, “Vibration compensation for high speed scanning tunneling microscopy,” *Rev. Sci. Instrum.*, vol. 70, pp. 4600–4606, 1999.

[85] G. Schitter, P. Menold, H. F. Knapp, F. Allgöwer, and A. Stemmer, “High performance feedback for fast scanning atomic force microscopes,” *Rev. Sci. Instrum.*, vol. 72, pp. 3320–3327, 2001.

[86] S. Salapaka, A. Sebastian, J. P. Cleveland, and M. V. Salapaka, “High bandwidth nano-positioner: A robust control approach,” *Rev. Sci. Instrum.*, vol. 73, pp. 3232–3241, 2002.

[87] A. Sebastian and S. Salapaka, “H (infinity) loop shaping design for nano-positioning,” *Proceedings of the American Control Conference, Denver, Colorado*, pp. 3708–3713, 2003.

[88] S. Sebastian, A. Salapaka, and M. V. Salapaka, “Systems tools applied to micro-cantilever based devices,” *Multidisciplinary Research in Control*, vol. LNCIS 289, pp. 83–99, 2003.

[89] S. Salapaka, T. De, and A. Sebastian, “Sample-profile estimate for fast atomic force microscopy,” *Appl. Phys. Lett.*, vol. 87, p. 053112, 2005.

[90] A. Sebastian, M. V. Salapaka, and J. P. Cleveland, “Robust control approach to atomic force microscopy,” *42nd IEEE Conference on Decision and Control, Maui, Hawaii*, pp. 3443–3444, 2003.

[91] R. Curtis, C. Pearson, P. Gaard, and E. Ganz, “A compact micropositioner for use in ultrahigh vacuum,” *Rev. Sci. Instrum.*, vol. 64, pp. 2687–2690, 1993.

[92] C. Renner, P. Niedermann, A. Kent, and O. Fischer, “A vertical piezoelectric inertial slider,” *Rev. Sci. Instrum.*, vol. 61, p. 030965, 1990.

[93] C. Meyer, O. Sqalli, H. Lorenz, and K. Karrai, “Slip-stick step-scanner for scanning probe microscopy,” *Rev. Sci. Instrum.*, vol. 76, p. 063706, 2005.

[94] G. Schitter, K. J. Astrom, B. DeMartini, G. E. Fantner, K. Turner, P. J. Thurner, and P. K. Hansma, “Design and modeling of a high-speed scanner for atomic force microscopy,” *Proceedings of the 2006 American Control Conference Minneapolis, Minnesota, USA*, vol. -, pp. –, 2006.

[95] B. Anczykowski, J. Cleveland, D. Krüger, V. Elings, and H. Fuchs, “Analysis of the interactionmechanisms in dynamicmode sfm by means of experimental data and computer simulation.” *Appl. Phys. A*, vol. 666, pp. S885–S889, 1998.

[96] H. Hölscher, “Q-controlled dynamic force spectroscopy,” *Surfice Science*, vol. 515, pp. 517–522, 2002.

[97] A. D. L. Humphris, J. Tamayo, and M. J. Miles, “Active quality factor control in liquids for force spectroscopy,” *Langmuir*, vol. 16, pp. 7891–7894, 2000.

[98] A. D. L. Humphris, A. N. Round, and M. J. Miles, “Enhanced imaging of dna via active quality factor control,” *Surface Science*, vol. 491, pp. 468–472, 2001.

[99] T. R. Rodríguez and R. García, “Theory of q control in atomic force microscopy,” *Appl. Phys. Lett.*, vol. 82, pp. 4821–4823, 2003.

[100] T. Sulchek, R. Hsieh, J. D. Adams, G. G. Yaralioglu, S. C. Minne, C. F. Quate, J. P. Cleveland, A. Atalar, and D. M. Adderton, “High-speed tapping mode imaging with active q control for atomic force microscope,” *Appl. Phys. Lett.*, vol. 76, pp. 1473–1475, 2000.

[101] J. Mertz, O. Marti, and J. Mlynek, “Regulation of a microcantilever response by force feedback,” *Appl. Phys. Lett.*, vol. 62, pp. 2344–2346, 1993.

[102] A. Sebastian, D. R. Sahoo, and M. V. Salapaka, “An observer based sample detection scheme for atomic force microscopy,” *42nd IEEE Conference on Decision and Control, Maui, Hawaii*, pp. 2132–2137, 2003.

[103] D. R. Sahoo, T. De, and M. V. Salapaka, “Observer based imaging methods for atomic force microscopy,” *44th IEEE Conference on Decision and Control, and the European Control Conference, Seville, Spain*, pp. 1185–1190, 2005.

[104] K. Karrai and R. D. Grober, “Piezoelectric tip-sample distance control for near field optical microscopes,” *Appl. Phys. Lett.*, vol. 66, pp. 1842–1844, 1995.

[105] K. Karrai, “Lecture notes on shear and friction force detection with quartz tuning forks,” *Ecole Thématique du CNRS*, vol. 1, pp. 1–23, 2000.

[106] M. H. C. S. F J Giessibl, S Hembacher and J. Mannhart, “Stability considerations and implementation of cantilevers allowing dynamic force microscopy with optimal resolution: the qplus sensor,” *Nanotechnology*, vol. 15, pp. S79–S86, 2004.

[107] A. G. Onaran, M. Balantekin, W. Lee, W. L. Hughes, B. A. Buchine, R. O. Guldiken, Z. Parlak, C. F. Quate, and F. L. Degertekin, “A new atomic force microscope probe with force sensing integrated readout and active tip,” *Rev. Sci. Instrum.*, vol. 77, p. 023501, 2006.

[108] D. Sarid, *Scanning Force Microscopy with applications to electric, magnetic and atomic forces.* Oxford University Press, 1994.

[109] J. E. L. Jones, “Cohesion,” *The proceedings of the physical society*, vol. 43, pp. 462–482, 1931.

[110] H. C. Hamaker, “The london - van der waals attraction between spherical particles,” *Physica*, vol. 4, pp. 1058–1072, 1937.

[111] F. London, “The general theory of molecular forces,” *Z. physik. Chem. B*, vol. 11, pp. 8–26, 1936.

[112] J. N. Israelachvili, *Intermolecular and Surface Forces.* Academic Press, 1991.

[113] U. Hartmann, “van der waals interactions between sharp probes and flat sample surfaces,” *Phys. Rev. B*, vol. 43, pp. 2404–2407, 1991.

[114] N. A. Burnham, R. J. Colton, and H. M. Pollock, “Interpretation of force curves in force microscopy,” *Nanotechnology*, vol. 4, pp. 64–80, 1993.

[115] B. Gady, D. Schleef, R. Reifenberger, D. Rimai, and L. P. DeMejo, “Identification of electrostatic and van der waals interaction forces between a micrometer-size sphere and a flat substrate,” *Phys. Rev. B*, vol. 53, pp. 8065–8070, 1996.

[116] C. Argento and R. H. French, “Parametric tip model and force-distance relation for hamaker constant determination from atomic force microscopy,” *J. Appl. Phys.*, vol. 80, pp. 6081–6090, 1996.

[117] S. Hirsekorn, U. Rabe, and W. Arnold, “Theoretical description of the transfer of vibrations from a sample to the cantilever of an atomic force microscope,” *Nanotechnology*, vol. 8, pp. 57–66, 1997.

[118] P. Johansson and P. Apell, “Geometry effects on the van der waals force in atomic force microscopy,” *Phys. Rev. B*, vol. 56, pp. 4159–4165, 1997.

[119] R. Erlandsson and P. Apell, “Progress in scanning probe microscopy: High resolution force microscopy and spectroscopy,” *Current Science*, vol. 78, pp. 1445–1457, 2000.

[120] B. Gotsmann, C. Seidel, B. Anczykowski, and H. Fuchs, “Conservative and dissipative tip-sample interaction forces probed with dynamic afm,” *Phys. Rev. B*, vol. 60, pp. 11 051–11 061, 1999.

[121] B. V. Derjaguin, V. M. Muller, and Y. P. Toporov, “Effect of contact deformations on the adhesion of particles,” *J. of Colloid and Inter. Sci.*, vol. 53, pp. 314–326, 1975.

[122] R. Kubo, “The fluctuation dissipation theorem,” *Reports on Progress in Physics*, vol. 29, pp. 255–284, 1966.

[123] M. V. Salapaka, H. S. Bergh, J. Lai, A. Majumdar, and E. McFarland, “Multi-mode noise analysis of cantilevers for scanning probe microscopy,” *J. Appl. Phys.*, vol. 81, pp. 2480–2487, 1997.

[124] S. Rast, C. Wattinger, U. Gysin, and E. Meyer, “The noise of cantilevers,” *Nanotechnology*, vol. 11, pp. 169–172, 2000.

[125] A. N. Cleland and M. L. Roukes, “Noise processes in nanomechanical resonators,” vol. 92, pp. 2758–2769, 2002.

[126] T. E. Schaffer, “Calculation of thermal noise in an atomic force microscope with a finite optical spot size,” *Nanotechnology*, vol. 16, pp. 664–670, 2005.

[127] R. Arinero and G. Leveque, “Vibration of the cantilever in force modulation microscopy analysis by a finite element model,” *Rev. Sci. Instrum.*, vol. 74, pp. 104–111, 2003.

[128] M. Hrouzek, A. Voda, M. Stark, and J. Chevrier, “Model of the cantilever used as a weak force sensor in atomic force microscopy,” *IFAC World congress 2005, Prague, Czech Republic*, 2005.

[129] H.-J. Butt and M. Jaschke, “Calculation of thermal noise in atomic force microscopy,” *Nanotechnology*, vol. 6, pp. 1–7, 1995.

[130] J. A. Turner, S. Hirsekorn, U. Rabe, and W. Arnold, "High frequency response of atomic-force microscope cantilevers," *J. Appl. Phys.*, vol. 82, pp. 966–979, 1997.

[131] G. Muralidharan, A. Mehta, S. Cherian, and T. Thundat, "Analysis of amplification of thermal vibrations of a microcantilever," *J. Appl. Phys.*, vol. 89, pp. 4587–4591, 2001.

[132] R. W. Stark, T. Drobek, and W. M. Heckl, "Thermomechanical noise of a free v-shaped cantilever for atomic-force microscopy," *Ultramicroscopy*, vol. 86, pp. 207–215, 2001.

[133] E. Dupas, G. Gremaud, A. Kulik, and J.-L. Loubet, "High frequency mechanical spectroscopy with an atomic force microscope," *Rev. Sci. Instrum.*, vol. 72, pp. 3891–3897, 2001.

[134] R. W. Stark, "Spectroscopy of higher harmonics in dynamic atomic force microscopy," *Nanotechnology*, vol. 15, pp. 347–351, 2004.

[135] J. P. R. W. Clough, *Dynamics of structures.* Mc Graw-Hill, 1993.

[136] J. P. Cleveland, B. Anczykowski, A. E. Schmid, and V. B. Elings, "Energy dissipation in tapping-mode atomic force microscopy," *Appl. Phys. Lett.*, vol. 72, pp. 2613–2615, 1998.

[137] K. Ogata, *Moder control engineering.* Prentice hal, 1997.

[138] ——, *Discrete time control systems.* Prentice hall India, 2000.

[139] J. P. Gauthier, H. Hammouri, and S. Othman, "A simple observer for nonlinear systems application to bioreactors," *IEEE Tran. on Automatic controle*, vol. 37, pp. 875–880, 1992.

[140] G. Bessancon, "High-gain observation with disturbance attenuation and application to robust fault detection," *Automatica*, vol. 39, pp. 1092–1102, 2003.

[141] G. Besancon, A. Voda, and J. Chevrier, "Force estimation in fundamental physics: an observer application," *2nd IFAC Symposium on System, Structure and Control, Oaxaca, Mexico*, pp. 1–5, 2004.

[142] D. R. Sahoo, A. Sebastian, and M. V. Salapaka, "Transient signal based sample detection in atomic force microscopy," *Appl. Phys. Lett.*, vol. 83, pp. 5521–5523, 2003.

[143] G. Besancon, A. Voda, M. Hrouzek, and J. Chevrier, "Observateur-controleur pour la mesure topographique par microscopie afm," *IEEE Conferance Internationale Francophone d Automatique, CIFA 2006, Bordeaux, France*, 2006.

[144] M. Hrouzek, G. Besancon, A. Voda, and J. Chevrier, "Observer based position detection of a cantilever in atomic force microscopy," *IFAC Mechatronics 2006, Heidelberg, Germany*, 2006.

[145] C. H. Metzger and K. Karrai, "Cavity cooling of a microlever," *Nature*, vol. 432, pp. 1002–1005, 2004.

[146] K. Karrai, "A cooling light breeze," *Nature*, vol. 444, pp. 41–42, 2006.

[147] S. Gigan, H. R. Bohm, M. Paternostro, F. Blaser, G. Langer, J. B. Hertzberg, K. C. Schwab, D. Bauerle, M. Aspelmeyer, and A. Zeilinger, "Self cooling of a micromirror by radiation pressure," *Nature*, vol. 444, pp. 67–70, 2006.

[148] P. F. Cohadon, A. Heidmann, and M. Pinard, "Cooling of a mirror by radiation pressure," *Phys. Rev. Lett.*, vol. 83, pp. 3174–3177, 1999.

[149] M. Pinard, P. F. Cohadon, T. Briant, and A. Heidmann, "Full mechanical characterization of a cold damped mirror," *Phys. Rev. A*, vol. 63, p. 013808, 2000.

[150] D. M. Welda and A. Kapitulnik, "Feedback control and characterization of a microcantilever using optical radiation pressure," *Appl. Phys. Lett.*, vol. 89, p. 164102, 2006.

[151] O. Arcizet, P. F. Cohadon, T. Briant, M. Pinard, and A. Heidmann, "Radiation pressure cooling and optomechanical instability of a micromirror," *Nature*, vol. 444, pp. 71–74, 2006.

[152] D. Kleckner and D. Bouwmeester, "Sub kelvin optical cooling of a micromechanical resonator," *Nature*, vol. 444, pp. 75–78, 2006.

[153] J.-M. Courty, A. Heidmann, and M. Pinard, "Quantum limits of cold damping with optomechanical coupling," pp. 1–10, 2001.

[154] B. D'Urso, B. Odom, and G. Gabrielse, "Feedback cooling of a one-electron oscillator," pp. 1–4.

[155] S. Killbourn, K. Skeldon, D. Robertson, and H. Ward, "Active damping of suspension wire violin modes in gravitational wave detectors," *Phys. Lett. A*, vol. 261, pp. 240–246, 1999.

[156] S. Liang, D. Medich, D. M. Czajkowsky, S. Sheng, J.-Y. Yuan, and Z. Shao, "Thermal noise reduction of mechanical oscillators by actively controlled external dissipative forces," *Ultramicroscopy*, vol. 84, pp. 119–125, 2000.

[157] A. Hopkins, K. Jacobs, S. Habib, and K. Schwab, "Feedback cooling of a nanomechanical resonator," pp. 1–10.

[158] D. Rugar and P. Grütter, "Mechanical parametric amplification and thermomechanical noise squeezing," *Phys. Rev. Lett.*, vol. 67, pp. 699–702, 1991.

[159] A. Naik, O. Buu, M. D. LaHaye, A. D. Armour, A. A. Clerk, M. P. Blencowe, and K. C. Schwab, "Cooling a nanomechanical resonator with quantum back-action," *Nature*, vol. 443, pp. 193–196, 2006.

[160] J. A. Sidles, J. L. Garbini, K. J. Bruland, D. Rugar, O. Zuger, S. Hoen, and C. S. Yannoni, "Magnetic resonance force microscopy," *Rev. Mod. Phys.*, vol. 67, pp. 249–265, 1995.

[161] R. W. Stark, G. Schitter, M. Stark, R. Guckenberger, and A. Stemmer, "State-space model of freely vibrating and surface-coupled cantilever dynamics in atomic force microscopy," *Phys. Rev. B*, vol. 69, p. 085412, 2004.

[162] S. Rast, C. Wattinger, U. Gysin, and E. Meyer, "Dynamics of damped cantilevers," *Rev. Sci. Instrum.*, vol. 71, pp. 2772–2775, 200.

[163] O. Kotaba, "Developement of the control system for atomic force microscopy," Master's thesis, Brno university of technology, Brno, Czech Republic, 2005.

[164] P. Brohacik, “Control program interface for atomic force microscopy,” Master’s thesis, VSB Technical University of Ostrava, Ostrava, Czech Republic, 2006.

[165] N. W. Jones and D. J. N. Limebeer, “A digital hinf controller for a flexible transmission system,” *Eur, J. of control*, vol. 1, pp. 134–140, 1995.

[166] D. J. Walker, “Contrl of a flexible transmission - a discrete time h-infinity loop shaping approach,” *Eur. J. of control*, vol. 1, pp. 141–147, 1995.

[167] I. D. Landau and G. Zito, *Digital Control Systems Design, Identification and Implementation*. Springer, 2006.

[168] I. D. Landau, A. Karimi, A. Voda, and D. Ray, “Robust digital control of flexible transmissions using the combined pole placement/sensitivity function shaping method,” *Eur. J. of control*, vol. 1, pp. 122–133, 1995.

[169] I. Landau and A. Karimi, “Robust digital control using pole placement with sensitivity function shaping method,” *Int. J. Robust Nonlinear Control*, vol. 8, pp. 191–210, 1998.

[170] G. Jourdan, G. Torricelli, M. Hrouzek, F. Comin, and J. Chevrier, “Limit in the reduction of the brownian motion in afm by cold damping back action of the detection noise,” in *Proceedings of International Conference on Nanoscience and Technology, Basel, Switzerland*, 2006.